

SILICON-BASED HYBRID ORGANIC-INORGANIC POLYMERS AND COATINGS

A Dissertation
Submitted to the Graduate Faculty
of the
North Dakota State University
of Agriculture and Applied Science

By

Hanzhen Bao

In Partial Fulfillment
for the Degree of
DOCTOR OF PHILOSOPHY

Major Department:
Coatings and Polymeric Materials

April 2012

Fargo, North Dakota

North Dakota State University
Graduate School

Title

SILICON-BASED HYBRID ORGANIC-INORGANIC

POLYMERS AND COATINGS

By

HANZHEN BAO

The Supervisory Committee certifies that this *disquisition* complies with North Dakota State University's regulations and meets the accepted standards for the degree of

DOCTOR OF PHILOSOPHY

SUPERVISORY COMMITTEE:

Dr. Bret Chisholm

Chair

Dr. Dean Webster

Dr. Stuart Croll

Dr. Kalpana Katti

Approved:

07/06/12

Date

Dr. Dean Webster

Department Chair

ABSTRACT

Interest in producing hybrid organic-inorganic (HOI) materials has increased rapidly due to the unique combination of properties from the organic and inorganic components. The goal of the research described is to develop various HOI materials and explore their applications in corrosion protection over aerospace aluminum alloys, impact resistant materials, and surface protection over thermoplastic substrates.

As a replacement to toxic chromate inhibitors, environmentally friendly magnesium-rich primers (Mg-rich primers) have been investigated to provide corrosion protection over aerospace aluminum alloys. HOI binders were produced from an alkoxy silane and silica via sol-gel chemistry, where the combined organic and inorganic components provide flexibility, adhesion, and barrier properties. The derived topcoated Mg-rich primers showed promising corrosion protection in a salt spray exposure test and are competitive with chromate-containing primers. The condensation catalyst, tetrabutyl ammonium fluoride (TBAF), played an important role in the performance of the HOI binders and the derived Mg-rich primers. It enabled higher crosslink density and better barrier properties, however, reacted with Mg particles during salt spray exposure and caused the formation of blisters. A non-ionic condensation catalyst, dibutyltin dilaurate (DBTDL), had lower catalyst strength, but was expected to eliminate the blister formation of topcoated Mg-rich primers.

Perfectly alternating polycarbonate-polydimethylsiloxane (PC-PDMS) multiblock copolymers were produced to create transparent impact resistant materials by confining the size of the rubber domains. The PC-PDMS block copolymers maintained high transparency at up to 62 wt% PDMS and shorter block length gave rise to larger partial miscibility. By incorporating

the PDMS blocks to dissipate energy, the PC-PDMS block copolymers had much better impact strength than pure PC oligomers.

Thermoset polycarbonate-polyhedral oligomeric silsesquioxane (PC-POSS) coatings were investigated to serve as surface coatings on PC substrate to provide abrasion resistance. The covalent bonding allowed high POSS loading at up to 18 wt% without sacrificing the transparency. The solvent composition and curing conditions largely determined the surface and bulk properties of the coatings. The incorporation of POSS molecules significantly increased the char yield and mechanical strength of the thermoset coatings, making them promising in surface protection applications.

ACKNOWLEDGMENTS

I would first of all like to thank my advisor, Dr. Bret Chisholm, who persistently gave the encouragement and guidance along in my PhD study, research, and the writing of the dissertation. Thanks for providing the opportunity for me to learn from you. Thanks for being there to offer help whenever I need, no matter which is related to research or not. You are one of the greatest professors I have ever met. My education and research would not have been possible without you.

I would also like to thank my other committee members, Dr. Stuart Croll, Dr. Dean Webster, and Dr. Kalpana Katti, for the time and efforts spent in reading, commenting, and giving suggestions on my dissertation and defense.

I gratefully acknowledge the help from Dr. Partha Majumdar, Dr. Andrey Chernykh, Dr. Jie He, and Dr. Seva Balbyshev, with whom I had great discussions over various issues encountered and the obtained results. The thoughts that have been shared are valuable to me. I would like to thank Rajana Sharma, Liz Crowley, and James Bahr for their contributions to the research. I would like to thank Heidi Docktor, Ken Croes, and Jared Risan for their assistance and support on instruments. Sincere thanks should also be given to Virginia Tech for instrument support for SAXS and TEM. I would like to thank everyone in Combi lab and CPM department who ever helped me and established a friendly relationship with me. Thanks for the funding provided from Durable Hybrid Coatings (DHC) and Defense Threat Reduction Agency (DTRA).

DEDICATION

I would like to dedicate my doctoral dissertation to my husband, Yinming Zhu, who has consistently supported me throughout my life and especially in my PhD study. Only with his love, understanding, encouragement, and sacrifice, I could persistently focus on my research and successfully complete my dissertation. The dissertation is also dedicated to my daughter, Emma Zhu, who brought a new meaning to my life.

I would also like to dedicate the dissertation to my father, Xingchang Bao, and my mother, Shanrong Gu, who came to Fargo to offer help taking care of Emma. And finally I would like to thank my sister, Chunju Gu, and her family for being in Fargo and forming a big family with us. My life would not have been so versatile without you.

TABLE OF CONTENTS

ABSTRACT	iii
ACKNOWLEDGMENTS	v
DEDICATION	vi
LIST OF TABLES	xiv
LIST OF FIGURES	xvi
LIST OF SCHEMES	xxiii
CHAPTER 1. GENERAL INTRODUCTION	1
1.1. Hybrid Organic-Inorganic (HOI) Materials	1
1.2. Organo-Silicon Compounds	3
1.2.1. Silica	4
1.2.2. Polydimethylsiloxane (PDMS)	7
1.2.3. Polyhedral Oligomeric Silsesquioxane (POSS).....	9
1.3. Synthetic Methods	11
1.3.1. Sol-Gel Chemistry	11
1.3.2. Hydrosilylation Chemistry	15
1.4. References	17
CHAPTER 2. ENVIRONMENTALLY FRIENDLY HYBRID ORGANIC-INORGANIC (HOI) MAGNESIUM-RICH PRIMER FOR CORROSION PROTECTION OF ALUMINUM ALLOYS.....	24
2.1. Abstract	24
2.2. Introduction	25
2.3. Experimental	27
2.3.1. Raw Materials	27

2.3.2.	Synthesis of HOI Binder Solutions.....	27
2.3.3.	Preparation of HOI Coatings.....	28
2.3.4.	Preparation of Mg-Rich Primers.....	29
2.3.5.	Instrumentation	30
2.4.	Results and Discussion	32
2.4.1.	Synthesis and Characterization of HOI Solutions	32
2.4.2.	Characterization of HOI Coatings	38
2.4.3.	Characterization of Mg-Rich Primers Based on HOI Binders	43
2.5.	Conclusion.....	46
2.6.	References	47
CHAPTER 3. HYBRID ORGANIC-INORGANIC (HOI) MATERIALS DEVELOPED BY AUTOMATED PARALLEL SYSTEM.....		50
3.1.	Abstract	50
3.2.	Introduction	50
3.3.	Experimental	51
3.3.1.	Raw Materials	51
3.3.2.	Automated Synthesis of HOI solutions	52
3.3.3.	Preparation of HOI Coatings.....	54
3.3.4.	Instrumentation	54
3.4.	Results and Discussion	56
3.4.1.	Synthesis and Characterization of HOI Solutions	56
3.4.2.	Characterization of HOI Coatings	62
3.5.	Conclusion.....	64
3.6.	References	65

CHAPTER 4. HYBRID ORGANIC-INORGANIC (HOI) MATERIALS—THE EFFECT OF CATALYST	67
4.1. Abstract	67
4.2. Introduction	67
4.3. Experimental	68
4.3.1. Raw Materials	68
4.3.2. Synthesis and Characterizaiton of HOI Solutions.....	68
4.3.3. Preparation of HOI Coatings.....	69
4.3.4. Instrumentation	69
4.4. Results and Discussion	70
4.4.1. Sythesis and Characterization of HOI Solutions	70
4.4.2. Characterization of HOI Coatings	71
4.5. Conclusion.....	74
4.6. References	74
CHAPTER 5. PERFECTLY ALTERNATING POLYCARBONATE-POLYDIMETHYLSILOXANE (PC-PDMS) MULTIBLOCK COPOLYMERS—PART I.....	75
5.1. Abstract	75
5.2. Introduction	76
5.3. Experimental	77
5.3.1. Raw Materials	77
5.3.2. Synthesis of Allyl-Polycarbonate (Allyl-PC)	77
5.3.3. Synthesis of Polycarbonate-Polydimethylsiloxane (PC-PDMS) Multiblock Copolymers.....	82
5.3.4. Instrumentation	84

5.4.	Results and Discussion	86
5.4.1.	Synthesis of Allyl-PCs	86
5.4.1.1.	TEA As A Catalyst	93
5.4.1.2.	TEBA As A Catalyst.....	95
5.4.2.	Synthesis of PC-PDMS Block Copolymers	96
5.4.3.	Glass Transition Temperature by MDSC	100
5.4.4.	Thermal Stability by TGA	103
5.4.5.	Viscoelastic Properties by DMA	105
5.4.6.	Surface Properties by AFM.....	106
5.4.7.	Catalyst Removal.....	106
5.4.8.	Optical Clarity.....	107
5.5.	Conclusion.....	109
5.6.	References	110
CHAPTER 6. PERFECTLY ALTERNATING POLYCARBONATE- POLYDIMETHYLSILOXANE (PC-PDMS) MULTIBLOCK COPOLYMERS—PART II.....		115
6.1.	Abstract	115
6.2.	Introduction	116
6.3.	Experimental	116
6.3.1.	Raw Materials	116
6.3.2.	Synthesis of PC-PDMS Block Copolymer.....	117
6.3.3.	Instrumentation	118
6.4.	Results and Discussion	122
6.4.1.	Synthesis of PC-PDMS Block Copolymers	122

6.4.2. Optical Clarity.....	122
6.4.3. Glass Transition Temperature by MDSC	123
6.4.4. Thermal Stability by TGA	130
6.4.5. Viscoelastic Properties by DMA	134
6.4.6. Water Contact Angle.....	137
6.4.7. AFM.....	139
6.4.8. Small Angle X-Ray Scattering (SAXS).....	140
6.4.9. TEM.....	143
6.4.10. Izod Impact Strength.....	144
6.5. Conclusion.....	145
6.6. References	146

**CHAPTER 7. POLYCARBONATE-POLYHEDRAL OLIGOMERIC SILSESQUIOXANE
(PC-POSS) THERMOSET COATINGS—THE EFFECT OF SOLVENT COMPOSITION
AND CURING CONDITION.....150**

7.1. Abstract	150
7.2. Introduction	150
7.3. Experimental	153
7.3.1. Raw Materials	153
7.3.2. Preparation of PC-POSS Thermoset Coatings.....	153
7.3.3. Instrumentation	155
7.4. Results and Discussion	157
7.4.1. Preparation of PC-POSS Thermoset Coatings	157
7.4.2. Surface Properties.....	159
7.4.3. Thermal Properties.....	163

7.4.4. Chemical Resistance	166
7.5. Conclusion.....	167
7.6. References	168
CHAPTER 8. POLYCARBONATE-POLYHEDRAL OLIGOMERIC SILSESQUIOXANE (PC-POSS) THERMOSET COATINGS—THE EFFECT OF POSS CONTENT AND CROSSLINK DENSITY	174
8.1. Abstract	174
8.2. Introduction	174
8.3. Experimental	176
8.3.1. Raw Materials	176
8.3.2. Preparation of PC-POSS Thermoset Coatings.....	176
8.3.3. Instrumentation	177
8.4. Results and Discussion	180
8.4.1. Preparation of PC-POSS Thermoset Coatings	180
8.4.2. Optical Clarity.....	185
8.4.3. Surface Properties.....	186
8.4.4. Thermal Properties.....	189
8.4.5. Coating Hardness.....	194
8.4.6. Abrasion Resistance.....	195
8.5. Conclusion.....	196
8.6. References	197
CHAPTER 9. OVERALL CONCLUSION.....	200
CHAPTER 10. FUTURE WORK.....	203
10.1. Novel HOI Binders for Mg-Rich Primers.....	203

10.2.	Perfectly Alternating PC-PDMS Multiblock Copolymers.....	204
10.3.	Thermoset PC-POSS Coatings.....	204
10.4.	Highly Pure Allyl-PCs.....	205

LIST OF TABLES

<u>Table</u>	<u>Page</u>
2.1. Description of HOI coatings produced from HOI solutions, noTBAF and wTBAF.....	28
2.2. Description of the Mg-rich primers produced from HOI solutions, noTBAF and wTBAF ..	29
3.1. Dispensing volume of chemicals (in mL) for twelve HOI solution syntheses	53
3.2. Dry film thickness (μm) of the HOI binders	55
5.1. Compositions (mmol) and summarized results of the allyl-PCs synthesized using TEA as a catalyst	80
5.2. Compositions (mmol) and summarized results of the allyl-PCs synthesized using TEBA as a catalyst	81
5.3. Composition of the twelve PC-PDMS block copolymers.....	83
5.4. Description of PC-b-PDMS copolymers.....	100
5.5. Thermal stability evaluated by TGA.....	104
5.6. PtO_2 removal treatment of PC-b-PDMS copolymers.....	107
6.1. Composition of the twelve PC-PDMS block copolymers produced	119
6.2. T_g s ($^{\circ}\text{C}$) obtained from MDSC.....	124
6.3. Thermal degradation evaluated by TGA in air.....	133
6.4. Interdomian spacing d of block copolymers.....	143

7.1. Compositions of the thermoset PC-POSS coatings produced	154
7.2. TGA data in N ₂ of PC-POSS coatings derived from CH ₂ Cl ₂ as a solvent and cured at RT	165
8.1. Compositions of the thermoset PC-POSS coatings produced.....	177
8.2. TGA results of PC3K-POSS coatings.....	192
8.3. DMA results of PC5K-POSS coatings.....	194

LIST OF FIGURES

<u>Figure</u>	<u>Page</u>
1.1. Example of a homogeneous (left) and a heterogeneous (right) HOI material.....	1
1.2. Main synthesis routes for the preparation of HOI materials.....	3
1.3. Structure of silicon-based compounds.....	4
1.4. Structure of silica particles with silanol (Si-OH) groups on the surface	6
1.5. Chemical structure of PDMS	8
1.6. Predicted phase morphology for AB diblock copolymers: spherical (S), cylindrical (C), gyroid (G), and lamellar (L).....	9
1.7. General structure of POSS	10
1.8. Formation and processing of sol-gel products	14
2.1. Schematic of aerospace coating systems	25
2.2. Synthetic process used to create the HOI solutions for making Mg-rich primers.....	33
2.3. ^1H -NMR spectra of silica sols produced both in absence (blue) and in presence (red) of catalyst TBAF.....	34
2.4. Chemical shifts of silicon compounds in ^{29}Si -NMR.....	35
2.5. ^{29}Si -NMR spectra of noTBAF and wTBAF HOI solutions	36
2.6. FTIR spectra of thin films of noTBAF and wTBAF HOI solutions	37

2.7. Particle size of colloidal silica, organosilane functionalized silica sols without, and with TBAF.....	37
2.8. FTIR spectra obtained from coatings produced from noTBAF and various curing conditions	39
2.9. FTIR spectra obtained from coatings produced from nwTBAF and various curing conditions	39
2.10. Relative intensity of the FTIR peak absorbance at (a) 3350 cm^{-1} (O-H stretching), (b) 1120 cm^{-1} (Si-O-CH ₃ stretching), (c) 905 cm^{-1} (Si-OH stretching), and (d) 480 cm^{-1} (Si-OCH ₃ bending) to the peak absorbance at 1496 cm^{-1} (C=C stretching in phenyl group of PhEtTMS)	40
2.11. DSC curves of HOI coatings	41
2.12. Glass transition temperature of coatings derived from noTBAF and wTBAF cured using various conditions	41
2.13. Low frequency (0.01 Hz) impedance of HOI coatings derived from noTBAF and wTBAF HOI solutions, as a function of curing conditions	42
2.14. Bode plots for Mg-rich primers.....	43
2.15. Images of scribed, topcoated Mg-rich primers derived from noTBAF system after B117 salt spray exposure as a function of exposure time and curing condition.....	44
2.16. Images of scribed, topcoated Mg-rich primers derived from wTBAF system after B117 salt spray exposure as a function of exposure time and curing condition.....	45
2.17. Image of a sliced blister from a topcoated sample based on wTBAF after salt spray exposure.....	45
3.1. An schematic illustration of experimental design of HOI solution synthesis using Chemspeed.....	57
3.2. Evaluation of Chemspeed Synthesis Station reproduction by comparing HOI solution synthesis by (a) product weight, (b) distillation product weight, and (c) total weight	58

3.3. Solid content of the HOI solutions produced by Chemspeed	59
3.4. ²⁹ Si-NMR spectra of the HOI solutions produced to compare the effect of PhEtTMS level in absence (a) and in presence (b) of TBAF	60
3.5. ²⁹ Si-NMR spectra of the HOI solutions produced to compare the effect of condensation catalyst TBAF at medium (a) and high (b) of PhEtTMS level	61
3.6. Particle size of the HOI solutions produced by Chemspeed	62
3.7. An schematic illustration of experimental design of HOI binder produced	63
3.8. Low frequency (0.01 Hz) impedance of coatings derived from noTBAF and wTBAF cured using various conditions	64
4.1. Solid content of HOI solutions produced without catalyst, with DBTDL and TBAF as catalyst respectively	70
4.2. Particle size of colloidal silica, the HOI solutions produced without catalyst, with DBTDL and TBAF as catalyst respectively	71
4.3. HOI binders produced under different curing conditions.....	72
4.4. FTIR spectra of HOI binders produced using different catalyst and cured under (a) 23C/24hr, (b) 80C/1hr, (c) 80C/24hr	73
5.1. A schematic illustration of the experimental design used for allyl-PC synthesis	79
5.2. A schematic illustration of experimental design for producing PC-PDMS block copolymer synthesis.....	82
5.3. FTIR spectra of bisphenol-A, eugenol and allyl-PC.....	87
5.4. ¹ H-NMR spectra of BPA, eugenol and allyl-PC.....	88
5.5. Example of ³¹ P-NMR spectra of allyl-PC for ppm OH quantification.....	90

5.6. Representative MALDI spectra displaying allyl-PC containing high eugenol end capping at both ends (top, B4 from Table 5.2), significant contamination with cyclic PCs (middle, A8 from Table 5.1), and contamination with both cyclics and linear polymers possessing a hydroxyl endgroup (bottom, A4 from Table 5.1)	92
5.7. GPC traces overlay of neat PC, PDMS, physical mixture of PC and PDMS, and PC-PDMS block copolymer.....	98
5.8. ¹ H-NMR spectra of PC& PDMS physical mix and PC-PDMS block copolymer.....	99
5.9. PC block glass transition temperature of PC-PDMS block copolymers with PC block length of (a) 3K, (b) 5K, and (c) 8K by MDSC.....	101
5.10. PDMS block glass transition temperature of PC-PDMS block copolymers with PDMS block length of (a) 5.3K, and (b) 12K by MDSC.....	102
5.11. TGA curves of PC-PDMS block copolymers with PC block length of (a) 3K, (b) 5K, and (c) 8K under N ₂	103
5.12. DMA curve of PC-PDMS block copolymers.....	105
5.13. AFM images of (a) allyl-PC and (b) a PC-PDMS block copolymer.....	106
5.14. Optical clarity of compression molded PC-b-PDMS copolymer samples after PtO ₂ removal.....	108
5.15. Images of approximately 1 mm thick compression molded films of a PC-PDMS block copolymer possessing 20 wt % PDMS and synthesized using the two-step process involving hydrosilylation (a) and a commercial PC-PDMS block copolymer possessing only 5 wt % PDMS (b).....	109
6.1. A schematic illustration of experimental design for PC-PDMS block copolymer synthesis.....	118
6.2. An image of solvent cast film of PC-PDMS block copolymers on glass slides.....	123
6.3. Representative MDSC thermograms obtained at temperatures between 40 to 160 °C	125

6.4. Representative MDSC thermograms obtained at temperatures between -170 to -10 °C.....	125
6.5. T_g data associated with the PC-rich phase as a function of the block Mns of the copolymers.....	126
6.6. The reduction in the T_g of the PC-rich phase as a function of block Mns.....	127
6.7. A comparison of PC-rich phase T_g at equivalent PC/PDMS ratio.....	128
6.8. TGA curves of PC-PDMS block copolymers with PC block length of (a) 3K, (b) 5K, and (c) 8K in air.....	131
6.9. TGA curves of PC-PDMS block copolymers with PDMS block length of (a) 0.7K, (b) 1.2K, (c) 5.3K, and (d) 12K in air.....	132
6.10. TGA char yield of the PC- <i>b</i> -PDMS copolymers in air.....	134
6.11. Storage moduli and loss tangent data for all three multiblock copolymers possessing the lowest Mn PDMS blocks	135
6.12. A comparison of viscoelastic properties at approximately equivalent PDMS content (i.e. 20 wt. % PDMS).....	136
6.13. The effect of PDMS block Mn on viscoelastic properties of block copolymers based on 3,000 g/mole PC blocks.....	137
6.14. Water contact angle of PC-PDMS block copolymers (the percentage values labeled on bars indicate the PDMS content of each block copolymer).....	138
6.15. AFM images of PC- <i>b</i> -PDMS copolymers compared with PC control.....	139
6.16. SAXS profiles of PC control, commercial PC-PDMS random copolymer, and synthesized block copolymers.....	141
6.17. SAXS profile of PC3K-PDMS5.3K_62%.....	142

6.18. TEM images of commercial PC-PDMS random copolymer and synthesized PC-PDMS block copolymers.....	144
6.19. Izod impact strength of commercial pure PC from Dow (C-PC), commercial PC-PDMS block copolymer from Sabic (C-PD-PDMS), and three synthesized PC-PDMS block copolymers with relatively low PDMS content (PC8K-PDMS0.7K_9%, PC5K-PDMS0.7K_13%, PC8K-PDMS1.2K_13%).....	145
7.1. A schematic illustration of the experimental design used for coating formulations	158
7.2. Images illustrating transparent, thermoset PC-POSS coating (left); and opaque, non-crosslinked PC-POSS coating from solution blend (right) over glass slide after applying identical curing condition.....	159
7.3. Water contact angle data of PC-POSS coatings.....	160
7.4. AFM images of PC-POSS coatings as a function of POSS wt %	162
7.5. AFM images of PC-POSS coatings illustrating the effects of solvent compositions and curing conditions on surface topography.....	162
7.6. T _g values of PC-POSS coatings.....	164
7.7. DSC overlay of second heating cycle of PC-POSS coatings derived from CH ₂ Cl ₂ as a solvent and cured at ambient conditions.....	164
7.8. Degree of swelling of thermoset PC-POSS coatings derived from CH ₂ Cl ₂ as a solvent and cured at ambient conditions	166
7.9. Degree of swelling values illustrating the effects of curing conditions	167
8.1. The combi-abraser used for abrasion test.....	180
8.2. A schematic illustration of the experimental design used for coating formulations.....	182
8.3. FTIR spectrum of (a) allyl-PC, (b) Octasilane-POSS® and PC-POSS coatings with (c) 8 wt% POSS and (d) 15 wt% POSS.....	183

8.4. Gel content and swelling degree of PC-POSS coatings based on 5K PC and 3K PC.....	185
8.5. Pictures of (a) PC5K-POSS physical mixture in absence of catalyst (top) and thermoset coatings (bottom) and (b) PC3K-POSS physical mixture in absence of catalyst (top) and thermoset coatings (bottom).....	185
8.6. UV-Vis spectra of (a) PC5K-POSS coatings and (b) PC3K-POSS coatings.....	186
8.7. Water contact angle of PC-POSS coatings.....	187
8.8. AFM images of (a) PC5K-POSS coatings and (b) PC3K-POSS coatings.....	188
8.9. DSC curves of (a) PC5K-POSS coatings and (b) PC3K-POSS coatings.....	190
8.10. TGA curves of PC and OctaSilane-POSS® controls, and PC-POSS coatings under N ₂	191
8.11. Char yield of PC-POSS coatings determined by TGA.....	193
8.12. Pendulum hardness of (a) PC5K-POSS coatings and (b) PC3K-POSS coatings.....	195
8.13. Abrasion resistance of PC-POSS coatings.....	196
9.1. The optical and mechanical properties of PC-PDMS block copolymers.....	201
9.2. Tunable surface and bulk properties of thermoset PC-POSS coatings by varying the preparation condition.....	202

LIST OF SCHEMES

<u>Scheme</u>	<u>Page</u>
1.1. Synthesis of silica via sol-gel chemistry.....	5
1.2. Synthesis of POSS by hydrolytic condensation	10
1.3. Hydrolysis and condensation of sol-gel chemistry	12
1.4. Hydrosilylation reactions	15
2.1. Half reactions and standard oxidation potential of Al and Mg.....	26
2.2. Synthesis of organically-modified silica in HOI solutions via sol-gel chemistry.....	33
5.1. Schematic representation of allyl-PC synthesis by interfacial polymerization.....	86
5.2. Hydroxyl and carboxyl groups derivatized by 1,2-phenylene phosphorochloridite (PPC) for ³¹ P-NMR analysis.....	90
5.3. Activation, condensation, and hydrolysis reactions in presence of TEA as a catalyst.....	94
5.4. Reactions in presence of TEBA as a phase transfer catalyst.....	95
5.5. Traditional PC-PDMS block copolymer synthesis.....	96
5.6. Two-step synthesis of perfectly alternating PC-PDMS block copolymer.....	97
7.1. A schematic illustrating the formation of crosslinked network involving allyl-PC and OctaSilane-POSS® to produce thermoset PC-POSS coating.....	157
8.1. A schematic illustrating the formation of crosslinked network involving allyl-PC and OctaSilane-POSS® to produce thermoset PC-POSS coating.....	181

CHAPTER 1. GENERAL INTRODUCTION

1.1. Hybrid Organic-Inorganic (HOI) Materials

Hybrid organic-inorganic (HOI) materials have been gaining intense interest over the past few decades. HOI materials help meet the demand of fast-developing technologies by combining the properties of organic and inorganic phases. The appealing features of HOI materials arise from the combination of different properties and functions of the organic phase (low density, high elasticity, good processability etc.) and the inorganic phase (thermal stability, hardness, high strength, low permeability etc.). HOI materials are not simply physical mixtures of the two phases, but hybridized materials with organic and inorganic phases interacting at the molecular level through weak or strong bonding. With limited domain size in the nanoscale range, the interface plays a predominant role in determining the properties of the HOI materials. HOI materials can be homogeneous or heterogeneous depending on synthetic method. Homogeneous HOIs contain miscible organic and inorganic components, while heterogeneous HOIs are nanoscale phase-separated materials with domain sizes ranging from angstroms to nanometers.¹ Examples of homogenous and heterogeneous HOIs are displayed in Figure 1.1, in which the homogeneous HOI material is a uniform system with strong hydrogen bonding between two phases and the heterogeneous HOI material is a polymer-clay nanocomposite.^{2,3}

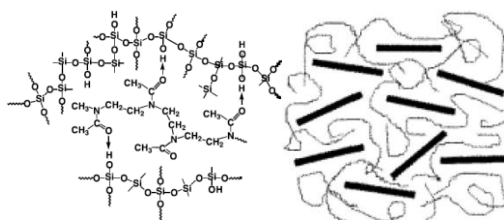


Figure 1.1. Example of a homogeneous (left) and a heterogeneous (right) HOI material. (Copied from Ref. 2 and 3)

The history of HOI materials dates back to the 8th century when Maya blue pigment, which is a blue indigo molecule embedded in a clay mineral, was used for painting, and it was found that Maya blue was able to withstand harsh environments for twenty centuries.¹ However, the concept of HOI materials was not well recognized until sol-gel chemistry was developed as a soft inorganic chemistry to produce the hybrid materials at nanometer range in the eighties. Besides sol-gel chemistry, the chemical strategies to make HOI materials include hydrothermal synthesis, the assembly or dispersion of nano-building blocks, and self-assembly procedures.¹ The chemical routes for the preparation of HOIs are summarized in an excellent review by Cle'ment Sanchez et al., as displayed in Figure 1.2. Sol-gel chemistry is the most intensively investigated method to produce HOI materials due to its appealing mild reaction conditions and simple requirement for setups. Through sol-gel chemistry, the HOI materials are produced from metal alkoxide (A_1) and bridged silsesquioxanes (A_2).⁴ The hydrothermal synthesis (A_3) describes a method for the preparation of crystalline hybrid materials under high pressure and temperature. Nano-building blocks (B_1 and B_2) are inorganic units dispersed into a polymer matrix while maintaining their integrity at the nanometer scale. The self-assembly method involves templated growth in the presence of surfactants (C_1), bridged silsesquioxane (C_2), and nano-building blocks (C_3). The combination of the above described methods (A, B and C) allows the generation of HOI materials with controlled hierarchical structure, named integrative synthesis (D).

The various synthesis routes allow the design of numerous versatile materials for different applications including optical components, sensors, catalyst supports, scratch-resistant coatings, barrier coatings, etc. Some of the HOI materials now are commercially available.

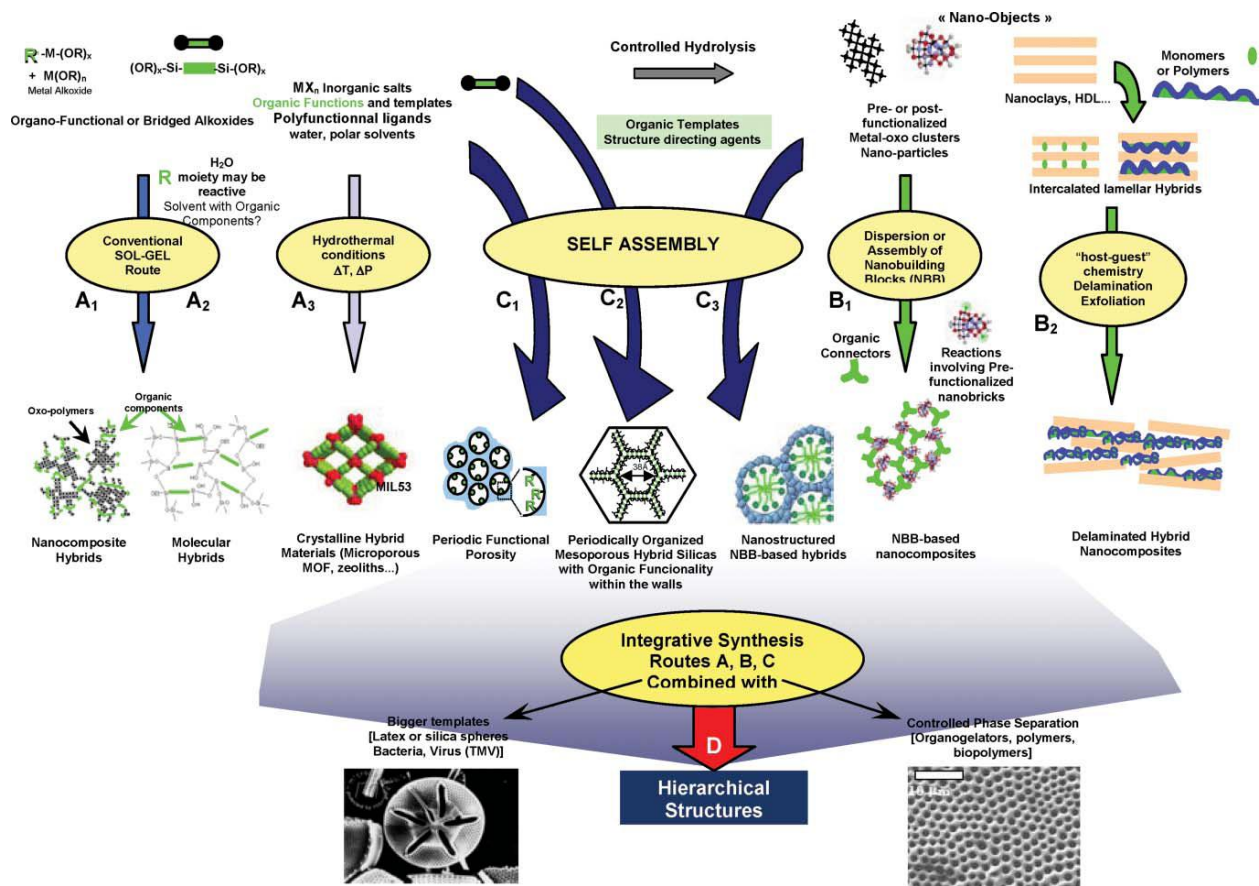


Figure. 1.2. Main synthesis routes for the preparation of HOI materials. (Copied from Ref. 1)

1.2. Organo-Silicon Compounds

Most silicon compounds exist in four forms depending on the number of oxygen atoms attached to silicon. The structures of the silicon compounds can be represented as $R_3SiO_{0.5}$, R_2SiO , $RSiO_{1.5}$ and SiO_2 when one, two, three and four oxygen atoms are attached to the silicon atom, as shown in Figure 1.3.⁵ The R group can be hydrogen, alkyl, aryl or other organic substituents. In the scope of our study presented in the upcoming chapters, the silicon compound utilized as inorganic phases covered all of them, silica (SiO_2) and phenethyl trimethoxysilane ($R_3SiO_{0.5}$), polydimethylsiloxane (R_2SiO), and polyhedral oligomeric silsesquioxane ($RSiO_{1.5}$) in Chapters 2-4, Chapters 5 and 6, and Chapters 7 and 8, respectively.

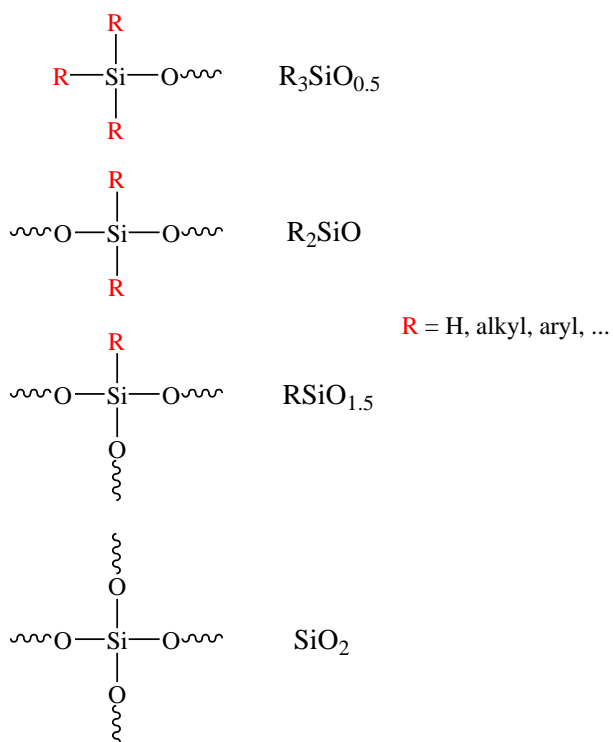
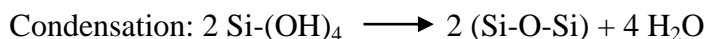
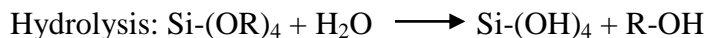


Figure 1.3. Structure of silicon-based compounds.

1.2.1. Silica

Silica, also known as silicon dioxide, is found to exist in various forms in nature such as sand, quartz and glass. These naturally occurring materials differ in their crystalline morphology. Synthetically, silica were produced in amorphous form by various methods including sol-gel technology in solution, pyrogenic method of burning silicon tetrachloride with hydrogen and oxygen at high temperature, and precipitation of a silicic acid solution.⁶ Of the three methods, sol-gel technology is intensively utilized by researchers for making HOI materials due to the easy manipulation and mild reaction conditions while the other two methods are usually used in industry to produce more condensed silica particles. The synthesis of spherical silica nanoparticles with narrow polydispersity through sol-gel chemistry was first reported by Stober

et al in 1968.^{7,8} The aqueous solution of silicon alkoxide undergoes hydrolysis and condensation reactions in the presence of ammonia as a catalyst, as displayed in Scheme 1.1.



Scheme 1.1. Synthesis of silica via sol-gel chemistry.

Colloidal silica was investigated in our study, which differs from common silica with respect to size. The colloidal system is a dispersion in which the particles, in the form of gas, liquid or gas, are dispersed in a continuous phase in the form of gas or liquid. Colloidal systems can be observed in our daily lives.⁹ Fog and smoke are liquid and solid particles dispersed in a continuous gas phase, respectively. Emulsion and sol are liquid and solid particles dispersed in a continuous liquid phase, respectively. The size of the dispersed particles should be within 1 to 1000 nm to be a colloidal system. It is so-called colloidal silica because it's sufficiently small not to be affected by gravitational forces and also sufficiently large to deviate from a true solution. The interactions between particles are dominated by short-range forces such as van der Waals attractions and surface charges. In colloidal systems, due to the high surface to volume ratio, the properties of the interface play a predominant role in the properties of the system. Colloidal systems have some interesting features making them different from other systems. The "Tyndall Effect" is an important characteristic of colloidal system, which describes the light scattering phenomena by colloidal particles.

The surface chemistry and geometry determine the stability of colloidal silica sols. There are mostly silanol (Si-OH) groups on the surfaces allowing for chemical modifications, which

can be isolated, paired or hydrogen bounded silanol groups.⁹ There are also siloxane bridges on the surfaces of silica particles. Figure 1.4 shows a general chemical structure of a silica particle with a majority of silanol groups on the surface. Due to the surface silanol groups, the colloidal silica nanoparticles keep their stability in water or organic solvent by surface charge repulsion. When gelled, silica particles are linked together and form a three-dimensional network. The destabilization of colloid silica can be accomplished by adding salts or electrolytes to interrupt the electrostatic repulsion.

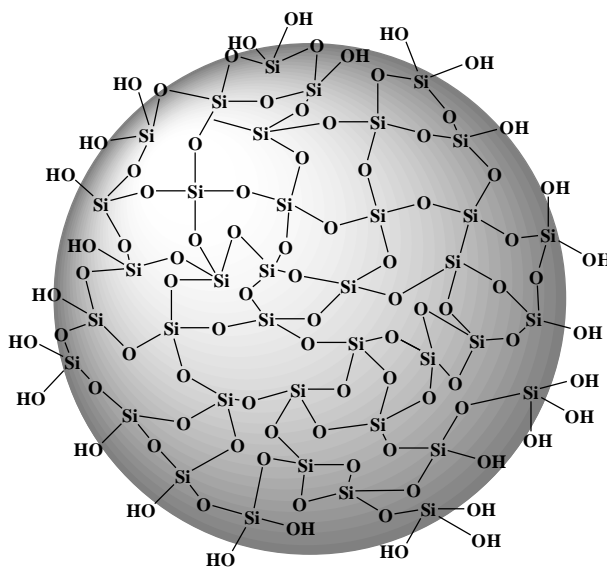


Figure 1.4. Structure of silica particles with silanol (Si-OH) groups on the surface.

The surface chemistry and geometry determine the stability of colloidal silica sols. There are mostly silanol (Si-OH) groups on the surfaces allowing for chemical modifications, which can be isolated, paired or hydrogen bounded silanol groups.⁹ There are also siloxane bridges on the surfaces of silica particles. Figure 1.4 shows a general chemical structure of a silica particle with a majority of silanol groups on the surface. Due to the surface silanol groups, the colloidal silica nanoparticles keep their stability in water or organic solvent by surface charge repulsion.

When gelled, silica particles are linked together and form a three-dimensional network. The destabilization of colloid silica can be accomplished by adding salts or electrolytes to interrupt the electrostatic repulsion.

HOI materials containing colloidal silica are produced mostly by in-situ synthesis from tetraethylorthosilicate (TEOS) via sol-gel chemistry.¹⁰ The silica nanoparticles are incorporated into the polymer matrix by encapsulating within polymer matrix to form core-shell architecture or interpenetrate with polymer chains used for sensor, target labeling, compatibility improvement with proteins.¹¹ Silica aerogel has been produced to increase the adhesion between Pt catalyst and carbon support to prevent catalyst leaching without decreasing the transport of solvent and fuels in fuel cell application.¹² Porosity created within silica act as immobilization site for dyes and transport ducts of ions.^{13,14} In addition, the incorporation of silica has enabled the improvements in mechanical properties,^{15,16} adhesion,^{12,13} gas permeation¹⁷, etc. Various polymers have been modified with silica via sol-gel chemistry, including polyvinyl alcohol, polyaniline, polyimide, polyelectrolyte like polyacrylic acid and poly(sodium styrenesulfonate), and so on.

1.2.2. Polydimethylsiloxane (PDMS)

Polydimethylsiloxane (PDMS) is a polymeric organosilicon compound which is commonly referred to as silicone. Attributed to its inorganic siloxane backbone and organic methyl groups, PDMS itself is an organic-inorganic compound. It is synthesized by reacting dimethyldichlorosilane (Me_2SiCl_2) with water, or by ring opening octamethylcyclotetrasiloxane (D_4).^{18,19} The chemical structure of PDMS is shown in Figure 1.5, in which the backbone

consists of repeating silicon and oxygen atoms with two methyl groups carried by each silicon atom. The siloxane linkage is responsible for the high flexibility of the backbone.

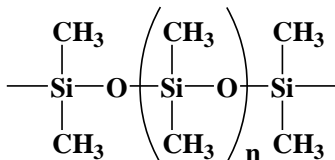


Figure 1.5. Chemical structure of PDMS.

Because of its unique chemical structure, the physical properties of PDMS are different from common thermoplastic resins. Depending on the degree of polymerization, PDMS is usually liquid or a viscoelastic solid at ambient conditions. It has low glass transition temperature. In addition to that, PDMS is chemically inert, non-toxic, biocompatible, non-flammable, hydrophobic, and has high oxygen permeability. Research has been carried out to improve properties including processability, flame retardancy, and surface hydrophobicity. The unique properties of PDMS allow this polymer to be widely used in various applications such as lubricants, contact lenses, biomedical devices, pervaporation membranes for fuel separation, crack-free glass, and so on.^{20,21,22}

Modifications of materials with PDMS were primarily achieved by blending, copolymerization, and the production of interpenetrating polymer networks (IPN).²⁰ Copolymers containing PDMS blocks/segments are an interesting class of materials due to the unique characteristics of PDMS compared to other polymers. PDMS has been copolymerized with various polymers including commonly used polystyrene,²³ polymethyl methacrylate,²⁴ polyamide,²⁵ polycaprolactone,²⁶ polyurethane,²⁷ polyethylene oxide,²⁸ specially metal complexed poly(ferrocenylsilanes),²⁹ and poly(ferrocenylphenylphosphine).³⁰ PDMS segments

may be copolymerized with other thermoplastics, forming various architectures such as diblock/multiblock copolymers, random copolymer, sequential copolymer, alternating copolymer, graft copolymer etc.

For block copolymers, depending on the block copolymer composition f and combination parameter χN where χ is the segment-segment interaction energy and N is the degree of polymerization, the phase morphology changes accordingly.³¹ As shown in Figure 1.6, there are basically four types of morphologies: spherical, cylindrical, gyroid and lamellar.

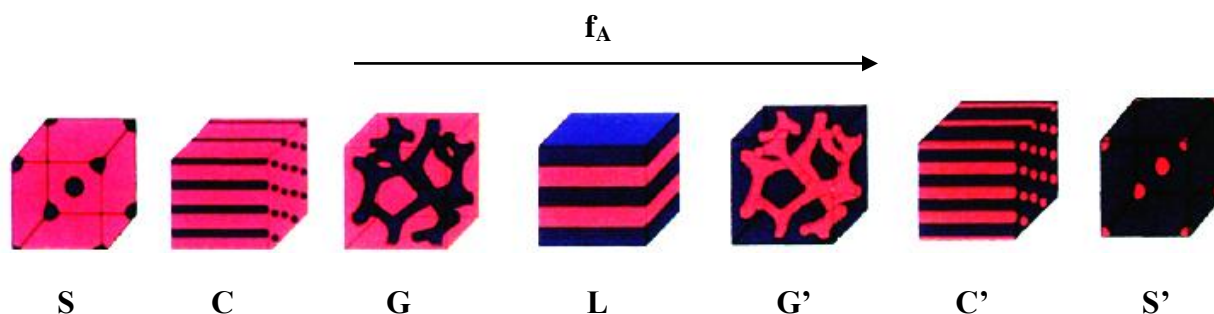


Figure 1.6. Predicted phase morphology for AB diblock copolymers: spherical (S), cylindrical (C), gyroid (G), and lamellar (L).³¹

The phase separation of block copolymers has obtained intense attentions due to the interesting morphologies. Small angle x-ray scattering (SAXS) is a powerful technique to determine the unique morphologies derived from the phase separation of PDMS block copolymers.³¹⁻³³ By calculating the q vector ratio between the scattering maximum peaks, the morphology of the block copolymer can easily be determined. Transmission electron microscopy (TEM) technique visually provides morphological information.

1.2.3. Polyhedral Oligomeric Silsesquioxane (POSS)

POSS is a ~ 2 nm, three-dimensional cage-like molecule that has eight silicon atoms at each corner with organic substituents attached.³⁴ The general structure of POSS is shown in

Figure 1.7. The three-dimensional cage serves to provide mechanical properties, while the organic substituents improve compatibility with polymers and allow for chemical modifications. POSS compounds are synthesized by hydrolytic condensation of trifunctional silane monomers RSiX_3 where R is a chemically stable organic substituent and X is a reactive alkoxy or halogenate group. The reaction scheme is shown in Scheme 1.1. The reactive peripheral organic groups make POSS molecules ideal for incorporating into polymers by covalent bonding, generating homogeneous HOI materials. Because of the high functionality of POSS compounds, the number of reactive functional groups can be changed for different modifications or to adjust the reactivity of the molecule. Therefore, partially or fully substituted POSS molecules are incorporated into various polymers through blending, grafting and copolymerization, making polymer/POSS blends, polymer with POSS as side groups or in backbone, polymer-POSS networks, or POSS-centered star polymers.³⁵⁻³⁷

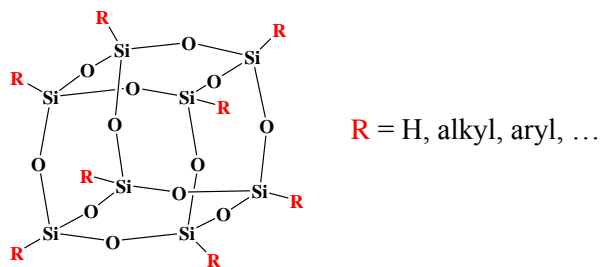
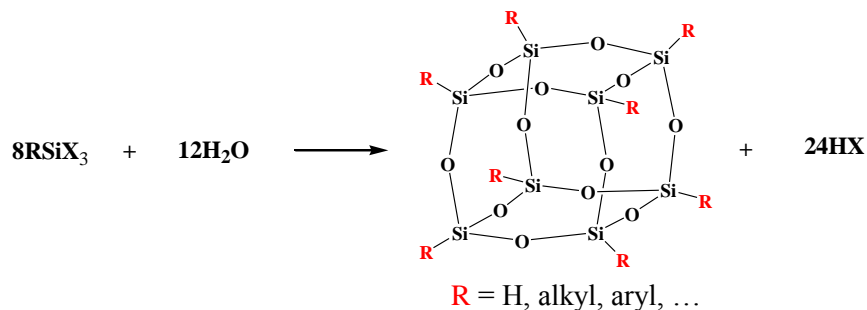


Figure 1.7. General structure of POSS.



Scheme 1.2. Synthesis of POSS by hydrolytic condensation.

The incorporation of POSS into polymers can result in significant enhancements of polymer properties, such as hardness, surface hydrophobicity, and mechanical properties and so on.³⁸ POSS compounds have been used in biomedical applications due to its environmentally-benign nature.³⁹ Most commonly used polymers such as polyethylene (PE), polypropylene (PP), polystyrene (PS), polyamide (PA), polyimide (PI), and polyurethane (PU) have been modified with POSS derivatives.⁴⁰

The POSS molecule used in our study is OctaSilane POSS[®] in which R = OSi(CH₃)₂H. It is selected for making PC-POSS thermoset coatings for its higher reactivity due to less steric hindrance and the lower cost as compared to OctaHydro POSS[®] in which R = H. It has been applied as nanofiller, crosslinker, or core and branch of dendrimers,^{41,42} for applications in the areas of antimicrobial coatings, corrosion protection, positive resists, sensors and so on.⁴³⁻⁴⁶

1.3. Synthetic Methods

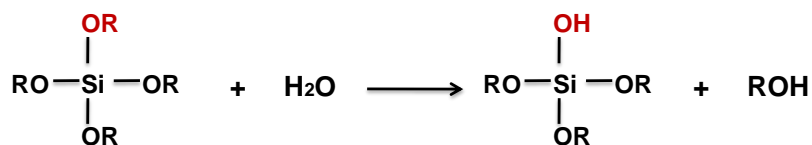
Various chemical strategies were developed to produce HOI materials, of which sol-gel chemistry and hydrosilylation chemistry are of interest here.

1.3.1. Sol-Gel Chemistry

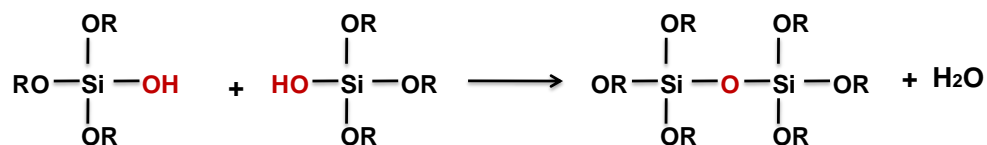
Sol-gel chemistry is the most commonly used method to make HOI materials. It is a conventional so-called “soft” chemistry because of its mild reaction conditions. The reactions are easy to perform, and no high reaction temperature is required. It has been widely used and provides an alternative for preparation of ceramics and glasses since 1844 when Ebelmen reported the synthesis of silica from silicon alkoxide.⁴⁷ However, the hydrolysis and condensation reactions were not well recognized until Mendeleev proposed the reactions in 1850s. Then the investigations on organosilicon compounds exploded in the 1930s. The

representative reaction scheme based on silicate alkoxide is described in Scheme 1.3, in which two reactions, hydrolysis and condensation, are involved. Usually, the metal alkoxides are not miscible with water, so alcohol is commonly added. The silanol groups are formed through hydrolysis, and then through condensation, the Si-O-Si siloxane groups are formed. Besides silicate alkoxide, non-silicate alkoxide based on transition metals such as Ti, V and Zr, and group IIIB metals such as B and Al are also important precursors. Silicon is less electropositive than the other metal elements, resulting in the less susceptibility to nucleophilic attack of silicon alkoxide and slower reaction kinetic of hydrolysis and condensation. Therefore a catalyst is usually added to promote the reactions. The most commonly used catalysts are mineral acids, ammonia, acetic acid, alkali metal hydroxide, fluoride ion for both hydrolysis and condensation reactions.⁴⁸

Hydrolysis



Condensation



Scheme 1.3. Hydrolysis and condensation of sol-gel chemistry.

The sol-gel reactions are influenced by various factors including pH, type and amount of catalyst, water to alkoxide ratio, concentration, and temperature. Regarding the pH effect, it has

been reported that silica particles grow in size in basic solution, while in acidic solution or in the presence of flocculated salts, the particles tend to form a three dimensional network and gel. Base or acid also play important roles in determining the structure of the sols and gels. It has been reported that acid tends to catalyze hydrolysis while base tends to catalyze the condensation. Therefore, silicate alkoxides undergo rapid hydrolysis and tend to form a more linear structure leaving unreacted silanol groups when catalyzed by an acid, while rapid condensation and tends to form denser networks with a high degree of branches when catalyzed by a base.

The products generated by sol-gel chemistry can be used to form fibers, films, or monolithic materials. The processing of sol-gel products is depicted in Figure 1.8. Sols are stable colloidal dispersion of solid particles in liquid. The stability derived from the negligible gravity and the Brownian motion of the solid particles with sizes in the nanometer range. The sol solution can be directly processed into solid materials of different shapes for applications in fibers, sensors, and catalyst supports. Gel, a three dimensional solid structure enclosing continuous liquid throughout the network, can be formed when sol particles are further condensed and linked together through chemical bonding. Further processing of gels by evaporating volatiles leads to the deformation and collapse of the three dimensional structure, resulting in the dried gel called a xerogel. A dense ceramic is produced when a xerogel is subjected to sintering. When a gel is dried in an autoclave under supercritical conditions, an aerogel without collapse of the solid structure can be formed due to the lack of capillary pressure. The high porosity of an aerogel and also a xerogel make them useful in various applications such as catalyst supports.

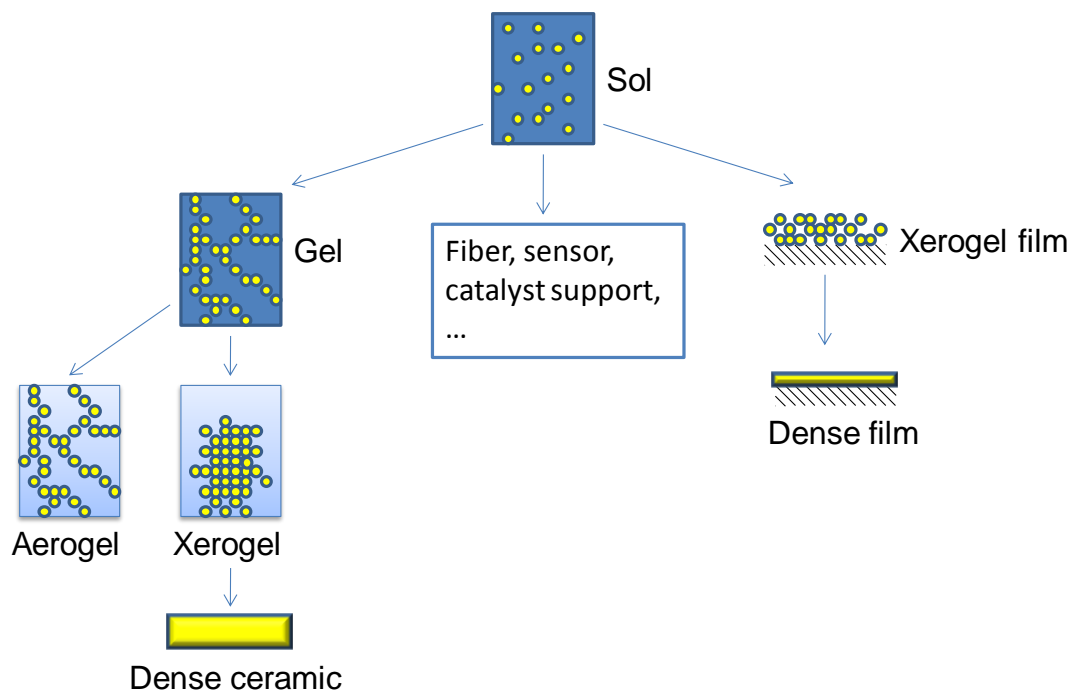
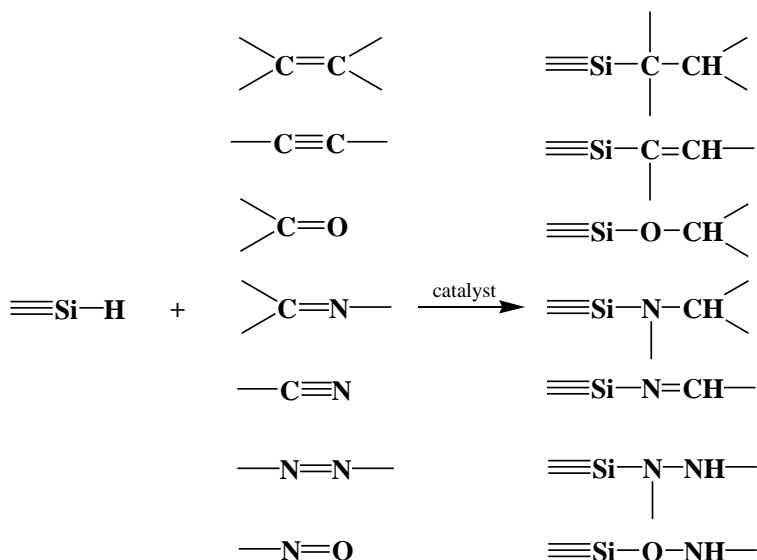


Figure 1.8. Formation and processing of sol-gel products.

Sol gel technology has been employed as a primary method to make numerous HOI materials for various applications. The preparation of sol-gel derived HOI materials have been accomplished by either simply mixing the metal precursors $M(OR)_4$ before sol-gel reactions with organic compounds or polymers where the organic and inorganic components interact through weak bonding, or using metal alkoxides $R'M(OR)_x$ as precursors when R' are functional groups allowing the strong chemical bonding between organic and inorganic phases.⁴⁹ The R' group can be certain functional groups such as the chromophores, or they can be polymerizable groups. The HOI materials produced by sol-gel method have been widely studied for optical, ferroelectric, biological, photosensitive/photochromic applications, proton conductor, and corrosion protection.^{50,51}

1.3.2. Hydrosilylation Chemistry

Hydrosilylation chemistry is a widely used chemical reaction in the preparation of organosilicon compounds with carbon-silicon linkages since the first discovery of this reaction between trichlorosilane and 1-octene reported in 1947.⁵² It is the second most important reaction to create the carbon-silicon linkage besides the Rochow process in which alkyl/aryl halide vapors react with silicon at fairly high temperature.⁵³ The silicon hydride group (Si-H) is added to unsaturated alkene or alkyne groups in the presence of a catalyst, as is shown in Scheme 1.4.



Scheme 1.4. Hydrosilylation reactions.

It was initially reported that the hydrosilylation reaction proceeds by a free-radical mechanism or hemolytic mechanism. Reactions could be initiated by commonly used organic peroxides and azo compounds and propagated after the thermally decomposed initiator radicals abstract hydrogen from hydrosilanes and formed the silyl-free radicals. Other than using initiators, the silyl-free radicals could also be generated under UV radiation. The hydrosilanes then undergo photolytic addition to olefins. Combination of the two initiator generation methods,

thermal decomposition and photolysis, can also enable the reactions to proceed. After initiation, the reaction would undergo propagation and finally be terminated by a chain transfer reaction with a hydrosilane.

However, most hydrosilylation reactions occur via a polar mechanism or heterolytic mechanism which involves nucleophilic attack on the silicon atom. The nucleophilic-electrophilic catalyst such as tertiary amines, phosphines, the supported metal catalysts such as carbon or SiO₂ supported Pt, Rh, Ru, Pd, Ni, the photo-/peroxide-initiated metal complexes such as Cr(CO)₆, Fe(CO)₅, the homogeneous transition metal complexes, and the supported transition metal complexes were used as catalysts for the hydrosilylation reaction proceeding in a heterolytic mechanism. Of these catalysts, the transition metal complexes are the most commonly used due to the high reactivity and selectivity.

Platinum compounds are the most commonly used catalysts for hydrosilylation because of their relatively high reactivity. There are primarily two types of platinum catalysts, Karstedt's catalyst and Speier's catalyst. Karstedt's catalyst is platinum complexed with divinyltetramethyldisiloxane, while Speier's catalyst is H₂PtCl₆. PtO₂ catalyst was also proven to be an efficient and versatile catalyst towards a variety of alkenes and allylamines.⁵⁴ The Chalk-Harrod mechanism is so far the most widely accepted mechanism of platinum catalyzed hydrosilylation.⁵⁵ Four steps are involved in hydrosilylation as described by Chalk-Harrod. Firstly oxidative addition of R₃Si-H to metal forming R₃Si-[M]-H, secondly coordination of alkene with metal, thirdly addition of alkene to metal center, and finally reductive elimination of metal forming Si-C bond. Hydrosilylation of olefins with Pt catalysts mostly follows the anti-

Markovnikov rule only leading to the terminal hydrosilylation product. With hydrosilylation, it is possible to modify silicone, unsaturated polymers, and to produce novel organosilicon materials.

1.4. References

1. Cle´ment Sanchez, Beatriz Julia´n, Philippe Belleville and Michael Popall, Applications of hybrid organic–inorganic nanocomposites, *J. Mater. Chem.*, 15, 2005, 3559–3592
2. Yoshiki Chujo, Organic – Inorganic Nano-Hybrid Materials, *KONA No.25*, 2007
3. J. Liu, W.-J. Boo, A. Clearfield, and H.-J. Sue, Intercalation and Exfoliation: A Review on Morphology of Polymer Nanocomposites Reinforced by Inorganic Layer Structures, *Materials and Manufacturing Processes*, 20, 2006, 143–151
4. Douglas A. Loy and Kenneth J. Shea, Bridged Polysilsesquioxanes. Highly Porous Hybrid Organic-Inorganic Materials, *Chem. Rev.* 95, 1995, 1431-1442
5. C. Eaborn, *Organosilicon compounds*, Butterworths Scientific Publications, 1960
6. E.F. Vansant, P. Van Der Voort, and K.C. Vrancken, *Characterization and chemical modification of the silica surface*, Elsevier 1995
7. W. Stober, A. Fink, E. Bohn, *J. Colloid Interface Sci.* 26, 1968, 62
8. Kota Sreenivasa Rao, Khalil El-Hami, Tsutomu Kodaki, Kazumi Matsushige, Keisuke Makino, A novel method for synthesis of silica nanoparticles, *Journal of Colloid and Interface Science* 289, 2005, 125–131
9. Horacio E. Bergna, William O. Roberts, *Colloidal silica—fundamentals and applications*, Taylor & Francis, 2006

10. Louis Mercier, and Thomas J. Pinnavaia, Direct Synthesis of Hybrid Organic-Inorganic Nanoporous Silica by a Neutral Amine Assembly Route: Structure-Function Control by Stoichiometric Incorporation of Organosiloxane Molecules, *Chem. Mater.* 12, 2000, 188-196
11. Colleen M. Janczak, Craig A. Aspinwall, Composite nanoparticles: the best of two worlds, *Anal Bioanal Chem*, 402, 2012, 83–89
12. Michele L. Anderson, Rhonda M. Stroud, and Debra R. Rolison, Enhancing the Activity of Fuel-cell Reactions by Designing Three-dimensional Nanostructured Architectures: Catalyst-modified Carbon-Silica Composite Aerogels, *Nano Lett.*, 2 (3), 2002, 235-240
13. Yining Shi and Carl J. Seliskar, Optically Transparent Polyelectrolyte-Silica Composite Materials: Preparation, Characterization, and Application in Optical Chemical Sensing, *Chem. Mater.* 9, 1997, 821-829
14. Colleen M. Janczak & Craig A. Aspinwall, Composite nanoparticles: the best of two worlds, *Anal Bioanal Chem* 402, 2012, 83–89
15. Zhongwei Niu, Zhenzhong Yang, Zhibing Hu, Yunfeng Lu, and Charles C. Han, Polyaniline-silica composite conductive capsules and hollow spheres, *Adv. Funct. Mater.* 2003, 13, N0. 12, December.
16. Xin Lu, Ian Manners, and Mitchell A. Winnik, Polymer/Silica Composite Films as Luminescent Oxygen Sensors, *Macromolecules* 2001, 34, 1917-1927
17. C. Joly, M. Smaïhi, L. Porcar, and R. D. Noble, Polyimide-Silica Composite Materials: How Does Silica Influence Their Microstructure and Gas Permeation Properties?, *Chem. Mater.* 1999, 11, 2331-2338

18. Stephen J. Clarson, *Silicones and silicone-modified materials*, American Chemical Society, 2000
19. Anthony J. O'Lenick, *Basic Silicone Chemistry – A Review*, *Silicone Spectator*, 1999, 1-23
20. Farhang Abbasi, Hamid Mirzadeh and Ali-Asgar Katbab, *Modification of polysiloxane polymers for biomedical applications: a review*, *Polym Int* 50, 2001, 1279-1287
21. Gongping Liu, Fenjuan Xiangli, Wang Wei, Sainan Liu, Wanqin Jin, *Improved performance of PDMS/ceramic composite pervaporation membranes by ZSM-5 homogeneously dispersed in PDMS via a surface graft/coating approach*, *Chemical Engineering Journal* 174, 2011, 495– 503
22. Olivier Foussaier, Michel Menetrier, Jean-Jacques Videau, Etienne Duguet, *Polydimethylsiloxane-based ORMOSIL microstructure: correlation with compressive behavior*, *Materials Letters* 42, 2000, 305–310
23. Eri Yoshida and Sachiko Tanimoto, *Living Radical Polymerization of Styrene by a Stable Nitroxyl Radical and Macroazoinitiator*, *Macromolecules* 30, 1997, 4018-4023
24. Adam Limer and David M. Haddleton, *Amide Functional Initiators for Transition-Metal-Mediated Living Radical Polymerization*, *Macromolecules* 39, 2006, 1353-1358
25. R. Rached, S. Hoppe, A. Jonquieres, P. Lochon, F. Pla, *A New Macroinitiator for the Synthesis of Triblock Copolymers PA12-b-PDMS-b-PA12*, *Journal of Applied Polymer Science*, 102, 2006, 2818–2831

26. Vesna V Antić, Marija V Pergal, Milutin N Govedarica, Mališa P Antić and Jasna Djonlagić, Copolymers based on poly(butylene terephthalate) and polycaprolactone-blockpolydimethylsiloxane-block-polycaprolactone, *Polym Int* 59, 2010, 796–807
27. Rebeca Hernandez, Jadwiga Weksler, Ajay Padsalgikar, James Runt, In vitro oxidation of high polydimethylsiloxane content biomedical polyurethanes: Correlation with the microstructure, *Journal of Biomedical Materials Research Part A*, 87(2), 2008, 546-56
28. Oliver Rheingans, Norbert Hugenberg, J. Robin Harris, Karl Fischer, and Michael Maskos, Nanoparticles Built of Cross-Linked Heterotelechelic, Amphiphilic Poly(dimethylsiloxane)-b-poly(ethylene oxide) Diblock Copolymers, *Macromolecules* 33, 2000, 4780-4790
29. Yishan Wang, Neil Coombs, Ayse Turak, Zheng-Hong Lu, Ian Manners, and Mitchell A. Winnik, Interfacial Staining of a Phase-Separated Block Copolymer with Ruthenium Tetroxide, *Macromolecules* 40, 2007, 1594-1597
30. Timothy J. Peckham, Jason A. Massey, Charles H. Honeyman, and Ian Manners, Living Anionic Polymerization of Phosphorus-Bridged [1]Ferrocenophanes: Synthesis and Characterization of Well-Defined Poly(ferrocenylphosphine) Homopolymers and Block Copolymers, *Macromolecules* 32, 1999, 2830-2837
31. Frank S. Bates and Glenn H. Fredrickson, Block copolymers-designer soft materials, *Phys. Today* 52(2), 1999, 32
32. Ian W. Hamley, Valeria Castelletto, Small-angle scattering of block copolymers in the melt, solution and crystal states, *Prog. Polym. Sci.* 29, 2004, 909–948

33. Ashish K. Khandpur, Stephan Foerster, Frank S. Bates, Ian W. Hamley, Anthony J. Ryan, Wim Bras, Kristoffer Almdal, Kell Mortensen, Polyisoprene-Polystyrene Diblock Copolymer Phase Diagram near the Order-Disorder Transition, *Macromolecules* 28, 1995, 8796-8806
34. Applications of Polyhedral Oligomeric Silsesquioxanes, Claire Hartmann-Thompson, Springer, 2011
35. Woojin Lee, Suolong Ni, Jianjun Deng, Byoung-Suhk Kim, Sushil K. Satija, Patrick T. Mather, and Alan R. Esker, Telechelic Poly(ethylene glycol)-POSS Amphiphiles at the Air/Water Interface, *Macromolecules*, 40 (3), 2007, 682-688
36. Hitoshi Araki and Kensuke Naka, Syntheses of Dumbbell-Shaped Trifluoropropyl-Substituted POSS Derivatives Linked by Simple Aliphatic Chains and Their Optical Transparent Thermoplastic Films, *Macromolecules*, 44 (15), 2011, 6039-6045
37. Weian Zhang, Jiayin Yuan, Stephan Weiss, Xiaodong Ye, Chunliang Li, and Axel H. E. Müller, Telechelic Hybrid Poly(acrylic acid)s Containing Polyhedral Oligomeric Silsesquioxane (POSS) and Their Self-Assembly in Water, *Macromolecules*, 44 (17), 2011, 6891-6898
38. Joanne Raghunath, George Georgiou, David Armitage, Showan N. Nazhat, Kevin M. Sales, Peter E. Butler, Alexander M. Seifalian, Degradation studies on biodegradable nanocomposite based on polycaprolactone/polycarbonate (80:20%) polyhedral oligomeric silsesquioxane, *Journal of Biomedical Materials Research Part A*, 91A (3), 2009, 834-844

39. Shiao-Wei Kuoa, Feng-Chih Chang, POSS related polymer nanocomposites, *Progress in Polymer Science* 36, 2011, 1649–1696
40. Samy A. Madbouly, Joshua U. Otaigbe, Recent advances in synthesis, characterization and rheological properties of polyurethanes and POSS/polyurethane nanocomposites dispersions and films, *Progress in Polymer Science* 34, 2009, 1283–1332
41. Irada S. Isayeva, Joseph P. Kennedy, Amphiphilic Membranes Crosslinked and Reinforced by POSS, *Journal of Polymer Science: Part A: Polymer Chemistry*, 42, 2004, 4337–4352
42. Manojk. Kolel-Veetil, Dawn D. Dominguez, Teddy M. Keller, Dendritic Networks Containing Polyhedral Oligomeric Silsesquioxane (POSS) and Carborane Clusters, *Journal of Polymer Science: Part A: Polymer Chemistry*, 46, 2008, 2581–2587
43. Partha Majumdera, Elizabeth Leea, Nathan Gubbinsa, Shane J. Stafsliena, Justin Danielsa, Clayton J. Thorsona, Bret J. Chisholm, Synthesis and antimicrobial activity of quaternary ammonium-functionalized POSS (Q-POSS) and polysiloxane coatings containing Q-POSS, *Polymer*, 50 (5), 2009, 1124–1133
44. Banaszak Holl, et al US Patent 5,858,544
45. Ratnam Sooriyakumaran, Hoa Truong, Linda Sundberg, Mark Morris, Bill Hinsberg, Hiroshi Ito, Robert Allen, Wu-Song Huang, Dario Goldfab, Sean Burns, and Dirk Pfeiffer, Positive Resists Based on Non-polymeric Macromolecules, *Journal of Photopolymer Science and Technology*, 18 (3), 2005, 425-429
46. Claire Hartmann-Thompson, Douglas L. Keeley, Petar R. Dvornic, Steven E. Keinath, Keith R. McCrea, Hydrogen-Bond Acidic Polyhedral Oligosilsesquioxane Filled Polymer Coatings

- for Surface Acoustic Wave Sensors, *Journal of Applied Polymer Science*, 104, 2007, 3171–3182
47. J.J. Ebelmen, *C. R. Acad. Sci.* 19, 1844, 398
48. C. Jeffrey Brinker, George W. Scherer, *Sol-Gel Science: The Physics and Chemistry of Sol-Gel Processing*, Academic Press, Inc., 1990
49. Fayna Mammeri, Eric Le Bourhis, Laurence Rozes and Clement Sanchez, Mechanical properties of hybrid organic–inorganic materials, *J. Mater. Chem.*, 15, 2005, 3787–3811
50. M. L. Zheludkevich, I. Miranda Salvado and M. G. S. Ferreira, Sol–gel coatings for corrosion protection of metals, *J. Mater. Chem.*, 15, 2005, 5099–5111
51. H. Schmidt, G. Jonschker, S. Goedicke and M. Mennig, The Sol-Gel Process as a Basic Technology for Nanoparticle-Dispersed Inorganic-Organic Composites, *Journal of Sol-Gel Science and Technology* 19, 2000, 39–51
52. Sommer L. H., Pietrusza E. W. and Whitmore F. C., *J. Am. Chem. Soc.*, 69, 1947, 188
53. John M. Zeigler, F. W. Gordon Fearon, *Silicon-Based Polymer Science-A Comprehensive Resource*, American Chemical Society, Washington, DC 1990
54. Nicolas Sabourault, Ge ´rard Mignani, Alain Wagner, and Charles Mioskowski, Platinum Oxide (PtO₂): A Potent Hydrosilylation Catalyst, *Organic Letters*, 4 (13), 2002, 2117-2119

CHAPTER 2. ENVIRONMENTALLY FRIENDLY HYBRID ORGANIC-INORGANIC (HOI) MAGNESIUM-RICH PRIMER FOR CORROSION PROTECTION OF ALUMINUM ALLOYS

2.1. Abstract

Magnesium-rich (Mg-rich) primers have been developed for corrosion protection of aluminum (Al) alloys by forming a galvanic couple between Mg particles and Al alloy substrates. Mg particles act as a sacrificial anode and corrode preferentially over Al, thus providing the protection. A hybrid organic-inorganic (HOI) binder based on organically-modified silica nanoparticles was studied to produce novel Mg-rich primers due to the the unique combination of both properties from organic and inorganic phases. The HOI binders were produced by reacting silica nanoparticles with phenethyltrimethoxysilane (PhEtTMS) via sol-gel chemistry. The variables investigated were the addition of a condensation catalyst, tetrabutylammonium fluoride (TBAF), and the curing condition. The HOI sol dispersions, HOI binders, and Mg-rich primers derived from HOI binders were characterized by particle size, proton nuclear magnetic resonance ($^1\text{H-NMR}$), silicon nuclear magnetic resonance ($^{29}\text{Si-NMR}$), fourier transform infrared spectroscopy (FTIR), differential scanning calorimetry (DSC), electrochemical impedance spectroscopy (EIS), and salt spray exposure. The condensation catalyst TBAF was found to have a profound impact on barrier properties and corrosion protection of the HOI binders. With TBAF, the organically-functionalized silica nanoparticles grew larger, and the derived HOI binder had higher crosslinking density and better barrier properties. However, when used in combination with Mg particles, severe blister formation was observed for the topcoated Mg-rich primer with TBAF upon salt spray exposure. This was attributed to the interaction of fluoride ion with Mg particles to produce hydrogen gas. In contrast, the topcoated Mg-rich primer produced without

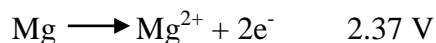
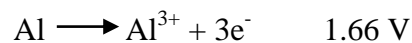
TBAF cured at 80 °C exhibited excellent corrosion protection after 4,400 hours salt spray exposure. No blister and corrosion products were found within coatings and in the scribed area.

2.2. Introduction

Hexavalent chromium has been recognized as the most effective corrosion inhibitor for metals. However, hexavalent chromium is known for its carcinogenicity and persistence in the environment.¹ As a result, new strategies have to be developed to create alternatives for corrosion protection. Efforts have been undertaken to have new inhibitor compounds, barrier coatings, conductive polymers, and other surface modification techniques as a means to prevent corrosion.² As a replacement to chromate inhibitors, novel environmentally friendly magnesium-rich (Mg-rich) primer systems have been developed for corrosion protection of aerospace aluminum (Al) alloys, analogous to zinc-rich primers for protecting steel.^{3,4} In an aerospace coating system, the Mg-rich primer is applied between the Al alloy substrate and polyurethane topcoat, as illustrated in Figure 2.1. The Mg-rich primer needs to provide corrosion protection and adhesion between the topcoat and substrate, while the topcoat should possess good barrier properties. The mechanism involved in the corrosion protection by Mg-rich primers includes the galvanic couple established between Mg pigments and Al alloy substrates. According to the electrochemical half reaction, Mg has a higher standard oxidation potential and is thus, more electrochemically active than Al, as shown in Scheme 2.1.^{5,6} Thereby, in a galvanic cell, Mg particles serve as a sacrificial anode and corrodes preferentially over the Al substrate.⁷



Figure 2.1. Schematic of aerospace coating systems.



Scheme 2.1. Half reactions and standard oxidation potential of Al and Mg.⁵

The interest in sol-gel derived HOI coatings arose from their mild reaction conditions, easy processing, environmentally friendly nature, and, most importantly, the unique combination of properties of organic and inorganic phases.^{4,8} The organic component provides the adhesion to topcoat and flexibility while the inorganic component provides the adhesion to metal substrates and barrier properties. The appealing feature of sol-gel chemistry in producing HOI materials enabled the wide application of this chemistry.

A combinatorial/high-throughput workflow was developed to produce promising HOI coatings for application as a binder system for Mg-rich primers.¹⁹ Results obtained using the workflow indicated that Mg-rich primers based on heterogeneous HOI binders derived from colloidal silica exhibited significantly better corrosion protection than Mg-rich primers based homogeneous HOI binders derived from TEOS. For the production of heterogeneous HOI binders, four different organosilanes and multiple other compositional and process parameters were varied using the high-throughput workflow. Based on screening results, PhEtTMS was identified as a useful organosilane for the production of stable colloidal silica dispersions in an organic medium. Based on this previous work, PhEtTMS was used as the organosilane for producing Mg-rich primers based heterogeneous HOI binders. For the Mg-rich primers based on heterogeneous HOI binders, the effect of using TBAF as a condensation catalyst and the effect of curing conditions on crosslink density and corrosion protection performance of the Mg-rich primers were investigated.

2.3. Experimental

2.3.1. Raw Materials

Aluminum alloy panels (AA 2024-T3) were obtained from Q-panel Lab Products, with the sizes of 20 cm x 10 cm x 1 mm. Prior to use, the panels were sandblasted to remove the oxide layer and then cleaned with hexane. Snowtex-O, a colloidal silica dispersion, was obtained from Nissan Chemical. According to the manufacturer, Snowtex-O has a pH of 2-4, silica content of 20-21 wt%, and average particle size of 10-20 nm. Tetrabutyl ammonium fluoride (TBAF, 1.0 M in tetrahydrofuran), isopropyl alcohol (IPA), and propylene glycol monomethyl ether acetate (PMA) were purchased from Sigma Aldrich. Phenethyl trimethoxysilane (PhEtTMS) was purchased from Gelest. Magnesium powder was obtained from Ecka Granules and had an average particle size of 25 microns. AntiTerra 204, a wetting agent, was obtained from BYK Chemie. Bentone 38, an anti-settling agent, was obtained from Elementis Specialties, Inc. Aerosil R812, a viscosity modifier, was obtained from Degussa Corporation. The polyurethane topcoat, MIL-PRF-85285D, was obtained from Deft Chemical Coatings, which is comprised of the pigmented polyester resin as component A and aliphatic isocyanate resin as component B. Salt water used for corrosion screening by immersion testing was 3 wt% sodium chloride in water purified by reverse osmosis. Chromium (III) acetylacetonate and acetone-d₆ for ²⁹Si-NMR were obtained from Alfa Aesar. All reagents were used without further purification.

2.3.2. Synthesis of HOI Binder Solutions

To a 2000 ml Erlenmeyer flask, 75 ml Snowtex-O and 108 ml IPA were mixed, and then 50 g of PhEtTMS was added using rapid, magnetic stirring. The mixture was then heated to reflux. After 2 hours of refluxing, the mixture was cooled to room temperature. Next, 612 g of

PMA was added under rapid stirring. The mixture was then split into two equal portions (305 g in each portion) to two 2000 ml, one-neck, round-bottomed flasks. To one of the two solutions, 0.40 g of the 1.0 M TBAF solution in THF was added. Each mixture was concentrated on a roto-evaporator in a 70 °C water bath.

2.3.3. Preparation of HOI Coatings

Prior to coating application, AA2024-T3 panels were cleaned and deoxidized by: 1) immersing for 10 minutes in a 45 °C aqueous detergent bath consisting of 137 g/L Oakite Aluminum Cleaner 164 agitated with bubbling air; 2) rinsing with deionized (DI) water; 3) immersing for 2 minutes in 55 °C DI water; 4) immersing in a an ambient temperature deoxidizer solution consisting of 25 wt% ferric sulfate, 3 wt% ferrous sulfate, 2 wt% sodium bifluoride, 5 wt% nitric acid, and 65wt % DI water agitated with bubbling nitrogen for 10 minutes; and 5) rinsing with DI water.

Table 2.1. Description of HOI coatings produced from HOI solutions, noTBAF and wTBAF.

HOI Coatings	HOI Solution	Curing Temp.	Curing Time	Dry Film
Designation	Utilized	(°C)	(hrs)	Thickness (µm)
noTBAF-23C/24hr	noTBAF	23	24	17.3 ± 4.2
noTBAF-80C/1hr	noTBAF	80	1	23.8 ± 11.2
noTBAF-80C/24hr	noTBAF	80	24	20.8 ± 10.7
wTBAF-23C/24hr	wTBAF	23	24	26.2 ± 11.1
wTBAF-80C/1hr	wTBAF	80	1	32.7 ± 11.8
wTBAF-80C/24hr	wTBAF	80	24	11.5 ± 5.9

The HOI coatings described in Table 2.1 were produced by creating an 8.5 cm x 18 cm rectangular reservoir on top of a substrate panel by adhering a 508 μm thick polyethylene frame to the panel, pouring approximately 6 mls of a HOI solution (i.e. noTBAF or wTBAF) into the reservoir, allowing the solvent to flash off in a ventilation hood, and subsequently curing at either room temperature ($\sim 23\text{ }^{\circ}\text{C}$) for 24 hours, $80\text{ }^{\circ}\text{C}$ for 1 hour, or $80\text{ }^{\circ}\text{C}$ for 24 hours.

2.3.4. Preparation of Mg-Rich Primers

Mg-rich primers based on HOI binders were prepared using the formulation shown in Table 2.2. Prior to mixing with Mg particles, the solids content of the HOI dispersions were adjusted to be 10 wt% with PMA.

Table 2.2. Description of the Mg-rich primers produced from HOI solutions, noTBAF and wTBAF.

Mg-Rich Primers	HOI Solution	Curing Temp.	Curing Time	Dry Film
Designation	utilized	($^{\circ}\text{C}$)	(hrs)	Thickness (μm)
Mg-noTBAF-23C/24hr	noTBAF	23	24	277 ± 46
Mg-noTBAF-80C/1hr	noTBAF	80	1	209 ± 40
Mg-noTBAF-80C/24hr	noTBAF	80	24	205 ± 39
Mg-wTBAF-23C/24hr	wTBAF	23	24	191 ± 32
Mg-wTBAF-80C/1hr	wTBAF	80	1	189 ± 42
Mg-wTBAF-80C/24hr	wTBAF	80	24	210 ± 76

Mg-rich primers were generated by first producing a solution blend consisting of 95.2 wt% of a HOI dispersion (i.e. noTBAF or wTBAF), 1.11 wt% AntiTerra 204, 2.54 wt% Bentone 38,

and 1.11 wt% Aerosil R812 and then dispersing Mg particles into the solution at a 63/37 wt/wt (HOI solution blend/Mg) ratio. Overall, Mg particles were added at 80 wt% in the primer formulations. Dispersion of Mg particles into the HOI dispersion blend was accomplished using a Speedmixer DAC 150FVZK from FlackTek Inc. Coating solutions were applied to cleaned and deoxidized panels using a Devilbiss GFG516 spray gun and cured at either room temperature (~ 23 °C) for 24 hours, 80 °C for 1 hour, or 80 °C for 24 hours. For salt spray exposure, panels were also topcoated using the Deft polyurethane and spray application. Curing of the topcoat was done at ambient conditions for a minimum of 24 hours.

2.3.5. Instrumentation

Solids content was determined gravimetrically by comparing the weight of the materials before and after heating the HOI solution samples at 200 °C in a vacuum oven overnight. The values were calculated by the following equation, where w_d and w_w are the weight of dry sample and wet sample, respectively.

$$\text{Solid (wt\%)} = \frac{w_d}{w_w} \times 100 \quad \text{Equation 2.1}$$

Particle size was measured using a Nicomp™ CW 380 Submicron Particle Sizer. Dilution of the colloid dispersions prior to measurement was done using IPA. Proton and silicon nuclear magnetic resonance spectroscopy ($^1\text{H-NMR}$ and $^{29}\text{Si-NMR}$) was done using a JEOL ECA 400 MHz NMR spectrometer. $^1\text{H-NMR}$ spectra were collected in deuterated chloroform using 16 scans and a pulse width of 14.6 μs , acquisition time of 2.18s, pulse angle of 45°, attenuation of 6dB, pulse time of 7.3 μs , receiver gain of 22, relaxation delay of 4s, and repetition time of 6.18s. $^{29}\text{Si-NMR}$ spectra were collected at 79.43MHz for ^{29}Si , and the acquisition parameters were a 62.5 kHz sweep width with an offset of 0 ppm, a relaxation delay of 5 seconds,

and an acquisition time of 0.262 s. Using these conditions, 14,000 scans were collected at an average temperature of 21.4 °C. The sample tubes were equipped with Teflon® bottoms and the lock solvent was acetone-d₆ with chromium (III) tris-acetylacetonate (Cr(acac)₃) added at a concentration of 0.25 M. Cr(acac)₃ was added in order to allow for complete relaxation recovery and quantitative spectra. A Bruker Optics Vertex 70 FT-IR was used to collect Fourier transform infrared (FTIR) spectra in transmission from samples deposited on a KBr plate. Spectra were analyzed using OPUS software from Bruker. The relative intensities of the FTIR peak absorbance were taken as the ratio of area integration to the internal standard peak absorbance. The area integrations were taken from 3550 – 3100 cm⁻¹ for (a) 3350 cm⁻¹ O-H stretching), from 1305 – 950 cm⁻¹ for (b) 1120 cm⁻¹ (Si-O-CH₃ stretching), from 950 – 860 cm⁻¹ for (c) 905 cm⁻¹ (Si-OH stretching), and from 500 – 400 cm⁻¹ for (d) 480 cm⁻¹ (Si-OCH₃ bending). For the internal standard peak absorbance, C=C stretching in phenyl group of PhEtTMS centered at 1496 cm⁻¹, the area integration was taken from 1510 – 1480 cm⁻¹. Differential scanning calorimetry (DSC) experiments were carried out using a DSC Q1000 from TA instruments equipped with an auto sampler. The experiments were conducted using a heat-cool-heat cycle extending from -50 °C to 100 °C at a heating/cooling rate of 10 °C/min, purged with N₂ at 50 ml/min. EIS was conducted with a Gamry MultiEchem 8 Electrochemical Workstation and Gamry Framework software. The electrolyte used was 3 wt% NaCl in DI water and the frequency range was 10⁴ Hz to 0.01 Hz with an applied 10 mV R.M.S. voltage vs. open circuit potential. A Ag/AgCl reference electrode and Pt mesh counter electrode were utilized. Salt spray corrosion testing was done according to ASTM B117 using a Q-FOG SSP cyclic corrosion tester. Before putting samples into the chamber, the coated panels were scribed using a Gravograph IM4 engraver and Gravostyle QuickClick 1.83 software and the edges and back of the panels covered with thick plastic tape to

limit exposure to just the scribed face of the panel. The salt fog was generated from a 5 % NaCl solution at 30 °C.

2.4. Results and Discussion

2.4.1. Synthesis and Characterization of HOI Solutions

The HOI solutions were synthesized using the process is illustrated in Figure 2.2 and the synthetic scheme is described in Scheme 2.2. As described in Figure 2.2, aqueous colloidal silica and PhEtTMS were first mixed in the presence of IPA which was used to stabilize PhEtTMS due to its poor stability in an aqueous solution. As a result, the hydrolysis of the methoxy groups of PhEtTMS occurred in the acidic pH environment. Then PMA, a high boiling solvent having a boiling point of 145-146 °C, was added to exchange with low boiling components (i.e. methanol, IPA, and water). The removal of low boiling protic components is necessary due to the potential reaction of the protic solvents with Mg particles to be used in Mg-rich primers. Before the solvent exchange step, the mixture solution was split into two equal portions, and TBAF, a condensation catalyst, was added into one of the portions to study the effect of TBAF on coating performance. Fluoride ion has been shown to be an effective catalyst for nucleophilic substitutions at a silicon atom due to the formation of a highly reactive pentacoordinate intermediate in which fluorine is a ligand.^{9,10} Finally, low boiling components were removed at reduced pressure to further drive hydrolysis and condensation reactions. As illustrated in Scheme 2.2, the whole process involved the hydrolysis of methoxy groups of PhEtTMS, and the condensation of derived silanol groups with surface silanol groups from silica nanoparticles.

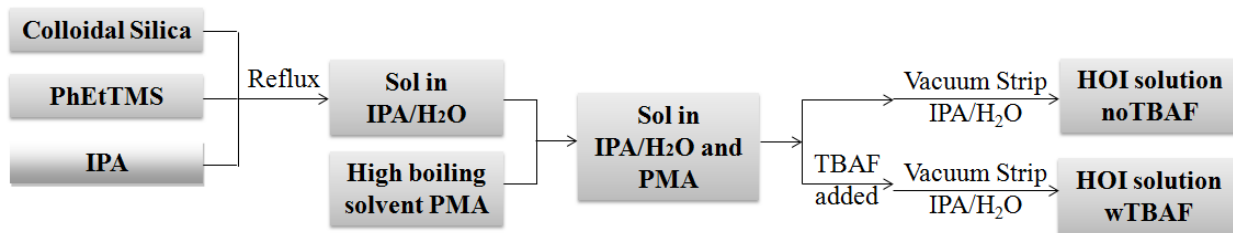
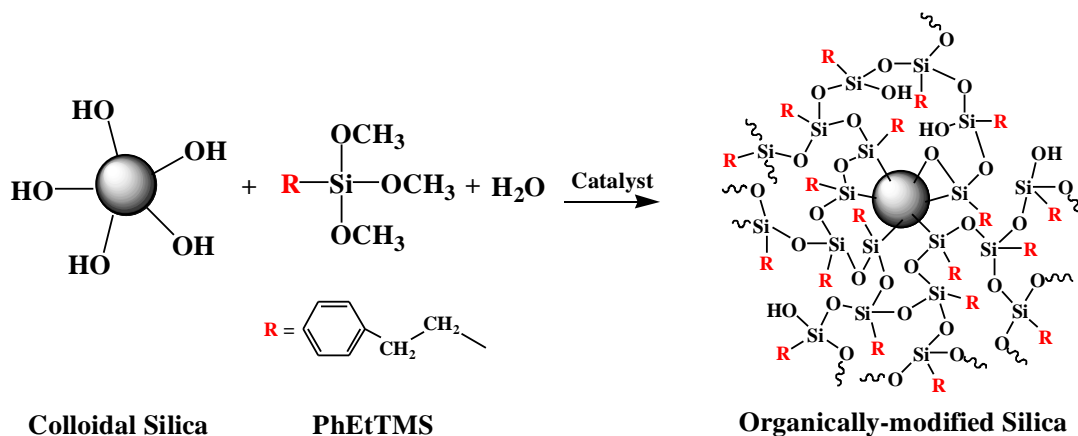


Figure 2.2. Synthetic process used to create the HOI solutions for making Mg-rich primers.



Scheme 2.2. Synthesis of organically-modified silica in HOI solutions via sol-gel chemistry.

The solids content of the mixture produced in the absence of TBAF (noTBAF) was determined to be 9.5 wt% while the solids content of the mixture produced in presence of TBAF (wTBAF) was determined to be 8.7 wt%. Confirmed by $^1\text{H-NMR}$ spectra, as shown in Figure 2.3, the low boiling solvents, methanol ($\delta = 3.49, 1.09$), IPA ($\delta = 1.22, 4.04$), and water ($\delta = 1.56$), were all eliminated after the solvent exchange process.¹¹

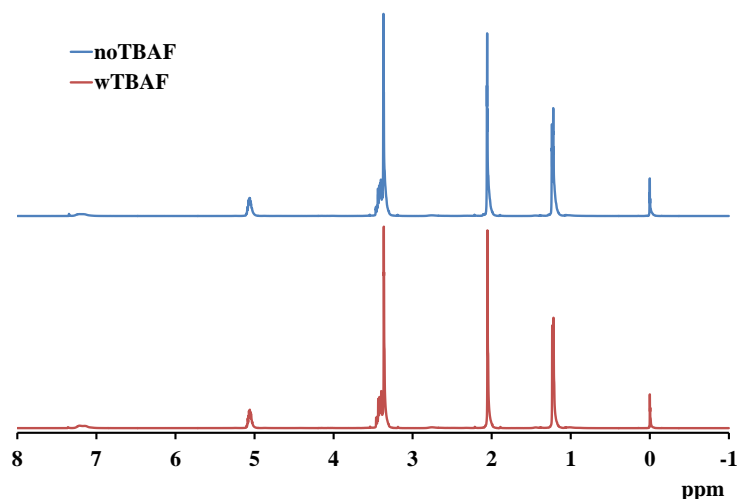


Figure 2.3. ^1H -NMR spectra of silica sols produced both in absence (blue) and in presence (red) of catalyst TBAF.

^{29}Si -NMR is extensively used in organosilicon research to identify the type and concentration of silicon bonds. The chemical shifts associated with the Si compounds are described in Figure 2.4. For trifunctional organosilane derivatives, four groups of peaks referred to as T peaks, T_0 , T_1 , T_2 , and T_3 , correspond to the trifunctional organosilicon species that undergo 0, 1, 2, and 3 condensation reactions, respectively. The ranges of typical chemical shift for the four groups of T peaks are -37 to -39 ppm for T_0 , -46 to -48 ppm for T_1 , -53 to -57 ppm for T_2 , and -61 to -66 ppm for T_3 .¹² For tetrafunctional organosilanes as shown in the bottom of Figure 2.4, five groups of peaks referred to as Q peaks, Q_0 , Q_1 , Q_2 , Q_3 , and Q_4 correspond to the tetrafunctional organosilicon species that undergo 0, 1, 2, 3, and 4 condensation reactions, respectively. The ranges of typical chemical shifts for the five groups of Q peaks are -72 to -82 ppm for Q_0 , -82 to -89 ppm for Q_1 , -92 to -96 ppm for Q_2 , -100 to -104 ppm for Q_3 , and ~ -110 ppm for Q_4 .¹²

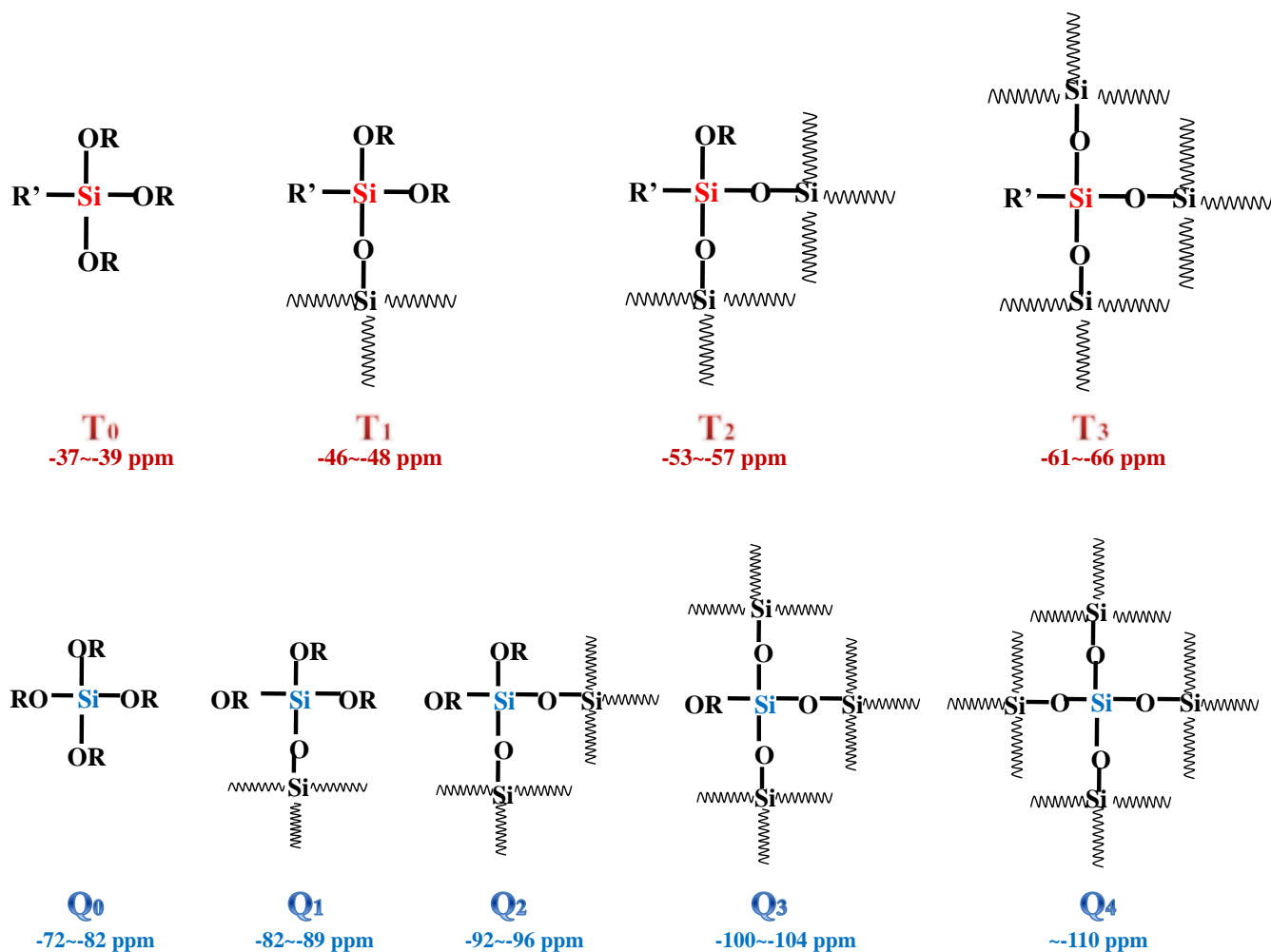


Figure 2.4. Chemical shifts of silicon compounds in ²⁹Si-NMR.

As a result, by using ²⁹Si-NMR, the extent of condensation can be determined. The ²⁹Si-NMR spectra of HOI solutions, noTBAF and wTBAF, are displayed in Figure 2.5, with PhEtTMS as a control. The PhEtTMS showed a primary T₀ peak and a small T₁ peak, indicating some dimers in the PhEtTMS. After hydrolysis and condensation, the T₀ peak disappeared for both noTBAF and wTBAF solutions, indicating that all PhEtTMS had undergone at least one condensation reaction. A higher T₃/T₁ ratio was observed for the HOI solution wTBAF,

indicating a higher extent of condensation resulted from the addition of the condensation catalyst TBAF. The huge Q₄ peaks stems from the Si-O linkages in the silica nanoparticles.

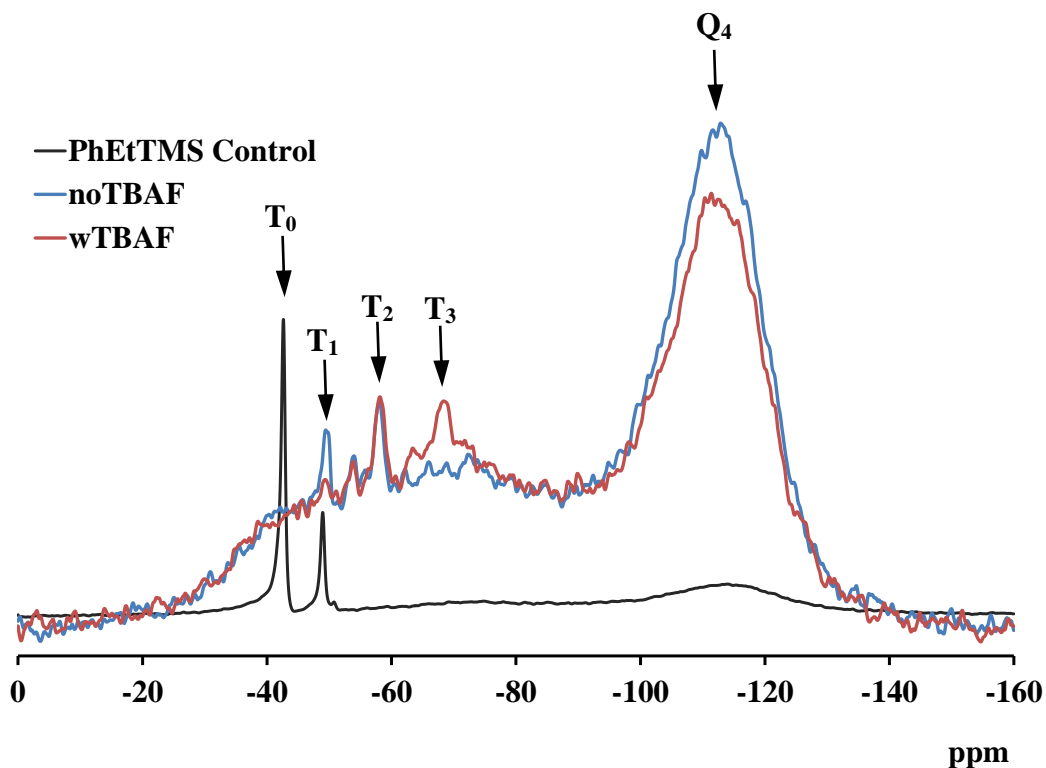


Figure 2.5. ²⁹Si-NMR spectra of noTBAF and wTBAF HOI solutions.

The FTIR spectra of noTBAF and wTBAF after deposition onto KBr pellets and solvent evaporation are shown in Figure 2.6. Due to film thickness variations, the band at 1496 cm⁻¹, which was attributed to C=C stretching of the phenyl group of PhEtTMS, was used to normalize the spectra. It can be found that the bands centered at 1120 cm⁻¹ and 480 cm⁻¹, which are attributed to Si-OCH₃ stretching and bending, and the bands centered at 3350 cm⁻¹ and 905 cm⁻¹, which are attributed to O-H and Si-OH stretching respectively, were all reduced when TBAF was used.¹³⁻¹⁵ This again indicates the higher extent of condensation resulted by the addition of TBAF catalyst.

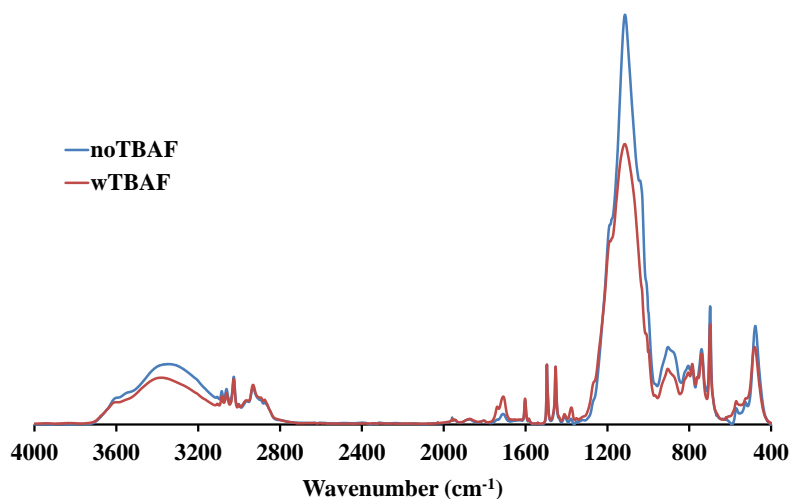


Figure 2.6. FTIR spectra of thin films of noTBAF and wTBAF HOI solutions.

The particle size of the organosilane functionalized silica nanoparticles is shown in Figure 2.7. Both the HOI solutions, noTBAF and wTBAF, have larger particle size than the unmodified colloidal silica, Snowtex-O. The condensation reactions between PhEtTMS and silica nanoparticles contributed to the particle size increase. The use of TBAF resulted in a greater particle size suggesting the higher extent of condensation, which is consistent with the results obtained from ^{29}Si -NMR and FTIR.

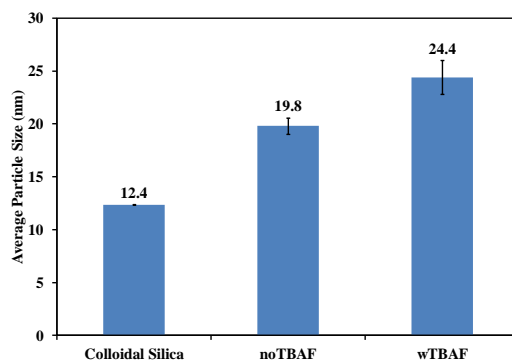


Figure 2.7. Particle size of colloidal silica, organosilane functionalized silica sols without, and with TBAF.

2.4.2. Characterization of HOI Coatings

The HOI solutions were then subjected to cure into clear coatings without adding Mg particles and the barrier properties examined. Small molecules such as water, oxygen, and electrolyte are essential for corrosion to occur. For corrosion protection of metals, barrier properties of coatings are important in preventing the small molecules from diffusing through coatings. For HOI coatings, barrier properties primarily depend on the crosslinking density achieved during cure. Therefore, the effect of curing conditions as well as the effect of TBAF catalyst on the crosslinking density of HOI coatings was investigated by FTIR and DSC. EIS was performed to measure the barrier properties. The cure conditions studied were ambient conditions ($\sim 23\text{ }^{\circ}\text{C}$) for 24 hours, $80\text{ }^{\circ}\text{C}$ for 1 hour, and $80\text{ }^{\circ}\text{C}$ for 24 hours.

Figures 2.8 and 2.9 display the FTIR spectra of HOI coatings derived from noTBAF and wTBAF HOI solutions, respectively, as a function of the curing condition. All spectra were normalized with the band at 1496 cm^{-1} which is attributed to C=C stretching in the phenyl group of PhEtTMS. In Figure 2.8, it can be observed that when thermal energy applied for curing increased from $23\text{C}/24\text{hr}$ to $80\text{C}/1\text{hr}$ and then to $80\text{C}/24\text{hr}$, the bands centered at 1120 cm^{-1} and 480 cm^{-1} , which are attributed to Si-OCH₃ stretching and bending, and the bands centered at 3350 cm^{-1} and 905 cm^{-1} , which are attributed to O-H and Si-OH stretching, respectively, all reduced, indicating the higher extent of condensation achieved during curing. The same trend was observed for HOI coatings based on wTBAF solution, as shown in Figure 2.9.

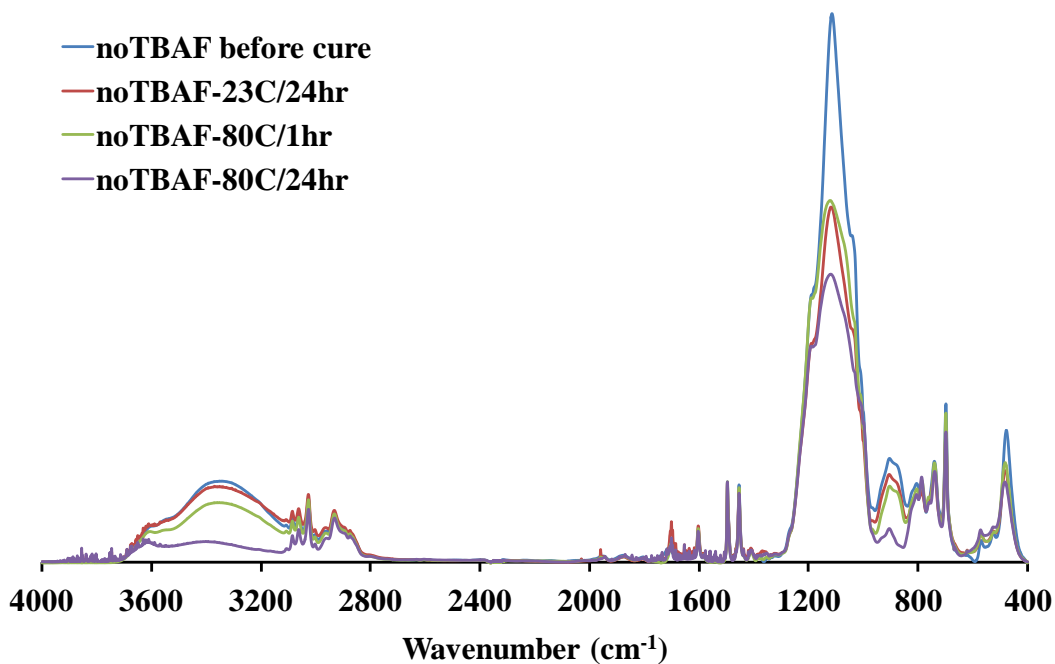


Figure 2.8. FTIR spectra obtained from coatings produced from noTBAF and various curing conditions.

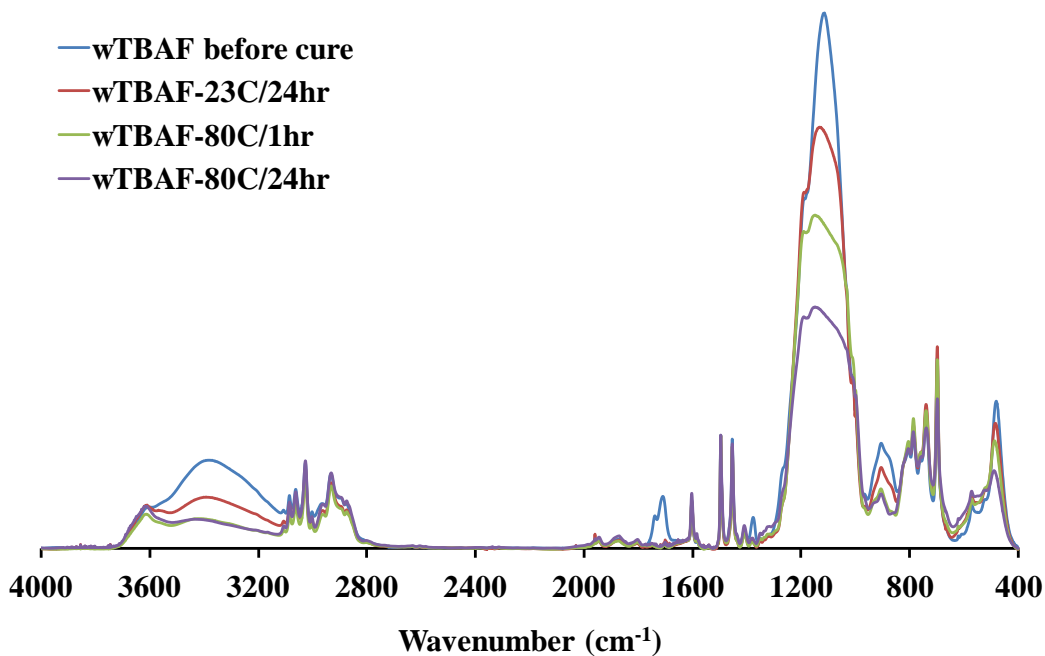


Figure 2.9. FTIR spectra obtained from coatings produced from wTBAF and various curing conditions.

The relative intensities of bands derived from O-H stretching (3350 cm^{-1}), Si-OCH₃ stretching (1120 cm^{-1}), Si-OH stretching (905 cm^{-1}), and Si-OH bending were calculated using C=C stretching as a standard band. The results are shown as a function of TBAF catalyst and curing condition in Figure 2.10. The trend that the condensation extent increased with extent of curing was again clearly demonstrated here. Besides, it can be found that, at a given curing condition, with the use of TBAF catalyst, the HOI coating tends to possess a higher extent of condensation.

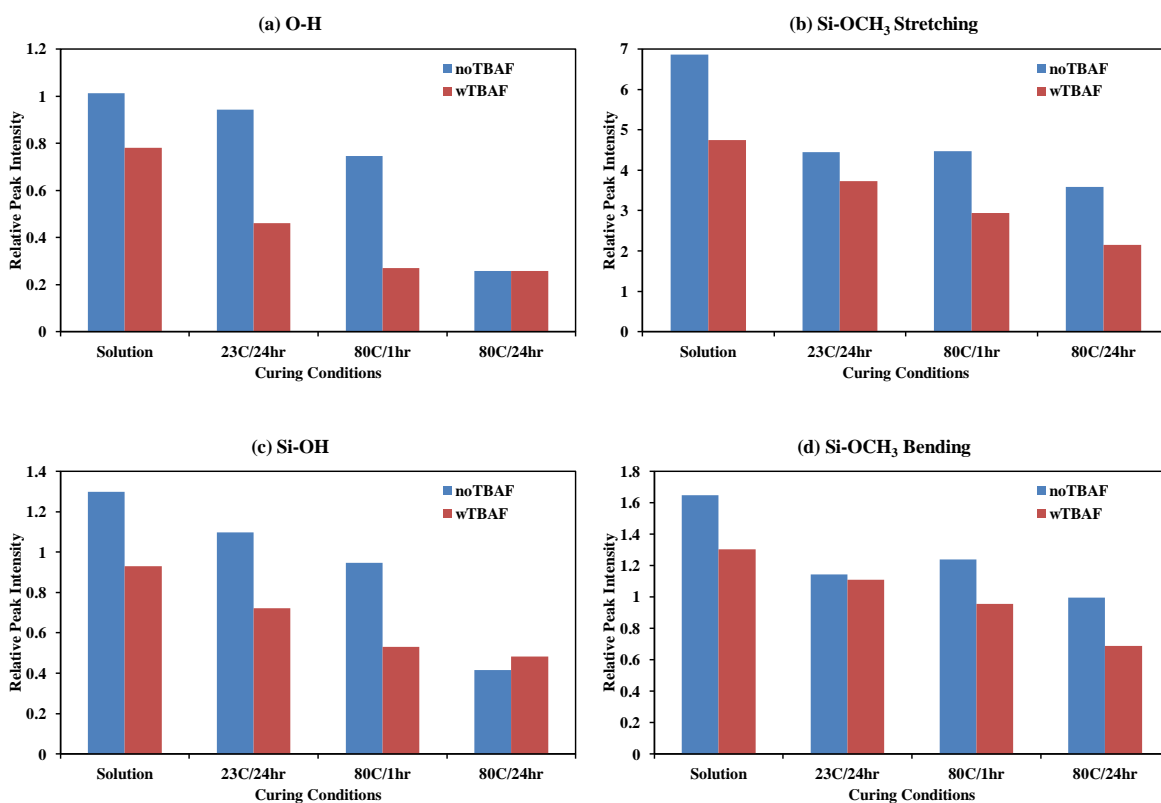


Figure 2.10. Relative intensity of the FTIR peak absorbance at (a) 3350 cm^{-1} (O-H stretching), (b) 1120 cm^{-1} (Si-O-CH₃ stretching), (c) 905 cm^{-1} (Si-OH stretching), and (d) 480 cm^{-1} (Si-OCH₃ bending) to the peak absorbance at 1496 cm^{-1} (C=C stretching in phenyl group of PhEtTMS).

The DSC thermograms and the glass transition temperatures (T_g s) are displayed in Figure 2.11 and Figure 2.12, respectively. For both noTBAF and wTBAF HOI coatings, the increased

T_g with the extent of curing indicates the higher crosslinking density achieved. With regard to the affect of TBAF, at each given curing condition, an increased T_g resulted from adding TBAF was observed, illustrating the effect of TBAF as a condensation catalyst.

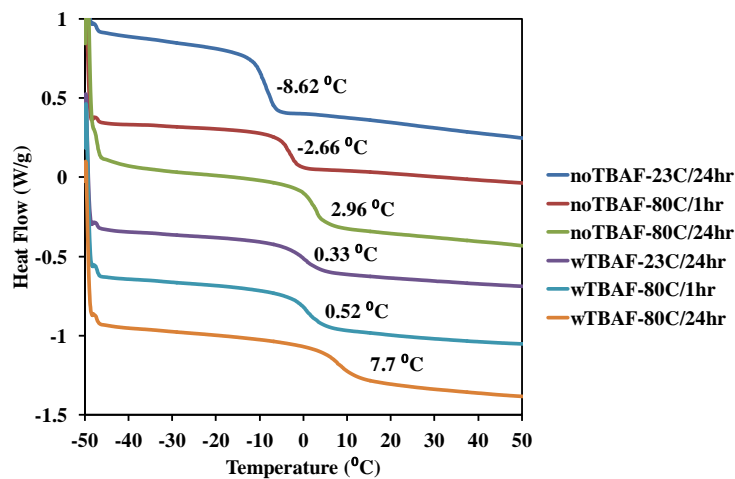


Figure 2.11. DSC curves of HOI coatings.

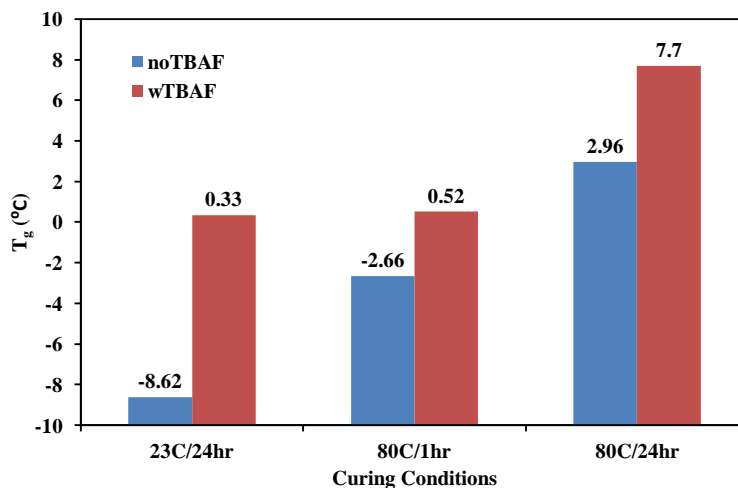


Figure 2.12. Glass transition temperature of coatings derived from noTBAF and wTBAF cured using various conditions.

The HOI clear coatings were prepared by casting the HOI solutions onto AA2024-T3 substrates for EIS measurement to determine the barrier properties. Shown in Figure 2.13 are the

low frequency (0.01 Hz) impedance values determined by generating Bode plots. It can be seen that both TBAF catalyst and curing condition have an impact on the barrier properties. For the coatings prepared from the noTBAF HOI solution, low frequency impedance increased with the extent of curing, indicating better barrier properties. While, for the coatings prepared from the wTBAF HOI solution cured at 80C/24hr condition did not yield to the high low frequency impedance than cured at 80C/1hr, which is attributed to the low film thickness as shown in Table 2.1. The film thickness of coating wTBAF-80C/24hr is only 1/3 of that of coating wTBAF-80C/1hr. With regard to the effect of TBAF, both noTBAF and wTBAF coatings cured at 23C/24hr condition showed comparably poor barrier properties due to the low crosslinking density. Curing at 80C/1hr or 80C/24hr, the coating barrier properties were substantially enhanced when TBAF catalyst was used. Overall, the addition of TBAF catalyst and high temperature curing gave rise to better barrier properties, due to the obtainment of higher crosslinking density.

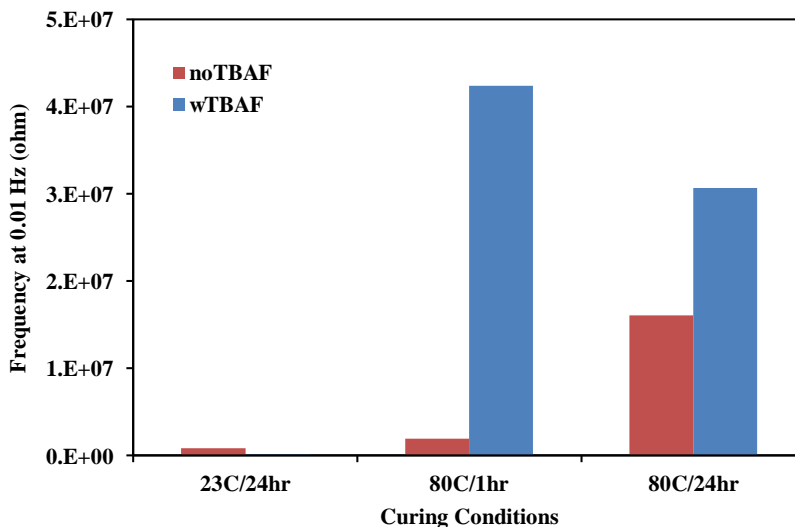


Figure 2.13. Low frequency (0.01 Hz) impedance of HOI coatings derived from noTBAF and wTBAF HOI solutions, as a function of curing conditions.

2.4.3. Characterization of Mg-Rich Primers Based on HOI Binders

Mg-rich primers were prepared using noTBAF and wTBAF HOI solutions and subjected to corrosion protection evaluation. The high concentration of Mg particles of 80 wt% was necessary to ensure close contact between Mg particles and between Mg particle and Al alloy substrate. The Mg-rich primers were tested by EIS for impedance/conductivity comparison, and the topcoated Mg-rich primers were evaluated for long-term corrosion protection behavior by accelerated salt spray exposure according to ASTM B117. Figure 2.14 shows Bode plots for the Mg-rich primers prepared under three curing conditions. It can be clearly observed that the addition of TBAF caused a substantial drop in low frequency impedance, indicating the enhanced conductivity. This might be attributed to higher crosslinking density and thus enhanced Mg interparticle contact resulting from the use of TBAF condensation catalyst. The other possibility is the disruption of the thin surface oxide layer of the Mg particles caused by fluoride ion during the film preparation process.

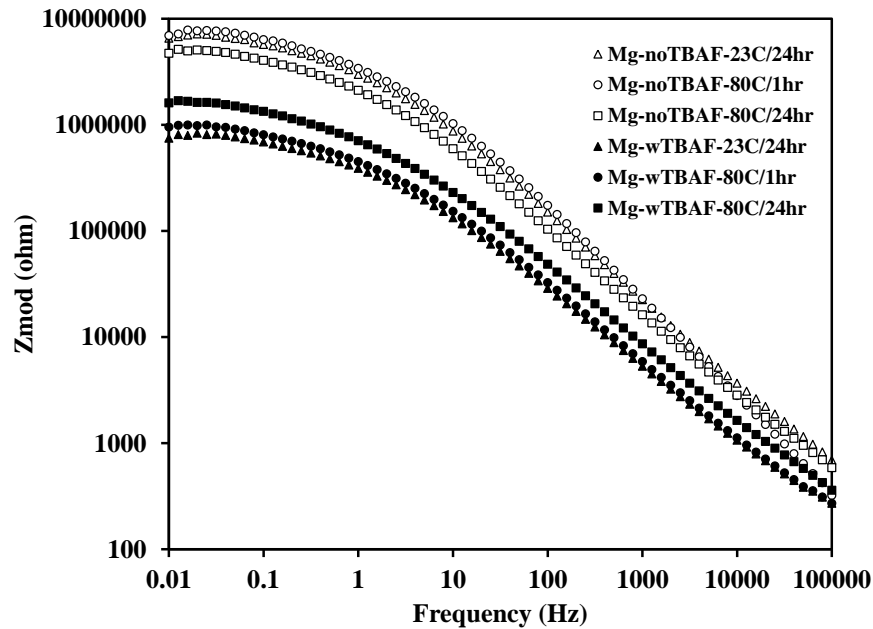


Figure 2.14. Bode plots for Mg-rich primers.

The long-term corrosion protection of the scribed, topcoated Mg-rich primers were evaluated by accelerated salt spray exposure, as shown in Figure 2.15 and Figure 2.16, for samples based on noTBAF system and wTBAF system, respectively. The samples were tested up to 4400 hours in salt spray chamber. Both the addition of TBAF and curing condition had a profound impact on the salt spray performance of the topcoated Mg-rich primers. From both figures, increasing the curing thermal energy led to better corrosion protection performance. By comparing Figure 2.15 with Figure 2.16, it can be seen that the presence of TBAF caused large scale blistering, while in absence of TBAF, the blistering was much less. So, it was surprisingly that, without TBAF, no blistering and corrosion products were observed for the topcoated Mg-rich primers cured at 80C/24hr even after 4,400 hours of salt spray exposure.



Figure 2.15. Images of scribed, topcoated Mg-rich primers derived from noTBAF system after B117 salt spray exposure as a function of exposure time and curing condition.

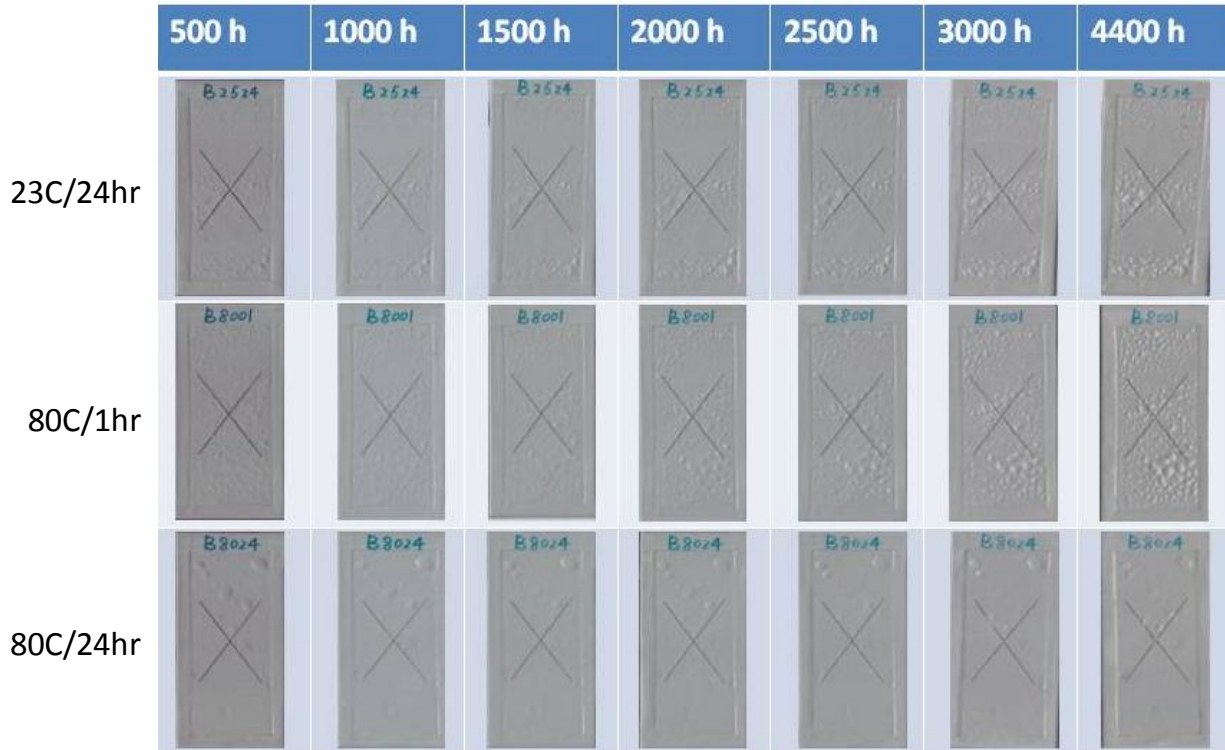


Figure 2.16. Images of scribed, topcoated Mg-rich primers derived from wTBAF system after B117 salt spray exposure as a function of exposure time and curing condition.

In order to understand the mechanism of extensive blistering formation in presence of TBAF catalyst, the origin of the blisters were examined by slicing out the blister, as shown in Figure 2.17. It was found that the blisters originated from within the Mg-rich primer layer.

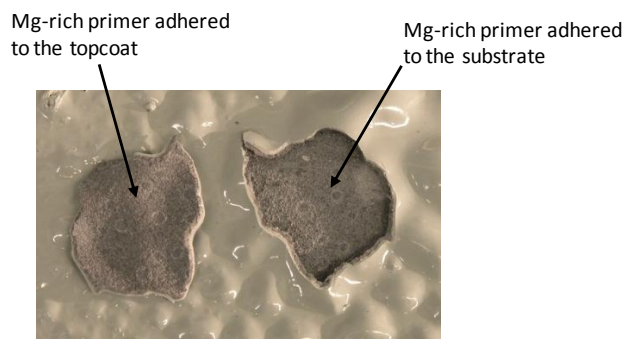


Figure 2.17. Image of a sliced blister from a topcoated sample based on wTBAF after salt spray exposure. The metallic gray material observed within the blister is the Mg-rich primer.

Therefore, it is believed that the blister formation was due to the interaction of fluoride ion of TBAF catalyst with the oxide layer of Mg particles, resulting in the disruption of the oxide layer and the exposure of bare Mg. Mg is a very reactive metal which oxidizes very rapidly upon contact with water, generating magnesium hydroxide and hydrogen gas. The hydrogen gas liberated is the direct source of blisters. Actually the interaction between magnesium oxide with fluoride ion generating magnesium fluoride has been reported elsewhere.¹⁶⁻¹⁸ Therefore, although TBAF was found to effectively promote the condensation reactions, leading to higher crosslink density and, thus, barrier properties, it reacts with the oxide layer of Mg particles, resulting in the rapid oxidation of Mg particles. The corrosion protection of Mg-rich primers in presence of TBAF was impaired and, thus, the TBAF catalyst should not be used for this application. However, without TBAF catalyst, the Mg-rich primers based on HOI systems provide excellent corrosion protection for Al alloy substrate when thoroughly cured.

2.5. Conclusion

Novel Mg-rich primers based on a HOI binder system were produced, and the effects of the addition of TBAF as a condensation catalyst and curing conditions on corrosion protection over Al alloy substrate, AA2024-T3, were investigated determined. It was found that higher thermal energy provided during curing led to higher crosslink density and better barrier properties. Similarly, with TBAF catalyst, greater particle size, higher crosslink density, and better barrier properties were achieved. However, the presence of TBAF was found to result in the disruption of oxide layer of Mg particles which led to the lower conductivity of the derived Mg-rich primers by EIS and blister formation of topcoated Mg-rich primers in salt spray exposure. The mechanism involved the reaction between fluoride ion and the oxide layer causing the exposure and consumption of Mg particles which resulted in the hydrogen gas release forming

blisters. A non-ionic catalyst is therefore expected to provide desirable barrier properties and corrosion protection without blister formation.

2.6. References

1. M. Megharaj, S. Avudainayagam, R. Naidu, Toxicity of Hexavalent Chromium and Its Reduction by Bacteria Isolated from Soil Contaminated with Tannery Waste, *Current Microbiology*, 47, 2003, 51-54
2. R.L. Twite, G.P. Bierwagen, Review of alternatives to chromate for corrosion protection of aluminum aerospace alloys, *Progress in Organic Coatings* 33, 1998, 91–100
3. Michael E. Nanna and Gordon P. Bierwagen, “Mg-rich coatings: A new paradigm for Cr-free corrosion protection of Al aerospace alloys,” *JCT Research*, 1(2), 2004, 69-80.
4. DuhuaWang, Gordon. P. Bierwagen, Sol–gel coatings on metals for corrosion protection, *Progress in Organic Coatings* 64, 2009, 327–338
5. Alda Simoes, Dante Battocchi, Dennis Tallman, and Gordon Bierwagen, “Assessment of the corrosion protection of aluminum substrates by a Mg-rich primer: EIS, SVET and SECM study,” *Prog. Org. Coat.*, 63, 2008, 260-266.
6. M. A. Brook, *Silicon in Organic, Organometallic, and Polymer Chemistry*, Wiley: New York, 2000, 97-99.
7. D. Battocchi, A. M. Simoes, D. E. Tallman, and G. P. Bierwagen, “Electrochemical behavior of a Mg-rich primer in the protection of Al alloys,” *Corros. Sci.*, 48(5), 2006, 1292-1306.

8. M. L. Zheludkevich, I. Miranda Salvado and M. G. S. Ferreira, Sol–gel coatings for corrosion protection of metals, *J. Mater. Chem.*, 15, 2005, 5099–5111
9. R. J. P. Corriu, C. Guerin, and J. J. E. Moreau, “Stereochemistry at Silicon,” in *Topics in Stereochemistry*, E. L. Eliel, S. H. Wilen, and N. L. Allinger Eds., Wiley: New York, 15, 1985, 43.
10. H. Furukawa, Y. Kato, N. Ando, M. Inoue, Y. K. Lee, I. Hazan, and H. Omura, “Cure Mechanism and Properties of Acrylosilane Coatings,” *Prog. Org. Coat.*, 24, 1994, 81-99.
11. Hugo E. Gottlieb, Vadim Kotlyar, and Abraham Nudelman, NMR Chemical Shifts of Common Laboratory Solvents as Trace Impurities, *J. Org. Chem.* 62, 1997, 7512-7515
12. Bret Chisholm and Jim Resue, UV-Curable, Hybrid Organic-Inorganic Coatings, International Waterborne, High-Solids, and Powder Coatings Symposium, February 26-28, 2003, New Orleans, LA
13. F. Hamelmann, U. Heinzmann, A. Szekeres, N. Kirov, T. Nikolova, Deposition of Silicon Oxide Thin Films in TEOS with Addition of Oxygen to the Plasma Ambient: IR Spectra Analysis, *Journal of Optoelectronics and Advanced Materials*, 7(1), 2005, 389 – 392
14. Jae Gyoung Gwon, Sun Young Lee, Geum Hyun Doh, Jung Hyeun Kim, Characterization of Chemically Modified Wood Fibers Using FTIR Spectroscopy for Biocomposites, *Journal of Applied Polymer Science*, 116, 2010, 3212–3219.
15. Sadiye Sener, Murat Erdemoglu, Meltem Aailturk, Hikmet Sayilkan, The Effect of Silane Modication on the Adsorptive Properties of Natural Pyrophyllite and Synthetic Titanium-Based Powders Prepared by the Sol-Gel Process, *Turk J Chem* 29, 2005, 487-495

16. C. S. Lin and Y. C. Fu, "Characterization of anodic films of AZ31 magnesium alloys in alkaline solutions containing fluoride and phosphate anions," *J. Electrochem. Soc.*, 153(10), 2006, B417-B424.
17. S. M. Maliyekkal, S. Shukla, L. Philip, and I. M. Nambi, "Enhanced fluoride removal from drinking water by magnesia-amended activated alumina granules," 140, 2008, 183-192.
18. Ram A. Sharma, "Fused fluoride electrolytes for magnesium oxide electrolysis in the production of magnesium metal," US Patent 5427657 issued June 27, 1995.
19. Bret J. Chisholm, Missy Berry, James Bahr, Jie He, Jun Li, Seva Balbyshev and Gordon P. Bierwagen, Combinatorial materials research applied to the development of new surface coatings XI: a workflow for the development of hybrid organic-inorganic coatings, *Journal of Coatings Technology and Research*, 7(1), 2010, 23-37.

CHAPTER 3. HYBRID ORGANIC-INORGANIC (HOI) MATERIALS DEVELOPED BY AUTOMATED PARALLEL SYSTEM

3.1. Abstract

The application of hybrid organic-inorganic (HOI) binders for making novel Mg-rich primers is highly desirable, thus, the synthesis of hybrid organic-inorganic (HOI) materials by sol-gel chemistry was further explored by using automated parallel reactor system, i.e. a Chemspeed Autoplant A-100TM Semi-Continuous Synthesis Station. The Chemspeed Synthesis Station allows the simultaneously automated synthesis of 12 reactions. The syntheses were accomplished by condensing silica nanoparticles with the alkoxy silane, phenethyltrimethoxysilane (PhEtTMS). The effects of adding the condensation catalyst, tetrabutylammonium fluoride (TBAF), silane content, and curing conditions were studied using solids content, particle size, ^{29}Si -NMR, and EIS. It was found that the increased silane content caused a significantly increased solids content, and better barrier properties were observed for 80°C/24hr cured HOI binders. However, the other properties of HOI solutions and HOI binders were irrelevant to the variables explored, which might be due to the batch-to-batch variation caused by the individual dispensing of the synthesis station.

3.2. Introduction

Magnesium-rich primers have been reported as an alternative replacement for toxic chromate inhibitors for corrosion protection of aluminum alloys. In the galvanic couple, Mg particles corrode preferentially over Al, providing cathodic protection and inhibiting corrosion. HOI materials are highly desirable binders for Mg-rich primers derived from the combined properties of both organic and inorganic components. Due to the complexity involved in the

synthesis of HOI binders, i.e. catalyst, pH, alkoxy silane type, a combinatorial workflow has been designed and used to study the effect of various factors on the stability of sols.¹ It was reported that the phenethyltrimethoxysilane (PhEtTMS) has been proved to be a good candidate for making stable sol solutions. However, the mechanisms involved are not well understood.

Combinatorial and high-throughput methods have been developed to accelerate the exploration and discovery of new materials in pharmaceutical application. Nowadays, combinatorial and high-throughput methods have been used in various applications including catalysts,² electronics,³ coatings,⁴ and so on. Due to the composition and process variables involved in polymer synthesis and preparation, a combinatorial and high-throughput method is highly desirable. The Chemspeed synthesis station is an automated parallel reactor system which has been used to synthesize waterborne PUDs (polyurethane dispersion),⁵ triazoles,⁶ hyperbranched polylysines,⁷ and polymer crystallization study.⁸ Here, a high-throughput method was applied by using a Chemspeed synthesis station to investigate the effects of variables on the properties of HOI solutions and binders.

3.3. Experimental

3.3.1. Raw Materials

Aluminum alloy panels (AA 2024-T3) were obtained from Q-panel Lab Products, with a size of 20 cm x 10 cm x 1 mm. Prior to use, the panels were sandblasted to remove the oxide layer and then cleaned with hexane. Snowtex-O, a colloidal silica dispersion, was obtained from Nissan Chemical. According to the manufacturer, Snowtex-O has a pH of 2-4, silica content of 20-21 wt%, and average particle size of 10-20 nm. Tetrabutyl ammonium fluoride (TBAF, 1.0 M in tetrahydrofuran), isopropyl alcohol (IPA), and propylene glycol monomethyl ether acetate

(PMA) were purchased from Sigma Aldrich. Phenethyl trimethoxysilane (PhEtTMS) was purchased from Gelest. Salt water used for corrosion screening by immersion testing was 3 wt% sodium chloride in water purified by reverse osmosis. Chromium (III) acetylacetonate and acetone-d₆ for ²⁹Si-NMR were obtained from Alfa Aesar. All reagents were used without further purification.

3.3.2. Automated Synthesis of HOI Solutions

The synthesis of HOI solutions were accomplished using a Chemspeed Autoplant A-100TM Semi-Continuous Synthesis Station which consists of 12 reactor modules. In each module, one of the two 100 mL vessels was used as the reactor vessel, the other as the feed vessel, and the 50 mL vessel was used as the trap for distillation products. Six formulations were designed based on two variables, the addition of the catalyst and three silane levels. Each formulation was replicated. The dispensing volume for each formulation was described in Table 3.1. Each reactor vessel was charged with 6.1 mL Snowtex-O, 8.7 mL IPA, and 1.0 mL PhEtTMS for lowSilane formulation or 2.0 mL for medSilane formulation or 3.9 mL for highSilane formulation. Each feed vessel was charged with 51.105 mL PMA (and 2 mL TBAF/IPA solution for wTBAF formulation which contains 0.0359 mL TBAF). The reactor vessel was heated at 60 °C to reflux and allowed to reflux for 2 hours with rapid stirring. The mixture was then cooled to room temperature before the content in the feed vessel was fed into the reactor using two syringe pumps on the reactor module under stirring. Each mixture was concentrated at 84 °C, and all distillation products, including IPA, water, and methanol, were collected by a condenser into the 50 mL vessel.

Table 3.1. Dispensing volume of chemicals (in mL) for twelve HOI solution syntheses.

Vessel	Chemical	noTBAF- lowSilane	noTBAF- medSilane	noTBAF- highSilane	wTBAF- lowSilane	wTBAF- medSilane	wTBAF- highSilane
Reactor vessel	Snowtex-O	6.1	6.1	6.1	6.1	6.1	6.1
	IPA	8.7	8.7	8.7	8.7	8.7	8.7
	PhEtTMS	1.0	2.0	3.9	1.0	2.0	3.9
Feed vessel	PMA	51.1	51.1	51.1	51.1	51.1	51.1
	TBAF/IPA	0	0	0	2	2	2

3.3.3. Preparation of HOI Coatings

Of the twelve HOI solutions synthesized in parallel, four solutions with low PhEtTMS to silica ratio formed a powder when subjected to heating. Thus only eight HOI solutions with medium and high PhEtTMS to silica ratio were applied onto aluminum substrate for curing. Prior to coating application, AA2024-T3 panels were cleaned and deoxidized by: 1) immersing for 10 minutes in a 45 °C aqueous detergent bath consisting of 137 g/L of Oakite Aluminum Cleaner 164 agitated with bubbling air; 2) rinsing with deionized (DI) water; 3) immersing for 2 minutes in 55 °C DI water; 4) immersing in a an ambient temperature deoxidizer solution consisting of 25 wt% ferric sulfate, 3 wt% ferrous sulfate, 2 wt% sodium bifluoride, 5 wt% nitric acid, and 65 wt% DI water agitated with bubbling nitrogen for 10 minutes; and 5) rinsing with DI water. The coatings described in Table 3.2 were produced by creating an 8.5 cm x 18 cm rectangular reservoir on top of a substrate panel by adhering a 508 µm thick polyethylene frame to the panel, pouring approximately 6 ml of a HOI mixture (i.e. noTBAF or wTBAF) into the reservoir, allowing the solvent to flash off in a ventilation hood, and subsequently curing at either room temperature (~ 23 °C) for 24 hours, 80 °C for 1 hour, or 80 °C for 24 hours.

3.3.4. Instrumentation

A Chemspeed Autoplant A-100TM Semi-Continuous Synthesis Station was used for the HOI solution synthesis, which consists of 12 reactor modules for parallel reactions. Each module contains two 100 mL stainless steel vessels and one 50 mL vessel, equipped with independent temperature control, mechanical stirring, N₂ gas purge and reflux cooling. Chemicals were charged into the vessels through syringe pumps by a robotic arm controlled by a computer. Solids content was determined gravimetrically by comparing the weight of the materials before and after heating the HOI solution samples at 200 °C in a vacuum oven overnight.

Table 3.2. Dry film thickness (μm) of the HOI binders.

Sample Designation	noTBAF-medSilane-23C/24hr	noTBAF-medSilane-80C/1hr	noTBAF-medSilane-80C/24hr	noTBAF-highSilane-23C/24hr	noTBAF-highSilane-80C/1hr	noTBAF-highSilane-80C/24hr
Set 1	29.8 ± 11.9	14.8 ± 4.9	17.1 ± 9.1	12.4 ± 6.4	20.3 ± 9.5	23.6 ± 11.1
Set 2	13.5 ± 9.5	12.6 ± 6.3	14.6 ± 6.4	26.2 ± 11.1	13.5 ± 2.8	17.9 ± 5.6
Sample Designation	wTBAF-medSilane-23C/24hr	wTBAF-medSilane-80C/1hr	wTBAF-medSilane-80C/24hr	wTBAF-highSilane-23C/24hr	wTBAF-highSilane-80C/1hr	wTBAF-highSilane-80C/24hr
Set 1	17.3 ± 4.2	9.5 ± 3.6	16.4 ± 5.0	31.6 ± 15.1	32.7 ± 11.7	24.7 ± 6.6
Set 2	7.7 ± 3.7	10.8 ± 6.7	11.5 ± 5.9	22.7 ± 8.9	23.8 ± 11.2	20.8 ± 10.7

The values of solid content were calculated by the following equation, where w_d and w_w are the weight of dry sample and wet sample, respectively.

$$\text{Solid (wt\%)} = \frac{w_d}{w_w} \times 100 \quad \text{Equation 3.1}$$

Particle size was measured using a Nicomp™ CW 380 Submicron Particle Sizer. Dilution of the colloid dispersions prior to measurement was done using IPA. Silicon NMR (^{29}Si NMR) spectra were collected at 79.43 MHz for ^{29}Si , and the acquisition parameters were a 62.5 kHz sweep width with an offset of 0 ppm, a relaxation delay of 5 seconds, and an acquisition time of 0.262 s. Using these conditions, 14,000 scans were collected at an average temperature of 21.4 °C. The sample tubes were equipped with Teflon® bottoms and the lock solvent was acetone- d_6 with chromium (III) tris-acetylacetonate ($\text{Cr}(\text{acac})_3$) added at a concentration of 0.25 M. $\text{Cr}(\text{acac})_3$ was added in order to allow for complete relaxation recovery and quantitative spectra. A Bruker Optics Vertex 70 FT-IR was used to collect Fourier transform infrared (FTIR) spectra in transmission from samples deposited on a KBr plate. Spectra were analyzed using OPUS software from Bruker. EIS was conducted with a Gamry MultiEchem 8 Electrochemical Workstation and Gamry Framework software. The electrolyte used was 3 wt% NaCl in DI water and the frequency range was 10^4 Hz to 0.01 Hz with an applied 10 mV R.M.S. voltage vs. open circuit potential. A Ag/AgCl reference electrode and Pt mesh counter electrode were utilized

3.4. Results and Discussion

3.4.1. Synthesis and Characterization of HOI Solutions

The variables explored were the catalyst and the silane to silica ratio, as illustrated in Figure 3.1. The effect of adding TBAF and without adding TBAF was compared. The silane to silica ratios (moles PhEtTMS per grams of silica) of 0.00325, 0.0065, and 0.013 were

investigated. Each formulation was replicated. Therefore, a total 12 reactions were carried out simultaneously by the synthesis station. All twelve formulations produced stable sol solutions.

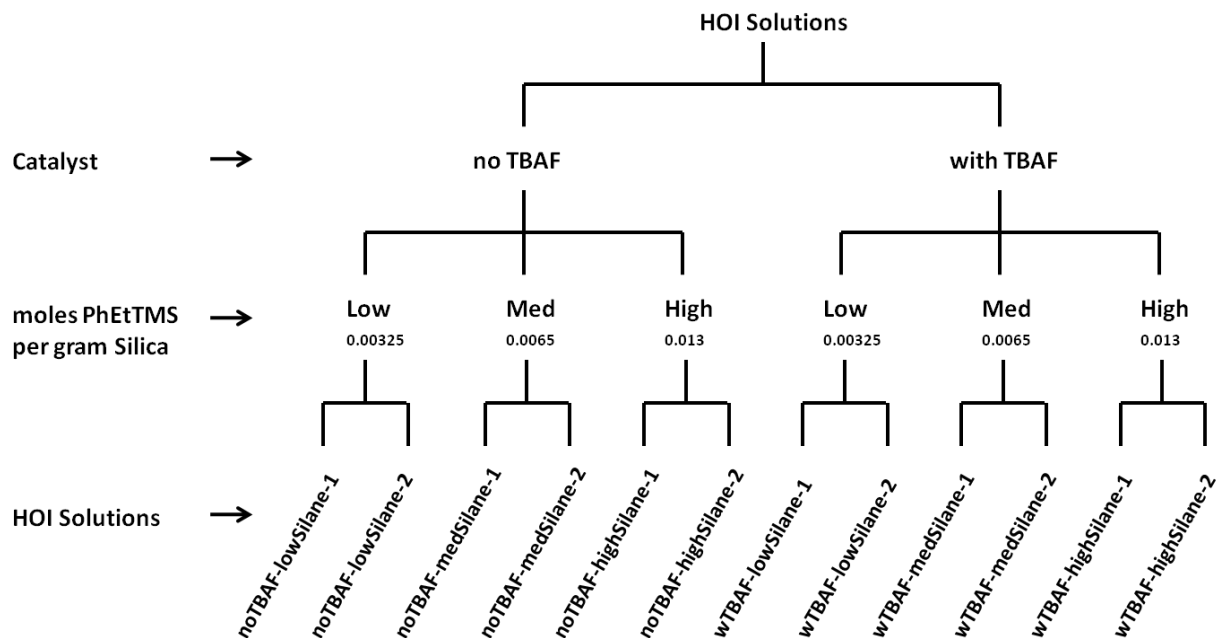


Figure 3.1. An schematic illustration of experimental design of HOI solution synthesis using Chemspeed. (Each formulation was replicated)

The effect of the variables were evaluated by comparing the weight of the synthesized HOI solution products, the distillation products, and the total products (HOI solution + distillate) in each reactor, as shown in Figure 3.2. The reproducibility using the Chemspeed Synthesis Station was displayed by comparing the weights of HOI solutions, distillates, and total products using two reactors based on the same formulation. It can be seen that the Chemspeed Synthesis Station reproduces well for most of the syntheses since the weight differences between two batches on the same formulation were minor.

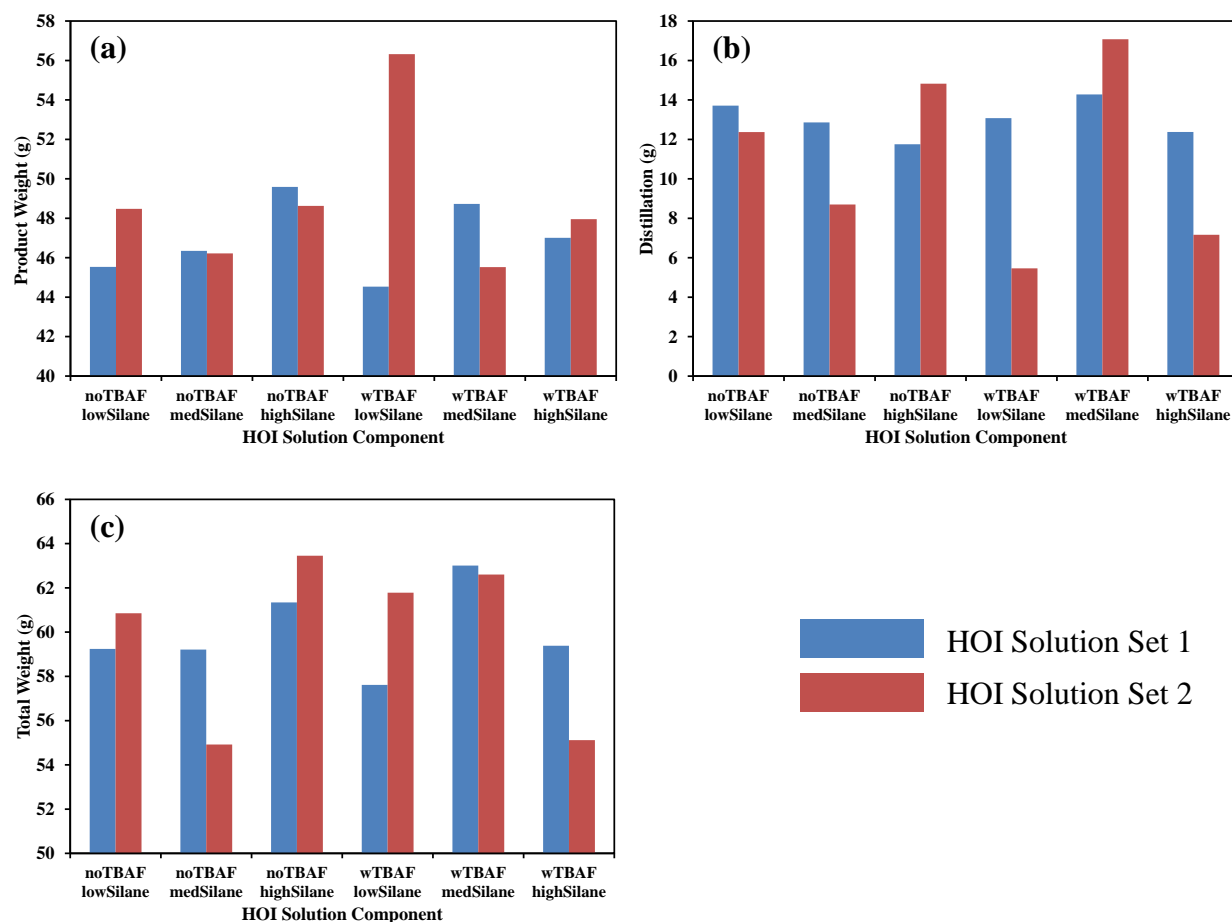


Figure 3.2. Evaluation of Chemspeed Synthesis Station reproduction by comparing HOI solution synthesis by (a) product weight, (b) distillation product weight, and (c) total weight.

Figure 3.3 displays the solids content of the HOI solutions. In contrast to the weight comparison, solid content shows a consistent increase with silane content for both HOI solutions without and with TBAF catalyst. And the replicated batches showed similar solid contents, indicating that the Chemspeed Synthesis Station reproduces very well for each formulation. By comparing the weight and solid content in evaluating the reproducibility of the Chemspeed Synthesis Station, it was concluded that the dispensing volume of the reactants in each reactor may vary but the ratio between the reactants were consistent. Similar reaction conditions, temperature, stirring, reflux, etc. were provided by Chemspeed Synthesis Station.

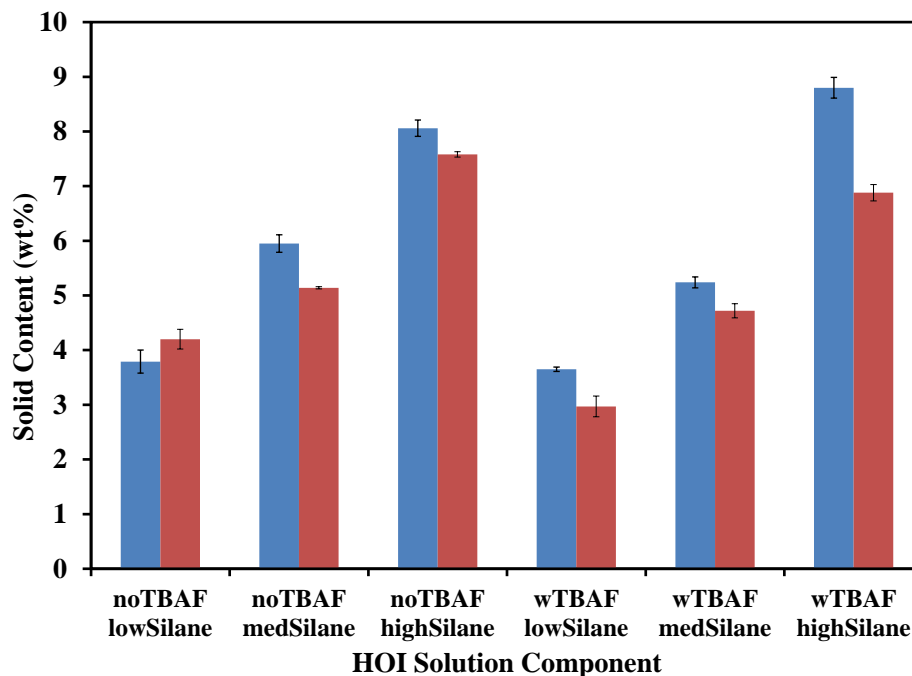


Figure 3.3. Solids content of the HOI solutions produced by Chemspeed.

Figure 3.4 and Figure 3.5 displays the ^{29}Si -NMR spectra of the HOI solutions, comparing the effect silane content and the addition of TBAF catalyst, respectively. The silane content did not seem to cause a large difference in silanol condensation when TBAF catalyst was not added as shown in Figure 3.4 (a) due to the similar peak intensity, however higher silane level caused higher silanol condensation when TBAF catalyst was added as indicated by the higher T_2 and T_3 peak intensities, as shown in Figure 3.4 (b). In contrast to what has been observed in Chapter 2, the addition of TBAF catalyst did not lead to the increased silanol condensation as shown here in Figure 3.5 (a) and (b). It may due to the batch-to-batch variation caused by the individual robotic dispensing.

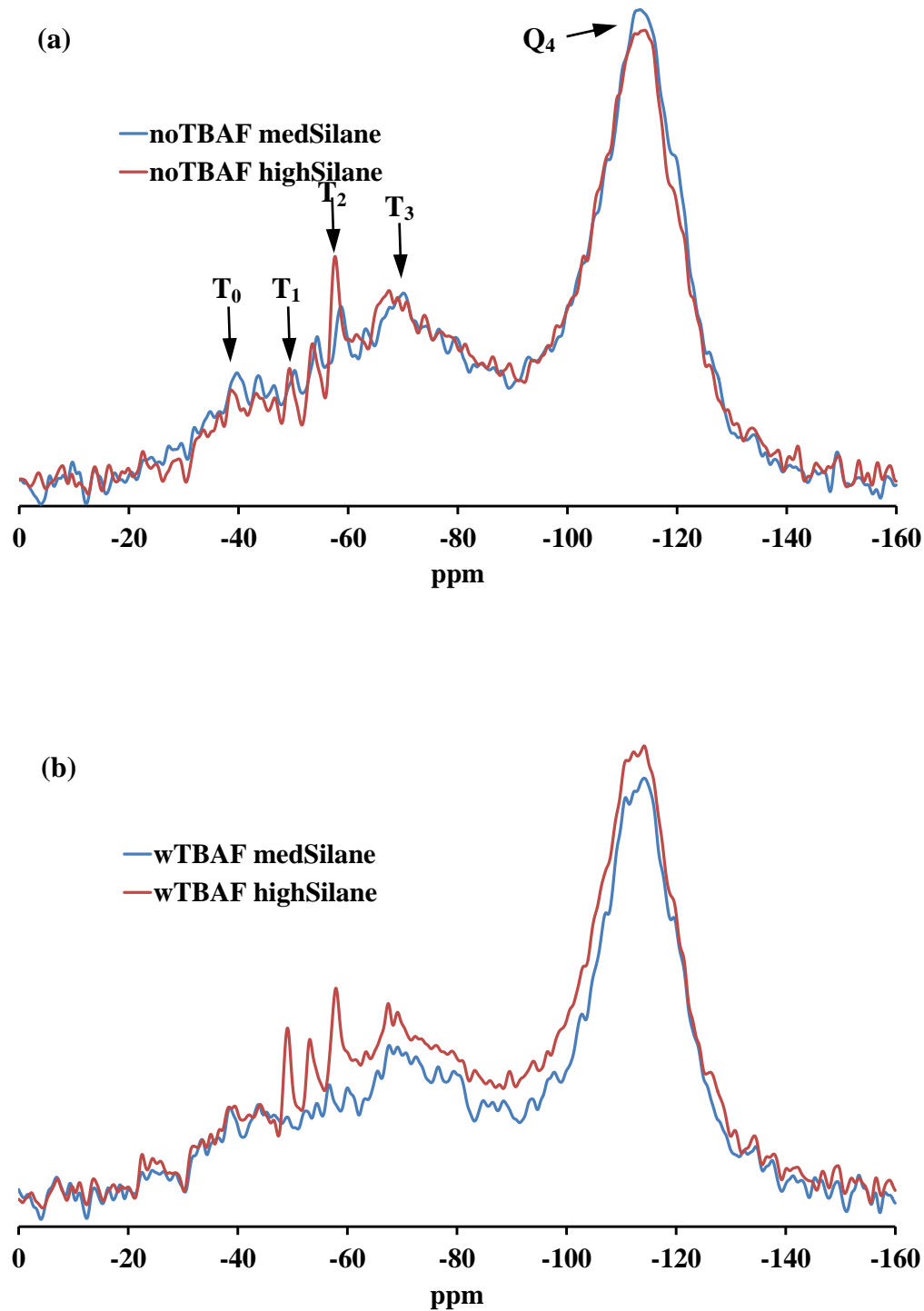


Figure 3.4. ²⁹Si-NMR spectra of the HOI solutions produced to compare the effect of PhEtTMS level in absence (a) and in presence (b) of TBAF.

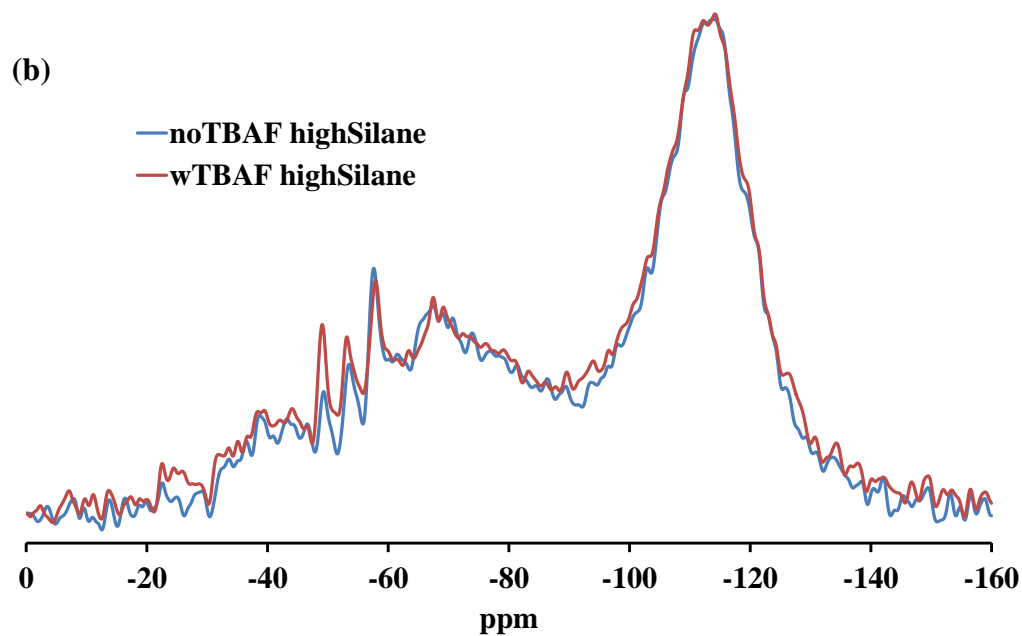
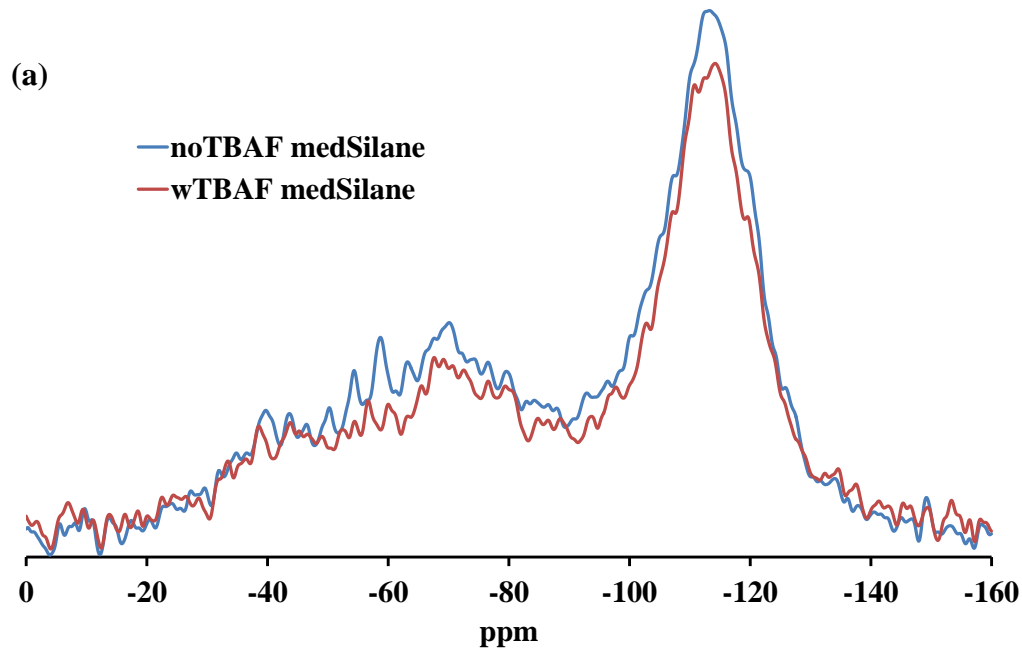


Figure 3.5. ^{29}Si -NMR spectra of the HOI solutions produced to compare the effect of condensation catalyst TBAF at medium (a) and high (b) of PhEtTMS level.

Figure 3.6 displays the particle size of the HOI solutions. The particle size appeared to be irrelevant to the silane content. As opposed to what has been observed in Chapter 2, the effect of adding TBAF catalyst on the particle size is negligible here. The lack of trends may indicate batch-to-batch variation caused by the synthesis station.

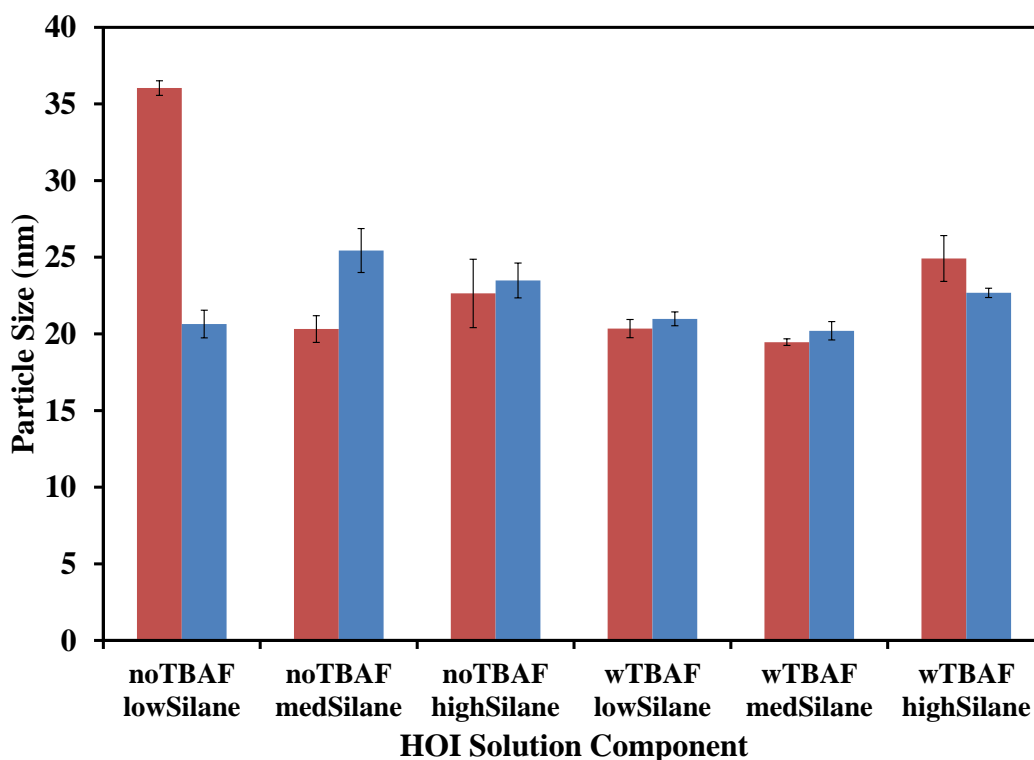


Figure 3.6. Particle size of the HOI solutions produced by Chemspeed.

3.4.2. Characterization of HOI Coatings

Due to the relative low extent of condensation and lack of covalent bonding between silica nanoparticles, the dried HOI solutions with low silane content were still individual particles and, thus, only the HOI solutions with medium and high silane content were subjected to curing onto AA2024-T3. Three curing conditions were applied, namely, room temperature for

24 hr (23C/24hr), 80 °C for 1 hr (80C/1hr), and 80 °C for 24 hr (80C/1hr). Therefore, with each formulation replicated, a total of 24 HOI binders were generated, as shown in Figure 3.7.

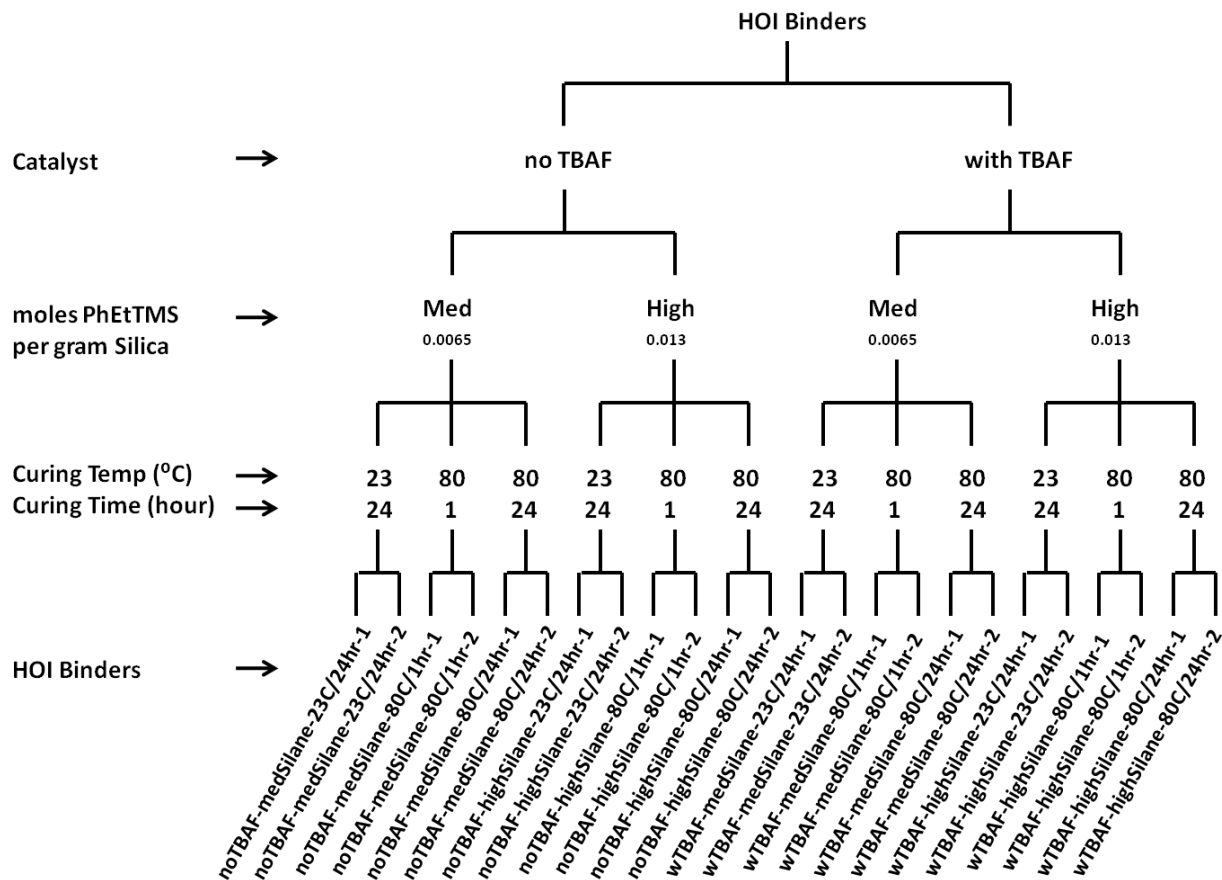


Figure 3.7. An schematic illustration of experimental design of HOI binder produced.

The barrier properties were tested using EIS. Figure 3.8 displays the low frequency (0.01 Hz) impedance of the coatings obtained from Bode plots. Generally, as shown in Figure 3.8, the low frequency impedance was influenced by curing conditions. In general, when higher thermal energy was applied to cure the coatings, the coatings showed better barrier properties due to the higher crosslinking density. The exceptions are the binders generated from HOI solutions, noTBAF-medSilane-1, wTBAF-medSilane-1 and wTBAF-medSilane-2, which did not always

show the higher low frequency impedance when higher thermal energy was applied to cure the coatings. This anomaly is most likely due to the difference in film thickness between the coatings, as shown in Table 3.2. With regard to the effect of adding TBAF catalyst and silane content, no obvious trend was observed.

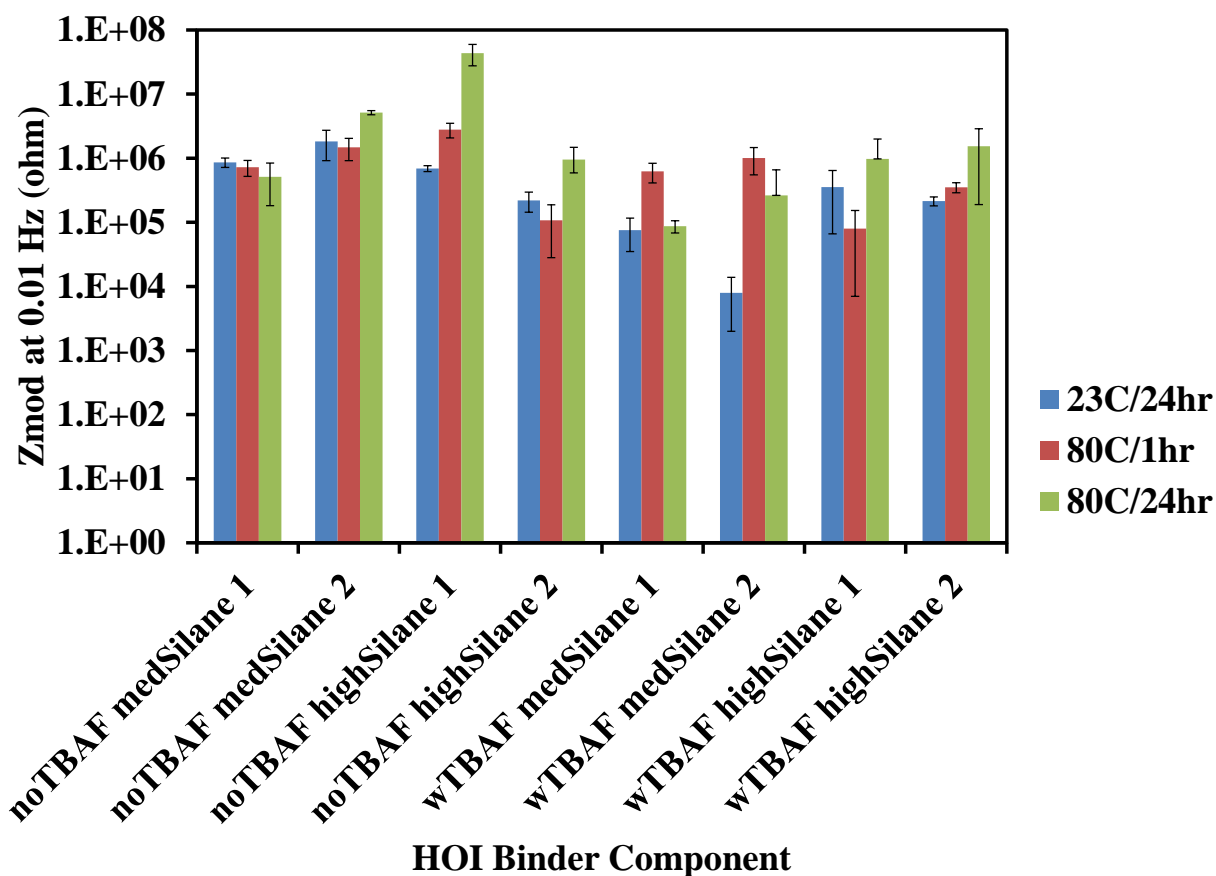


Figure 3.8. Low frequency (0.01 Hz) impedance of coatings derived from noTBAF and wTBAF cured using various conditions.

3.5. Conclusion

The HOI binders for making Mg-rich primers were automated and parallelly prepared using a Chemspeed Autoplant A-100TM Semi-Continuous Synthesis Station. The Chemspeed synthesis station reproduced very well on the syntheses based on the same formulation. The solid

content showed a clear trend with the increase of silane content, whereas the other properties, i.e. particle size, condensation extent, barrier property, did not change with the variables explored, which was not consistent with what was observed in Chapter 2. This may be attributed to batch-to-batch variation when the synthesis station dispensed the reactants and the control of the reaction condition for individual reactors.

3.6. References

1. Bret J. Chisholm, Missy Berry, James Bahr, Jie He, Jun Li, Seva Balbyshev, Gordon P. Bierwagen, Combinatorial materials research applied to the development of new surface coatings XI: a workflow for the development of hybrid organic–inorganic coatings, *J. Coat. Technol. Res.*, 7 (1), 2010, 23–37.
2. Peijun Cong, Robert D. Doolen, Qun Fan, Daniel M. Giaquinta, Shenheng Guan, Eric W. McFarland, Damodara M. Poojary, Kyle Self, Howard W. Turner, and W. Henry Weinberg, High-Throughput Synthesis and Screening of Combinatorial Heterogeneous Catalyst Libraries, *Angew. Chem. Int. Ed.* 38(4), 1999, 483-488
3. Wilhelm F. Maier, Klaus Stowe, and Simone Sieg, Combinatorial and High-Throughput Materials Science, *Angew. Chem. Int. Ed.* 46, 2007, 6016 – 6067
4. Bret Chisholm, Radislav Potyrailo, James Cawse, Ronald Shaffer, Michael Brennan, Chris Molaison, Donald Whisenhunt, Bill Flanagan, Dan Olson, Jay Akhave, Dennis Saunders, Ali Mehrabi, Mark Licon, The development of combinatorial chemistry methods for coating development I. Overview of the experimental factory, *Progress in Organic Coatings* 45, 2002, 313–321

5. Mohammed J. Nasrullah, James A. Bahr, Christy Gallagher-Lein, Dean C. Webster, Richard R. Roesler, Peter Schmitt, Automated parallel polyurethane dispersion synthesis and characterization, *J. Coat. Technol. Res.*, 6 (1) 2009, 1–10.
6. Ibtissem Jlalila, Claire Beauvineau, Sophie Beauvière, Esra Önen, Marie Aufort, Aymeric Beauvineau, Eihab Khaba, Jean Herscovici, Faouzi Meganem, and Christian Girard, Automated Synthesis of a 96 Product-Sized Library of Triazole Derivatives Using a Solid Phase Supported Copper Catalyst, *Molecules* 15, 2010, 3087-3120
7. Markus Scholl, Tuan Q. Nguyen, Bernd Bruchmann, Harm-Anton Klok, The Thermal Polymerization of Amino Acids Revisited; Synthesis and Structural Characterization of Hyperbranched Polymers from L-Lysine, *Journal of Polymer Science: Part A: Polymer Chemistry*, 45, 2007, 5494–5508.
8. Alastair J. Florence, Andrea Johnston, Philippe Fernandes, Norman Shankland and Kenneth Shankland, An automated platform for parallel crystallization of small organic molecules, *J. Appl. Cryst.* 39, 2006, 922–924

CHAPTER 4. HYBRID ORGANIC-INORGANIC (HOI) MATERIALS—THE EFFECT OF CATALYST

4.1. Abstract

Condensation catalysts were found to have a profound effect on the properties of HOI binders as well as the corrosion protection for aluminum alloys, as discussed in Chapter 2, which led to the catalyst exploration on the synthesis of HOI binders. The non-ionic catalyst, dibutyltin dilaurate (DBTDL), and the ionic catalyst, tetrabutyl ammonium fluoride (TBAF), were compared with respect to their ability to catalyze the condensation of the HOI binders. Preliminary results were obtained by characterizing the HOI solutions using solid content, particle size, and FTIR. Both catalysts promoted the condensation reaction. But the condensation extent was found to be lower when DBTDL was used as a catalyst, as compared with TBAF, suggesting the weaker catalysis strength of the non-ionic catalyst.

4.2. Introduction

The catalyst plays an important role in determining the structure of the products derived from sol-gel technology. A basic catalyst tends to catalyze the condensation reaction leading to the formation of a more compact structure, while an acid catalyst tends to catalyze hydrolysis reactions leading to the formation of more linear structures. Besides the impact on the formation of structure, the catalyst also affects the corrosion protection behavior of Mg-rich primers, as discussed in Chapter 2. It has been found that TBAF, working as a condensation catalyst for synthesizing HOI binders via sol-gel chemistry, leads to the oxidation of Mg particles and hydrogen gas liberation during salt spray exposure, resulting in blistering formation. A non-ionic catalyst was proposed to replace TBAF to prevent the ion release and the interaction with Mg

particles. Therefore, a non-ionic catalyst, dibutyltin dilaurate (DBTDL), was studied and compared with TBAF.

4.3. Experimental

4.3.1. Raw Materials

Snowtex-O, a colloidal silica dispersion, was obtained from Nissan Chemical. According to the manufacturer, Snowtex-O has a pH of 2-4, silica content of 20-21 weight percent, and average particle size of 10-20 nm. Tetrabutyl ammonium fluoride (TBAF, 1.0 M in tetrahydrofuran), dibutyltin dilaurate (DBTDL), isopropyl alcohol (IPA), and propylene glycol monomethyl ether acetate (PMA) were purchased from Sigma Aldrich. Phenethyl trimethoxysilane (PhEtTMS) was purchased from Gelest. All reagents were used without further purification.

4.3.2. Synthesis and Characterization of HOI Solutions

75 mls of Snowtex-O and 108 mls of IPA were combined in a 2000 ml Erlenmeyer flask. 50 g of PhEtTMS was slowly added to this mixture using rapid, magnetic stirring. The mixture was then heated to reflux and allowed to reflux for 2 hours. The mixture was then cooled to room temperature before 612 g of PMA was added using rapid stirring. The mixture was then split into three equal portions (203 g in each portion) and each portion poured into a pre-weighed, 2,000 ml, one-neck, round-bottomed flask. To two of the three solutions, 0.27 g of the 1.0 M TBAF solution in THF and DBTDL was added, respectively. Each mixture was concentrated on a roto-evaporator that utilized a 70 °C water bath. Essentially all of the isopropanol, water, and methanol were removed from the mixtures as indicated by the change in weight of the solution

and proton nuclear magnetic resonance spectroscopy. The solids content of both mixtures was determined gravimetrically.

4.3.3. Preparation of HOI Coatings

Prior to coating application, AA2024-T3 panels were cleaned and deoxidized by: 1) immersing for 10 minutes in a 45 °C aqueous detergent bath consisting of 137 g/L Oakite Aluminum Cleaner 164 agitated with bubbling air; 2) rinsing with deionized (DI) water; 3) immersing for 2 minutes in 55 °C DI water; 4) immersing in a an ambient temperature deoxidizer solution consisting of 25 wt% ferric sulfate, 3 wt% ferrous sulfate, 2 wt% sodium bifluoride, 5 wt% nitric acid, and 65wt % DI water agitated with bubbling nitrogen for 10 minutes; and 5) rinsing with DI water. The HOI coatings were produced by creating an 8.5 cm x 18 cm rectangular reservoir on top of a substrate panel by adhering a 508 µm thick polyethylene frame to the panel, pouring approximately 6 mls of a HOI solution (i.e. noCatalyst or DBTDL or TBAF) into the reservoir, allowing the solvent to flash off in a ventilation hood, and subsequently curing at either room temperature (~ 23 °C) for 24 hours, 80 °C for 1 hour, or 80 °C for 24 hours.

4.3.4. Instrumentation

Solids content was determined gravimetrically by comparing the weight of the materials before and after heating the HOI solution samples at 200 °C in a vacuum oven overnight. The values were calculated by the following equation, where w_d and w_w are the weight of dry sample and wet sample, respectively.

$$\text{Solid (wt\%)} = \frac{w_d}{w_w} \times 100 \quad \text{Equation 4.1}$$

Particle size was measured using a Nicomp™ CW 380 Submicron Particle Sizer. Dilution of the colloid dispersions prior to measurement was done using IPA. A Bruker Optics Vertex 70 FT-IR was used to collect Fourier transform infrared (FTIR) spectra in transmission from samples deposited on a KBr plate. Spectra were analyzed using OPUS software from Bruker.

4.4. Results and Discussion

4.4.1. Synthesis and Characterization of HOI Solutions

Figure 4.1 displays the solids content of the HOI solutions produced without using any catalyst, using DBTDL and TBAF as catalyst, respectively. The three HOI solutions showed a similar solids content.

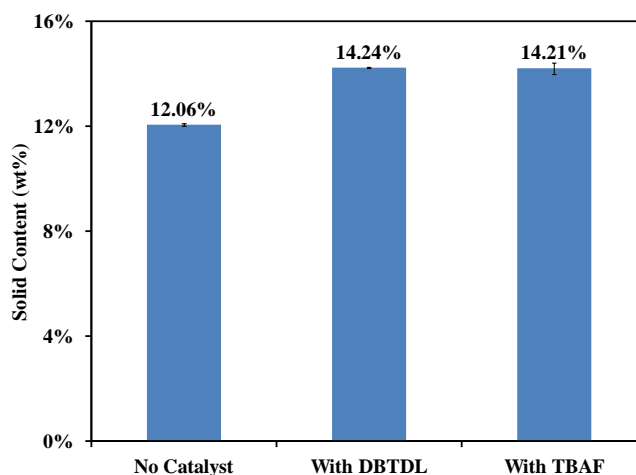


Figure 4.1. Solids content of HOI solutions produced without catalyst, with DBTDL and TBAF as catalyst, respectively.

Figure 4.2 displays the particle size of the colloidal silica as a control, the HOI binders produced without using any catalyst, using DBTDL and TBAF as catalyst, respectively. The particle size increase when PhEtTMS was used to modify the colloidal silica nanoparticle surface.

The increase was enhanced when using condensation catalyst, DBTDL and TBAF. By comparing the two condensation catalysts, it clearly shows that the ionic TBAF catalyst allows greater extent of condensation, resulting in larger functionalized silica nanoparticles. Similar relatively low condensation extent caused by using DBTDL catalyst was reported elsewhere.¹ In contrast, fluoride catalyst is one of the most effective condensation catalysts, the mechanism of which was proposed to involve the displacement of OH⁻ by F⁻ and thereby the reduced electron density and higher susceptibility to nucleophilic attack of silicon atom.² It was also proposed by Iler that the higher condensation rate by fluoride anion catalyst resulted from the temporarily increased coordination of silicon from four to five or six.³

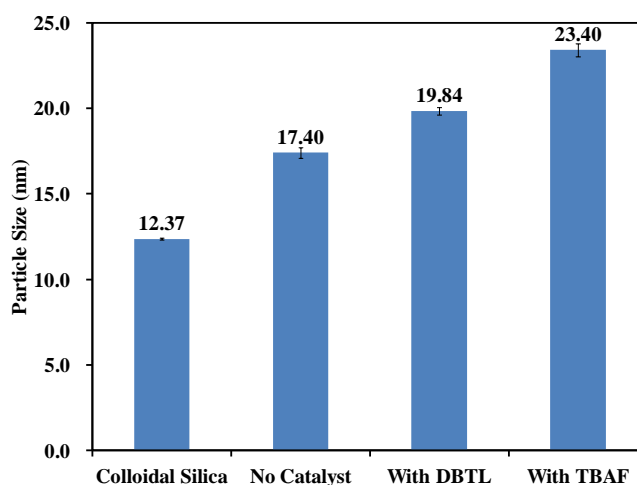


Figure 4.2. Particle size of colloidal silica, the HOI solutions produced without catalyst, with DBTDL and TBAF as catalyst, respectively.

4.4.2. Characterization of HOI Coatings

FTIR was used to characterize the condensation extent of the HOI coatings. Figure 4.3 presents the FTIR spectra of the HOI coatings produced with DBTDL catalyst under three different curing conditions. The results were consistent with what was observed before, the reduction of the band centered at 1120 cm^{-1} (Si-O-CH₃ asymmetric stretching) as well as the

bands at 3350 cm^{-1} (SiO-H), 905 cm^{-1} (Si-OH) and 480 cm^{-1} (SiO-CH₃ bending) indicates a higher extent of condensation.

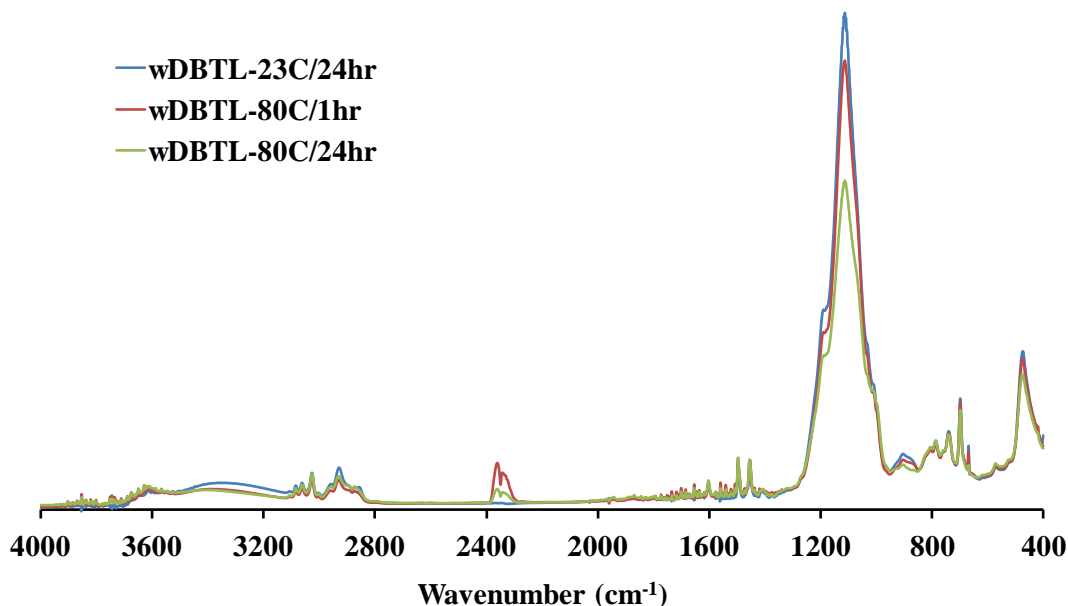


Figure 4.3. HOI binders produced under different curing conditions

Figure 4.4 (a)-(c) displays the FTIR spectra of the HOI coatings as a function of catalyst under different curing conditions. Under all three curing conditions, the reduction of the bands centered at 3350 cm^{-1} (SiO-H) and 905 cm^{-1} (Si-OH) could be observed, suggesting the higher extent of condensation resulted from using the condensation catalyst DBTDL and TBAF. TBAF caused higher curing extent than DBTDL. However, the intensity of the band centered at 1120 cm^{-1} (Si-O-CH₃ asymmetric stretching) and 480 cm^{-1} (SiO-CH₃ bending) was not reduced for hydrolysis reaction. This may be attributed to the less extent of hydrolysis during curing with the condensation catalysts.

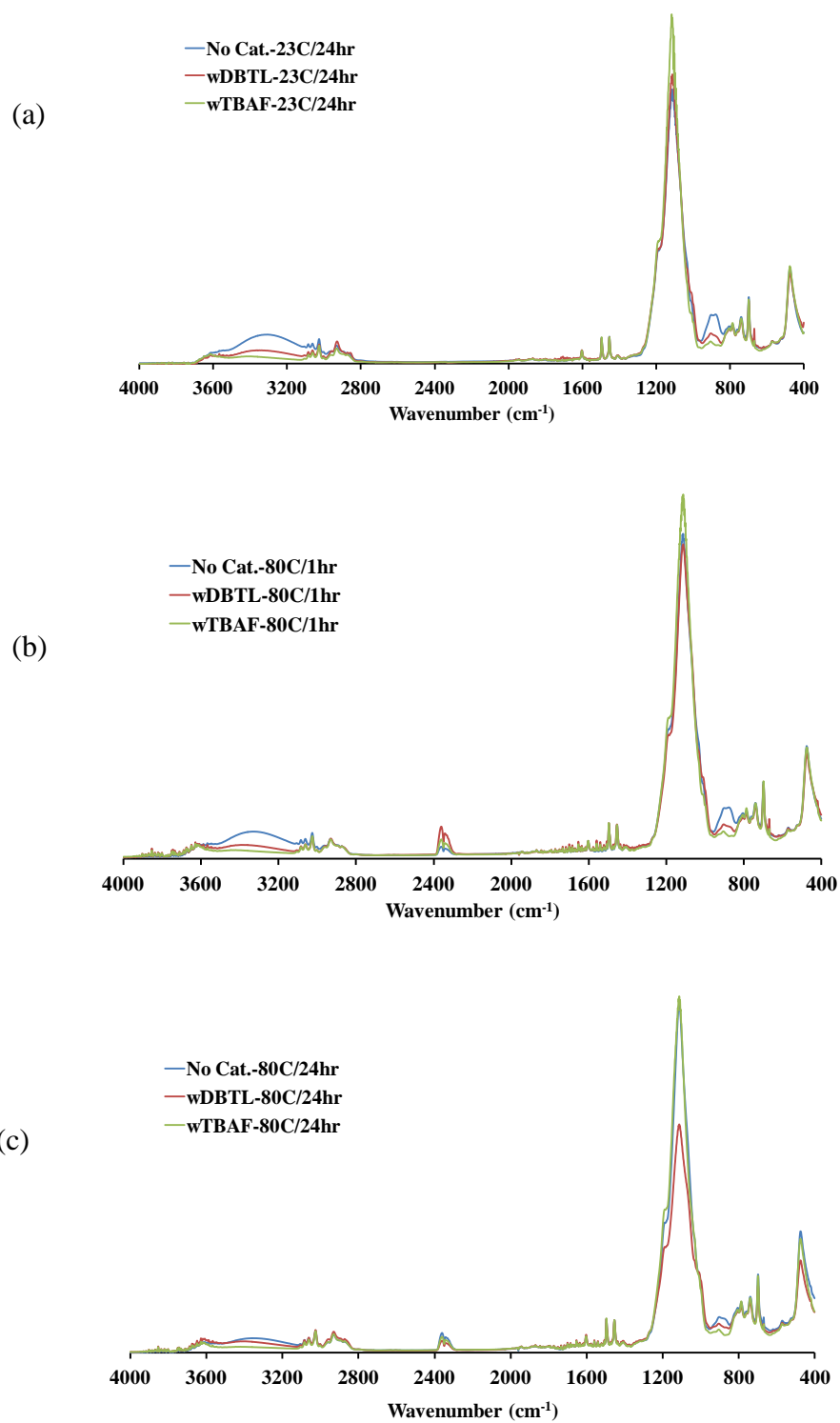


Figure 4.4. FTIR spectra of HOI binders produced using different catalyst and cured under (a) 23C/24hr, (b) 80C/1hr, (c) 80C/24hr.

4.5. Conclusion

The non-ionic dibutyltin dilaurate (DBTDL) catalyst and ionic tetrabutyl ammonium fluoride (TBAF) catalyst were compared with respect to their capability of catalyzing condensation reactions of the HOI binders. Preliminary results were obtained based on the characterization of particle size and FTIR. Both catalysts promoted the condensation reaction, while the DBTDL tends to have less impact on the condensation reaction than TBAF.

4.6. References

1. Guru S. Rajan, Gil S. Sur, James E. Mark, Dale W. Schaefer, Gregory Beaucage, Preparation and Characterization of Some Unusually Transparent Poly(dimethylsiloxane) Nanocomposites, *Journal of Polymer Science: Part B: Polymer Physics*, 41, 2003, 1897–1901.
2. R.J.P. Corriu, D. LeClercq, A. Vioux, M. Pauthe, and J. Phalippou in *Ultrastructure Processing of Advanced Ceramics*, eds. J.D. Mackenzie and D.R. Ulrich, Wiley, New York, 1988, 113-126
3. R.K. Iler, *The Chemistry of Silica*, Wiley, New York, 1979

CHAPTER 5. PERFECTLY ALTERNATING POLYCARBONATE- POLYDIMETHYLSILOXANE (PC-PDMS) MULTIBLOCK COPOLYMERS—PART I

5.1. Abstract

Perfectly alternating PC-PDMS multiblock copolymers were produced using a two-step synthesis method, which involved the interfacial polymerization of a linear allyl-terminated PC and the subsequent hydrosilylation coupling of allyl-terminated PC and hydride-terminated PDMS. By this method, the PC-PDMS block copolymers with controlled block length and alternating block architecture were obtained. In the first step of the synthesis, the pure allyl-terminated PC was synthesized by interfacial polymerization of bisphenol-A (BPA), triphosgene (TPG), and eugenol as an end-capping monomer. Two different catalysts were investigated, triethylamine (TEA) and the phase transfer catalyst, triethylbenzylammonium chloride (TEBA). Other variables explored for the synthesis were BPA/eugenol mole ratio, concentration of TPG, and concentration of the catalyst. The allyl-terminated PCs were characterized using proton and phosphorous nuclear magnetic resonance spectroscopy ($^1\text{H-NMR}$, $^{31}\text{P-NMR}$), gel-permeation chromatography (GPC), and matrix-assisted laser desorption/ionization time-of-flight mass spectroscopy (MALDI-TOF). Pure allyl-terminated PCs were obtained by using the phase transfer catalyst. In the second step of this method, the successful formation of PC-PDMS block copolymers was demonstrated by GPC and $^1\text{H-NMR}$. The modulated differential scanning calorimetry (MDSC) results indicated the partial miscibility of PDMS phase with the PC phase especially for short PDMS block lengths. Phase inversion could be observed from dynamic mechanical analysis (DMA). Morphological characterization using atomic force microscopy (AFM) showed nanoscale phase separation. Significantly increased char yield of the block copolymers as compared to pure PC was demonstrated by thermogravimetric analysis (TGA).

The synthesized PC-PDMS block copolymers exhibited high optical clarity at up to 62 wt% PDMS content. In comparison with a commercial PC-PDMS block copolymer, the synthesized block copolymer showed higher optical clarity, indicating a finer morphology from the uniform alternating block architecture.

5.2. Introduction

Bisphenol-A-based polycarbonate (PC) is generally recognized as the most impact resistant, transparent engineering thermoplastic available.^{1,2} While PC exhibits exceptionally good impact strength for an engineering thermoplastic, it has a tendency to undergo brittle failure in notched impact tests.³ While rubber toughening of PC by melt blending rubber particles into the PC can significantly increase impact properties, the particles generally scatter visible light resulting in opaque materials.⁴ To overcome this deficiency, block copolymer structures have been investigated in which rubbery polymer segments are incorporated directly into the PC backbone to limit rubber domain size and produce transparent materials. Polycarbonate-polysiloxane (PC-PSiO) block copolymers were first synthesized by Vaughn in the 1960s.⁵⁻⁷ The method involved reacting phosgene with bisphenol A (BPA) and a phenolic-terminated PDMS. The phenolic terminated PDMS can be prepared by reaction of a chloro-terminated siloxane with excess BPA, or, alternatively, by hydrosilation of a hydride-terminated siloxane with a functionalized phenolic compound. The phenol end-capped PDMS can then easily be incorporated into polycarbonate via interfacial polymerization.⁸ The majority of the synthesis strategies for PC-PSiO multiblock copolymers involve the reaction of a polydimethylsiloxane (PDMS) modified with nucleophilic end-groups with BPA and phosgene. As a result of the synthesis method, the resulting copolymers possess polydisperse block lengths which affect their

optical and mechanical properties.⁷ Depending on the PDMS block length and loading, the resulting PC-PDMS block copolymers are either a flexible elastomer, or a rigid thermoplastic. Various surface and bulk properties were studied and the PC-PDMS block copolymers were found to be more flame retardant, wear resistant, aging resistant and pure PC.⁹⁻¹² Herein, our study describes a novel two-step synthesis method to generate PC-PDMS block copolymers which possess controlled block lengths and a perfectly alternating block architecture.

5.3. Experimental

5.3.1. Raw Materials

Bisphenol-A (BPA), triphosgene (TPG), 4-allyl-2-methoxyphenol (eugenol), 2,5-dihydroxybenzoic acid (DHB), potassium-trifluoroacetate, sodium hydroxide (NaOH), triethylamine (TEA), triethylbenzylammonium chloride (TEBA), 1,2-phenylene phosphorochloridite, 2,4,6-trichlorophenol, deuterated chloroform (CDCl_3 , containing 0.03 % TMS), chromium (III) acetylacetonate, methanol, 1,1,2,2-tetrachloroethane (TCE), and platinum oxide (PtO_2) were obtained from Aldrich. Anhydrous methylene chloride (CH_2Cl_2) and tetrahydrofuran (THF) were purchased from VWR. Hydride-terminated PDMSs with a hydride equivalent weight of 350 g/mole (DMS-H03), 550 g/mole (DMS-H11), 2,500 g/mole (DMS-H21), and 6,000 g/mole (DMS-H25) were obtained from Gelest. TCE was dried with molecular sieves activated at 300 °C. All the other reagents were used as received.

5.3.2. Synthesis of Allyl-Polycarbonate (Allyl-PC)

As a means to develop a process for producing allyl-PCs with high purity and controlled molecular weight, a series of polymerizations were conducted in which reagent concentrations and catalyst composition was varied. The two catalysts investigated were TEA and TEBA.

Figure 5.1 displays a schematic of the experimental design. A total of 24 unique allyl-PCs were prepared. A representative procedure for synthesizing allyl-PC with TEA as a catalyst is as follows (A16 in Table 5.1): To a 1 L flask equipped with a high-speed overhead stirrer, nitrogen inlet, inlet tube for TPG addition, outlet tube connected to a NaOH scrubbing solution, and a thermometer, 4.79 g of BPA (21 mmol), 0.69 g of eugenol (4.2 mmol), and 5.04 g of NaOH (126 mmol) were dissolved in 200 mL of H₂O and cooled below +5 °C using an ice bath. TPG (2.49 g, 8.4 mmol) was dissolved in 200 mL of anhydrous CH₂Cl₂ in a 500 mL one-neck, round-bottom flask inside a glove box. To the polymerization reactor, TEA (0.30 g, 3.0 mmol) was added to the aqueous phase just before addition of the TPG solution. The TPG solution was added to the aqueous phase under high speed stirring (900 rpm) using a syringe pump. Reaction temperature was kept below +5 °C during the TPG addition. After completion of the TPG addition, high-speed stirring was continued for 90 minutes at a temperature below +15 °C. The CH₂Cl₂ phase was separated and washed with water until the pH of the aqueous phase was 7.0. Allyl-PC was isolated from CH₂Cl₂ by precipitation into methanol. The precipitate was filtered, dried at 80 °C under vacuum, and characterized using proton nuclear magnetic resonance spectroscopy (¹H-NMR), phosphorous-31 NMR (³¹P-NMR), gel-permeation chromatography (GPC), and matrix-assisted laser desorption/ionization time-of-flight (MALDI-TOF) mass spectroscopy.

A representative procedure for synthesizing an allyl-PC using TEBA as the catalyst is as follows (B4 in Table 5.2): To a 1 L flask equipped with a high-speed overhead stirrer, nitrogen inlet, inlet tube for TPG addition, outlet tube connected to a NaOH scrubbing solution, and a thermometer, 4.79 g of BPA (21 mmol), 0.35 g of eugenol (2.1 mmol), and 5.04 g of NaOH (126 mmol) were dissolved in 200 mL of H₂O and cooled below +5 °C using an ice bath. TPG

(2.49 g, 8.4 mmol) and TEBA (0.68 g, 3.0 mmol) were dissolved in 200 mL of anhydrous CH_2Cl_2 in a 500 mL one-neck, round-bottom flask inside a glove box. The organic phase was added to the aqueous phase under high speed stirring (900 rpm) using a syringe pump. Reaction temperature was kept below $+5\text{ }^\circ\text{C}$ during the TPG addition. After completion of the TPG addition, high-speed stirring was continued for 90 minutes at a temperature below $+15\text{ }^\circ\text{C}$. The CH_2Cl_2 phase was separated and washed with water until the pH of the aqueous phase was 7.0. Allyl-PC was isolated from CH_2Cl_2 by precipitation into methanol. The precipitate was filtered, dried at $80\text{ }^\circ\text{C}$ under vacuum and characterized using $^1\text{H-NMR}$, $^{31}\text{P-NMR}$, GPC, and MALDI-TOF mass spectroscopy.

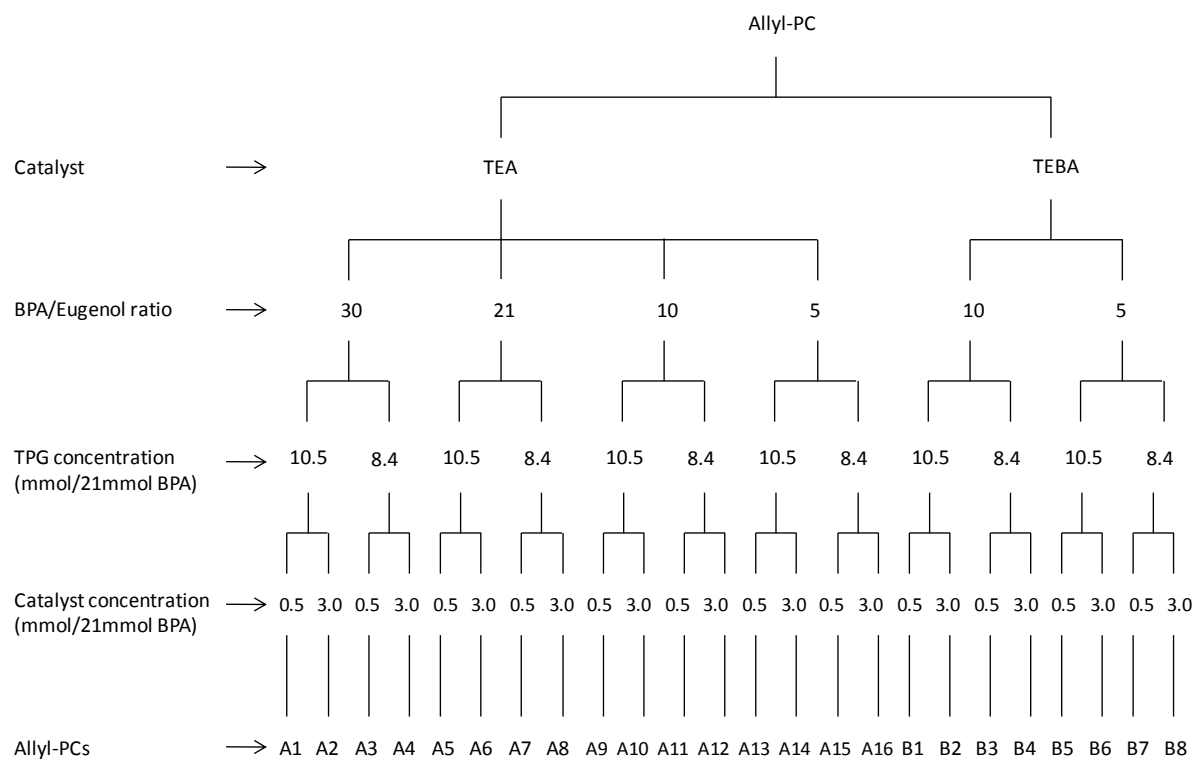


Figure 5.1. A schematic illustration of the experimental design used for allyl-PC synthesis. For each composition, 21.00 mmol of BPA was used.

Table 5.1. Compositions (mmol) and summarized results for the allyl-PCs synthesized using TEA as a catalyst. For each composition, 21.0 mmol of BPA was used.

Entry	Eug	TPG	TEA	M _n (NMR)	M _n (GPC)	PDI (GPC)	ppm OH	Linear allyl-PC ± std (%)	PC molecular structure
A1	0.70	10.5	0.50	14184	16296	2.4	188	42.6 ± 6.1	Eug-PC-Eug, Cyclic-PC
A2	0.70	10.5	3.00	9984	8045	1.9	535	44.3 ± 7.0	Eug-PC-Eug, Cyclic-PC
A3	0.70	8.4	0.50	17975	24115	2.7	57.55	55.2 ± 1.2	Eug-PC-Eug, Cyclic-PC, HO-PC-Eug
A4	0.70	8.4	3.00	11303	9095	1.8	367.4	49.8 ± 4.5	Eug-PC-Eug, Cyclic-PC, HO-PC-Eug
A5	1.0	10.5	0.50	12233	11040	4.2	104	52.0 ± 2.5	Eug-PC-Eug, Cyclic-PC
A6	1.0	10.5	3.00	6466	6495	1.8	1523	57.6 ± 1.3	Eug-PC-Eug, Cyclic-PC
A7	1.0	8.4	0.50	13700	18435	2.6	85.7	74.5 ± 1.5	Eug-PC-Eug, Cyclic-PC
A8	1.0	8.4	3.00	12563	8303	1.8	165.3	69.2 ± 2.8	Eug-PC-Eug, Cyclic-PC
A9	2.1	10.5	0.50	8269	11155	3.3	105.2	73.8 ± 2.7	Eug-PC-Eug, Cyclic-PC, HO-PC-Eug
A10	2.1	10.5	3.00	5989	6772	1.7	1177.9	64.5 ± 3.8	Eug-PC-Eug, Cyclic-PC, HO-PC-Eug
A11	2.1	8.4	0.50	7333	11839	2.7	77.9	78.7 ± 2.4	Eug-PC-Eug, Cyclic-PC, HO-PC-Eug
A12	2.1	8.4	3.0	4754	5934	1.6	175.9	79.9 ± 4.5	Eug-PC-Eug, Cyclic-PC, HO-PC-Eug
A13	4.2	10.5	0.50	5698	7216	3.2	94.2	72.7 ± 1.3	Eug-PC-Eug, Cyclic-PC
A14	4.2	10.5	3.00	5589	5527	1.7	1267.5	72.5 ± 1.2	Eug-PC-Eug, Cyclic-PC, HO-PC-OH, HO-PC-Eug
A15	4.2	8.4	0.50	5214	7409	2.7	60.7	83.9 ± 0.5	Eug-PC-Eug, Cyclic-PC
A16	4.2	8.4	3.00	3543	4785	1.6	70.3	98.4 ± 1.3	Eug-PC-Eug

Table 5.2. Compositions (mmol) and summarized results of the allyl-PCs synthesized using TEBA as a catalyst. For each composition, 21.0 mmol of BPA was used.

Entry	Eug	TPG	TEBA	M _n (NMR)	M _n (GPC)	PDI (GPC)	ppm OH	Linear allyl-PC ± std (%)	PC molecular structure
B1	2.1	10.5	0.50	9196	7837	1.5	NA	30.1 ± 2.1	Eug-PC-Eug, HO-PC-Eug, HO-PC-OH
B2	2.1	10.5	3.00	9029	14246	1.5	94.2	98.0 ± 0.4	Eug-PC-Eug
B3	2.1	8.4	0.50	7478	7047	1.5	6326	51.9 ± 3.2	Eug-PC-Eug, HO-PC-Eug, HO-PC-OH
B4	2.1	8.4	3.00	9585	19272	1.6	44.9	97.2 ± 0.9	Eug-PC-Eug
B5	4.2	10.5	0.50	4979	5752	1.5	10591	87.1 ± 1.1	Eug-PC-Eug, HO-PC-Eug, HO-PC-OH
B6	4.2	10.5	3.00	5477	10176	1.5	140.6	97.4 ± 2.3	Eug-PC-Eug
B7	4.2	8.4	0.50	4662	5444	1.5	6123	67.5 ± 0.4	Eug-PC-Eug, HO-PC-Eug
B8	4.2	8.4	3.00	4843	9050	1.7	57.8	98.1 ± 1.3	Eug-PC-Eug

5.3.3. Synthesis of Polycarbonate-Polydimethylsiloxane (PC-PDMS) Multiblock Copolymers

Copolymers

Figure 5.2 shows the experimental design of the twelve PC-PDMS block copolymers produced using three allyl-PCs and four hydride-PDMSs with different molecular weights. The three allyl-PCs used had molecular weights of 3257, 4891, and 7714 g/mol, respectively, as determined by $^1\text{H-NMR}$, and were simply denoted as PC3K, PC5K and PC8K, respectively. The four PDMSs used, DMS-H03, DMS-H11, DMS-H21, and DMS-H25 had molecular weights of 741, 1187, 5301, and 12422 g/mol, respectively, as determined by $^1\text{H-NMR}$, and were simply denoted as PDMS0.7K, PDMS1.2K, PDMS5.3K and PDMS12K, respectively. The PDMS content of the block copolymers varied between 9 and 79 wt%, as shown in Figure 5.2.

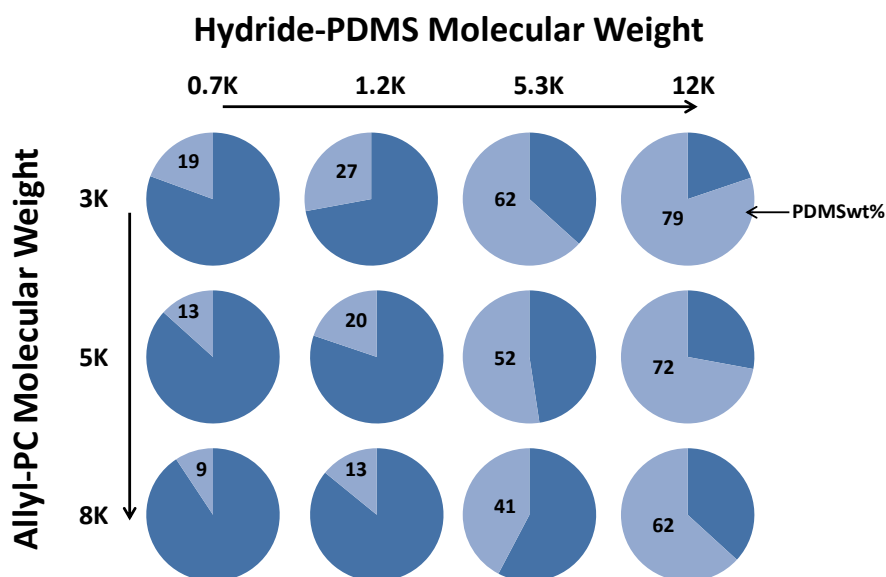


Figure 5.2. A schematic illustration of the experimental design for producing PC-PDMS block copolymers.

Table 5.3 describes the composition of the 12 block copolymers. The stoichiometry between silicon hydride and vinyl groups was kept at 1:1. The syntheses were conducted at 5 wt%

concentration and PtO₂ was used at 0.1-0.6 wt%. Twelve gram batches of each polymer were produced. A representative procedure of synthesizing PC-PDMS block copolymers (PC5K-PDMS1.2K_20%) is as follows: To a 500 mL round-bottom flask equipped with a nitrogen inlet and condenser, 9.66 g of eugenol-terminated PC (1.97 mmol of vinyl groups) was dissolved in 228 g of anhydrous TCE. To the solution, 2.34 g of DMS-H11 (1.97 mmol of hydride groups) and 0.045 g PtO₂ were added and the reaction was conducted at 120 °C under nitrogen flow for 24 hours. The PC-PDMS block copolymer was isolated by precipitation into methanol, vacuum filtering to collect the precipitate, and drying for 48 hours at 80 °C under vacuum.

Table 5.3. Composition of the twelve PC-PDMS block copolymers.

PC-b-PDMS samples	Mn (PC) g/mol	Mn (PDMS) g/mol	PDMS Content (wt%)
PC3K-PDMS0.7K_19%	3257	741	19
PC3K-PDMS1.2K_27%	3257	1187	27
PC3K-PDMS5.3K_62%	3257	5300	62
PC3K-PDMS12K_79%	3257	12422	79
PC5K-PDMS0.7K_13%	4891	741	13
PC5K-PDMS1.2K_20%	4891	1187	20
PC5K-PDMS5.3K_52%	4891	5300	52
PC5K-PDMS12K_72%	4891	12422	72
PC8K-PDMS0.7K_9%	7714	741	9
PC8K-PDMS1.2K_13%	7714	1187	13
PC8K-PDMS5.3K_41%	7714	5300	41
PC8K-PDMS12K_62%	7714	12422	62

5.3.4. Instrumentation

$^1\text{H-NMR}$ and $^{31}\text{P-NMR}$ were conducted using a JEOL 400 MHz spectrometer at 25 °C. For $^1\text{H-NMR}$, CDCl_3 was used as a solvent. For each sample, sixteen scans were obtained with a relaxation delay of 4 s. Tetramethylsilane was used as an internal standard. $^{31}\text{P-NMR}$ was used to determine end-capping efficacy by measuring phenolic (OH) end-group content of the allyl-PC samples synthesized. The methodology utilized has been previously described by Chan et al.¹³ 1,2-phenylene phosphorochloridite was used as the derivatizing agent and 2,4,6-trichlorophenol was used as the internal standard. The solvent was CDCl_3 with chromium tris-acetyl acetate added as a shiftless relaxation agent. For each sample one thousand scans were obtained with a relaxation delay of 2 s.

Gel-permeation chromatography (GPC) was performed using a Symyx Rapid-GPC with an evaporative light scattering detector (PL-ELS 1000). Samples for GPC were prepared in THF at a concentration of 1 mg/mL. Molecular weights of polycarbonates were determined relative to polystyrene standards.

MALDI-TOF mass spectra were recorded using a Bruker Ultraflex II spectrometer equipped with a 1.85 m linear flight tube and a smart beam laser. All mass spectra were obtained in positive ion and reflection mode. DHB (10 mg/mL in THF) was used as a matrix, potassium-trifluoroacetate (2 mg/mL in THF) was used as the cationizing agent, and polymer samples were dissolved in THF (1-2 mg/mL). A 10 μL portion of the matrix, 2 μL of the cationizing agent, and 2 μL of the polymer were mixed together, and a 2 μL sample solution was spotted on the target plate. All data were processed using Flex analysis.

Modulated DSC was carried out using a Q2000 Modulated Differential Scanning Calorimeter manufactured by TA Instruments. Data analysis was performed with TA Universal Analysis software. The calorimeter was calibrated with sapphire and indium standards. Samples of about 13 mg were loaded into a Tzero aluminum pans while an empty pan was used as a reference. A modulation amplitude of 0.531 °C and a period of 100 s was used at a heating rate of 2 °C/min when samples were modulated at 180-0 °C and 25-180 °C.

Dynamic mechanical analysis (DMA) was performed using a DMA Q800 dynamic mechanical analyzer over the temperature range of -150 °C to +160 °C at a heating rate of 5 °C/min with experiment parameters of 0.01 % strain, 0.01 N preload force, and 10 Hz frequency. Sample films were made by hot pressing at 180 °C and cutting into strips with a width of 5 mm. The thicknesses of the samples were around 100 µm, and the distance between clamps was around 15 mm.

Thermal gravimetric analysis (TGA) was carried using a TGA Q500 thermal analyzer in the temperature range of +25 °C to +800 °C at a heating rate of 20 °C/min. Samples of about 10 mg were tested under N₂ purged at 60 ml/min.

Water contact angle measurements were carried out using an automated surface energy measurement unit manufactured by Symyx Discovery Tools, Inc. and First Ten Angstroms.^{14,15} Three measurements were taken for each sample using the sessile drop method and the data reported as the average and standard deviation.

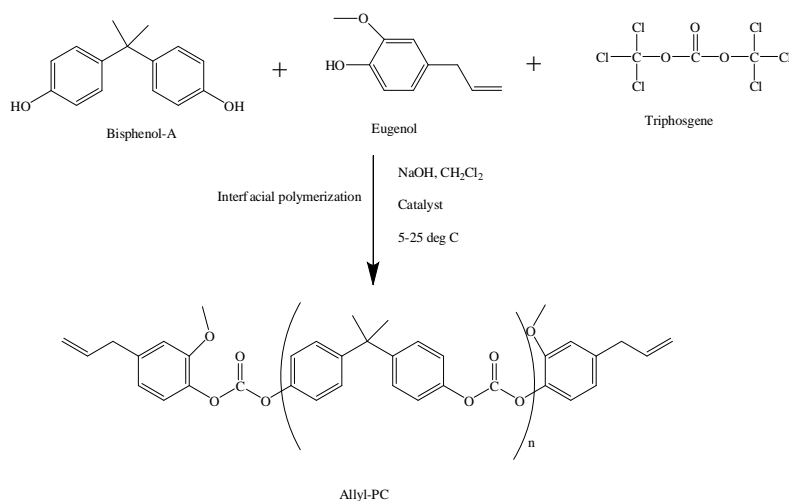
Atomic force microscopy (AFM) was conducted in tapping mode at ambient conditions with a Dimension 3100® microscope and a Nanoscope IIIa controller from Veeco Incorporated. Topographical images were collected in air at room temperature using a single-lever silicon

probe from NanosensorsTM. Cantilever length, width, and thickness of the silicon probe were $225 \pm 10 \mu\text{m}$, $25 \pm 7.5 \mu\text{m}$, and $3.0 \pm 1.0 \mu\text{m}$, respectively. The spring constant was 0.5-9.5 N/m with a resonant frequency of 75 kHz. The set point ratio was 0.8-0.9. Polymer samples were spin coated over glass slides using 10 wt % solutions in CH_2Cl_2 .

5.4. Results and Discussion

5.4.1. Synthesis of Allyl-PCs

A series of allyl-PCs were synthesized by reacting BPA, TGP, and eugenol through interfacial polymerization, as shown in Scheme 5.1. Eugenol was used as an end-capping monomer and TPG as the carbonate source. TPG, a solid at room temperature, was used as a less dangerous substitute for the highly toxic phosgene gas typically used to prepare PCs.¹⁶ Kricheldorf et al. have shown that the products of polycondensation of BPA were highly sensitive to reaction conditions when TPG was used.¹⁷ Hence, the concentration of TPG was considered as one of the variables to explore. The other variables for this investigation included catalyst composition and concentration and BPA/eugenol mole ratio.



Scheme 5.1. Schematic representation of allyl-PC synthesis by interfacial polymerization.

Successful polymerizations were confirmed using FTIR and $^1\text{H-NMR}$, as shown in Figure 5.3 and Figure 5.4, respectively. In Figure 5.3, the disappearance of the hydroxyl bands centered at 3350 cm^{-1} and 3520 cm^{-1} originating from BPA and eugenol, along with the emergence of the carbonyl band centered at 1770 cm^{-1} , demonstrated the successful interfacial polymerization. Similarly, in Figure 5.4, the polycarbonate retained all characteristic peaks from BPA and eugenol, except the reacted hydroxyl groups. Table 5.1 describes the compositional details and characterization data for the 16 allyl-PCs produced using TEA as a catalyst; while Table 5.2 describes the same information for the 8 allyl-PCs produced using TEBA as a catalyst.

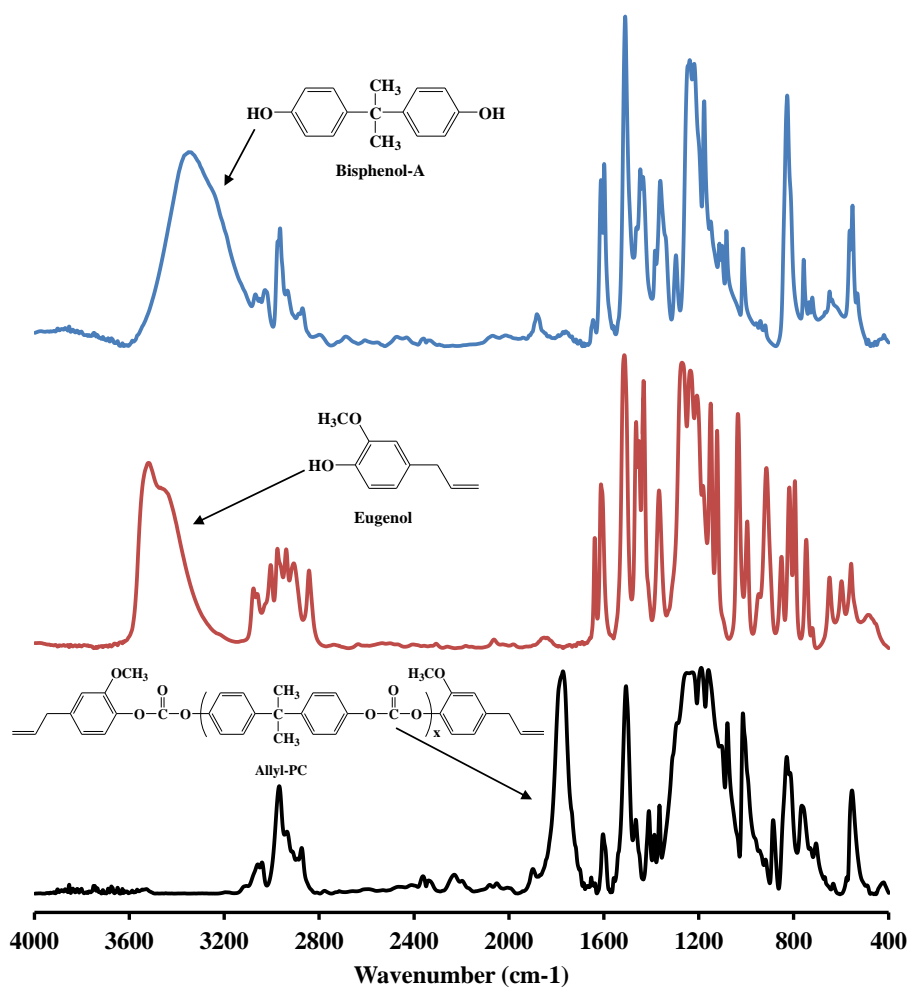


Figure 5.3. FTIR spectra of bisphenol-A, eugenol and allyl-PC.

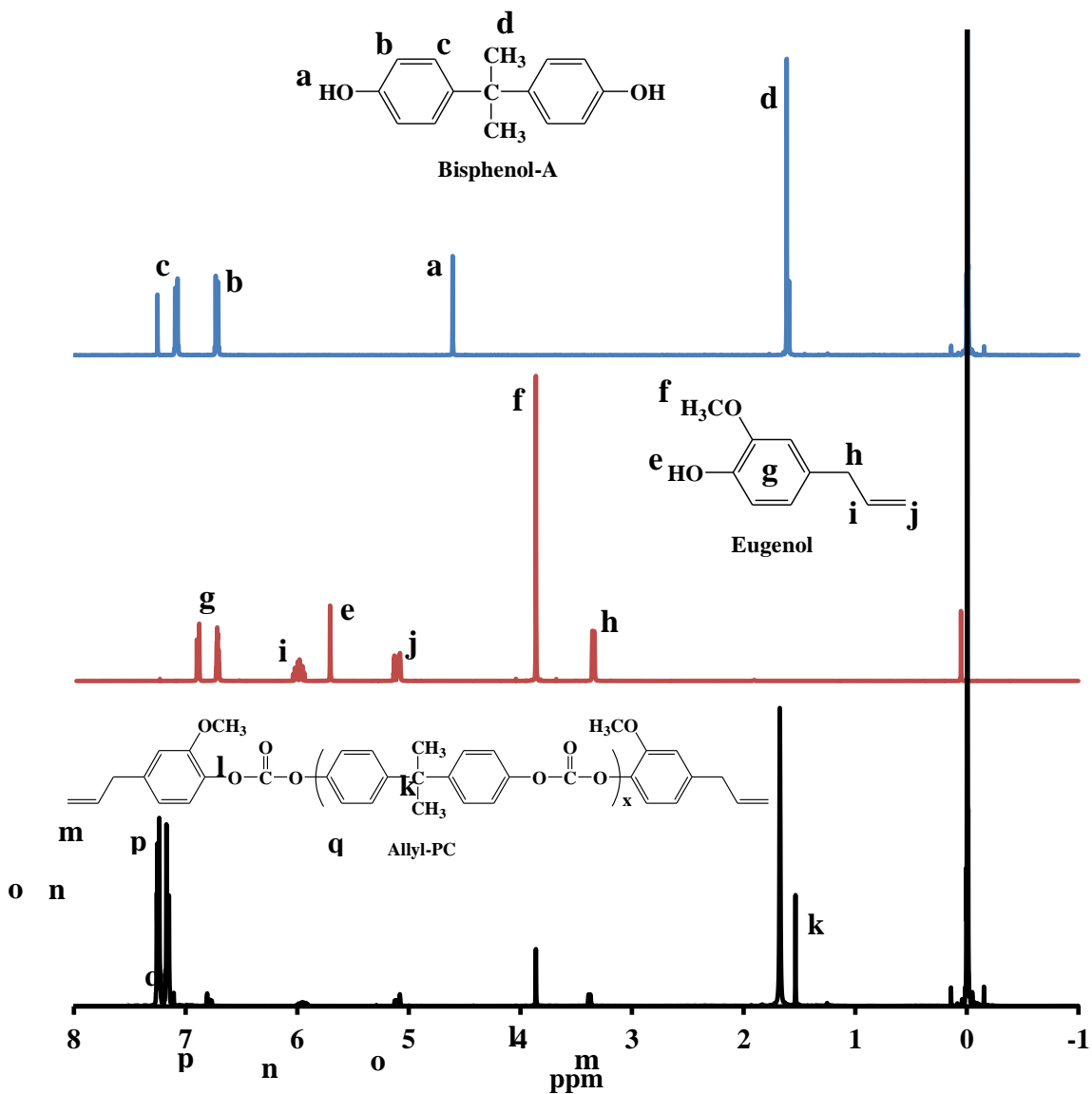


Figure 5.4. ¹H-NMR spectra of BPA, eugenol and allyl-PC.

The number-average molecular weight (M_n) of the allyl-PCs was controlled by tailoring the relative concentration of BPA to eugenol according to the following equations:

$$DP = (2 \times \text{moles of BPA}) / (\text{moles of eugenol}) \quad \text{Equation 5.1}$$

$$M_n = DP \times M_r \quad \text{Equation 5.2}$$

where DP is the degree of polymerization and Mr is the molecular weight of the repeat unit (254.29 g/mol). From ¹H-NMR spectra, the ratio of the normalized isopropylidene proton resonances of BPA at 1.68 ppm and 1.55 ppm to that of the normalized methoxy proton resonances of eugenol at 3.86 ppm was used to calculate Mn of allyl-PCs produced according to the following equation:

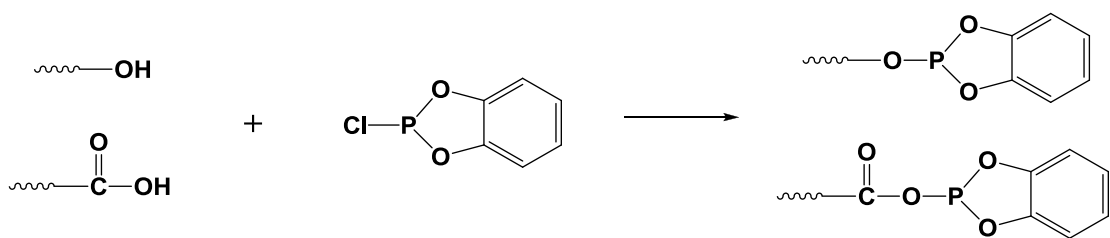
$$Mn \text{ (NMR)} = \frac{[I(1.68)+I(1.55)]/6}{I(3.86)/6} \times 254.29 + 354.15 \quad \text{Equation 5.3}$$

where I is the peak integration value associated with the respective protons and 354.15 g/mole is added for the contribution from the end groups. The experimentally derived results of Mn for each allyl-PC produced are listed in Tables 5.1 and 5.2.

The values of “ppm OH: as listed in Table 5.1 and Table 5.2 were quantitated using ³¹P NMR analysis. The reactive hydroxyl and carboxylic acid groups are derivatized by 1,2-phenylene phosphorochloridite (PPC) as shown in Scheme 5.2, and could be detected by ³¹P-NMR. Thus, the hydroxyl groups which were not end-capped with eugenol were quantified by calculating the peak intensity against the internal standard, as shown in Figure 5.5, using the following equation:

$$ppm \text{ OH} = \text{Moles of Std} * \frac{\text{Integral PC}}{\text{Integral Std}} * 17 * \frac{1}{\text{Wt of PC}} * 10^6 \quad \text{Equation 5.4}$$

where the moles of the standard and the weight of PC were determined experimentally, and *integral PC* and *integral standard* were determined according to the ³¹P-NMR spectrum.



Scheme 5.2. Hydroxyl and carboxyl groups derivatized by 1,2-phenylene phosphorochloridite (PPC) for ^{31}P -NMR analysis.

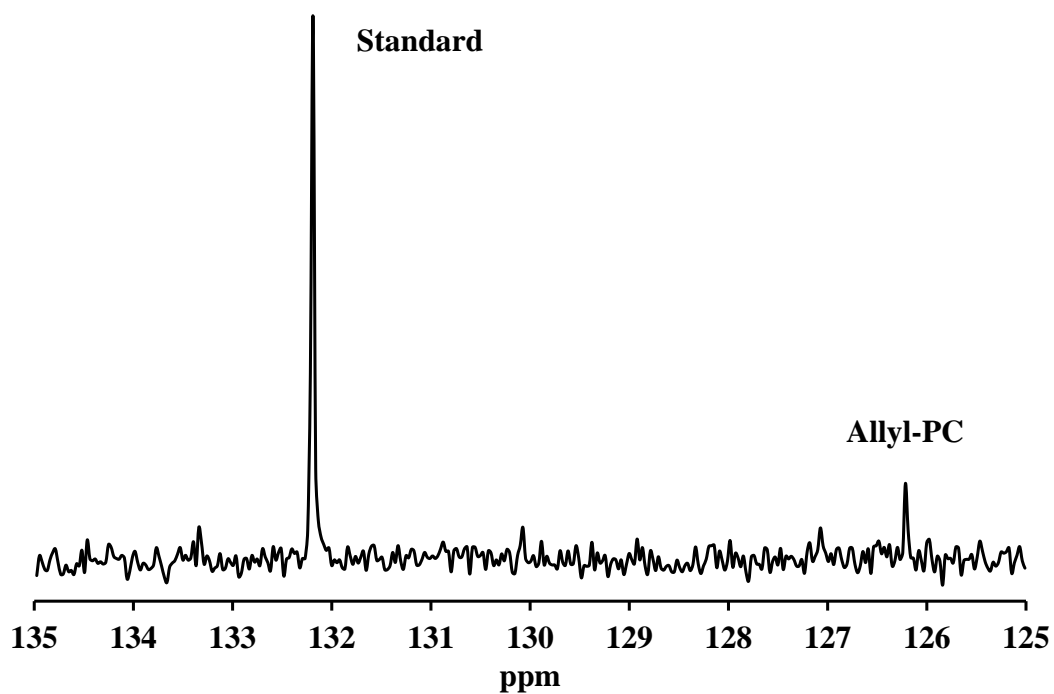


Figure 5.5. Example of ^{31}P -NMR spectra of allyl-PC for ppm OH quantification.

The results of the amount of uncapped hydroxyl end groups are listed in Table 5.1 and Table 5.2.

MALDI-TOFMS was used to characterize the molecular structure of the allyl-PCs produced. Many researchers have demonstrated the utility of MALDI-TOFMS for determining

detailed polymer sample compositional factors such as end-group composition and the presence of cyclic structures in the sample.¹⁸⁻²¹ Figure 5.6 shows representative MALDI spectra obtained for the allyl-PCs produced. The spectrum obtained from sample B4 (Table 5.2) is representative of an allyl-PC with very high eugenol end-capping and no cyclic structures. The spectrum obtained from sample A8 (Table 5.1) is representative of an allyl-PC containing a mixture of linear and cyclic structures with the linear structures possessing end-groups derived from eugenol. The spectrum obtained from sample A4 (Table 5.1) is representative of an allyl-PC possessing a mixture of linear and cyclic structures with the linear structures possessing end-groups derived from both eugenol and BPA. The mole fraction of each component (i.e. eugenol-capped linear structures, cyclics, BPA end-capped structures) in the allyl-PC samples produced was calculated using the following equations:

$$I_{T1} = \sum I_{p1} * \frac{M_{p1} - M_{e1} - M_{e2} - M_c}{M_r} \quad \text{Equation 5.5}$$

$$\text{Mole\% of } T1 = \frac{I_{T1}}{\sum I_{Tn}} * 100 \quad \text{Equation 5.6}$$

where I_{T1} is the total signal intensity of the component T1, I_{p1} is the intensity of each oligomer peak of T1, M_{p1} is the mass of each oligomer peak of T1, M_{e1} is the mass of one end group, M_{e2} is the mass of the second end group, M_c is the mass of the cation, M_r is the mass of the repeat unit, and I_{Tn} is the total signal intensity of the component Tn ($n = 1, 2, 3 \dots$ etc). The results of the mole fraction of linear allyl-PC are listed in Tables 5.1 and Table 5.2.

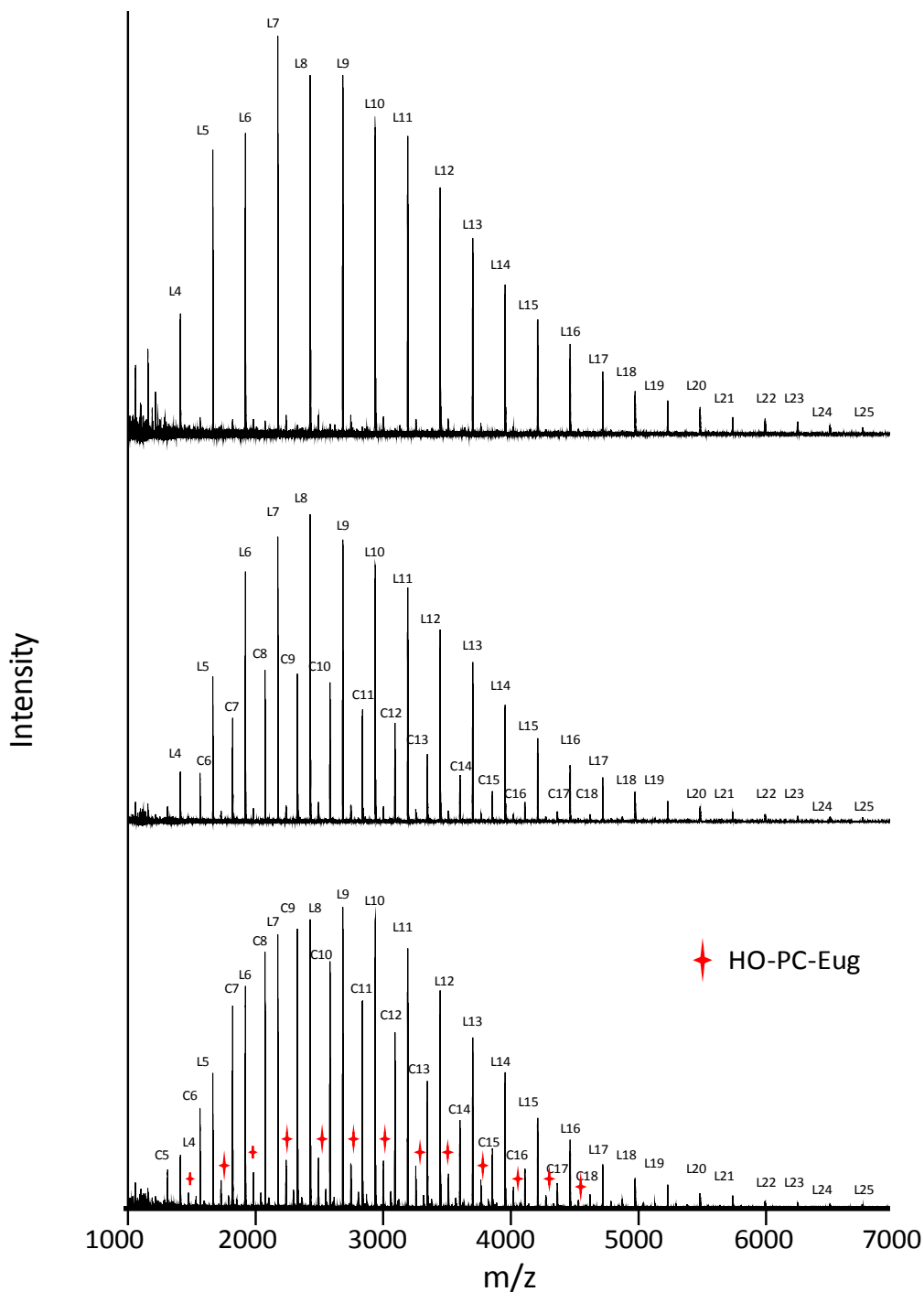


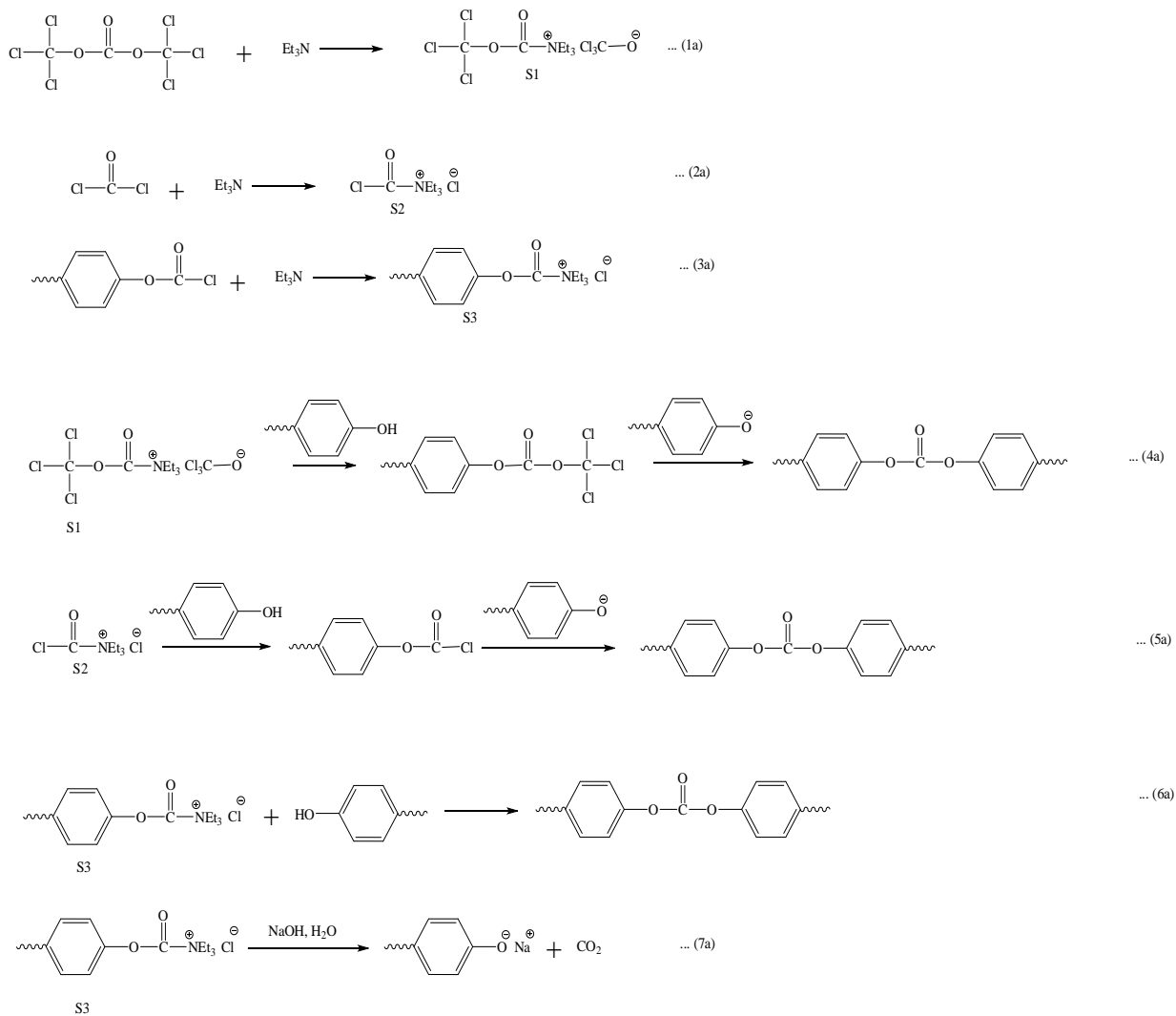
Figure 5.6. Representative MALDI spectra displaying allyl-PCs containing high eugenol end capping at both ends (top, B4 from Table 5.2), significant contamination with cyclic PCs (middle, A8 from Table 5.1), and contamination with both cyclics and linear polymers possessing a hydroxyl endgroup (bottom, A4 from Table 5.1). L= Linear allyl-PCs, C= cyclic PCs, and + = linear PCs with a hydroxyl end group.

5.4.1.1. TEA as a Catalyst

The series of PCs described in Table 5.1 were synthesized using TEA as a catalyst. TEA has been used as a catalyst for interfacial phosgenation of BPA with phosgene, diphosgene, and TPG.^{17,22-25} The results listed in Table 5.1 show that, keeping the other variables constant, increasing TEA concentration produced allyl-PCs with lower molecular weights, narrow molecular weight distributions (PDI), and higher OH end-group concentrations (compare A9 vs. A10, A11 vs. A12 etc in Table 5.1). As illustrated in Scheme 5.4, TEA can activate TPG, phosgene, and chloroformate by forming acylammonium salts S1, S2, and S3, respectively.^{17,24} Due to their hydrophilic nature, acylammonium salts may diffuse into the water-phase, enhancing the reaction rates of both condensation and hydrolysis. Condensation reactions generate stable carbonate linkages to form PCs via reactions 4a to 6a shown in Scheme 5.4. With higher TEA concentration, condensation reactions resulted in faster eugenol consumption and produced allyl-PCs with lower molecular weights. Hydrolysis of acylammonium salt S3 can form hydroxyl groups via reaction 7a. As polymerization progresses the concentration of BPA and eugenol decrease and hydrolysis becomes more likely towards the end of the polymerization. Keeping the other variables constant, increasing the concentration of TEA resulted in higher OH end-group concentrations.

The use of an excess of phosgene or TPG in the synthesis of PC using TEA as a catalyst has been previously reported.^{17,24} Since TEA catalyzes not only condensation but also hydrolysis, Brunelle et al. recommended utilizing 10%-20% excess of phosgene.²⁴ Kricheldorf et al. utilized TPG at a concentration that corresponded to a 100% molar excess of phosgene to synthesize

linear and cyclic PCs.¹⁷ For this study, the molar ratio of TPG/BPA corresponded to either a 20% or 50% molar excess of phosgene.



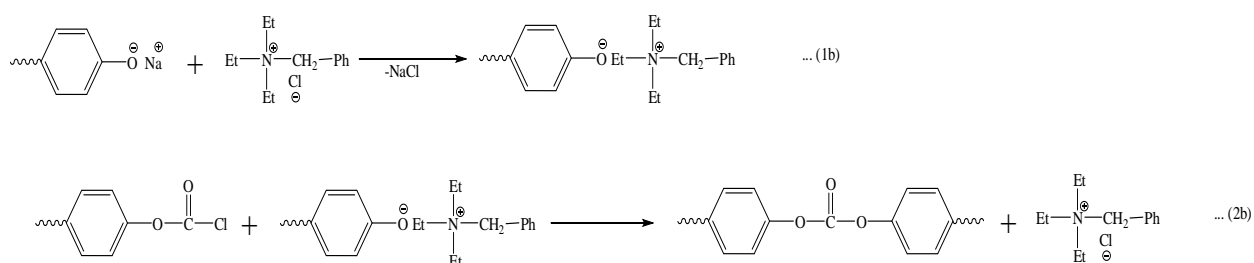
Scheme 5.3. Activation, condensation, and hydrolysis reactions in presence of TEA as a catalyst.

The results listed in Table 5.1 show that, keeping the other variables constant, decreasing the concentration of TPG resulted in allyl-PCs with lower OH end-group concentrations (compare A14 to A16, A13 to A15, A10 to A12, etc. in Table 5.1). This result can be explained as follows: A higher excess of TPG would be expected to result in a higher concentration of

BPA-chloroformate end-groups after the complete consumption of eugenol. With TEA as the catalyst, the BPA-chloroformate can readily form acylammonium salt S3 which can be readily hydrolyzed toward the end of the polymerization when BPA is largely depleted.

5.4.1.2. TEBA as a Catalyst

The series of allyl-PCs described in Table 5.2 were synthesized using TEBA as a catalyst. Use of a phase transfer catalysts such as TEBA for PC synthesis has been previously described.^{17,23,24} Unlike TEA, TEBA cannot activate phosgene, TPG, or chloroformate groups which reduces hydrolysis reactions.^{17,24} The catalytic effect of TEBA is achieved by activating phenoxide groups through counter-ion exchange, as shown by reaction 1b in Scheme 5.5.



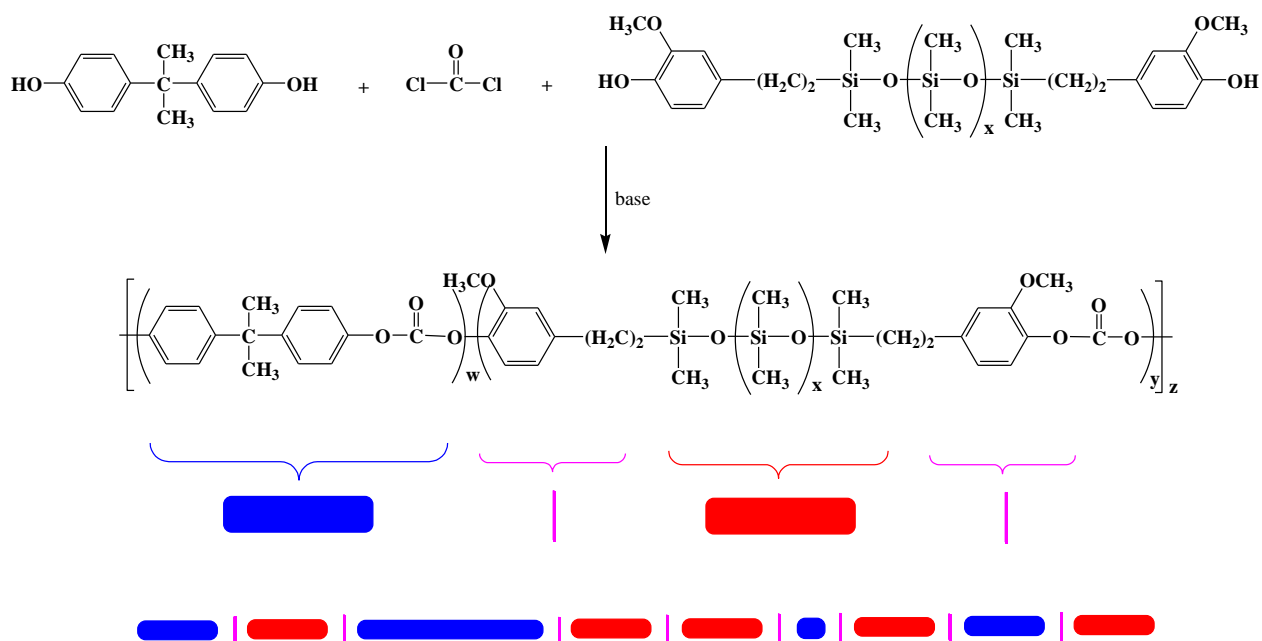
Scheme 5.4. Reactions in presence of TEBA as a phase transfer catalyst.

Due to this activation, phenoxide ions can be more readily transferred to the organic phase which favors the phosgenation reaction (reaction 2b) to form carbonates. The results listed in Table 5.2 show that, keeping other variables constant, increasing TEBA concentration resulted in allyl-PCs with higher molecular weights, lower OH end-group concentrations, and lower contents of cyclics (compare B3 to B4, B5 to B6, and B7 to B8 in Table 5.2). With the use of TEBA as a catalyst, trends observed with respect to molecular weight and OH end-group content were the opposite to those observed with the use of TEA as a catalyst. This difference most likely is due to the fact that higher TEBA concentration only favors carbonate formation and not

hydrolysis. The results listed in Table 5.2 show that, keeping the other variables constant, increasing TPG concentration produced allyl-PC samples with higher OH end-group contents (compare B6 to B8, B5 to B7, etc. in Table 5.2).

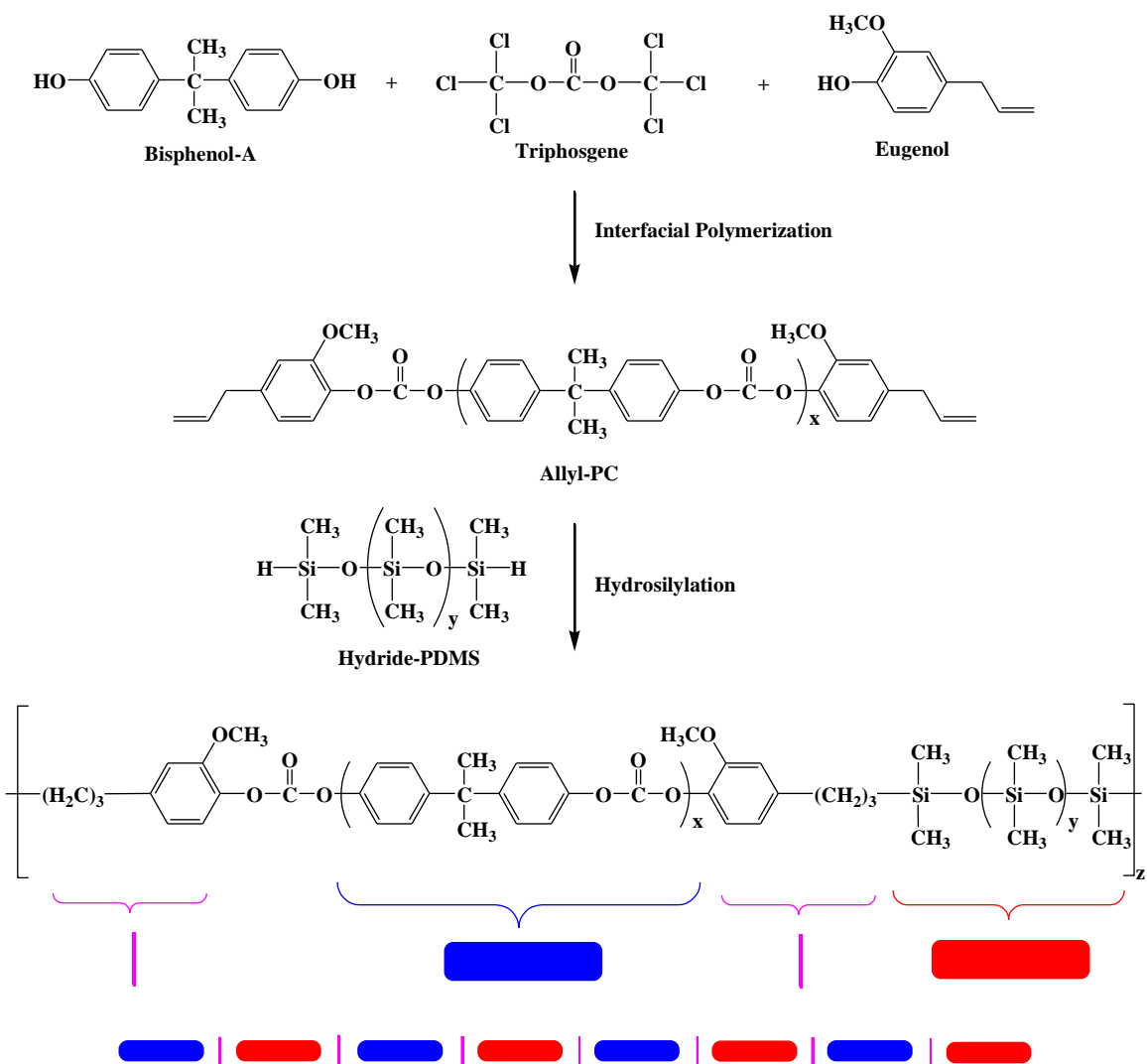
5.4.2. Synthesis of PC-PDMS Block Copolymers

PC-PDMS multiblock copolymers have been previously synthesized using several different techniques. One of the first synthetic methods for producing PC-PDMS multiblock copolymers involved reaction mixtures consisting of BPA, α,ω -dichloro-terminated-polydimethylsiloxane oligomers, and phosgene.^{5,7,26} With this synthetic method, block architecture could not be well controlled. For example, the number of PC repeat units in a PC block could be as low as two if a single phosgene molecule reacted with two BPA-end-capped polydimethylsiloxanes. In addition, successive polydimethylsiloxane (PDMS) blocks can exist by reaction of BPA with two α,ω -dichloro-terminated-PDMS oligomers.



Scheme 5.5. Traditional PC-PDMS block copolymer synthesis.

The majority of the methods used to synthesize PC-PDMS multiblock copolymers involve the reaction of a PDMS modified with nucleophilic end-groups with BPA and phosgene. As shown in Scheme 5.5 and similar to the early work based on the use of α,ω -dichloro-terminated-PDMS oligomers, these methods do not enable the formation of multiblock copolymers with controlled block architectures. As a result, block lengths are extremely polydisperse which affects phase morphology and, thus, optical and mechanical properties.²⁷



Scheme 5.6. Two-step synthesis of perfectly alternating PC-PDMS block copolymer.

The successful production of highly pure linear allyl-PC enabled the synthesis of PC-PDMS block copolymers with perfectly alternating structure. The perfectly alternating PC-PDMS block copolymers had been reported to be produced through different functional end groups.⁹ The hydrosilylation reaction is versatile in building silicon-carbon (Si-C) linkages and producing organo-silicon compounds. It was utilized here to synthesize PC-PDMS block copolymers where the two blocks are linked by Si-C bonds. The perfectly alternating multiblock architectures were then built by selecting the two blocks with certain molecular weight as shown in Scheme 5.6. As described in Figure 5.2, twelve block copolymers were synthesized.

A representative successful block copolymerization was demonstrated using GPC. As shown in Figure 5.7, hydrosilylation resulted in a loss of the low retention time shoulder of the physical mixture associated with hydride-PDMS and a shift in the peak retention time to lower retention time.

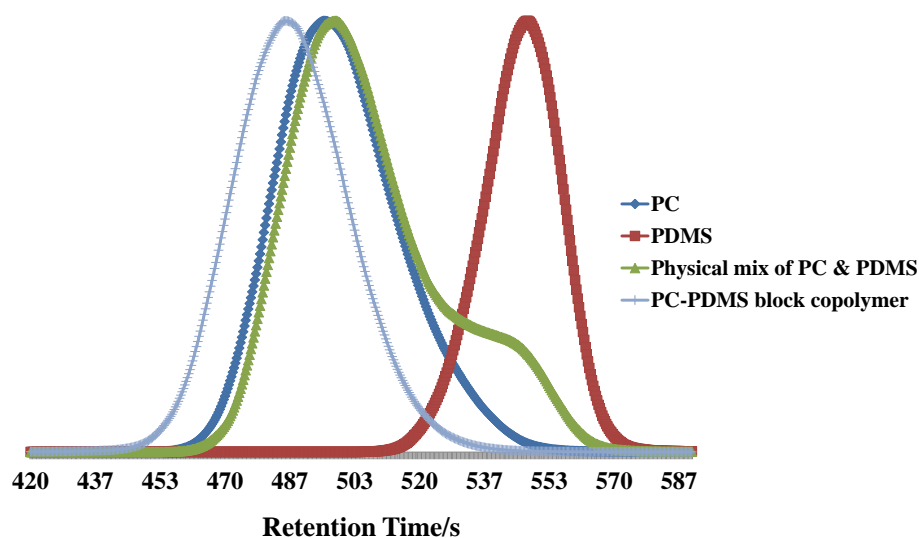


Figure 5.7. GPC traces of neat PC, PDMS, a physical mixture of PC and PDMS, and a PC-PDMS block copolymer.

A representative successful coupling was also demonstrated using $^1\text{H-NMR}$. As shown in Figure 5.8, hydrosilylation resulted in almost complete disappearance of peaks associated with the vinyl group of the allyl-PC and the peak associated with the hydride group of the PDMS.

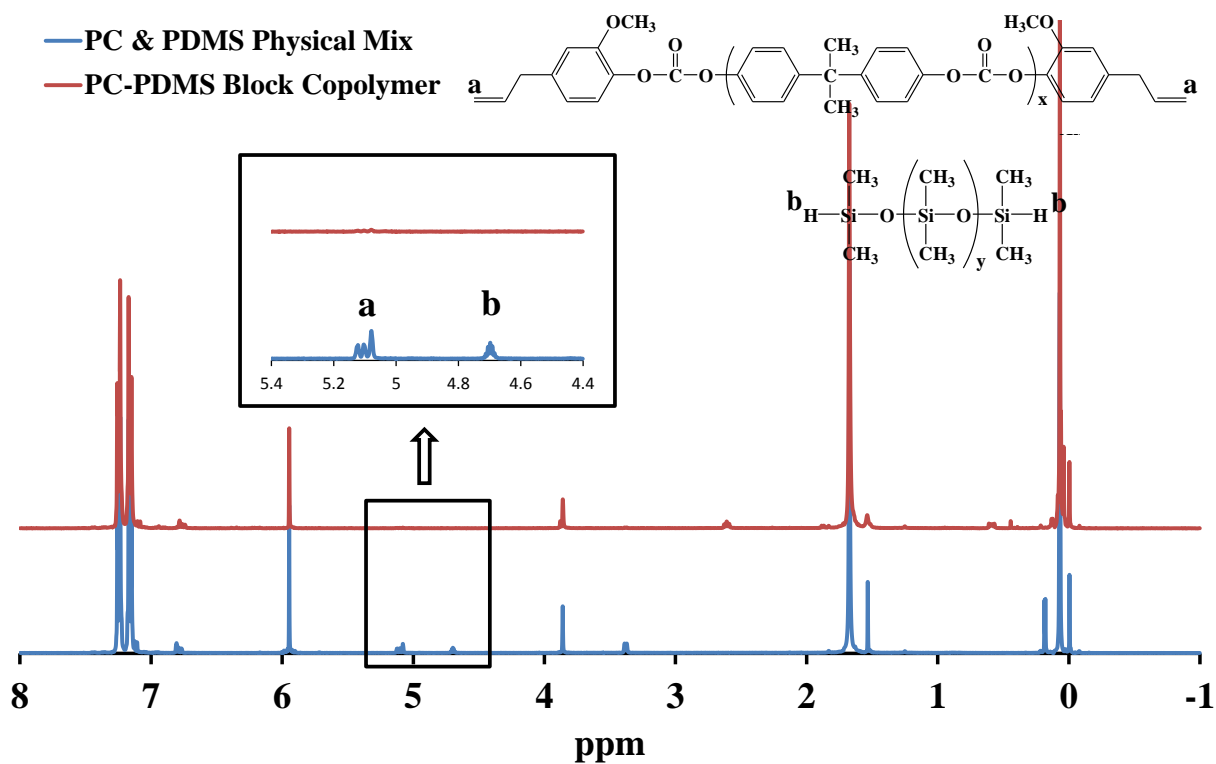


Figure 5.8. $^1\text{H-NMR}$ spectra for PC& PDMS physical mix and PC-PDMS block copolymer.

The compositions of the block copolymers produced are described in Table 5.4, where the theoretical PDMS content was calculated and the experimental PDMS content was determined by $^1\text{H-NMR}$. It can be seen that the values of experimental PDMS content and theoretical PDMS content are very close. The relative molecular weight M_n and PDI were determined by GPC.

Table 5.4. Description of PC-*b*-PDMS copolymers.

PC- <i>b</i> -PDMS samples	Mn (PC) g/mol	Mn (PDMS) g/mol	Theoretical PDMS wt%	Experimental PDMS wt%	Mn (g/mol)	PDI
PC3K-PDMS0.7K_19%	3257	741	19	17	16493	1.7
PC3K-PDMS1.2K_27%	3257	1187	27	26	19093	1.7
PC3K-PDMS5.3K_62%	3257	5300	62	61	25706	1.7
PC3K-PDMS12K_79%	3257	12422	79	76	15243	1.9
PC5K-PDMS0.7K_13%	4891	741	13	12	14342	1.6
PC5K-PDMS1.2K_20%	4891	1187	20	18	18327	1.6
PC5K-PDMS5.3K_52%	4891	5300	52	50	19548	1.6
PC5K-PDMS12K_72%	4891	12422	72	68	28348	1.7
PC8K-PDMS0.7K_9%	7714	741	9	7	17558	1.5
PC8K-PDMS1.2K_13%	7714	1187	13	12	28102	1.6
PC8K-PDMS5.3K_41%	7714	5300	41	37	26633	1.6
PC8K-PDMS12K_62%	7714	12422	62	58	29113	1.6

5.4.3. Glass Transition Temperature by MDSC

Modulated DSC (MDSC), instead of conventional DSC, was used to study to glass transition behavior of the block copolymers. MDSC is superior than DSC in studying block copolymers due to its capability of modulating the temperature and separating the kinetic and thermodynamic component of the heat flow.³² The glass transition temperature was used to

evaluate the phase separation of the block copolymers. Two glass transition temperatures indicate separate phases within the block copolymers. Thermograms showing the T_g of the PC phases of the block copolymers are shown in Figure 5.9 and those of the PDMS phases of the block copolymers are shown in Figure 5.10.

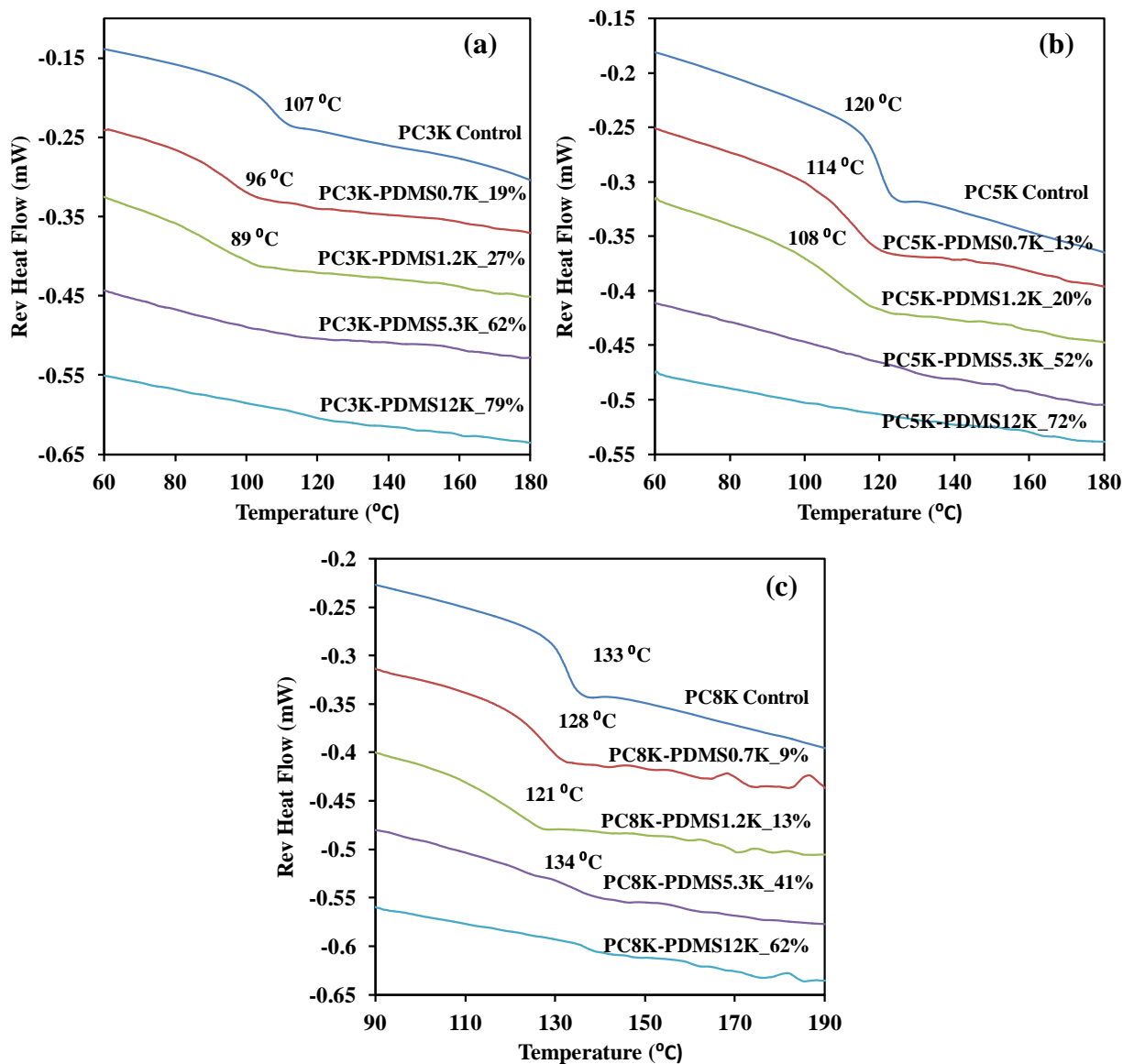


Figure 5.9. PC block glass transition temperature of PC-PDMS block copolymers with PC block length of (a) 3K, (b) 5K, and (c) 8K by MDSC.

The glass transitions of the PC domains are only observable for low PDMS content samples. Even at 41 wt% of PDMS (sample PC8K-PDMS5.3K_41% in Figure 5.9 (c)), there is just a shallow step in the MDSC thermograph. The glass transition temperature of the PC hard phase decreased when copolymerized with PDMS as shown in Figure 5.9, indicating partial miscibility of PDMS with the PC. And PDMS blocks with longer block length (1.2 K) have better compatibility with PC domains than those with shorter block length (0.7 K). It's worth to mention that even though sample PC8K-PDMS5.3K_41% showed slight glass transition of PC hard phases, the T_g value is 1 °C higher than PC control, indicating the poor miscibility of the two phases. The PC phase glass transition of PC-PDMS block copolymers with high PDMS content (>41 wt%) could not be detected by MDSC due the low content of dispersed PC phase.

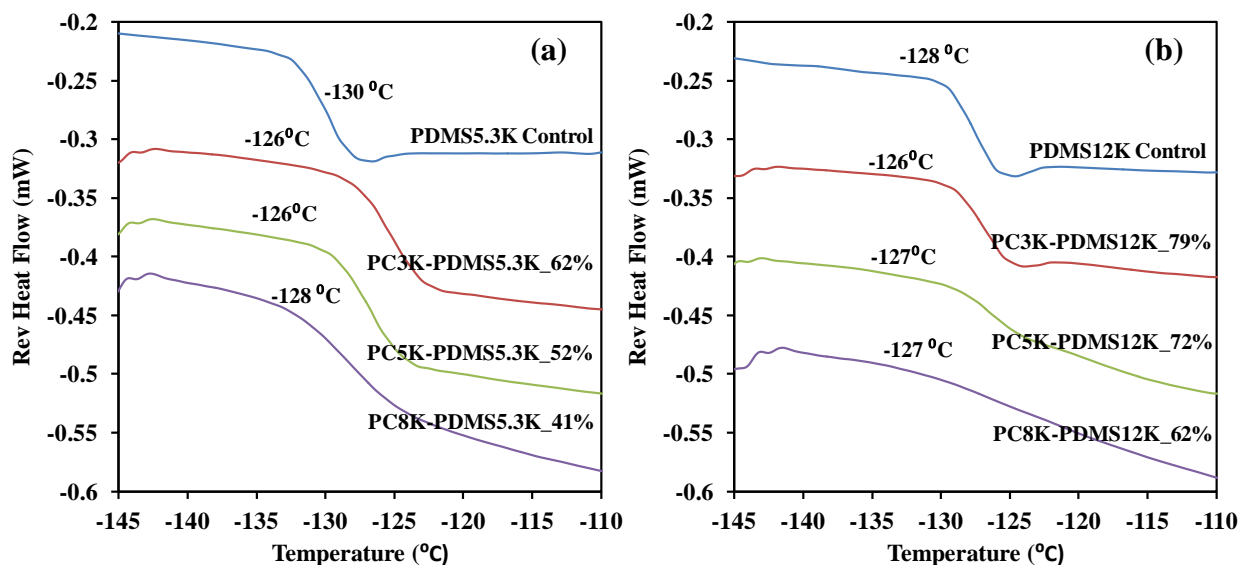


Figure 5.10. PDMS block glass transition temperature of PC-PDMS block copolymers with PDMS block length of (a) 5.3K, and (b) 12K by MDSC.

To further illustrate the miscibility of the PC hard domains and the PDMS soft domains, especially for the block copolymer samples with high PDMS content for which the PC block

glass transitions were not able to be detected, it is also of interest to compare the PDMS glass transition temperatures of the block copolymers. Not all data are shown here, because from Figure 5.9 we are sure that no glass transition would be detected for samples with low PDMS content (<20 wt%). The thermographs of the synthesized block copolymers were overlaid with respect to the PDMS block lengths of 5.3K and 12Kas shown in (a) and (b) in Figure 5.10, respectively. Upon block copolymerization with PC, the PDMS block glass transition temperatures were increased. The increases of T_g for PDMS blocks provide for their evidence of partial miscibility.

5.4.4. Thermal Stability by TGA

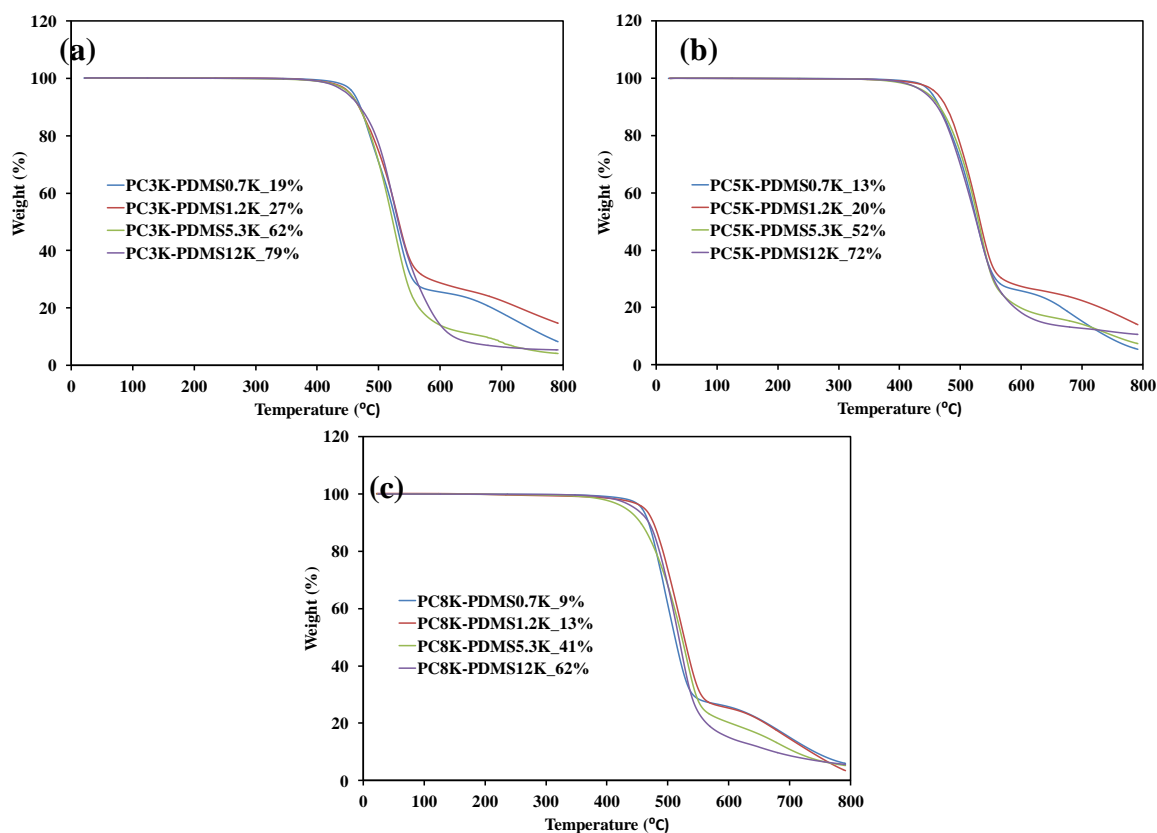


Figure 5.11. TGA curves of PC-PDMS block copolymers with PC block length of (a) 3K, (b) 5K, and (c) 8K under N_2 .

The thermal degradation behavior of PC-PDMS block copolymers in N₂ were evaluated by TGA as shown in Figure 5.11. It can be seen from the degradation profiles, the PC-PDMS block copolymers undergo a two-stage decomposition when copolymerized with short PDMS chains (0.7K), and gradually shift to a one-stage decomposition when longer PDMS blocks are introduced. The two-stage thermal degradation profile is associated the thermal degradation behavior of pure PC.²⁸ The one-stage thermal degradation profile is attributed to the PDMS thermal degradation.^{29,30}

Table 5.5. Thermal stability evaluated by TGA.

PC-b-PDMS samples	T_d (°C)	T_{.5wt%} (°C)	T_{.10wt%} (°C)	Residue (wt%)
PC3K-PDMS0.7K_19%	531.90	458.35	470.40	8.262
PC3K-PDMS1.2K_27%	531.12	452.41	468.09	14.71
PC3K-PDMS5.3K_62%	526.07	451.43	468.28	4.131
PC3K-PDMS12K_79%	523.63	447.21	469.63	5.443
PC5K-PDMS0.7K_13%	525.52	452.18	463.86	5.487
PC5K-PDMS1.2K_20%	530.06	459.96	476.68	14.02
PC5K-PDMS5.3K_52%	534.68	444.47	466.28	7.418
PC5K-PDMS12K_72%	531.97	441.48	462.89	10.67
PC8K-PDMS0.7K_9%	494.46	457.56	468.50	5.894
PC8K-PDMS1.2K_13%	522.24	460.86	476.15	3.495
PC8K-PDMS5.3K_41%	530.36	431.03	455.38	5.161
PC8K-PDMS12K_62%	521.17	446.98	469.20	5.649

The temperature at maximum degradation rate, 5 wt% mass loss, 10 wt% mass loss, and weight percent of char residue were listed in Table 5.5. The initial degradation temperature decreased as the PDMS concentration increased. The similar result has been reported elsewhere.¹² The char yield did increase with the PDMS content, due to the complete combustion of PDMS under N₂.³⁰

5.4.5. Viscoelastic Properties by DMA

The viscoelastic properties of PC-PDMS block copolymers are dependent on both PDMS content and PDMS block length. Figure 5.12 shows the DMA curves of three block copolymers. As can be seen from Figure 5.12 (a), the three representative block copolymers have totally different response to the dynamic stimuli. Samples PC5K-PDMS1.2K_20% and PC3K-PDMS1.2K_27% showed a clear glass transition of PC blocks while sample PC3K-PDMS5.3K_62% only showed a glass transition of PDMS block. This indicates that at room temperature, samples PC5K-PDMS1.2K_20% and PC3K-PDMS1.2K_27% are in the glassy state while sample PC3K-PDMS5.3K_62% is in the rubbery state. The phase inversion occurs at a PDMS loading between 27 to 62 weight percent. The similar result has been reported that the elastomer type block copolymers are those with 40-70 wt% PDMS.²⁶

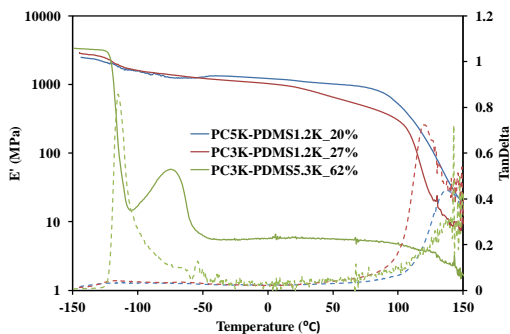


Figure 5.12. DMA curve of PC-PDMS block copolymers.

5.4.6. Surface Properties by AFM

Successful block copolymerization was expected to result in bulk materials possessing a two-phase morphology. On the surface, the segregation of a component with low surface energy occurs in multiblock copolymers. All PDMS-containing block copolymers exhibit PDMS segregation on the surface and even 6 wt% PDMS content can result in 95 wt% PDMS on surface upon annealing.^{29,31} All kinds of factors, polymer composition, architecture, as well as the casting solvent, play important roles in determining the surface composition and properties.²⁸ Figure 6 displays AFM images of films of allyl-PC and a PC-PDMS block copolymer produced using the novel two-step approach. It can be seen that the PC-PDMS block copolymer possessed a heterogeneous surface comprised of PDMS nanodomains.

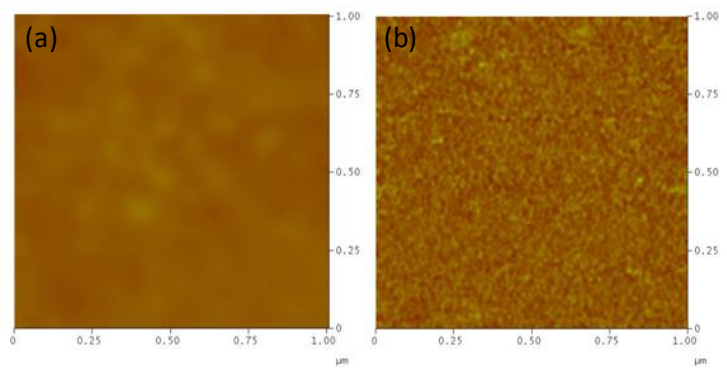
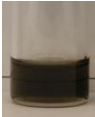
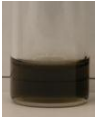








Figure 5.13. AFM images of (a) allyl-PC and (b) a PC-PDMS block copolymer.

5.4.7. Catalyst Removal

Due to the high level of PtO₂ catalyst, the PC-PDMS block copolymers were colored after precipitation and drying under vacuum. PtO₂ removal treatments were conducted as shown in Table 5.6. Four treatments were compared and removal by passing through an Al₂O₃ column was the most effective.

Table 5.6. PtO₂ removal treatment of PC-b-PDMS copolymers.

Treatment	Charcoal RT	Charcoal reflux	Al ₂ O ₃ column	Al ₂ O ₃ -charcoal column
Before				
After				
Yield (wt%)	53.2	51.7	58.8	21.5

5.4.8. Optical Clarity

After color removal, the block copolymers were compression molded into circle pellets and were subjected to optical clarity comparison as shown in Figure 5.14. The refractive indices of PC (1.586) and PDMS (1.400) are significantly different. Thus the combined effect of big domain size and RI mismatch leads to increased scattering that results in increased haze, and eventually the material becoming opaque. For block copolymers as shown, it is amazingly interesting that the high optical clarity could be maintained at up to 62 wt% PDMS content for sample PC3K-PDMS5.3K_62%. In contrast, although have less PDMS content of 52 wt% and 41 wt% for sample PC5K-PDMS5.3K_50% and PC8-PDMS5.3K_41%, the big domain size resulted from long block length lead to the macroscopically phase separated morphology. It has been reported the clear block copolymers show PDMS domain size around 20 nm while the opaque samples show PDMS domains larger than 30 nm.¹¹

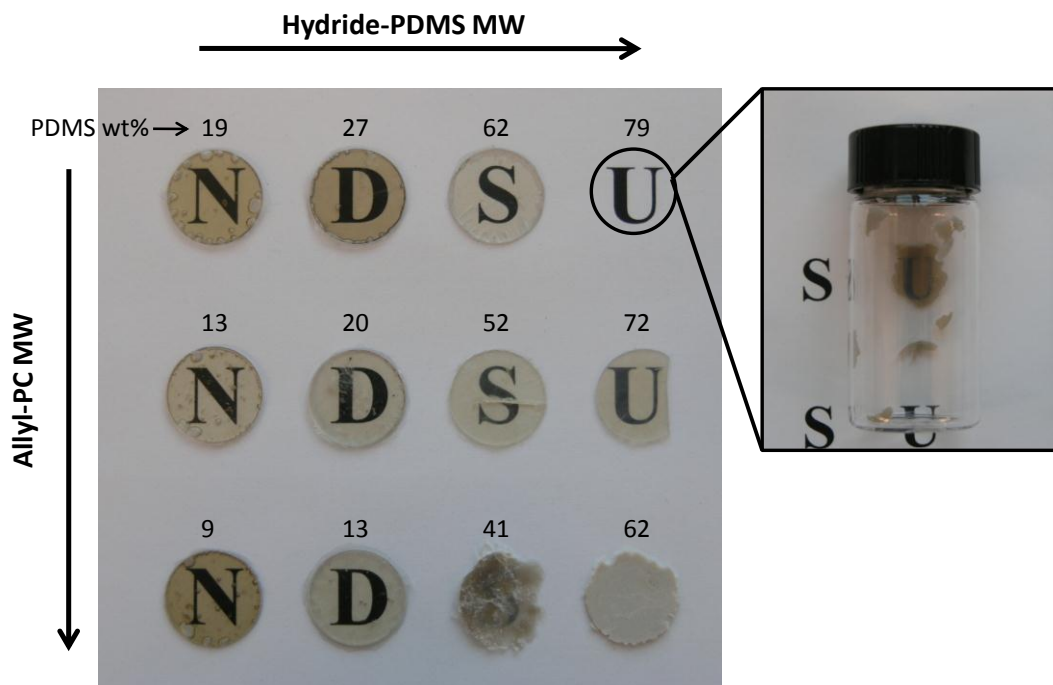


Figure 5.14. Optical clarity of compression molded PC-b-PDMS copolymer samples after PtO_2 removal.

A comparison of optical clarity was made between a synthesized PC-PDMS block copolymer produced using the novel synthetic method described here to a commercial PC-PDMS block copolymer available from SABIC. Figure 5.15 displays images of compression molded films approximately 1 mm in thickness processed under same condition. At this thickness, the commercial PC-PDMS block copolymer film was quite hazy while the block copolymer produced using the two-step method involving coupling by hydrosilylation was transparent. The amber color associated with the latter block copolymer was due to the PtO_2 catalyst used for hydrosilylation.

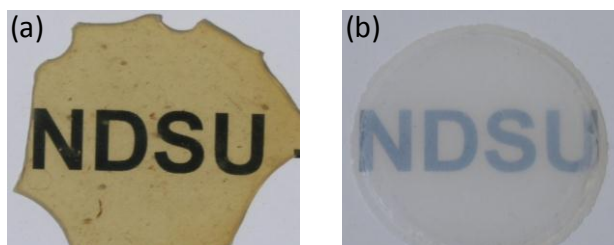


Figure 5.15. Images of approximately 1 mm thick compression molded films of a PC-PDMS block copolymer possessing 20 wt % PDMS and synthesized using the two-step process involving hydrosilylation (a) and a commercial PC-PDMS block copolymer possessing only 5 wt % PDMS (b).

5.5. Conclusion

Interfacial polymerization conditions were identified that allowed for the synthesis of highly pure linear allyl-PCs. It was found that catalyst composition, catalyst concentration, and TPG concentration were the primary factors that affected the purity of allyl-PCs. The phase transfer catalyst, TEBA, was the catalyst that produced allyl-PCs with a low content of cyclics and low content of OH end-groups especially when used in conjunction with a relatively low TPG concentration.

With these allyl end-functional oligomers/polymers, PC-PDMS block copolymers were successfully produced using commercially available hydride-PDMS and coupling the end-functional PC and PDMS oligomers/polymers using hydrosilylation. The PDMS segments are partially miscible with PC hard domains, leading to the decreased PC block glass transition temperature. At PDMS content ranging from 27 – 62 wt%, phase inversion occurs for the homogeneous block copolymers. Nanoscale phase separation and surface segregation of PDMS segments were observed. The incorporation of PDMS blocks changed the thermal decomposition mechanism however did not have a big impact on the thermal stability of blocked copolymers. The synthesized PC-PDMS block copolymers exhibited high optical clarity up to 62 wt% PDMS

content. And comparison of the optical properties of the a PC-PDMS block copolymer produced with this method to that of a commercially available PC-PDMS block copolymer showed that the former, which gives a perfectly alternating block copolymer architecture, provided higher optical clarity. The higher optical clarity suggests smaller PDMS domains resulting from the more uniform block copolymer structure.

5.6. References

1. E. E. Bostick, "Introduction and Historical Background" in Handbook of Polycarbonate Science and Technology, D. G. Legrand and J. T. Bendler, Eds., 2000, Marcel Dekker, New York.
2. S. Smith, Chem. Rev., 13, 2004, 29.
3. K. Cho, J. Yang, S. Yoon, M. H. Sobha, and V. Nair, Toughening of polycarbonate: Effect of particle size and rubber phase contents of the core-shell impact modifier, J. Appl. Polym. Sci., 95, 2005, 748.
4. C. Cheng, N. Peduto, A. Hotner, E. Baer, P. R. Soskey, and G. J. Mylonakis, Comparison of some butadiene-based impact modifiers for polycarbonate, J. Appl. Polym. Sci., 53, 1994, 513.
5. H. A. Vaughn, The synthesis and properties of alternating block polymers of dimethylsiloxane and bisphenol-A carbonate, J. Polym. Sci., Part B, Polym. Lett. 7(3), 1969, 569-572.
6. H.A. Vaughn, U.S. Patent 3,189,662, 1965.

7. H.A. Vaughn, U.S. Patent 3,419,634, 1968.
8. I. M. Raigorodskii and E. Goldberg, E., Russ. Chem. Rev., 56, 1987, 1893.
9. Yu Seung Kim, Jinlian Yang, Sheng Wang, Ajit K. Banthia, James E. McGrath, Surface and wear behavior of bis-(4-hydroxyphenyl) cyclohexane (bis-Z) polycarbonate/polycarbonate–polydimethylsiloxane block copolymer alloys, *Polymer* 43, 2002, 7207–7217.
10. Krishna Maruvada, Cristina Cojocariu, Cristina Cojocariu, Flame Retardancy of Polycarbonate-PDMS Copolymer Compositions, Society of Plastics Engineers Annual Technical Conference 2009.
11. Dibakar Dhara, A. Purushotham, Niles Rosenquist, William D. Richards, Krishna Maruvada, Gautam Chatterjee, Physical Aging of Polycarbonate Block Copolymers: Ductility Rejuvenation below the Glass Transition Temperature, *POLYMER ENGINEERING AND SCIENCE*, 49(9), 2009, 1719-1726.
12. Akio Nodera, Toshitaka Kanai, Flame Retardancy of a Polycarbonate–Polydimethylsiloxane Block Copolymer: The Effect of the Dimethylsiloxane Block Size, *Journal of Applied Polymer Science*, 100, 2006, 565–575.
13. Chan, KP, Argyropoulos, DS, White, DM, Yeager, GW, Hay, AS, "Facile Quantitative Analysis of Hydroxyl End Groups of Poly(2,6-dimethyl-1,4-phenylene oxide)s by ³¹P NMR Spectroscopy." *Macromolecules*, 27 (22), 1994, 6371-6375.
14. Majumdar, P, Christianson, DA, Roesler, RR, Webster, DC, "Optimization of coating film deposition when using an automated high throughput coating application unit." *Prog. Org. Coat.*, 56 (2-3), 2006, 169-177.

15. Majumdar, P, Stafslie, S, Daniels, J, Webster, DC, "High throughput combinatorial characterization of thermosetting siloxane-urethane coatings having spontaneously formed microtopographical surfaces." *J. Coat. Technol. Res.*, 4 (2), 2007, 131-138.
16. Pasquato, L, Modena, G, Cotarca, L, Delogu, P, Mantovani, S, "Conversion of Bis(trichloromethyl) Carbonate to Phosgene and Reactivity of Triphosgene, Diphosgene, and Phosgene with Methanol." *J. Org. Chem.*, 65 (24), 2000, 8224-8228.
17. Kricheldorf, HR, Bohme, S, Schwarz, G, Schultz, C-L, "Cyclic Polycarbonates by Polycondensation of Bisphenol A with Triphosgene " *Macromolecules*, 37 (5), 2004, 1742-1748.
18. Montaudo, G, Samperi, F, Montaudo, MS, "Characterization of synthetic polymers by MALDI-MS." *Prog. Polym. Sci.*, 31 (3), 2006, 277-357.
19. Chen, H, He, M, Pei, J, He, H, "Quantitative Analysis of Synthetic Polymers Using Matrix-Assisted Laser Desorption/Ionization Time-of-Flight Mass Spectrometry." *Anal. Chem.*, 75 (23), 2003, 6531-6535.
20. Yan, W, Gardella, JA, Wood, TD, "Quantitative analysis of technical polymer mixtures by matrix assisted laser desorption/ionization time of flight mass spectrometry." *J. Am. Soc. Mass Spectrom.*, 13 (8), 2002, 914-920.
21. Liu, J, Loewe, RS, McCullough, RD, "Employing MALDI-MS on Poly(alkylthiophenes): Analysis of Molecular Weights, Molecular Weight Distributions, End-Group Structures, and End-Group Modifications." *Macromolecules*, 32 (18), 1999, 5777-5785.

22. Marks, MJ, Munjal, S, Namhata, S, Scott, DC, Bosscher, F, De, LJA, Klumperman, B, "Randomly branched bisphenol a polycarbonates. I. Molecular weight distribution modeling, interfacial synthesis, and characterization." *J. Polym. Sci., Part A: Polym. Chem.*, 38 (3), 2000, 560-570.
23. Kricheldorf, HR, Boehme, S, Schwarz, G, Schultz, C-L, "Syntheses of cyclic polycarbonates by the direct phosgenation of bisphenol M." *J. Polym. Sci., Part A: Polym. Chem.*, 43 (6) 2005, 1248-1254.
24. Brunelle, DJ, Smigelski, PM, Jr., Boden, EP, "Evolution of polycarbonate process technologies." *ACS Symp. Ser.*, 898 (Advances in Polycarbonates) 2005, 8-21.
25. Marks, MJ, Newton, J, "Branching by reactive end groups. II. Synthesis, branching, and melt rheology of (Meth)acrylate/p-t-butylphenol-coterminated bisphenol A polycarbonates." *J. Polym. Sci., Part A: Polym. Chem.*, 38 (13), 2000, 2340-2351.
26. M. Pixton, N. Moghe, S. Rajagopalan, and N. Rosenquist, ANTEC, 2006, 2655.
27. G. E. Niznik, and D. G. Legrand, *J. Polym. Sci., Polym. Symp.*, 60, 1977, 97.
28. Hengzhong Zhuang and Joseph A. Gardella, Jr., Polycarbonate and Polydimethylsiloxane (BPAC-PDMS) Random Block Copolymers, *Macromolecules* 1997, 30, 3632-3639.
29. Xin Chen and Joseph A. Gardella, Jr., Surface Modification of Polymers by Blending Siloxane Block Copolymers, *Macromolecules* 1994, 27, 3363-3369.
30. G. Camino, S.M. Lomakin, M. Lazzari, Polydimethylsiloxane thermal degradation Part 1. Kinetic aspects, *Polymer* 42, 2001, 2395–2402.

31. Xin Chen, Helen F. Lee, and Joseph A. Gardella, Jr. Effects of Structure and Annealing on the Surface Composition of Multiblock Copolymers of Bisphenol A Polycarbonate and Poly(dimethylsiloxane), *Macromolecules*, 26 (17), 1993, 4601-4605.
32. P. S. Gill, S. R. Sauerbrunn and M. Reading, Modulated differential scanning calorimetry, *Journal of Thermal Analysis and Calorimetry*, 40 (3), 1993, 931-939

CHAPTER 6. PERFECTLY ALTERNATING POLYCARBONATE- POLYDIMETHYLSILOXANE (PC-PDMS) MULTIBLOCK COPOLYMERS—PART II

6.1. Abstract

Perfectly alternating PC-PDMS block copolymers were produced using a two-step synthesis method. Due to the high level of PtO₂ catalyst used for hydrosilylation catalyst removal to obtain colorless materials was difficult, as reported in Chapter 5. As a result, the synthetic method was optimized to use lower levels of PtO₂ catalyst. With only 1/10 the amount of PtO₂ catalyst, high molecular weight and much lighter color of PC-PDMS block copolymers were achieved. The PC-PDMS block copolymers obtained were characterized using modulated differential scanning calorimetry (MDSC), thermogravimetric analysis (TGA), dynamic mechanical analysis (DMA), water contact angle, atomic force microscopy (AFM), small angle X-ray scattering (SAXS), transmission electron microscopy (TEM) and Izod impact test. The PDMS segments were found to be partially miscible with PC hard domains, leading to a decrease in the PC-rich phase glass transition temperature and a slightly increased PDMS-rich phase glass transition temperature. At a PDMS content between 27 and 62 wt%, phase inversion occurred for the block copolymers. Surface segregation of PDMS segments was observed resulting in hydrophobic surfaces. In air, the incorporation of PDMS blocks significantly increased the char yield and slowed down the thermal decomposition rate. The synthesized PC-PDMS block copolymers exhibited high optical clarity at up to 62 wt% PDMS content. As evident by SAXS, the lamellar morphology was confirmed. A nanophase separated morphology was observed by TEM and SAXS.

6.2. Introduction

To reduce the notch sensitivity of polycarbonates (PCs), they are often toughened by impact modifiers. Block copolymer structures have been investigated to limit rubber domain size and produce transparent materials. Highly pure linear allyl-PCs were successfully prepared and coupled with hydride-terminated PDMS through hydrosilylation, as described in Chapter 5. These block copolymers exhibit the potential to be transparent impact resistance materials. Initially PtO₂ catalyst was used due to its easy removal.¹ However, the high levels of PtO₂ initially used resulted in difficulty in removal. Removal of the catalyst was time-consuming and resulted in significant loss of polymer. In this study, the level of catalyst, reaction concentration, stoichiometric ratio and other reaction parameters were optimized.

For block copolymers, nanophase separated morphology is an interesting subject to study. By varying the volume ratio between components, spherical, cylindrical, gyroid, and lamellar morphologies can be observed.² The determination of morphologies is important to understanding the structure-property relationships of block copolymers. Thereby, TEM and SAXS were performed to investigate the morphologies. Izod impact strength of the block copolymers were also tested.

6.3. Experimental

6.3.1. Raw Materials

Highly pure allyl-PCs with molecular weights (Mn) of 3,100 g/mol, 4,800 g/mol and 7,200 g/mol (determined by ¹H-NMR) were synthesized using the process described in Chapter 5. 1,1,2,2-tetrachloroethane (TCE) and platinum oxide (PtO₂) were obtained from Aldrich. Hydride-terminated PDMS with a hydride equivalent weight of 350 g/mole (DMS-H03), 550

g/mole (DMS-H11), 2,500 g/mole (DMS-H21), and 6,000 g/mole (DMS-H25) were obtained from Gelest. The TCE was dried with molecular sieves activated at 300 °C. All other reagents were used as received.

6.3.2. Synthesis of PC-PDMS Block Copolymer

Figure 6.1 shows the experimental design used to produce twelve PC-PDMS block copolymers based on three different PCs and four different PDMSs that differed with respect to molecular weight. The three allyl-PCs possessed molecular weights of 3,100, 4,800, and 7,200 g/mol as determined by ¹H-NMR, and were simply denoted as PC3K, PC5K and PC8K, respectively. The four PDMSs used, DMS-H03, DMS-H11, DMS-H21, and DMS-H25, have molecular weights of 740, 1,200, 5,300, and 12,400 g/mol as determined by ¹H-NMR, and were denoted as PDMS0.7K, PDMS1.2K, PDMS5.3K and PDMS12K, respectively. The PDMS content of the block copolymers varied between 9-79 wt%. Table 6.1 describes the compositions of the 12 block copolymers produced. The stoichiometry ratio between silicon hydride and vinyl group was kept at 1.1 : 1. The syntheses were conducted at a concentration of 20 wt%, and PtO₂ catalyst was used at 0.5 mol% relative to vinyl groups. The PtO₂ catalyst solution was prepared by dispersing PtO₂ into TCE at a 0.1 wt% concentration and sonicating for 20 min. A representative procedure for synthesizing a PC-PDMS block copolymer (PC5K-PDMS1.2K_20%) is as follows: To a 250 mL round-bottom flask equipped with a nitrogen inlet and condenser, 15.73 g of eugenol-terminated PC (3.27 mmol) was dissolved in 80 g of anhydrous TCE. To the solution, 4.27 g of DMS-H11 (3.60 mmol) and 7.42 g of the PtO₂ catalyst dispersion (contain 7.42 mg PtO₂) was added and the reaction was conducted at 120 °C under nitrogen for 24 hours. The PC-PDMS block copolymer was isolated by precipitation into methanol, vacuum filtering, and drying for 48 hours at 80 °C under vacuum.

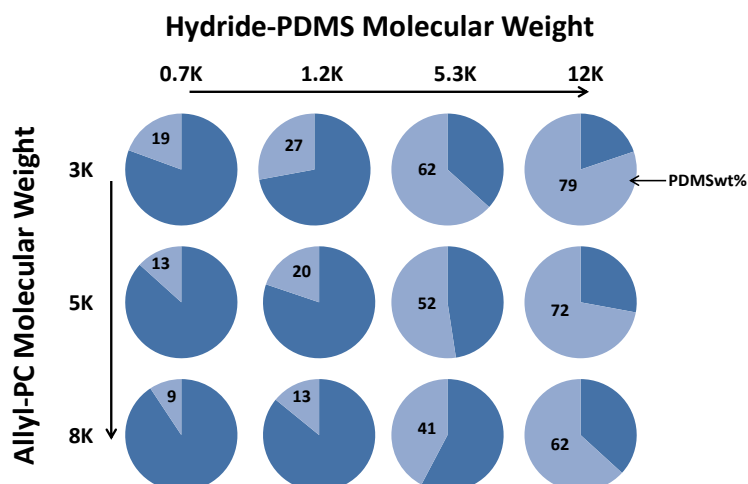


Figure 6.1. A schematic illustration of experimental design for PC-PDMS block copolymer synthesis.

6.3.3. Instrumentation

$^1\text{H-NMR}$ was conducted using a JEOL 400 MHz spectrometer at 25 °C. For $^1\text{H-NMR}$, CDCl_3 was used as a solvent. For each sample, sixteen scans were obtained with a relaxation delay of 4 s. Tetramethylsilane was used as an internal standard

Gel-permeation chromatography (GPC) was performed using a Symyx Rapid-GPC with an evaporative light scattering detector (PL-ELS 1000). Samples for GPC were prepared in THF at a concentration of 1mg/mL. Molecular weights of allyl-PCs and PC-PDMS block copolymers were determined relative to polystyrene standards.

Thermal gravimetric analysis (TGA) was carried using a TGA Q500 thermal analyzer under an air atmosphere in the temperature range of +25 °C to +800 °C at a heating rate of 20 °C/min. Samples of about 10 mg were tested using an air purge rate of at 60 ml/min.

Table 6.1. Composition of the twelve PC-PDMS block copolymers produced.

PC-b-PDMS samples	Mn (PC) g/mol	Mn (PDMS) g/mol	Theoretical PDMS wt%	Experimental PDMS wt%*	Mn (PC-b-PDMS) g/mol	PDI
PC3K-PDMS0.7K_19%	3,100	740	19	19.3	32450	1.7
PC3K-PDMS1.2K_27%	3,100	1,200	27	27.3	33010	1.8
PC3K-PDMS5.3K_62%	3,100	5,300	62	61.8	43730	1.7
PC3K-PDMS12K_79%	3,100	12,400	79	78.5	49080	1.8
PC5K-PDMS0.7K_13%	4,800	740	13	12.9	33500	1.7
PC5K-PDMS1.2K_20%	4,800	1,200	20	19.3	39180	1.6
PC5K-PDMS5.3K_52%	4,800	5,300	52	51.3	39840	1.6
PC5K-PDMS12K_72%	4,800	12,400	72	70.6	43500	1.7
PC8K-PDMS0.7K_9%	7,200	740	9	8.2	42770	1.6
PC8K-PDMS1.2K_13%	7,200	1,200	13	13.9	44950	1.5
PC8K-PDMS5.3K_41%	7,200	5,300	41	40.4	36100	1.5
PC8K-PDMS12K_62%	7,200	12,400	62	61.9	39250	1.5

*: Experimental PDMS wt% were measured by ¹H-NMR.

Modulated DSC was carried out using a Q2000 Modulated Differential Scanning Calorimeter manufactured by TA Instruments. Data analysis was performed with TA Universal Analysis software. The calorimeter was calibrated with sapphire and indium standards. Samples of about 13 mg of were loaded into a Tzero aluminum pan, while an empty pan was used as a reference. A modulation amplitude of 0.531 °C and a period of 100 s was used with a heating rate of 2 °C/min when samples were modulated between -180-0 °C and 25-180 °C. The whole test profile is described as following: Samples were equilibrated at 300 °C for 3 min, ramped to -180 °C at 20 °C/min and held for 3 min. Modulation was started from -180 to 0 °C at a heating rate of 2 °C/min using a period of 100 s and amplitude of ± 0.531 °C, and then ramp again from 0 to 25 °C at 20 °C/min. Finally, the sample was modulating again from 25 to 180 °C at 2 °C/min using a period of 100 s and amplitude of ± 0.531 °C. The sample chamber was purged with helium at 25 ml/min.

Dynamic mechanical analysis (DMA) was performed using a DMA Q800 Dynamic Mechanical Analyzer in the temperature range of -150 °C to +160 °C at a heating rate of 5 °C/min with experimental parameters of 0.01 % strain, 0.01 N preload force, and 10 Hz frequency. Sample films were made by hot pressing at 180 °C and cutting into strips with a width of 5 mm. The thicknesses of the samples were around 100 μm , and the length between the clamps was around 15 mm.

Water contact angle measurements on the block copolymer films were carried out using an automated surface energy measurement unit manufactured by Symyx Discovery Tools, Inc. and First Ten Angstroms. Three measurements were taken for each film using the sessile drop method and the data reported as the average and standard deviation.

Atomic force microscopy (AFM) was conducted in tapping mode at ambient conditions with a Dimension 3100® microscope and a Nanoscope IIIa controller from Veeco Incorporated. Topographical images were collected in air, at room temperature, using a single-lever silicon probe from Nanosensors™. Cantilever length, width, and thickness of the silicon probe was $225 \pm 10 \mu\text{m}$, $25 \pm 7.5 \mu\text{m}$, and $3.0 \pm 1.0 \mu\text{m}$, respectively. The spring constant was 0.5-9.5 N/m with a resonant frequency of 75 kHz. The set point ratio was 0.8-0.9. Polymer samples were spin coated over glass slides using 10 wt % solutions in CH_2Cl_2 .

SAXS experiments were performed using a Rigaku S-Max 3000 3 pinhole SAXS system equipped with a rotating copper anode emitting X-rays with a wavelength of 0.154 nm ($\text{Cu K}\alpha$). The q-range was calibrated using a silver behenate standard. Two-dimensional SAXS patterns were obtained using a fully integrated 2D multiwire, proportional counting, gas-filled detector, with an exposure time of 1 hour. SAXS data was corrected for sample thickness, sample transmission, and background scattering. All SAXS data was analyzed using SAXSGUI software to obtain radially integrated SAXS intensity versus scattering vector q (SAXS), where $q=(4\pi/\lambda)\sin(\theta)$, θ is one half of the scattering angle and λ is the wavelength of X-ray profiles. Block copolymer samples were produced by compression molding at 180 °C for 30 minutes.

TEM measurements were carried out using a Hitachi HD-2300 STEM with energy dispersive X-ray spectroscopy (EDS) at 200 kV. Thin sample sections were prepared by microtoming and placed onto a 3 mm Cu TEM grid

Izod impact strength test followed ASTM D256 standard in this study to determine impact strength of notched samples under 4.497 N weight and 334.949 mm radius condition. The tests are carried out using a Izod impact test machine by Tinius Olse. For Izod impact strength

testing, the block copolymers are compression molded according to the procedure described below. Prior to molding, the mold was cleaned by acetone. To the preheated mold at 270 °C for 2 hours in an oven, 4 g of molding material was added to the square mold cavity with the plug on, or 6.5 g of materials to the rectangular mold cavity. The mold system kept heating for half an hour at 270 °C while preheating the compression machine to 150 °C. After 1.5 hour heating, materials melt completely and the mold system was placed into the compression machine and stayed for 5 minutes for cooling. Next 1 metric ton pressure was applied to the mold system and remained for an hour at 150 °C and for another hour after turning off the temperature of the compression machine. The final specimen was taken out when the mold cooled down to room temperature, and then cut into the dimension for required tests.

6.4. Results and Discussion

6.4.1. Synthesis of PC-PDMS Block Copolymers

Through optimization of reaction parameters, high molecular weight block copolymers with little color were obtained. The molecular weights obtained are listed in Table 6.1. In comparison with the molecular weights previously obtained in Chapter 5, it was found that the optimized reaction conditions allowed for higher molecular weights to be produced. Due to the low level of catalyst, PtO₂ was not removed from the block copolymers. The low level of catalyst had negligible influence on the appearance of the compression molded samples. The optical, thermal, and physical properties are discussed below.

6.4.2. Optical Clarity

The block copolymers were cast from chloroform to form uniform films on glass slides at room temperature. An image of the films produced is shown in Figure 6.2. It is interesting that

the transparency of the PC-PDMS block copolymers could be maintained at up to 62 wt% PDMS for sample PC3K-PDMS5.3K_62%. For samples PC8K-PDMS5.3K_41%, PC3K-PDMS12K_79%, PC5K-PDMS12K_72%, and PC8K-PDMS12K_62%, the opacity of the block copolymers arose from the combined effect of the mismatch of refractive indices and large domain sizes.^{3,4} The refractive indices of PC and PDMS are 1.585 and 1.4, respectively.²² Therefore, the opaque samples should have relatively large domains as a result of phase separation.

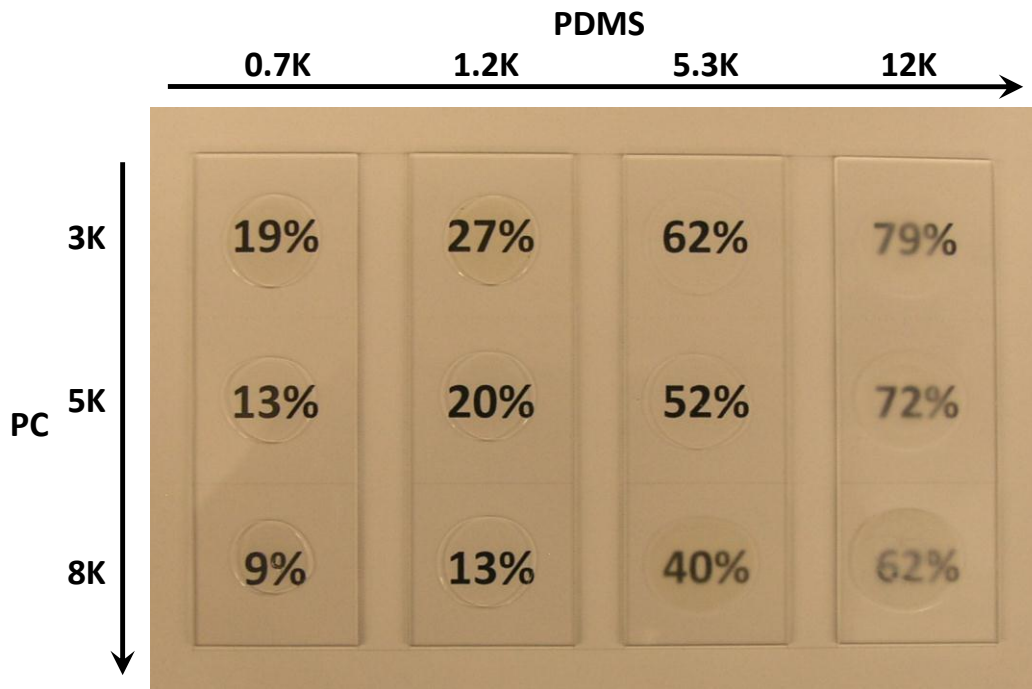


Figure 6.2. An image of solvent cast film of PC-PDMS block copolymers on glass slides. The numbers below the slides indicate the weight percent PDMS in the polymers.

6.4.3. Glass Transition Temperature by MDSC

Due to the low sensitivity of conventional DSC for detecting glass transition behaviors of block copolymers, Modulated DSC (MDSC) was used. MDSC is superior than conventional DSC in its capability of separating non-reversible kinetic component heat flow (thermal history)

and reversible thermodynamic heat flow (glass transition, crystallization) by running a sinusoidal temperature modulation.⁵ The thermal properties of the allyl-terminated PCs, hydride-terminated PDMSs, and the PC-PDMS multiblock copolymers were characterized using MDSC. Figure 6.3 displays representative MDSC thermograms obtained over the temperature range of 40 to 160 °C, while Figure 6.4 displays representative MDSC thermograms over the temperature range of -170 °C to -10 °C. Over the temperature range of 40 to 160 °C, MDSC measurements were obtained in triplicate to account for experimental error.

Table 6.2. T_g s (°C) obtained from MDSC.

		PDMS Mn				
		No PDMS	0.7K	1.2K	5.3K	12K
PC Mn	No PC	----	-143	-139	-130	-128
	3K	109	82 \pm 2.0/Not obs.	86 \pm 1.7/-136	98 \pm 3.0/-125	Not obs./-121
	5K	122	101 \pm 2.1/Not obs.	105 \pm 1.7/Not obs.	109 \pm 1.2/-126	Not obs./-125
	8K	134	116 \pm 1.4/Not obs.	117 \pm 2.9/Not obs.	135 \pm 2.5/-121	133 \pm 3.1/-121

Table 6.2 lists the T_g values obtained. For allyl-terminated PCs, T_g was dependent on Mn and all of the allyl-terminated PCs possessed T_g s well below that typically obtained for relatively high molecular weight PC. The T_g measured by MDSC for commercially available PC with an Mn of 27,800, obtained by GPC and expressed relative to polystyrene standards, was determined to be 145 °C. These results indicate that all three of the allyl-terminated PCs possessed Mns below the critical molecular weight required for polymer entanglement.

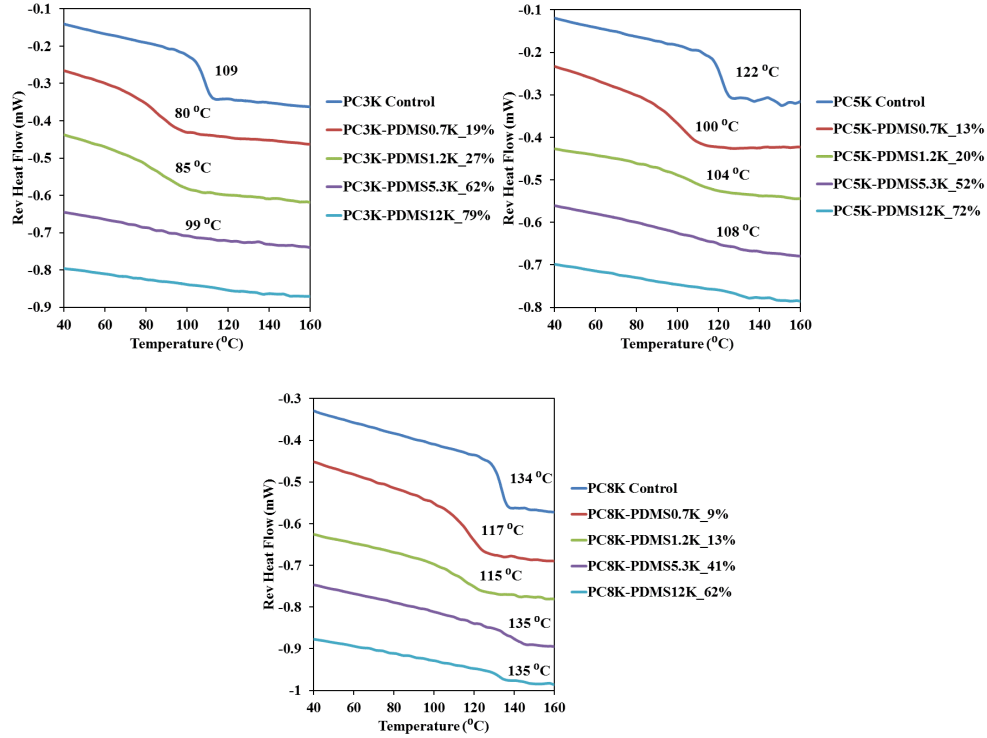


Figure 6.3. Representative MDSC thermograms obtained at temperatures between 40 to 160 °C.

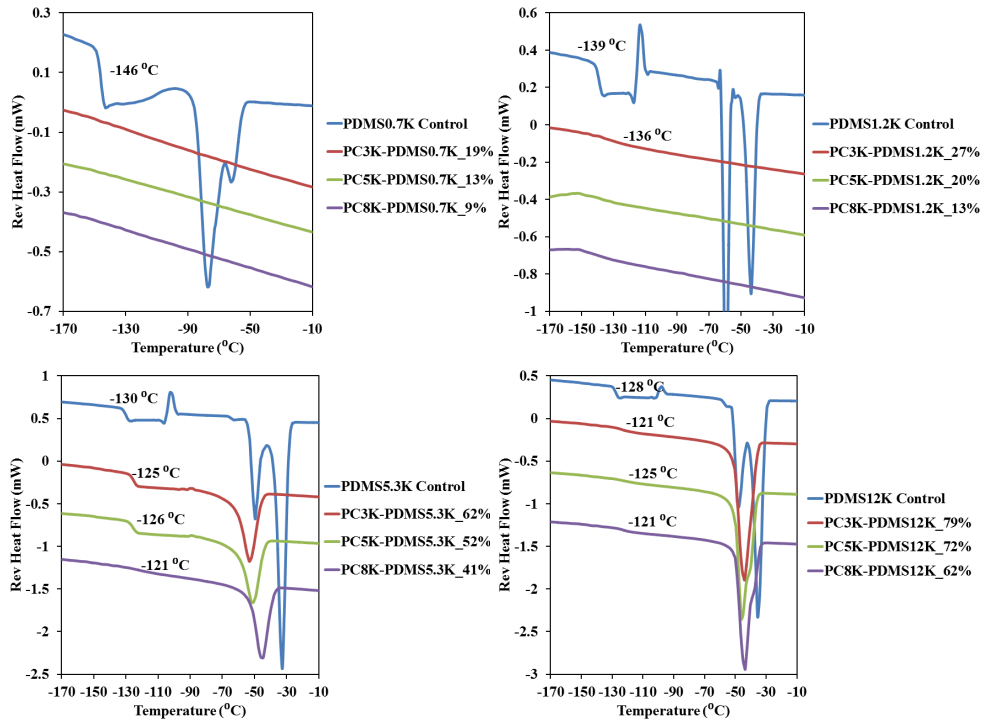


Figure 6.4. Representative MDSC thermograms obtained at temperatures between -170 to -10 °C.

For PC-PDMS multiblock copolymers possessing a PDMS content below 70 weight percent, the T_g of the PC-rich phase could be identified using MDSC. For these copolymers possessing a PDMS content below 70 weight percent, the T_g associated with the PC-rich phase varied significantly with copolymer composition. Figure 6.5 displays T_g data associated with the PC-rich phase as a function of the block M_n s of the copolymers. From Figure 6.5, it can be seen that the presence of the short 700 g/mole PDMS blocks dramatically reduces the T_g s of the PC-rich phase compared to the pure allyl-terminated PCs.

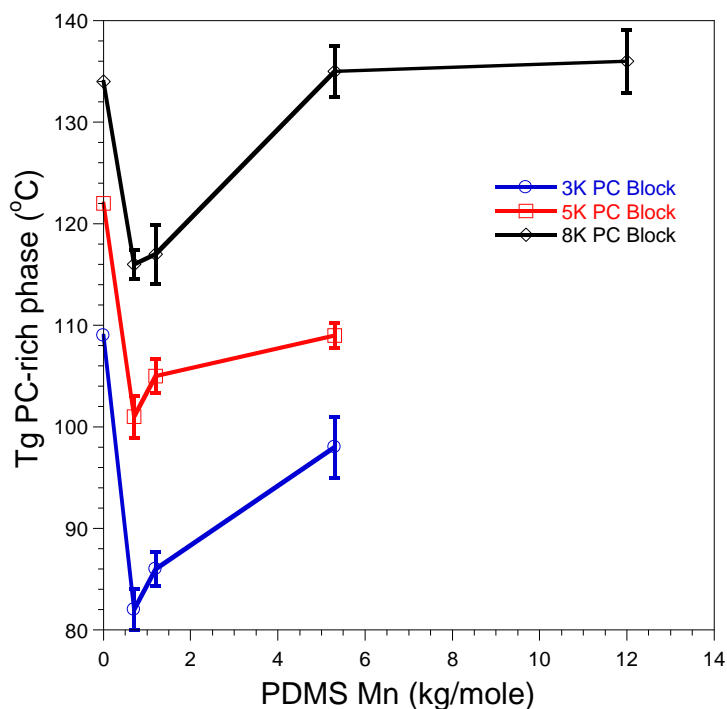


Figure 6.5. T_g data associated with the PC-rich phase as a function of the block M_n s of the copolymers.

In general, the magnitude of the reduction in PC-rich phase T_g decreased with increasing PC block M_n as shown in Figure 6.6. This result indicates that, despite the very large difference in solubility parameter between PC ($\delta=9.5$) and PMDS ($\delta=7.3$) of 2.2, significant partial

miscibility between the PC and PDMS blocks occurs and, as expected, the degree of partial miscibility decreases with increasing block molecular weight. For the multiblock copolymers possessing the highest molecular weight PC block (i.e. 8,000 g/mole) and PDMS blocks of 5,300 g/mole or higher, no reduction of the PC T_g was observed indicating that the block were of sufficient molecular weight to result in complete separation of PDMS segments from the PC phase.

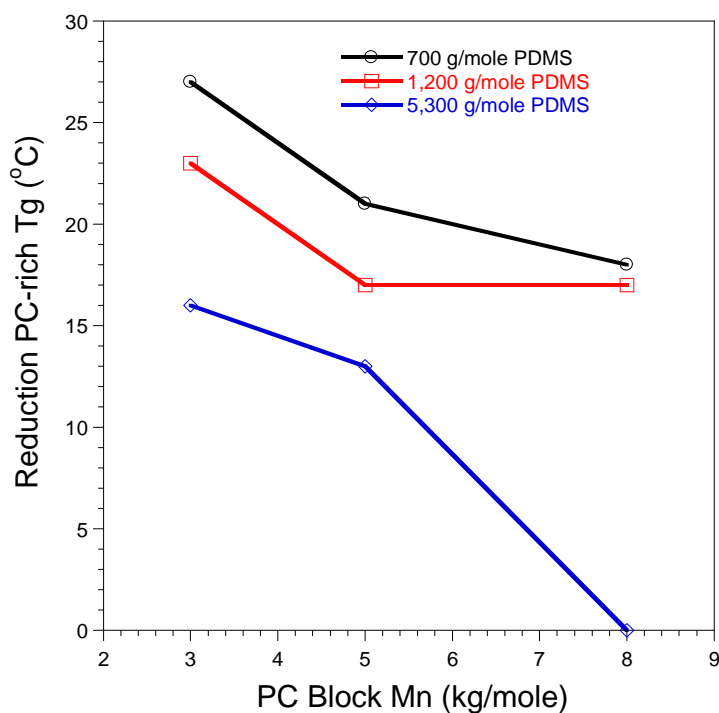


Figure 6.6. The reduction in the T_g of the PC-rich phase as a function of block Mns.

To further illustrate the influence of block Mns on the degree of partial miscibility, Figure 6.7 was generated which provides a comparison of multiblock copolymers with equivalent or similar PC/PDMS ratio but differing block Mns. As shown in the figure,

copolymers with short block M_n s consistently produced multiblock copolymers with a lower T_g for the PC-rich phase.

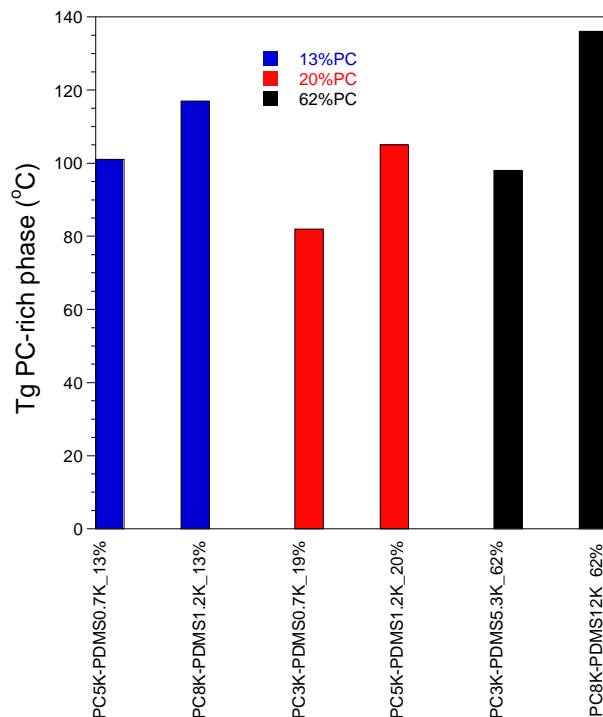


Figure 6.7. A comparison of PC-rich phase T_g at equivalent PC/PDMS ratio.

As shown in Figure 6.4, all of the hydride-terminated PDMSs used to produce the PC-PDMS multiblock copolymers exhibited a glass transition and melting endotherm. With exception of the lowest M_n hydride-terminated PDMS, they also exhibited a crystallization exotherm associated with cold crystallization. Both T_g and melting temperature were found to vary with molecular weight. With regard to T_g , it increased with increasing M_n which, for this relatively low M_n range, can be attributed to the greater segmental mobility of the polymer chain ends. With regard to the melting behavior, all four of the hydride-terminated PDMSs exhibited two melting peaks. The observation of two melting peaks for PDMS has been observed by

others and attributed to the presence of two distributions of crystallites with different degrees of perfection/thickness. As discussed by Aranguren²³, the lower melting endotherm is associated with imperfect, relatively thin crystallites formed upon cooling at a rate of 2 °C/min; while the higher temperature endotherm is associated with thicker, more perfect crystallinities produced as a result of cold crystallization and crystal reorganization that occurs during the course of the MDSC heating process. For the lowest molecular weight hydride-terminated PDMS, the melting temperatures of the endotherms were much lower than for the other three higher Mn hydride-terminated PDMSs, which can be explained by the higher number of polymer chain ends that essentially serve as defects in the crystallites. For the 1.2K PDMS, the two melting points were higher than that for the 0.7K PDMS but lower than that for the 5.3K PDMS, which can be attributed to an endgroup concentration effect as just discussed. Compared to the two highest Mn PDMSs, the 1.2K showed a significant difference in the relative area of the lower melting endotherm to the higher melting endotherm. The 1.2K PDMS displayed a higher fraction of the lower melting, less perfect crystallites than was observed for the higher Mn PDMSs. Again, this result is a consequence of the difference in the number of polymer chain ends.

With regard to the PC-PDMS block copolymers, none of the block copolymers based on the lowest molecular weight PDMS exhibited a T_g or crystalline phase associated with the presence of a PDMS-rich phase. This result suggests that the short 0.7K PDMS blocks are unable to produce a separate phase of sufficient volume to produce these low temperature transitions. For the multiblock copolymers based on the 1.2K PDMS, a very diffuse, subtle inflection in the range between -140 and -120 °C can be observed indicative of a PDMS-rich phase T_g . However, no melting transitions were observed indicating that the presence of the PC blocks and interactions between PDMS and PC chain segments inhibit PDMS crystallization.

For the PC-PDMS copolymers based on the two highest Mn PDMS blocks (i.e. 5.3K and 12K), both a T_g and a melting endotherm were observed, but no cold crystallization was observed for all the copolymers. For the copolymers based on the 5.3K PDMS, T_m increased slightly with increasing PC block Mn and only one melting endotherm was observed with a peak temperature below that attributed to the more stable crystallites observed for the pure 5.3K PDMS. The observation of a T_g indicates that a separate PDMS-rich phase exists for these block copolymers. In addition, the slight increase in T_m with increasing PC block Mn suggests less interaction of PDMS segments with PC segments which enables thicker, more perfect PDMS crystallites to be formed. For the copolymers based on the highest Mn PDMS, the melting transition also varied systematically with PC block molecular weight. For the block copolymer based on the lowest Mn PC (i.e. PC3K-PDMS12K_79%), a single melting endotherm was observed while the melting temperature for the copolymer based on 5K or 8K PDMS displayed a melting temperature with a shoulder on the high temperature side of the endotherm. This result also suggests that increasing PC block molecular weight enables greater phase separation between PDMS and PC segments such that thicker, more stable PDMS crystallites can be formed.

6.4.4. Thermal Stability by TGA

The thermal degradation behavior of PC-PDMS block copolymers in air was evaluated using TGA, as shown in Figure 6.8 and Figure 6.9. It can be seen from the degradation profiles in Figure 6.8 that pure allyl-PCs undergo complete thermal degradation following a two-stage profile in air without leaving any char yield. The PC-PDMS block copolymers undergo a two-stage decomposition when copolymerized with short PDMS chains, and gradually shifted to a near-one-stage decomposition when longer PDMS blocks are introduced. The two-stage thermal degradation profile is associated the thermal degradation behavior of pure PC under air.⁷ The

near-one-stage thermal degradation profile is attributed to the PDMS thermal degradation under air.⁸

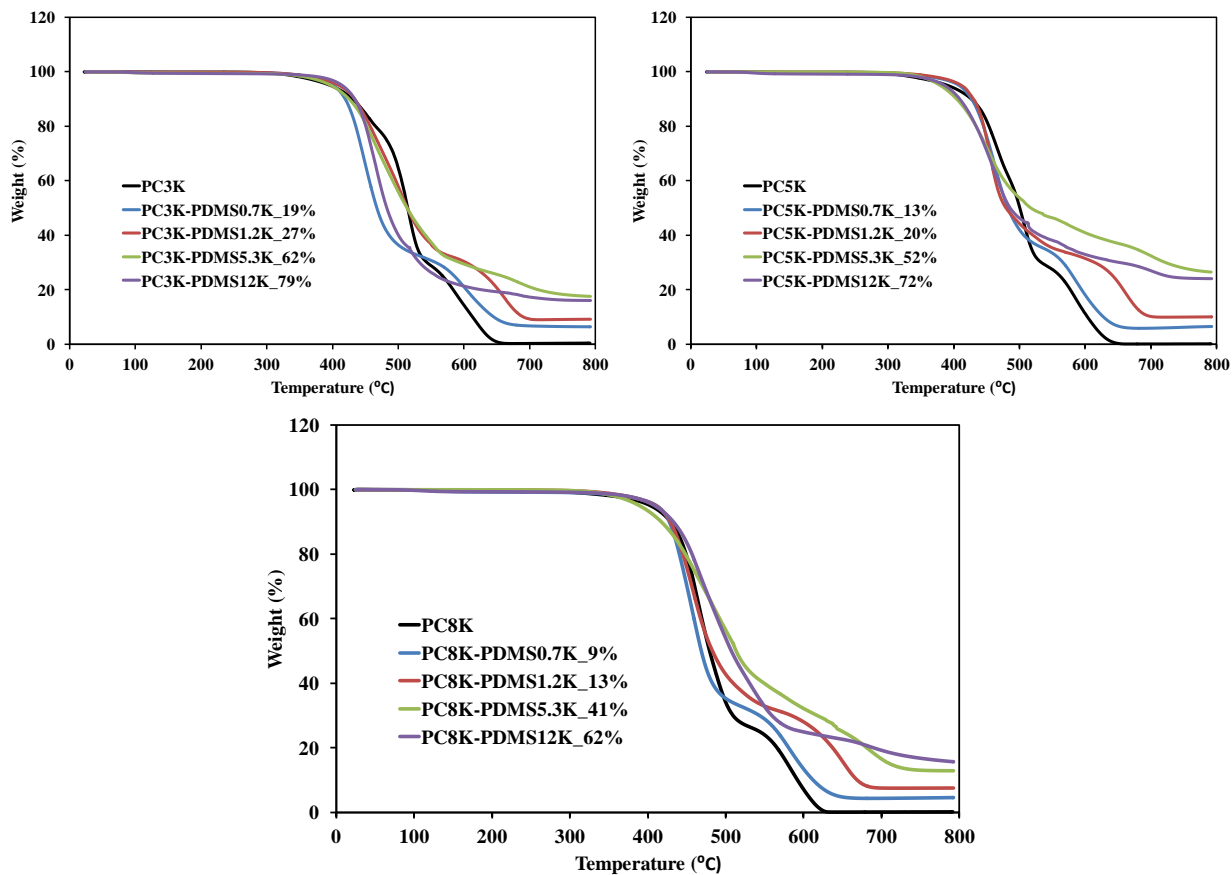


Figure 6.8. TGA curves of PC-PDMS block copolymers with PC block length of (a) 3K, (b) 5K, and (c) 8K in air.

Figure 6.9 displays TGA curves of the block copolymers compared with pure PDMS. Pure PDMSs, especially the PDMSs with low molecular weights, are not thermally stable but yielding high amount of char residues. After being copolymerized with PC, the PC-PDMS block copolymers are much more thermally stable due to the restricted PDMS segments.

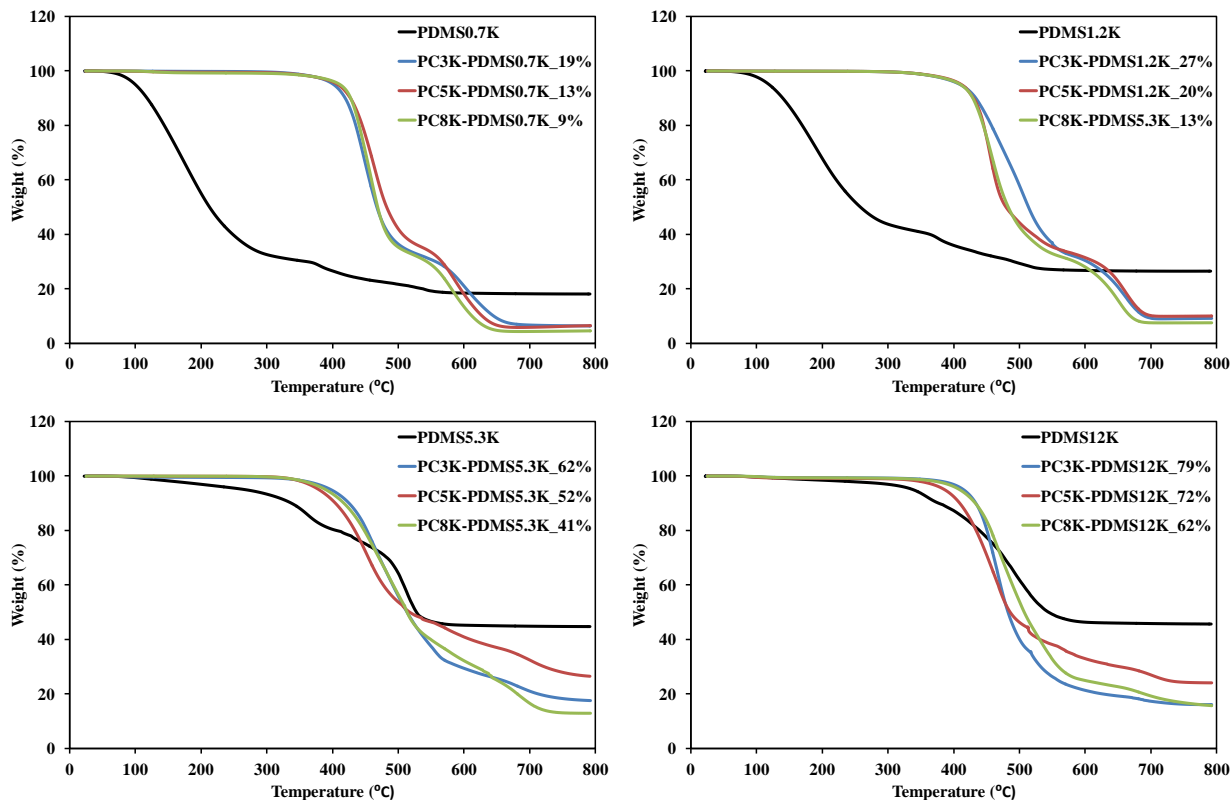


Figure 6.9. TGA curves of PC-PDMS block copolymers with PDMS block length of (a) 0.7K, (b) 1.2K, (c) 5.3K, and (d) 12K in air.

The temperature at maximum degradation rate, 5 wt% mass loss, 10 wt% mass loss, and weight percent of char residue are listed in Table 6.3. Figure 6.6 shows the char yield of the block copolymers. By comparing the $T_{-5\text{wt}\%}$ and $T_{-10\text{wt}\%}$ values, it can be found that the block copolymers with PDMS 5.3K blocks start to degrade preferentially than with other PDMS blocks. As compared with the thermal decomposition behavior under N_2 in Chapter 5, the char yield of the block copolymers after heating under air is substantially higher. This is attributed to the formation of oxidized silica on the surface preventing the residue from further decomposition.

Table 6.3. Thermal degradation evaluated by TGA in air.

PC-b-PDMS samples	T_d (°C)	T_{.5wt%} (°C)	T_{.10wt%} (°C)	Residue (wt%)
PC3K-PDMS0.7K_19%	448.04	401.80	419.28	6.34
PC3K-PDMS1.2K_27%	505.72	409.68	433.47	9.06
PC3K-PDMS5.3K_62%	460.81	397.68	425.21	17.61
PC3K-PDMS12K_79%	466.97	415.06	433.78	16.03
PC5K-PDMS0.7K_13%	463.92	408.38	427.30	6.52
PC5K-PDMS1.2K_20%	454.89	411.62	429.86	10.05
PC5K-PDMS5.3K_52%	452.95	379.57	404.68	26.38
PC5K-PDMS12K_72%	468.97	386.17	409.23	23.99
PC8K-PDMS0.7K_9%	457.65	411.57	427.67	4.49
PC8K-PDMS1.2K_13%	457.56	410.41	429.09	7.44
PC8K-PDMS5.3K_41%	484.42	389.63	417.38	12.87
PC8K-PDMS12K_62%	467.20	408.98	432.76	15.73

In general, the overall char yield of the block copolymers increased with an increase of PDMS block length, as shown in Figure 6.10. This can be attributed to the greater thermal stability of the inorganic Si-O polymer backbone and the higher PDMS content of block copolymers possessing longer PDMS blocks. Correlating with the low initial degradation temperature, it was found the block copolymers with PDMS 5.3K blocks tends to undergo less

sharp decomposition. This may be attributed to the moderate domain size of the PDMS phase which was reported to be more flame retardant than the block copolymers with either smaller or bigger domain size.^{9,10} It is interesting that the char yield of block copolymers with PC 5K block length is higher than those with PC 3K and 8K blocks.

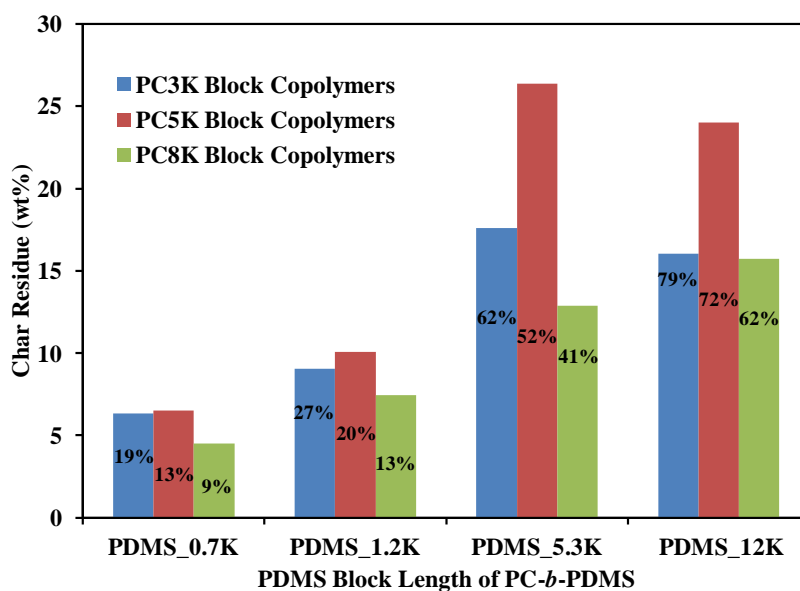


Figure 6.10. TGA char yield of the PC-*b*-PDMS copolymers in air.

6.4.5. Viscoelastic Properties by DMA

In addition to MDSC, phase behavior was also characterized using DMA. Due to issues with the ability to form free standing films with adequate mechanical properties for testing, only 6 of the 12 samples could be characterized using DMA. The mechanical properties of PC-PDMS block copolymers are strongly affected by block ratio and block molecular weights.¹¹ Figure 6.11 displays storage moduli and loss tangent data for all three multiblock copolymers possessing the lowest Mn PDMS blocks. Consistent with the MDSC data, all three block copolymers exhibited a T_g associated with a PC-rich phase that decreased with decreasing PC molecular weight. In

addition to a reduction in the T_g of the PC-rich phase with decreasing PC Mn, the transition broadened with decreasing PC Mn consistent with a greater extent of partial miscibility between the PC phase and PDMS segments. Further, all of the block copolymers exhibit a subtle relaxation over the temperature range extending from about 30 °C to 70 °C. The magnitude of this transition appears to increase with increasing PDMS block content suggesting that it may be associated with polymer chain segments located in the interphase between PC-rich and PDMS-rich phases.

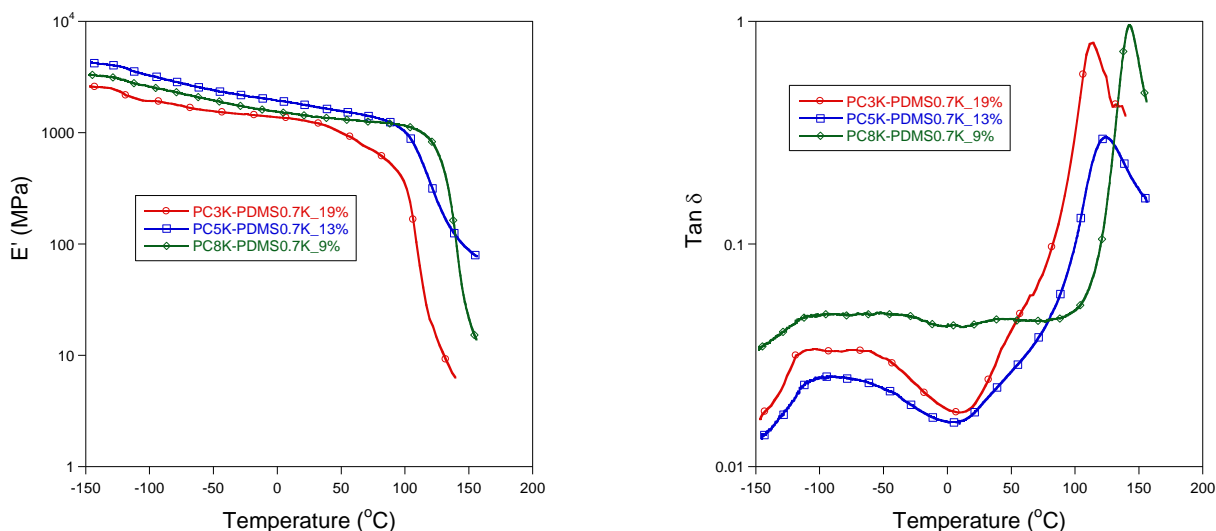


Figure 6.11. Storage moduli and loss tangent data for all three multiblock copolymers possessing the lowest Mn PDMS blocks.

Figure 6.12 provides a comparison of viscoelastic properties at approximately equivalent PDMS content (i.e. 20 wt. % PDMS). As shown in Figure 7, the block copolymer based on the higher Mn PC and PDMS blocks exhibited a higher T_g for the PC-rich phase consistent with less partial miscibility between PC segments and PDMS segments.

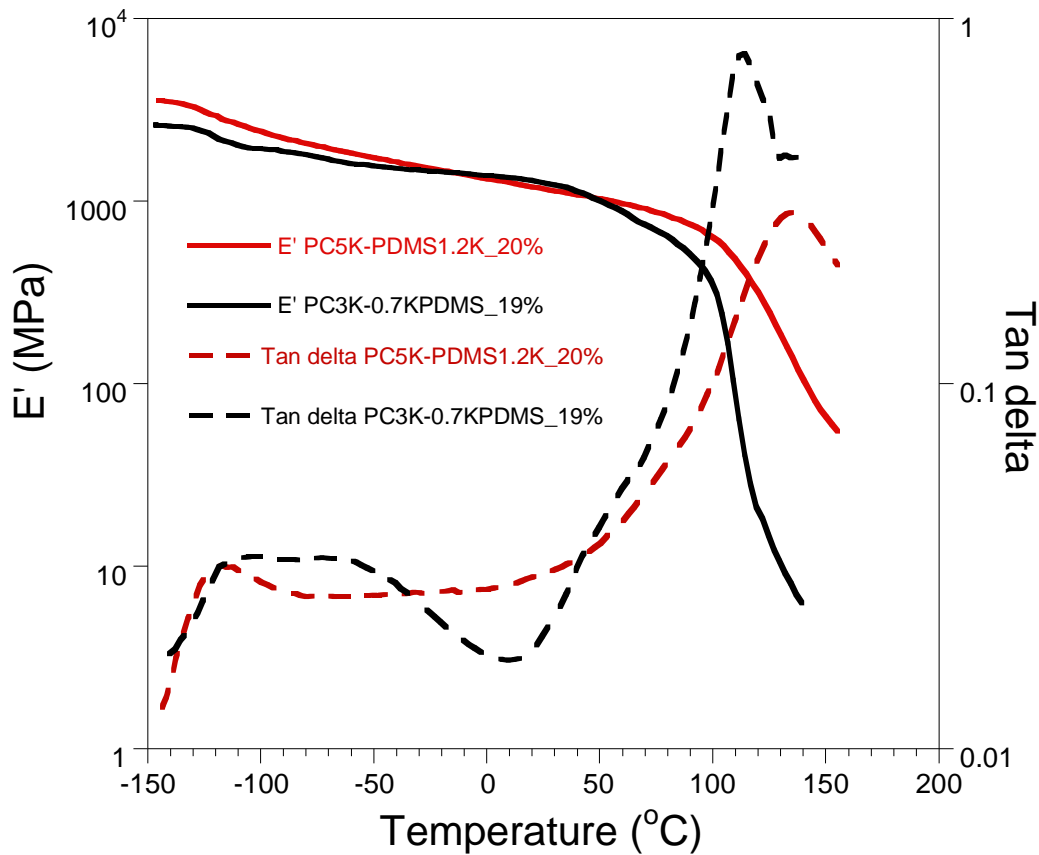


Figure 6.12. A comparison of viscoelastic properties at approximately equivalent PDMS content (i.e. 20 wt. % PDMS).

Figure 6.13 illustrates the effect of PDMS block M_n on viscoelastic properties. As shown in the figure, increasing the PDMS block M_n from 1.2 Kg/mole to 5.3 Kg/mole, which corresponds to an increase in PDMS content from 27 to 62 weight percent, caused a dramatic change in viscoelastic properties. At 62 weight percent PDMS, the storage modulus dropped by more than two orders of magnitude when the sample was heated beyond the T_g of the PDMS-rich phase. In addition, an increase in storage modulus was observed at temperatures just above the PDMS-rich phase T_g . This increase in storage modulus can be attributed to cold crystallization

of PDMS segments. The large drop in storage modulus after reaching the PDMS-rich phase T_g clearly indicates that the PDMS segments formed the continuous phase in this sample.

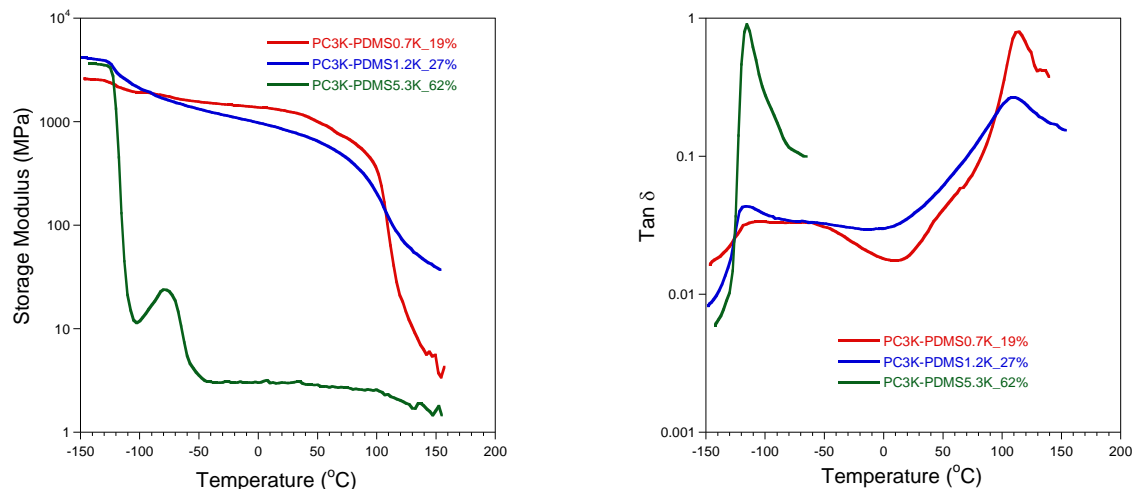


Figure 6.13. The effect of PDMS block Mn on viscoelastic properties of block copolymers based on 3,000 g/mole PC blocks.

6.4.6. Water Contact Angle

Water contact angle measurements were performed to analyze the surface energy of the block copolymers. The results were plotted in Figure 6.14. Even though the water contact angle result of PC controls were not shown in the figure due to the low molecular weight and poor film formation of the PC oligomers especially when molecular weight is 3 K, the impact of PDMS block on the surface energy of the block copolymers was remarkable. It has been determined that the water contact angle was 89 ° for PC with 5 K molecular weight. In general, water contact angle was increase with the increase of PDMS block length, suggesting the existence of PDMS on the air/solid interface. However, the impact of PC block length on the surface energy of the block copolymers was negligible. This is attributed to the high mobility of PDMS polymer

chains and the freezing of PC polymer chains at room temperature. The PC segments remain in glassy state within bulk regardless of molecular weight, while PDMS segments migrate towards air/solid interface and longer PDMS block lengths allows higher extent of PDMS segregation. Meanwhile, it is interesting that sample PC8K-PDMS1.2K_13% showed lower surface energy than sample PC5K-PDMS0.7K_13%, and so as to sample PC8K-PDMS12K_62% and sample PC3K-PDMS5.3K_62%, suggesting surface energy is affected by block length regardless of PDMS content. This again illustrates the effect of PDMS block length on the surface segregation. The component with low surface energy in multiblock systems tends to change the surface property of the system.

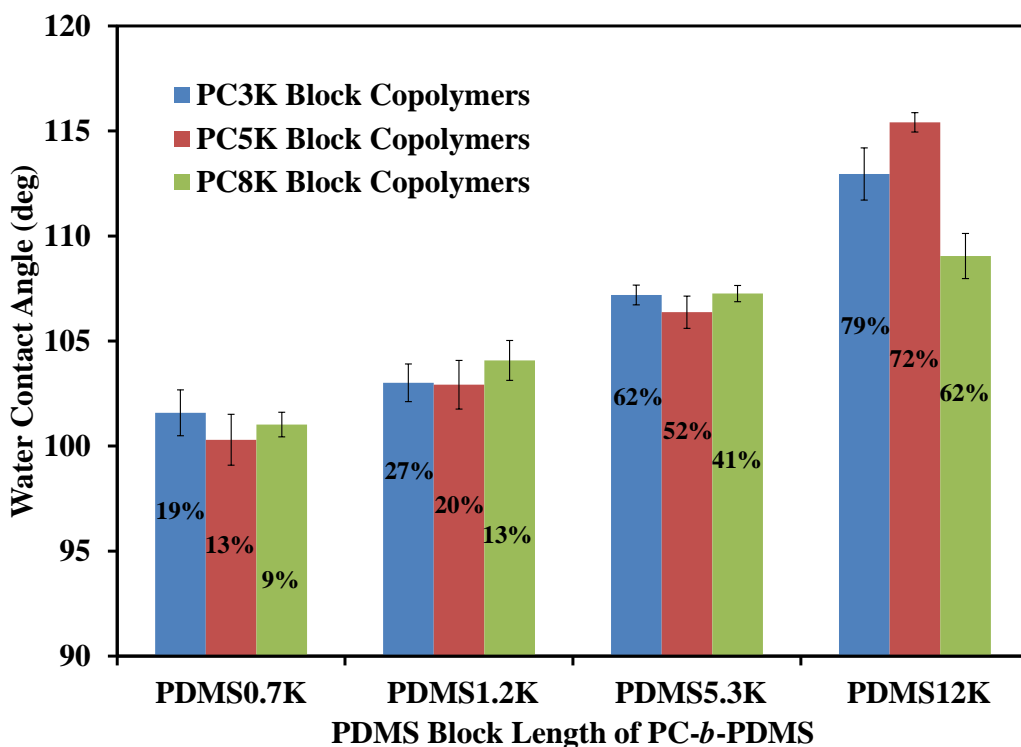


Figure 6.14. Water contact angle of PC-PDMS block copolymers (the percentage values labeled on bars indicate the PDMS content of each block copolymer).

6.4.7. AFM

The surface morphology of the pure PC control and block copolymers was imaged by AFM as shown in Figure 6.15. Since the pure PC oligomers don't have good film formation property due to the low molecular weight, especially for PC 3K sample, PC 5K was coated and represents as control. It can be seen from the images that the surface heterogeneity increased when PDMS blocks were incorporated compared with PC control. PDMS block length plays an important role in determining the surface morphology of the block copolymers. With the increase of the PDMS block length, more PDMS segments segregate onto the surface making the surface more heterogeneous. Finally the surface is wholly covered by longest PDMS blocks, resulting in smooth surface again. This has been reported before that flexible PDMS chains tend to migrate onto solid/air interface, leading to the higher content of PDMS than bulk.¹³ And even only 6 wt% PDMS content could result in 95 wt% of PDMS concentration on surface upon annealing at certain temperature.¹⁴

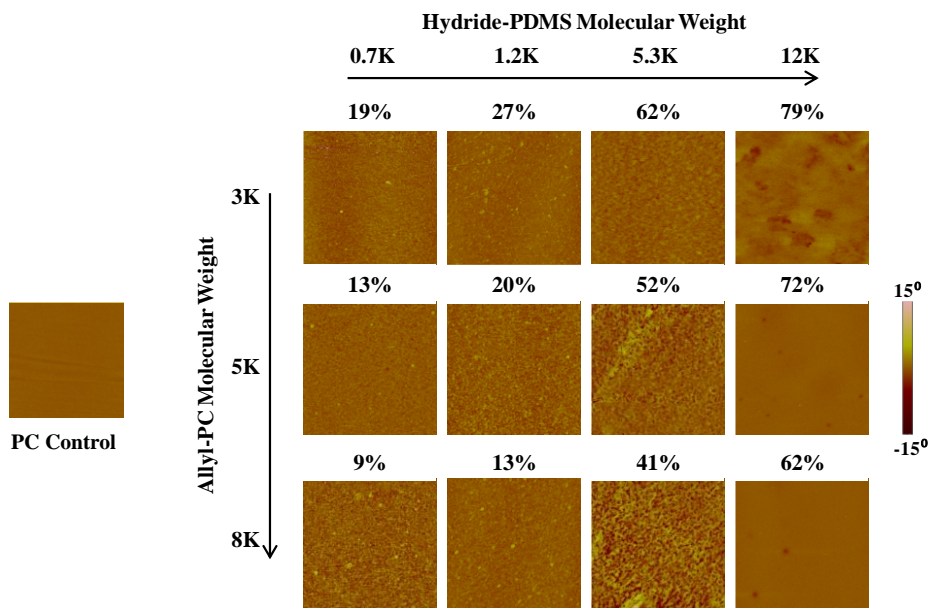


Figure 6.15. AFM images of PC-*b*-PDMS copolymers compared with PC control.

6.4.8. Small Angle X-Ray Scattering (SAXS)

PDMS-containing block copolymers form two-phase morphologies due to the difference in solubility parameters of the two components.¹⁵ SAXS is a primary technique to determine the phase separated morphologies. From SAXS, important characteristics, such as the mean values of interdomain spacing, domain boundary diffuseness and degree of microphase separation may be obtained.¹⁶ The samples were analyzed by SAXS to get more information about morphology. To ensure the phase separation for SAXS characterization, the block copolymer samples were annealed above glass transition temperature at 180 °C for 30 min and quenched down to room temperature. Figure 6.16 shows the SAXS profiles of PC control, commercial PC-PDMS copolymer, and the synthesized PC-PDMS block copolymers. For pure PC, no scattering peak was observed. For block copolymer samples, scattering peaks appeared depending on the degree of phase separation, indicating the nanophase separated morphology. The samples with low PDMS content showed weak and broad maximum, indicating the lack of high order reflection. The weak and broad scattering peaks in SAXS profiles is owing to the density fluctuation in phase separated state.¹⁷ The absence of higher order of reflections is a consequence of a wide spread in lamellar thickness and the absence of regular stacking of lamella.¹⁸ However, for commercial PC-PDMS copolymers with only 5 wt% PDMS content, the scattering peak is more pronounced than that of synthesized PC-PDMS block copolymers with low PDMS content, i.e. 9 and 13 wt%. This suggests that the commercial copolymer has a higher nanophase separated morphology and a higher order of the phase separated structure. The sharp scattering peak started to emerge from block copolymer sample with 20 % PDMS. And with the increase of PDMS content, the scattering peak become more pronounced and sharper, especially for samples with 27 % and 62 % PDMS.

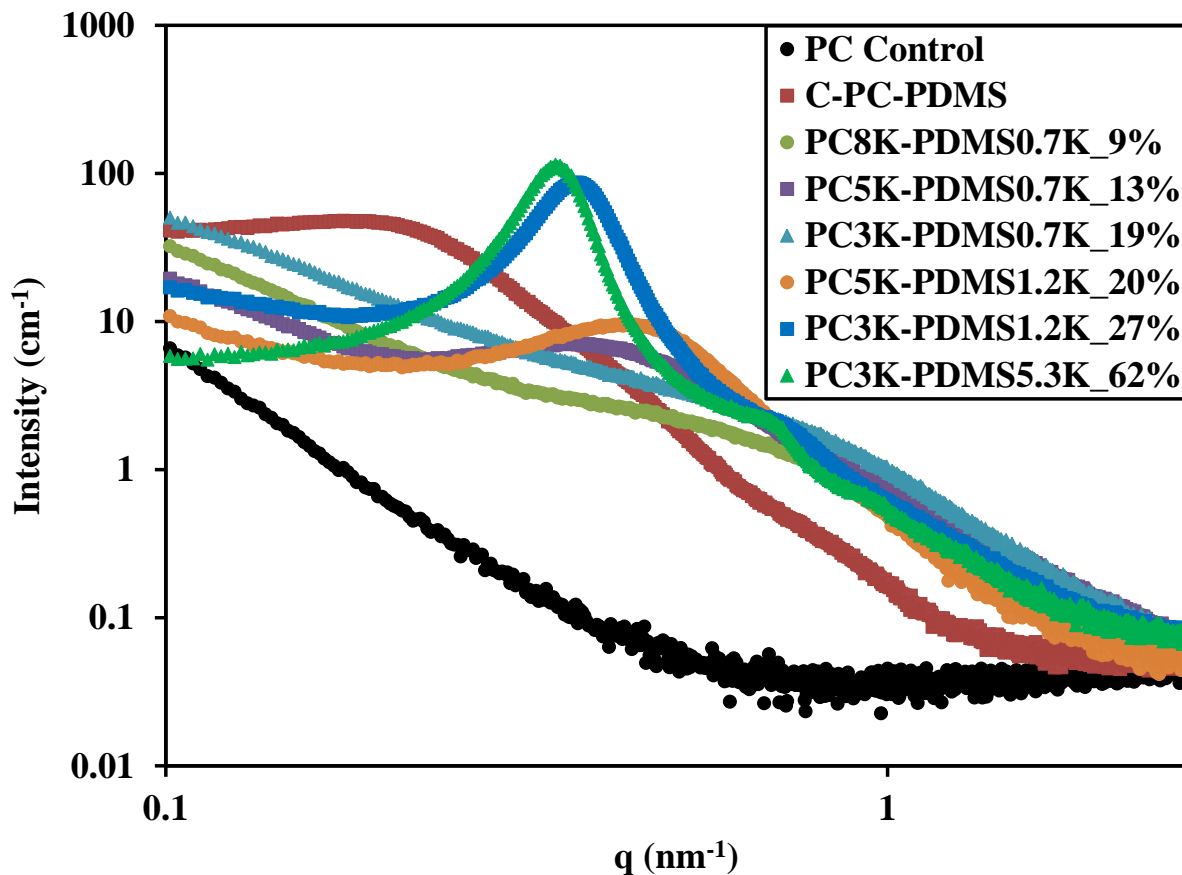


Figure 6.16. SAXS profiles of PC control, commercial PC-PDMS random copolymer, and synthesized block copolymers.

To determine the morphology of the block copolymers, it is essential to calculate the ratios of the q vector of scattering peaks. However, for most of the samples up to 27 % PDMS, it is difficult due to the limited number of peaks. The result is not accurate if given information is deficient. Take sample PC3K-PDMS1.2K_27% for example, only two peaks at q vectors ratio of ca. 1 : 2 could be observed. There are numerous possibilities of the morphology. Enough information could only be obtained from sample PC3K-PDMS5.3K_62%, of which the SAXS profile is shown in Figure 6.17. Four scattering peaks were captured even though low order reflections were detected for the later three peaks. Interestingly, the ratio of $q_1 : q_2 : q_3 : q_4$ is ca. 1 : 2 : 3 : 4, suggesting a predominantly lamellar morphology.

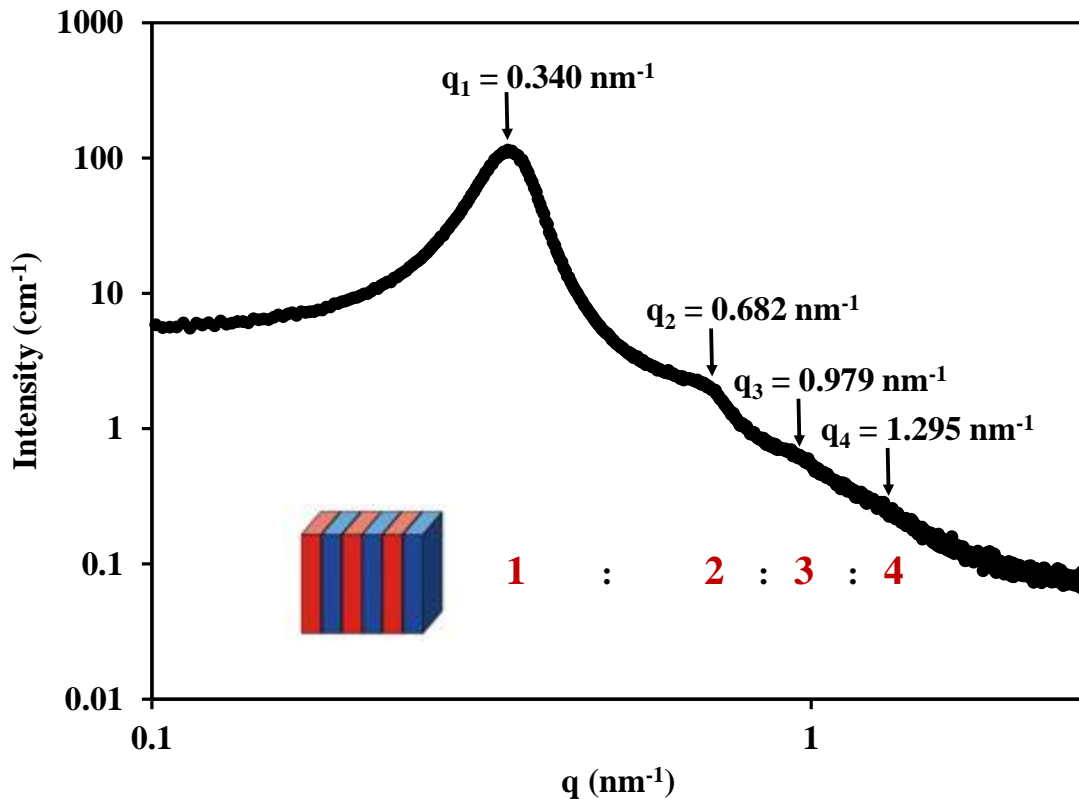


Figure 6.17. SAXS profile of PC3K-PDMS5.3K_62%.

Although the morphology could not be determined for the other samples with low content of PDMS, the interdomain spacing could be extracted from SAXS profile. The interdomain spacing is an important parameter in quantifying the domain size.¹⁹ The interdomian spacing d is related to peak scattering vector q_{max} in the following relationship.²⁰

$$d (nm) = \frac{2\pi}{q_{max}} \quad \text{Equation 6.1}$$

Results of the interdomain spacing d were calculated and listed in Table 6.3. Commercial PC-PDMS block copolymer showed a large interdomian spacing which is not indicative of the large domain size but because of the low content of PDMS and large spacing between small PDMS domains. Starting from 19 wt% PDMS content, as shown in Table 6.4, the interdomian

spacing increases with PDMS content. The d values here are related to the PDMS domain size.¹⁶ Longer PDMS blocks gave rise to larger interdomain spacing and larger domain size.

Table 6.4. Interdomian spacing d of block copolymers.

Block Copolymers	d (nm)
C-PC-PDMS	31.6
PC3K-PDMS0.7K_19%	8.4
PC5K-PDMS1.2K_20%	13.6
PC3K-PDMS1.2K_27%	17.0
PC3K-PDMS5.3K_62%	18.5

6.4.9. TEM

Figure 6.18 displays TEM images of commercial PC-PDMS random copolymers and the synthesized PC-PDMS block copolymers. Dark spherical PDMS domians can be observed in commercial copolymer containing 5 wt% PDMS. For synthesized block copolymer with 9 wt% PDMS, only one phase is observed, indicating the miscible two phases. This is consistent with MDSC result where only one T_g of PC-rich phase was observed and the T_g was significantly depressed compared with pure PC. With the increase of PDMS content, lamellar morphology was observed for samples containing 13 wt% and 19 wt% PDMS.

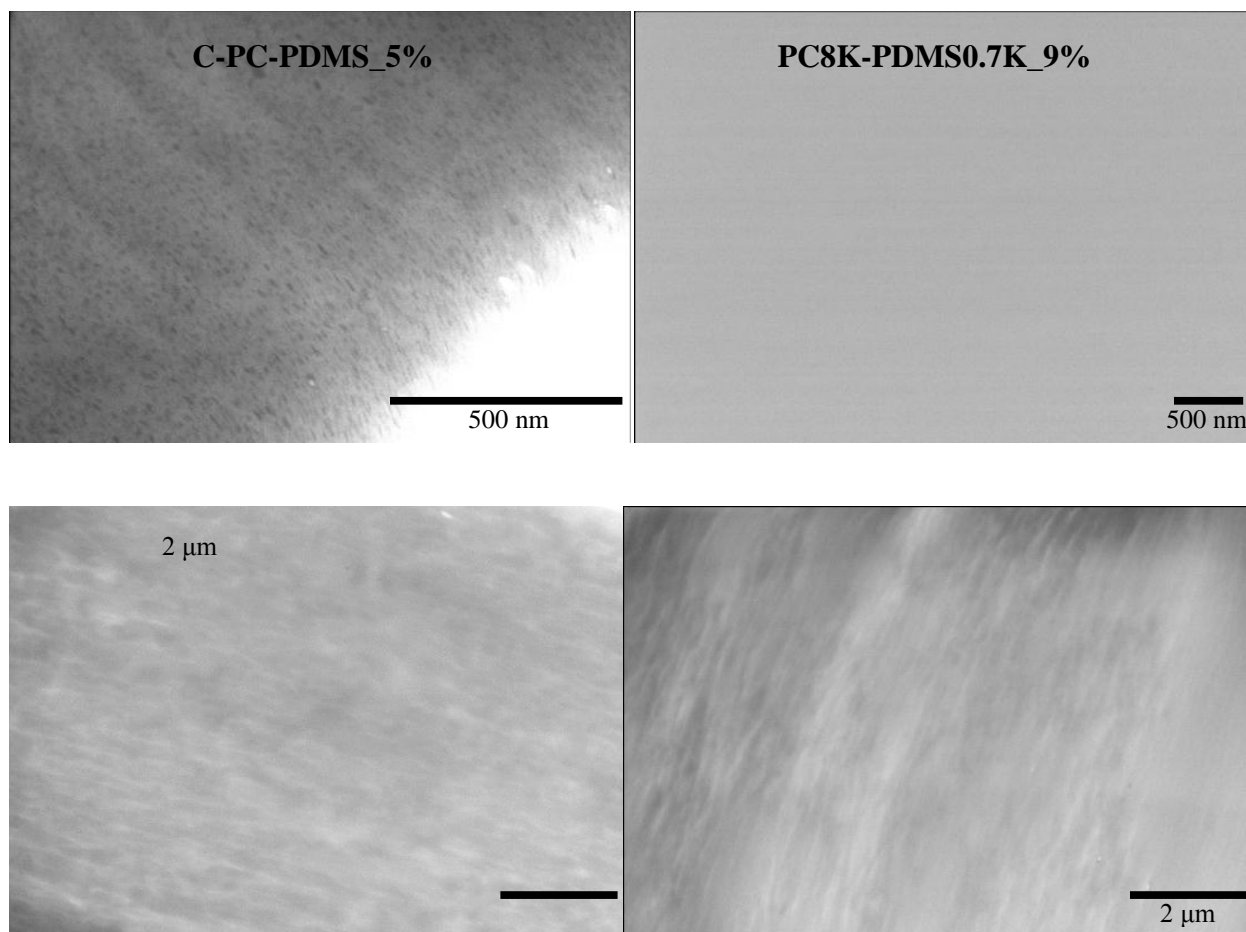


Figure 6.18. TEM images of commercial PC-PDMS random copolymer and synthesized PC-PDMS block copolymers.

6.4.10. Izod Impact Strength

The mechanical properties of PC-PDMS block copolymers are also dependent on both PDMS content and PDMS block length. The block copolymer could be either an elastomer when PDMS content is high and block length is short, or a hard thermoplastic when PDMS content is low and block length is long.²¹ Only the hard thermoplastic type block copolymers were tested here for Izod impact strength with the commercial pure PC and commercial PC-PDMS block copolymer for comparison. The results are shown in Figure 6.19. The commercial PC-PDMS block copolymer has a much better notch resistance than synthesized block copolymers, which is

attributed to the low PDMS content of only 5 wt%. It is interesting that with the same PDMS content between sample PC5K-PDMS0.7K_13% and PC8K-PDMS1.2K_13%, the latter sample gave rise to better notch resistance, which may due to the higher extent of chain entanglement resulted from higher molecular weight and longer PC and PDMS block length. Although the synthesized PC-PDMS block copolymers have the Izod impact strength only comparable to commercial pure PC, they are definitely more notch resistant than pure allyl-PCs because the oligomers even shatter with hands and were not able to be processed to molded samples.

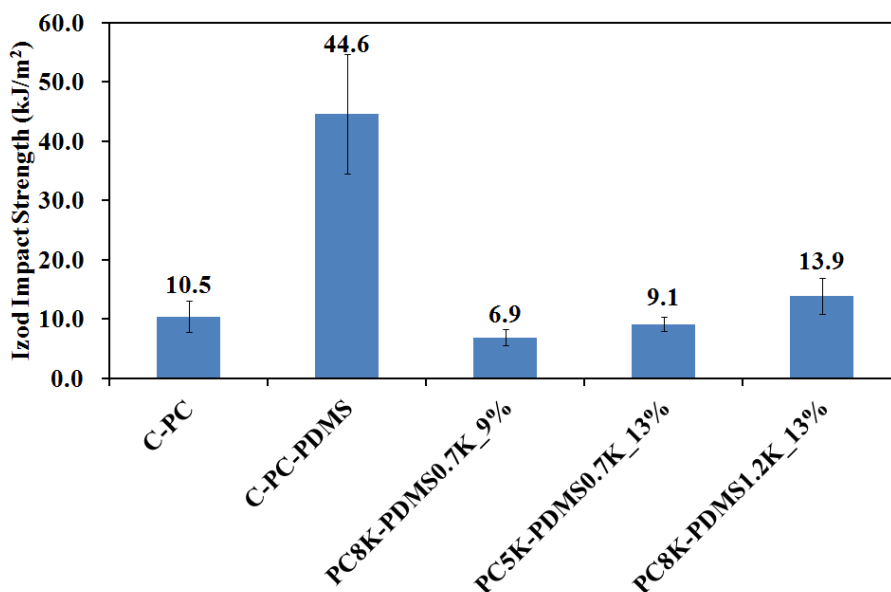


Figure 6.19. Izod impact strength of commercial pure PC from Dow (C-PC), commercial PC-PDMS block copolymer from Sabic (C-PD-PDMS), and three synthesized PC-PDMS block copolymers with relatively low PDMS content (PC8K-PDMS0.7K_9%, PC5K-PDMS0.7K_13%, PC8K-PDMS1.2K_13%).

6.5. Conclusion

Reaction conditions and parameters were optimized to get high molecular weight using low content of PtO₂. Perfectly alternating PC-PDMS block copolymers were successfully produced using the new synthetic method. With low levels of PtO₂, the catalyst removal is not

necessary in order to get high optical clarity. The PDMS segments are partially miscible with PC hard domains, leading to the decreased PC block glass transition temperature. Shorter PC and PDMS blocks tend to have better miscibility with each other. At PDMS content ranging from 27 – 62 wt%, phase inversion occurs for the homogeneous block copolymers. Surface segregation of PDMS segments was observed resulting in hydrophobic surface. Especially for long PDMS blocks the surface are almost covered by PDMS. Under air, the incorporation of PDMS blocks significantly increased the char yield and slowed down the thermal decomposition rate. The synthesized PC-PDMS block copolymers exhibited high optical clarity at up to 62 wt% PDMS content. As evident by SAXS, the lamellar morphology was confirmed. Nanophase separated morphology was observed by TEM and SAXS. The synthesized block copolymers have much better notch resistance than pure allyl-PCs.

6.6. References

1. Nicolas Sabourault, Ge´rard Mignani, Alain Wagner, and Charles Mioskowski, Platinum Oxide (PtO₂): A Potent Hydrosilylation Catalyst, *Organic Letters*, 4 (13), 2002, 2117-2119
2. Stephan Förster and Markus Antonietti, Amphiphilic Block Copolymers in Structure-Controlled Nanomaterial Hybrids, *Adv. Mater.* 10 (3), 1998, 195-217.
3. Dibakar Dhara, A. Purushotham, Niles Rosenquist, William D. Richards, Krishna Maruvada, Gautam Chatterjee, Physical Aging of Polycarbonate Block Copolymers: Ductility Rejuvenation below the Glass Transition Temperature, *POLYMER ENGINEERING AND SCIENCE*, 49(9), 2009, 1719-1726.

4. Masaya Okamoto, Relationship between the Composition of Polycarbonate Copolymers and the Refractive Index, *Journal of Applied Polymer Science*, 84, 2002, 514–521.
5. S.R Rabel, J.A Jona, M.B Maurin, Applications of modulated differential scanning calorimetry in preformulation studies, *Journal of Pharmaceutical and Biomedical Analysis*, 1999, 21 (2), 339–345
6. T. Dollase, H. W. Spiess, M. Gottlieb and R. Yerushalmi-Rozen, Crystallization of PDMS: The effect of physical and chemical crosslinks, *Europhys. Lett.*, 60 (3), 2002, 390–396.
7. Shumei Liu, Hua Ye, Yongsheng Zhou, Jihui He, Zhijie Jiang, Jianqing Zhao, Xianbo Huang, Study on flame-retardant mechanism of polycarbonate containing sulfonate-silsesquioxane-fluoro retardants by TGA and FTIR, *Polymer Degradation and Stability* 91, 2006, 1808-1814
8. G. Camino, S.M. Lomakin, M. Lazzari, Polydimethylsiloxane thermal degradation Part 1. Kinetic aspects, *Polymer* 42, 2001, 2395–2402
9. Akio Nodera, Toshitaka Kanai, Flame Retardancy of a Polycarbonate–Polydimethylsiloxane Block Copolymer: The Effect of the Dimethylsiloxane Block Size, *Journal of Applied Polymer Science*, 100, 2006, 565–575.
10. Akio Nodera, Toshitaka Kanai, Relationship Between Thermal Degradation Behavior and Flame Retardancy on Polycarbonate–Polydimethylsiloxane Block Copolymer, *Journal of Applied Polymer Science*, 102, 2006, 1697–1705.
11. S. Thomas and A George, *Eur. Polym. J.* 28, 1992, 145.

12. C. Bauwens-Crowet, J-C. Bauwens, Effect of thermal history on the tensile yield stress of polycarbonate in the β transition range, *Polymer*, 24 (7), 1983, 921–924
13. Xin Chen, Helen F. Lee, and Joseph A. Gardella, Jr. Effects of Structure and Annealing on the Surface Composition of Multiblock Copolymers of Bisphenol A Polycarbonate and Poly(dimethylsiloxane), *Macromolecules*, 26 (17), 1993, 4601-4605
14. Xin Chen and Joseph A. Gardella, Jr., Surface Modification of Polymers by Blending Siloxane Block Copolymers, *Macromolecules* 27, 1994, 3363-3369
15. Silicon-containing polymers: the science and technology of their synthesis and applications, Richard G. Jones, Wataru Ando, and Julian Chojnowski, Kluwer academic publishers, 2000
16. Ian W. Hamley, Valeria Castelletto, Small-angle scattering of block copolymers in the melt, solution and crystal states, *Prog. Polym. Sci.* 29, 2004, 909–948
17. Strobl, G. *The Physics of Polymers*; Springer: Berlin, 2007.
18. Huub A. M. van Aert, Laurent Nelissen, Piet J. Lemstra, Daniel J. Brunelle, Poly(bisphenol A carbonate)–poly(dimethylsiloxane) multiblock copolymers, *Polymer* 42, 2001, 1781–1788
19. S. D. Smith, J. M. DeSimone, H. Huang, G. York, D. W. Dwight, G. L. Wilkes, and J. E. McGrath, Synthesis and Characterization of Poly(methyl methacrylate)-g-poly(dimethylsiloxane) Copolymers. 1. Bulk and Surface Characterization, *Macromolecules* 25, 1992, 2575-2581

20. Taeyi Choi, Jadwiga Weksler, Ajay Padsalgikar, Rebeca Hernández, and James Runt, Polydimethylsiloxane-Based Polyurethanes: Phase-Separated Morphology and In Vitro Oxidative Biostability, *Aust. J. Chem.* 62, 2009, 794–798
21. M. Pixton, N. Moghe, S. Rajagopalan, and N. Rosenquist, ANTEC, 2655 (2006).
22. James E. Mark, *Polymer Data Handbook*, Oxford University Press, 2009.
23. M. I. Aranguren, “Crystallization of polydimethylsiloxane: effect of silica filler and curing,” *Polymer*, 39, 1998, 4897-4903.

CHAPTER 7. POLYCARBONATE-POLYHEDRAL OLIGOMERIC SILSESQUIOXANE (PC-POSS) THERMOSET COATINGS—THE EFFECT OF SOLVENT COMPOSITION AND CURING CONDITION

7.1. Abstract

Thermoset polycarbonate/polyhedral oligomeric silsesquioxane (PC-POSS) coatings with hydrophobic surfaces, enhanced thermal properties, and chemical resistance were prepared. A high purity allyl-PC was solution blended with OctaSilane-POSS® molecules, which possess eight silicon hydride groups per molecule. Crosslinking/curing was accomplished by the addition of Karstedt's catalyst which promotes hydrosilylation. The variables explored in the study were POSS content, solvent composition, and curing conditions. Coatings were characterized using water contact angle, atomic force microscopy (AFM), differential scanning calorimetry, and thermogravimetric analysis. The thermoset PC-POSS coatings showed higher glass transition temperature, higher char formation, and higher chemical resistance compared to pure PC. AFM topographical images of the coatings derived from CH₂Cl₂ as a solvent showed a nanoscopic distribution of POSS molecules at the coating/air interface, enabling the production of transparent, hydrophobic surfaces even at low POSS loadings

7.2. Introduction

Aromatic polycarbonates (PCs), one of the most important engineering thermoplastics available, possess a combination of various unique properties such as high impact resistance, transparency, dimensional stability, electrical resistance, and high glass transition temperature.¹⁻⁴ Synthesis of aromatic PCs by reacting hydroquinone or resorcinol with phosgene in pyridine was first reported by Einhorn in 1898.⁴ A few years later, Bischoff et al. reported the synthesis of

aromatic PCs using a transesterification process. However, due to difficulties in processing and characterization, no further development was achieved until 1953. In 1953, Schnell and Fox independently discovered Bisphenol-A PCs.⁵⁻⁷ Later, in 1958, the amine catalyzed interfacial process became the most common route for the production of commercial PCs.⁴ Currently, global commercial production of PC is over 3 million metric tons/year for various applications such as aircraft dials, bullet-proof windows, films, and electrical parts.^{8,9}

Despite PCs exceptionally good mechanical, optical, and thermal properties, it has poor chemical resistance.¹⁰⁻¹² Incorporation of PC into a three dimensional network structure by functionalization and subsequent crosslinking could improve its chemical resistance. Synthesis of aromatic PCs with reactive end groups has been described in the literature.^{10, 13-17} Seow et al. synthesized a series of COOH-functionalized PCs via ring-opening polymerization, which were conjugated with aliphatic amines to form amine-functionalized PCs for gene therapy.¹⁵ Marks et al. reported the synthesis of a series of PCs with p-t-butylphenol as the nonreactive end group and 4-hydroxybenzocyclobutene, methacrylate, and m-ethynylphenol as reactive end groups.^{16, 17} The reactive end groups were heat activated to produce crosslinked or long-chain-branched PCs. Improvements in melt strength and melt elasticity were achieved with branched-PCs compared to linear PCs. Synthesis of vinylphenylcarbonate-terminated PCs and their thermal curing to form crosslinked polycarbonate networks was reported by Knauss et al.^{10, 11} Adelman et al.¹⁸ and Stix et al.¹⁹ described the use of a chain stopper possessing a terminal double bond and conjugated double bonds, respectively, to synthesize functional PCs by interfacial polymerization with phosgene. Use of 4-allyl-2-methoxyphenol (eugenol) as a chain stopper to prepare allyl-functional PCs (allyl-PCs) was reported by Kim, et al.²⁰ Phosgene was used as the

carbonate source in making these polymers. However, detailed structural analysis in order to confirm the absence of cyclic structures and effective end capping were not performed.

Polyhedral oligomeric silsesquioxane (POSS) molecules with a unique cage-like structure and nanoscale dimensions (1-3 nm in diameter) have been widely used to produce novel polymer nanocomposites to enhance thermal, mechanical, and rheological properties of the polymer matrices.²¹⁻²⁶ The reinforcement is provided by the rigid silica core of the POSS molecule while the organic functional groups provide compatibility with the matrix polymer. If the organic functional groups have reactive functionalities, they can be incorporated into a polymer matrix by covalent bonding. In the case of non-reactive functionalities, incorporation of POSS molecules into a polymer matrix can be achieved by non-covalent interactions such as dipole-dipole, hydrogen bonding, and π - π interactions. The effects of the incorporation of POSS into a PC matrix to produce PC-POSS nanocomposites have been investigated using solution- and melt-blending processes.²⁷⁻³⁰ For octaphenyl-POSS, good dispersion was achieved up to 5 wt% incorporation in PC. Above this level of octaphenyl-POSS, micron-sized aggregates of octaphenyl-POSS was observed.²⁷ When trisilanolphenyl-POSS was used, slight enhancements in tensile and storage modulus were reported with increasing POSS content, but ductility was reduced.²⁹ The lack of conformational flexibility of the phenyl rings of PC was thought to prevent preferential π - π interactions with phenyl-substituted POSS molecules, resulting in limited compatibility. Iyer et al. reported a significant decrease in glass transition temperature at higher levels of trisilanolphenyl-POSS due to plasticization of the PC matrix by the POSS molecules.³⁰ Interestingly, incorporation of trisilanolphenyl-POSS into phenoxy resin, which, compared to PC, possesses 2-hydroxypropyl groups instead of carbonate groups, resulted in

enhanced thermomechanical properties suggesting the formation of specific interactions between the trisilanolphenyl-POSS and the phenoxy resin matrix.³⁰

Covalent bonding between POSS and PC was thought to be a potential route to improving compatibility and thereby preventing gross phase separation. In addition, the formation of covalent bonding between PC and POSS would provide solvent resistance enabling new applications for PC. This chapter describes the use of allyl-PCs in the production of thermoset PC-POSS materials. These novel thermoset PC-POSS nanocomposites were expected to be useful as protective coatings over different substrates including PC.

7.3. Experimental

7.3.1. Raw Materials

Highly pure allyl-PC with a molecular weight (M_n) of 5,000 g/mol (determined by 1H -NMR) was synthesized using the process described in Chapter 5. Platinum (0)-1,3-divinyl-1,1,3,3-tetramethyl disiloxane complex (Karstedt's catalyst) and 1,1,2,2-tetrachloroethane (TCE) were obtained from Aldrich. OctaSilane-POSS® was obtained from Hybrid Plastics. The TCE was dried with molecular sieves activated at 300 °C. All other reagents were used as received.

7.3.2. Preparation of PC-POSS Thermoset Coatings

Thermoset PC-POSS coatings were prepared by reacting the allyl-PC with OctaSilane-POSS® in the presence of Karstedt's catalyst. Stock solutions of 10 wt % allyl-PC and 2.0 wt % OctaSilane-POSS® were individually prepared in two different solvents, CH_2Cl_2 and TCE, respectively. Table 7.1 describes the compositions and curing conditions of the coatings prepared. Coating solutions were prepared by combining, in an 8 ml vial, the allyl-PC stock solution and 2.0 μ L of Karstedt's catalyst and the mixture magnetically stirred for 5 minutes

before adding the OctaSilane-POSS® solution. After adding the OctaSilane-POSS® solution, the mixture was mixed well for 30 seconds using a vortex mixer and then 1.0 mL of the coating solution was deposited over a 2.54 cm X 7.62 cm glass slide using a pipette and subsequently cured to form a thermoset coating.

Table 7.1. Compositions of the thermoset PC-POSS coatings produced. Each mixture contained 1.0 g of 10 wt% solution of allyl-PC B8 (0.02 mmol) from Table 2 in either CH₂Cl₂ or TCE. The POSS solution was a 2 wt% solution of POSS in either CH₂Cl₂ or TCE. Amount of Karstedt's catalyst was 2.0 µL for each formulation.

Coating *	SiH:Vinyl	POSS solution (g)	POSS content		Solvent	Curing condition
			mmol	wt%		
PC-Control	---	0.00	0.00	0.00	CH ₂ Cl ₂	RT
PC-POSS(2.53)-S1-C1	0.5 : 1.0	0.56	0.01	2.53	CH ₂ Cl ₂	RT
PC-POSS(5.06)-S1-C1	1.0 : 1.0	1.12	0.02	5.06	CH ₂ Cl ₂	RT
PC-POSS(7.13)-S1-C1	1.5 : 1.0	1.68	0.03	7.13	CH ₂ Cl ₂	RT
PC-POSS(9.24)-S1-C1	2.0 : 1.0	2.24	0.04	9.24	CH ₂ Cl ₂	RT
PC-POSS(11.32)-S1-C1	2.5 : 1.0	2.80	0.05	11.32	CH ₂ Cl ₂	RT
PC-POSS(13.24)-S1-C1	3.0 : 1.0	3.35	0.06	13.24	CH ₂ Cl ₂	RT
PC-POSS(2.53)-S2-C1	0.5 : 1.0	0.56	0.01	2.53	TCE	RT
PC-POSS(5.06)-S2-C1	1.0 : 1.0	1.12	0.02	5.06	TCE	RT
PC-POSS(7.13)-S2-C1	1.5 : 1.0	1.68	0.03	7.13	TCE	RT
PC-POSS(9.24)-S2-C1	2.0 : 1.0	2.24	0.04	9.24	TCE	RT
PC-POSS(11.32)-S2-C1	2.5 : 1.0	2.80	0.05	11.32	TCE	RT
PC-POSS(13.24)-S2-C1	3.0 : 1.0	3.35	0.06	13.24	TCE	RT

Table 7.1. (continued)

Coating *	SiH:Vinyl	POSS solution (g)	POSS content		Solvent	Curing condition
			mmol	wt%		
PC-POSS(2.53)-S1-C2	0.5 : 1.0	0.56	0.01	2.53	CH ₂ Cl ₂	RT+120
PC-POSS(5.06)-S1-C2	1.0 : 1.0	1.12	0.02	5.06	CH ₂ Cl ₂	RT+120
PC-POSS(7.13)-S1-C2	1.5 : 1.0	1.68	0.03	7.13	CH ₂ Cl ₂	RT+120
PC-POSS(9.24)-S1-C2	2.0 : 1.0	2.24	0.04	9.24	CH ₂ Cl ₂	RT+120
PC-POSS(11.32)-S1-C2	2.5 : 1.0	2.80	0.05	11.32	CH ₂ Cl ₂	RT+120
PC-POSS(13.24)-S1-C2	3.0 : 1.0	3.35	0.06	13.24	CH ₂ Cl ₂	RT+120
PC-POSS(2.53)-S2-C2	0.5 : 1.0	0.56	0.01	2.53	TCE	RT+120
PC-POSS(5.06)-S2-C2	1.0 : 1.0	1.12	0.02	5.06	TCE	RT+120
PC-POSS(7.13)-S2-C2	1.5 : 1.0	1.68	0.03	7.13	TCE	RT+120
PC-POSS(9.24)-S2-C2	2.0 : 1.0	2.24	0.04	9.24	TCE	RT+120
PC-POSS(11.32)-S2-C2	2.5 : 1.0	2.80	0.05	11.32	TCE	RT+120
PC-POSS(13.24)-S2-C2	3.0 : 1.0	3.35	0.06	13.24	TCE	RT+120

* S1 = solvent CH₂Cl₂, S2 = solvent TCE, C1 = solvent flash and curing at ambient conditions (RT), and C2 = a 15 minute solvent flash followed by curing at 120 °C for 1 hour (RT+120)

7.3.3. Instrumentation

Water contact angle measurements on the coatings were carried out using an automated surface energy measurement unit manufactured by Symyx Discovery Tools, Inc. and First Ten Angstroms.^{31,32} Three measurements were taken on each coating using the sessile drop method and the data reported as the average and standard deviation.

Atomic force microscopy (AFM) studies were performed in tapping mode using a Dimension 3100® microscope with a Nanoscope IIIa controller from Veeco Incorporated. Topographical images were collected in air, at room temperature, using a single-lever silicon probe from Nanosensors™. Cantilever length, width, and thickness of the silicon probe were $225 \pm 10 \mu\text{m}$, $25 \pm 7.5 \mu\text{m}$, and $3.0 \pm 1.0 \mu\text{m}$, respectively. The spring constant was 0.5-9.5 N/m with a resonant frequency 75 kHz. The set point ratio was 0.8-0.9.

Differential scanning calorimetry (DSC) experiments were carried out using a DSC Q1000 from TA instruments equipped with an auto sampler. About 5.0 mg of sample were measured. The experiments were conducted using a heat-cool-heat cycle extending from +25 °C to +200 °C at a heating/cooling rate of 10°C/min. Thermal gravimetric analysis (TGA) was carried using a TGA Q500 thermal analyzer under a nitrogen atmosphere in the temperature range of +25 °C to +800 °C at a heating rate of 20 °C/min, purged with N₂ at 50ml/min.

The solvent-swelling test to evaluate chemical resistance of the thermoset POSS-PC coatings was carried out following the method described by Nakamura and Ishida.³³ A rectangular sample with length of 15 mm and width of 5 mm was immersed in CH₂Cl₂ at room temperature for 10 min. After removing from the solvent, the length, L_x (mm), of the immersed sample was measured. The degree of swelling was calculated using the following equation:

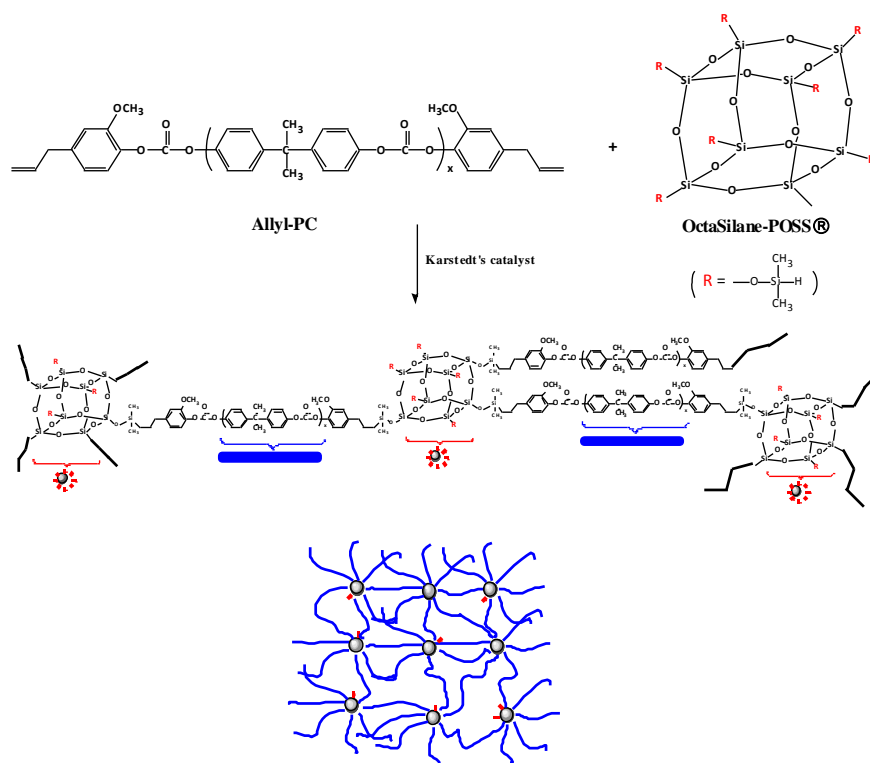
$$\text{The degree of swelling (\%)} = [(L_x - 15)/15] \times 100 \quad \text{Equation 7.1}$$

Three samples were tested for each coating composition. Average degree of swelling and standard deviation was reported.

7.4. Results and Discussion

7.4.1. Preparation of PC-POSS Thermoset Coatings

Scheme 7.1 illustrates the process that was used to produce the nanocomposite coatings. The process consisted of solution blending an allyl-PC with OctaSilane POSS® and Karstedt's catalyst. With this process, crosslinking and incorporation of POSS molecules into the PC matrix occurs via hydrosilylation reactions. OctaSilane-POSS® was chosen for the study because the eight Si-H groups of OctaSilane-POSS® are a siloxane unit away from the inorganic cage as compared to OctaHydro-POSS® ($H_8O_2Si_8$) which was expected to reduce issues of steric hindrance with respect to hydrosilylation with allyl-PC.^{34,35}



Scheme 7.1. A schematic illustrating the formation of crosslinked network involving allyl-PC and OctaSilane-POSS® to produce thermoset PC-POSS coating.

The variables investigated for the study were POSS content, solvent composition, and curing conditions. POSS content was varied from 2.53 wt % to 13.24 wt % by changing Si-H:vinyl ratio from 0.5:1.0 to 3.0:1.0. The two solvents used for the investigation were CH₂Cl₂ and TCE. They are both good solvents for allyl-PC and OctaSilane-POSS®, however, their volatilities differ substantially. At 20 °C, CH₂Cl₂ has a vapor pressure of 352.2 mm of Hg, while TCE has a vapor pressure of only 8.0 mm of Hg. Curing was done using two different methods. One of the methods simply consisted of solvent flash and curing at ambient conditions, while the other method consisted of a 15 minute solvent flash followed by curing at 120 °C for 1 hour. Figure 7.1 displays a schematic of the experimental design used for the investigation.

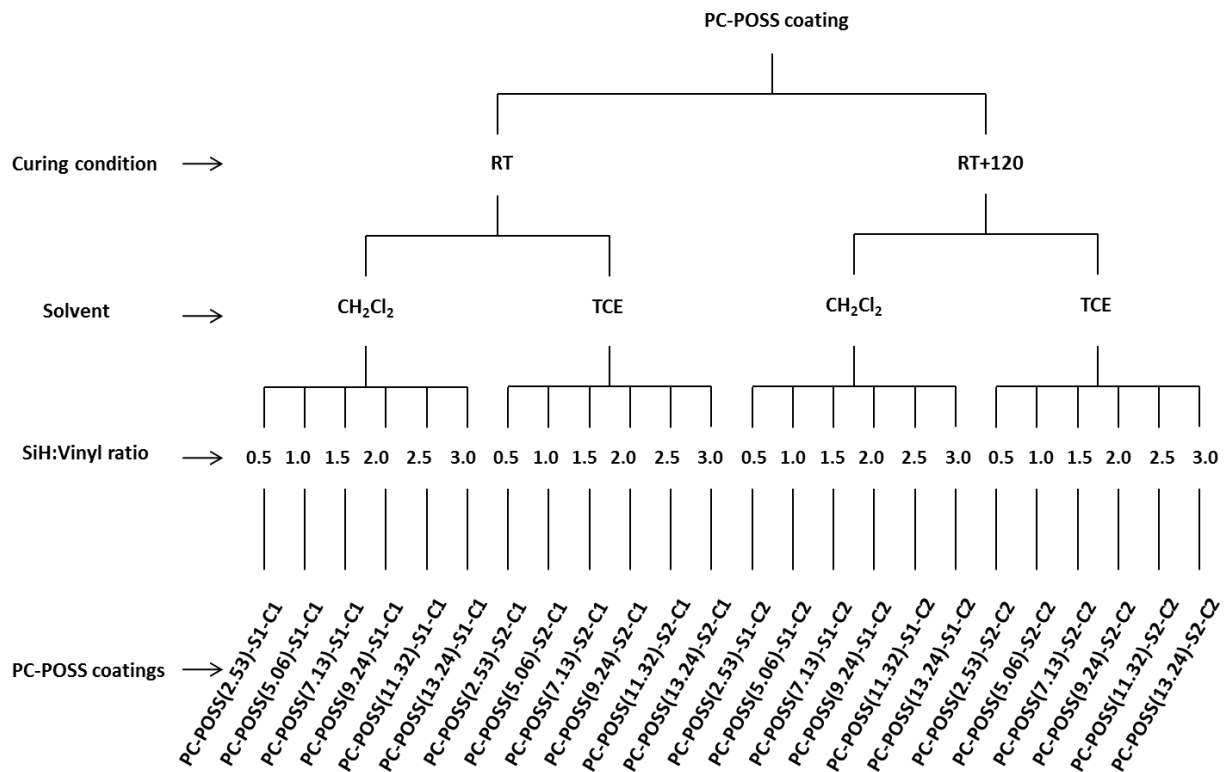


Figure 7.1. A schematic illustration of the experimental design used for coating formulations. RT is solvent flash and curing at ambient conditions, and RT+120 is a 15 minute solvent flash followed by curing at 120 °C for 1 hour.

The incompatibility between POSS molecules and PC even at 2.5 wt % loading, when prepared by physical blending, has been reported by Zhao et al.²⁷ The nanocomposites prepared by these investigators were translucent or opaque indicating gross phase separation. In contrast, for the thermoset nanocomposites prepared as a part of this study, the PC-POSS nanocomposite coatings were transparent up to ~11 wt % POSS. This result indicates that covalently bonding POSS molecules to the PC matrix greatly inhibits gross phase separation. To illustrate, two PC-POSS blends were prepared and cast onto glass slides. The two blends were identical with the exception that only one of the blends received the Karstedt's catalyst required for hydrosilylation to occur. Figure 7.2 displays images of the coated glass slides. The coating produced without the Karstedt's catalyst was highly opaque while the crosslinked coating was completely transparent, thereby illustrating the utility of covalent bonding between the two components to prevent large-scale phase separation upon solvent evaporation.

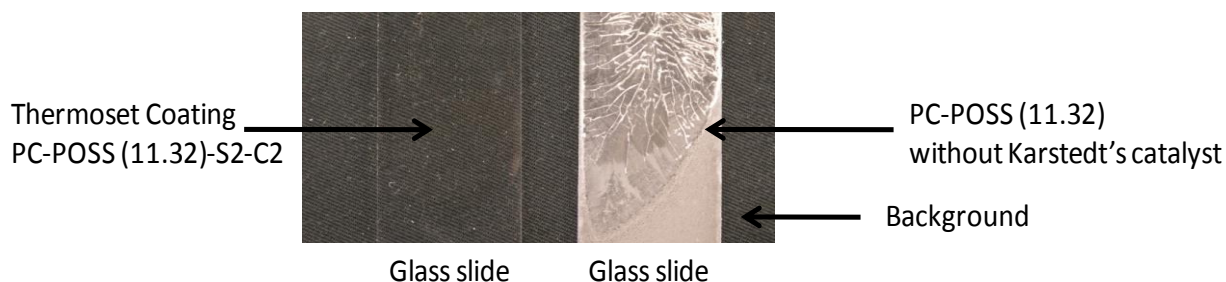


Figure 7.2. Images illustrating transparent, thermoset PC-POSS coating (left); and opaque, non-crosslinked PC-POSS coating from solution blend (right) over glass slide after applying identical curing condition.

7.4.2. Surface Properties

Figure 7.3 displays water contact angle data for the PC-POSS coatings as a function of the variables investigated. The water contact angle for a film of pure allyl-PC was 89.5 °. Interestingly, solvent composition was found have a major effect on water contact angle. The

thermoset PC-POSS coatings derived from CH_2Cl_2 were more hydrophobic than pure allyl-PC as well as analogous coatings derived from TCE as the solvent. The increase in hydrophobicity observed for the coatings based on CH_2Cl_2 as the solvent suggested greater surface segregation of hydrophobic POSS molecules to coating/air interface.

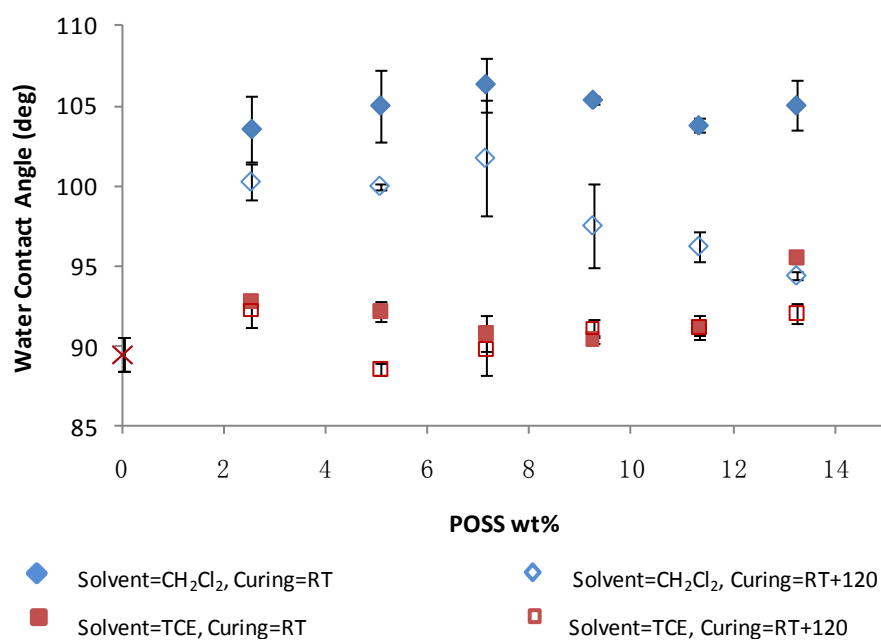


Figure 7.3. Water contact angle data of PC-POSS coatings.

This result may be due to the difference in volatility between CH_2Cl_2 and TCE. It would be expected that the lower volatility solvent (i.e. TCE) would allow for greater extents of hydrosilylation to occur before the majority of the solvent is vaporized and the coating becomes vitrified. The higher extent of hydrosilylation would inhibit diffusion of POSS molecules to the coating/air interface because more POSS molecules would be covalently bound to the PC matrix. In contrast, the higher volatility of CH_2Cl_2 allows less time for hydrosilylation reactions during film formation enabling more POSS molecules to diffuse to the coating/air interface. With regard to the effect of cure conditions, no significant influence of cure conditions on water contact was observed for the coatings based on TCE as the solvent. In contrast, the water contact angles

obtained for the coatings based on CH_2Cl_2 as the solvent were systematically lower when curing was done using the two-step process (i.e. 15 minute flash at ambient conditions followed by 1 hour at 120 °C) than those same coatings cured at ambient conditions. Consistent with the discussion used to explain the variations in water contact angle observed as a function of solvent composition, the lower water contact angles obtained using the two-step cure most likely resulted from higher extents of hydrosilylation resulting from the 120 °C heat treatment which effectively inhibited migration of POSS molecules to the coating/air interface.

In order to understand the trends observed for water contact angle data, AFM was used to characterize coating surface topography. The AFM images displayed in Figure 7.4 were all obtained from coatings produced using CH_2Cl_2 as a solvent and cured at ambient conditions. As expected, a homogeneously smooth surface morphology was obtained for the pure PC coating. Nanoscale surface roughness increased with increasing POSS content indicating the presence of POSS molecules at the coating/air interface which is consistent with the water contact angle data.^{36,37} The AFM images displayed in Figure 7.5 show the affects of solvent composition and curing conditions on surface topography. Most of the coatings derived from TCE as the solvent possessed a homogeneously smooth surface topography indicating a relative lack of POSS molecules at the coating/air interface which is consistent with the water contact data. However, as shown in Figure 7.5 (d), at the relatively high POSS content of 11.32 wt % the coating based on TCE and cured at ambient conditions showed larger scale surface features which suggest the formation of POSS agglomerates at the coating/air interface. The analogous coating cured using the elevated temperature cure (Figure 7.5 (h)), was smooth suggesting that the high temperature “locks” the POSS molecules in the PC matrix via hydrosilylation before they can migrate to the coating/air interface.

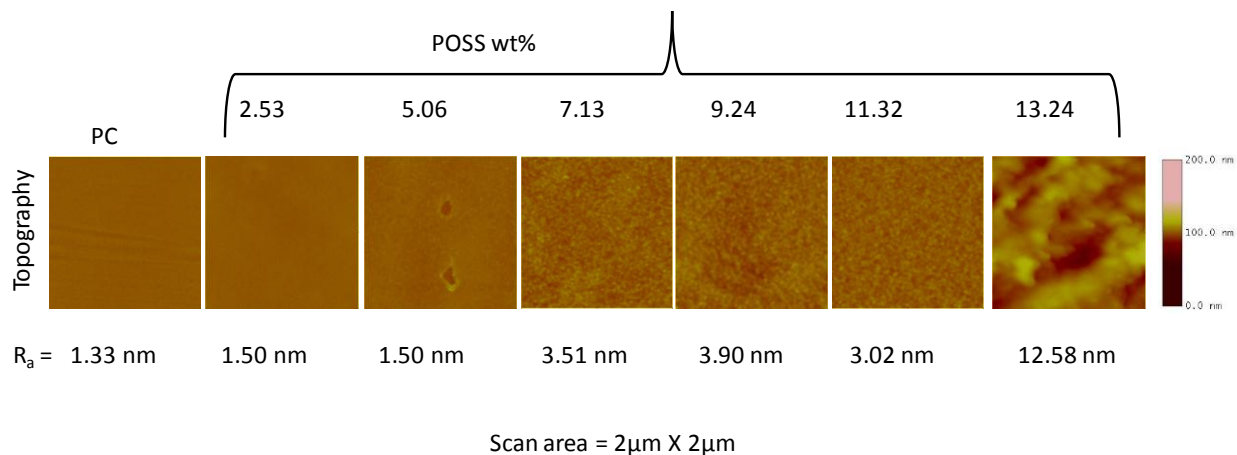


Figure 7.4. AFM images of PC-POSS coatings as a function of POSS wt %. R_a is mean roughness.

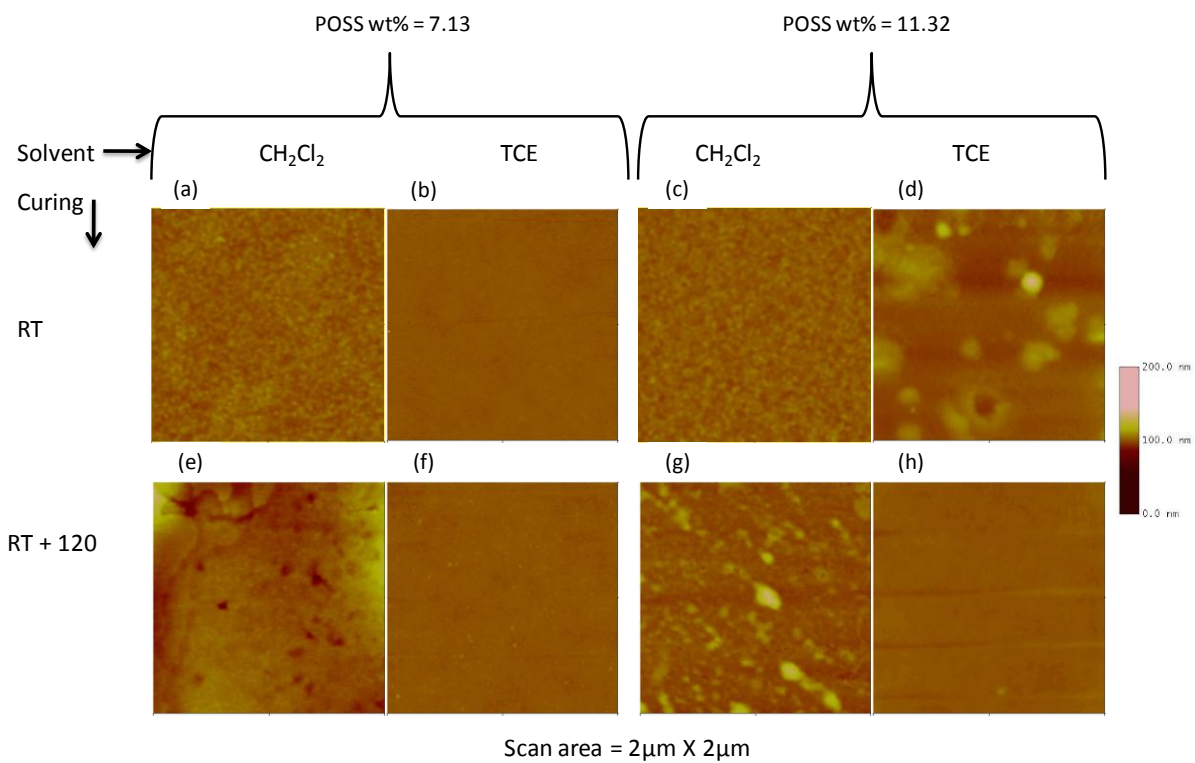


Figure 7.5. AFM images of PC-POSS coatings illustrating the effects of solvent compositions and curing conditions on surface topography.

7.4.3. Thermal Properties

The thermal properties of PC-POSS coatings were characterized using DSC and TGA. Figure 7.6 displays the glass transition temperature (T_g) of the coatings as a function of the variables of interest. Zhao et al. have reported that POSS molecules as viscous fluid or as crystalline solid, when blended with PC matrix, could act as a plasticizer by decreasing the packing density of the polymer matrix around the POSS molecules.²⁷ As a result, polymer free volume increased which decreased the T_g values. However, in this study, a sharp increase in T_g values were observed with POSS containing coatings. This was due to the incorporation of rigid POSS molecules into the three dimensional network structures by crosslinking. The T_g values of the coatings produced using CH_2Cl_2 as a solvent and cured at ambient conditions passed through a maximum at 7.13 wt % of POSS content which corresponds to Si-H:vinyl ratio 1.5:1.0. This indicates that maximum crosslinking was achieved with slight excess of Si-H concentrations when the coatings were cured under ambient conditions. At a higher POSS content (> 9.0 wt %), un-reacted residual POSS molecules could plasticized the matrix resulted in a drop in T_g values. The DSC curves of the second heat cycle of this series are shown in Figure 7.7 for illustration purpose. With accelerated curing, the drop in T_g values above 7.13 wt % of POSS content was insignificant for the coatings produced using CH_2Cl_2 as a solvent. This might be a result of additional crosslinking during accelerated curing which prevented the plasticization effects of POSS molecules. With TCE, slow evaporation of the solvent at ambient conditions allowed completion of crosslinked network structure formation. Hence, accelerated curing did not have a dramatic effect on T_g values at higher POSS content.

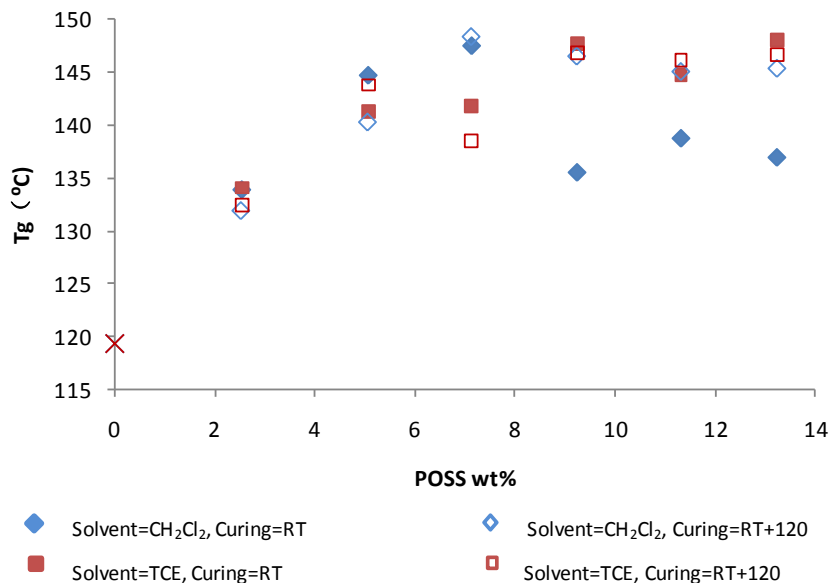


Figure 7.6. Tg values of PC-POSS coatings.

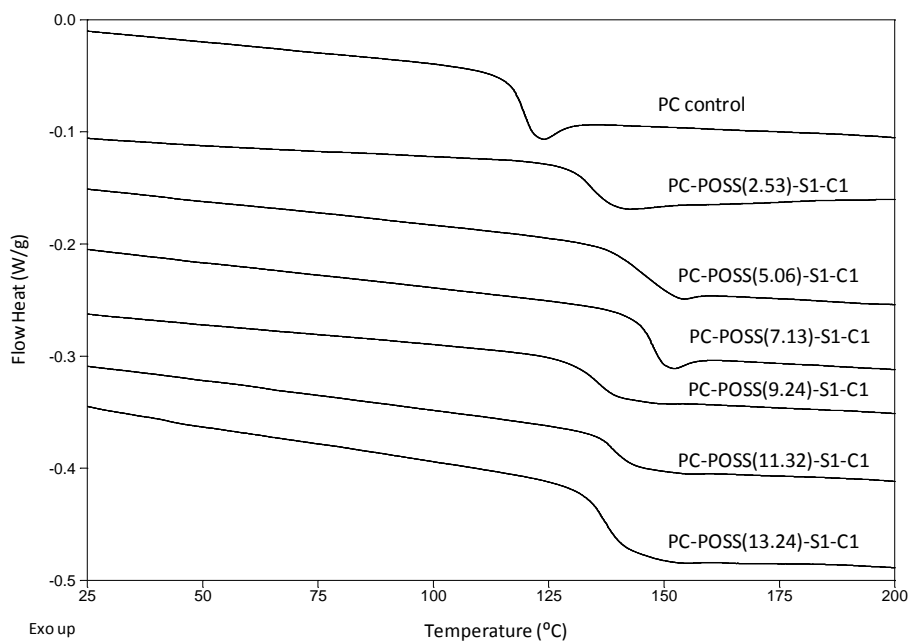


Figure 7.7. DSC overlay of second heating cycle of PC-POSS coatings derived from CH₂Cl₂ as a solvent and cured at ambient conditions.

The influence of POSS molecules on thermal degradation of coatings was evaluated using TGA. Coating compositions derived from CH₂Cl₂ as a solvent and cured at ambient

conditions were compared. Table 7.2 displays the results of onset of degradation temperature i.e. the temperature of 5 wt % weight loss ($T_{-5\%}$), temperature of maximum weight loss rate (T_{\max}), and the fraction of the char residue. The $T_{-5\%}$ and T_{\max} for pure PC was 431 and 525 °C, respectively. With incorporation of POSS molecules, a significant increase in both $T_{-5\%}$ and T_{\max} was observed only with highest POSS content coating. The lack of enhancement in thermal stability with PC-POSS coatings might be due to complex degradation behavior of the PC which includes hydrolysis/alcoholysis of carbonate linkages, chain scission of isopropylidene linkages, branching, and crosslinking at higher temperature.³⁸⁻⁴⁰ The siloxane units attached with POSS molecules could degrade below 500 °C and overall thermal stability of PC-POSS coatings decreased. Later, POSS converted to molecular silica and produced char residue. However, the amount of char was considerably higher in PC-POSS coatings (up to 30.0 wt %) compared to the pure PC (1.7 wt %) and also higher compared to the wt % of POSS in the coatings.

Table 7.2. TGA data in N₂ of PC-POSS coatings derived from CH₂Cl₂ as a solvent and cured at RT.

Coating	T_{-5wt%} (°C)	T_{max} (°C)	Char Residual (wt%)
PC-Control	431.17	524.77	1.68
PC-POSS(2.53)-S1-C1	420.83	520.58	11.60
PC-POSS(5.06)-S1-C1	429.88	525.03	18.37
PC-POSS(7.13)-S1-C1	436.51	525.93	22.77
PC-POSS(9.24)-S1-C1	406.82	507.64	31.42
PC-POSS(11.32)-S1-C1	450.99	523.29	25.62
PC-POSS(13.24)-S1-C1	452.53	533.47	27.04

7.4.4. Chemical Resistance

One of the primary disadvantages associated with the use PC in many applications is its' poor solvent resistance. PC is readily soluble in several common solvents especially chlorinated solvents such as CH_2Cl_2 , TCE, and chloroform, and subjection of PC to a wide variety of chemicals can cause stress cracking of PC. Since crosslinking prevents solubilization and the degree of swelling resulting from immersion of a crosslinked sample in a solvent of interest is related to the degree of crosslinking, it was of interest to conduct solvent swelling experiments. Figure 7.8 displays the effect of POSS content on the degree of swelling for films cast from CH_2Cl_2 and cured at ambient conditions. The swelling solvent used was CH_2Cl_2 . The swelling values passed through a minimum at approximately 7.0 wt % POSS, indicating that this optimum POSS content provides maximum crosslink density. This is consistent with the T_g values obtained from DSC which passed through a maximum at approximately 7.0 wt % POSS for this series of coatings.

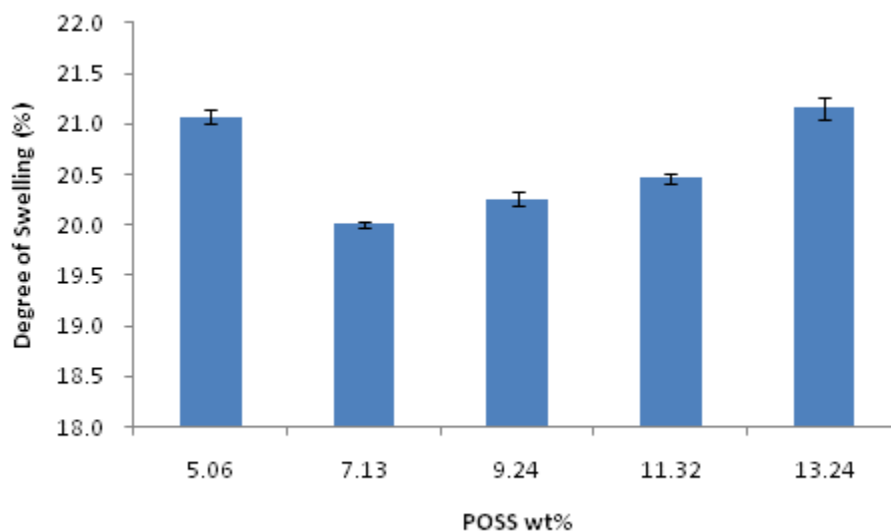


Figure 7.8. Degree of swelling of thermoset PC-POSS coatings derived from CH_2Cl_2 as a solvent and cured at ambient conditions. Error bars represent one standard deviation.

Figure 7.9 shows the effect of cure conditions on solvent swelling. Although the trend between solvent swelling and POSS content was the same as that observed for films cured at ambient conditions, films cured using a 15 minute solvent flash followed by curing at 120 °C for one hour consistently showed lower solvent swelling. This result indicates that curing at ambient conditions does not result in a fully crosslinked network. The thermal treatment at 120 °C for one hour drives a higher extent of cure.

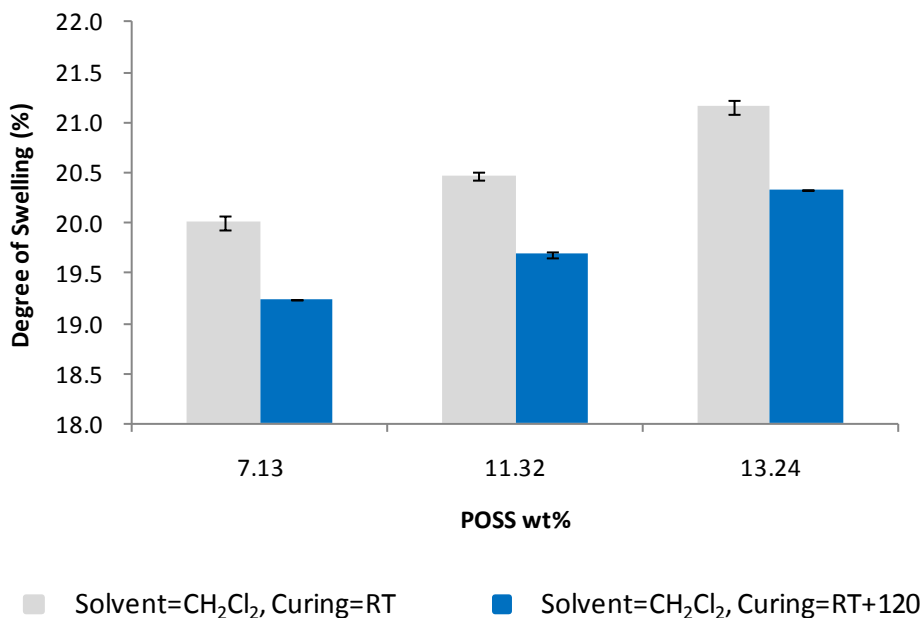


Figure 7.9. Degree of swelling in CH₂Cl₂ values illustrating the effects of curing conditions. Error bars represent one standard deviation.

7.5. Conclusion

A highly pure allyl-PC was used to produce a series of thermoset PC-POSS coatings using hydrosilylation as the crosslinking reaction. The effects of POSS content, solvent composition, and curing conditions were investigated in detail. Water contact angle data and AFM topographical images showed that the distribution of POSS molecules in the coating was highly dependent on solvent composition and cure conditions. Use of the more volatile solvent,

CH₂Cl₂, resulted in higher water contact angles and nanoscale surface roughness indicative of greater segregation of POSS molecules to the coating/air interface. In addition, curing at 120 °C as opposed to room temperature reduced water contact angles and nanoscale surface roughness. These results were explained in terms of the relative rates of hydrosilylation and solvent evaporation. The allyl-PC and POSS are incompatible and as solvent is evaporated there is a thermodynamic driving force for phase separation and migration of the lower surface energy POSS molecules to the coating/air interface. Use of the more slowly evaporating solvent (i.e. TCE) and the higher cure temperature enable higher extents of hydrosilylation to occur before the solvent is largely gone which largely inhibits phase separation and surface migration by covalent attachment of the POSS molecules to the PC matrix.

Thermal analysis of the coatings showed significant increases in PC T_g as a result of crosslinking with POSS. In addition, the nanocomposite films showed major increases in char after thermal decomposition compared to the pure allyl-PC. At the higher POSS contents, the amount of char was close to 30 wt % which is much higher than the 1.7 wt % obtained for pure allyl-PC. With regard to chemical resistance, an optimum POSS content of approximately 7.0 wt % was found that minimized solvent swelling. This result indicated that this POSS level enabled the high crosslink density at a given cure condition.

7.6. References

1. Sweileh, BA, Al-Hiari, YM, "Synthesis and Thermal Properties of Polycarbonates Based on Bisphenol A by Single-phase Organic Solvent Polymerization." *J. Polym. Res.*, 13 (3), 2006, 181-191.

2. Marks, MJ, "Interfacial synthesis and characterization of random and segmented block bisphenol A-tetrabromobisphenol A copolycarbonates." *J. Appl. Polym. Sci.*, 52 (4) 1994, 467-81.
3. Kosky, PG, Silva, JM, Guggenheim, EA, "The aqueous phase in the interfacial synthesis of polycarbonates. Part 1. Ionic equilibria and experimental solubilities in the BPA-sodium hydroxide-water system." *Ind. Eng. Chem. Res.*, 30 (3) 1991, 462-7
4. Brunelle, DJ, Smigelski, PM, Jr., Boden, EP, "Evolution of polycarbonate process technologies." *ACS Symp. Ser.*, 898 (Advances in Polycarbonates) 2005, 8-21.
5. Schnell, H, "Polycarbonates, a group of new types of thermoplasts-preparation and properties of aromatic polyesters of carbonic acid." *Angew. Chem.*, 68, 1956, 633-40
6. Schnell, H, "Linear aromatic polyesters of carbonic acid." *J. Ind. Eng. Chem. (Washington, D. C.)*, 51, 1959, 157-60
7. Fox, DW, "Linear aromatic polycarbonates." US Patent 314432, 1964.
8. Serini, V, *Polycarbonates*. Wiley-VCH Verlag GmbH & Co. KGaA, 2000.
9. Bhatnagar, MS, "Polycarbonates - part III Crystal structure and morphology of polycarbonates." *Pop. Plast. Packag.*, 46 (12), 2001, 67-73
10. Knauss, DM, McGrath, JE, "Polycarbonate networks. 1. Synthesis and characterization of vinylphenyl carbonate terminated oligomers." *Polymer*, 43 (24), 2002, 6407-6414

11. Knauss, DM, Yoon, T-H, McGrath, JE, "Polycarbonate networks. Part 2. Cure study and determination of mechanical, adhesive, and crystallization properties." *Polymer*, 43 (24), 2002, 6415-6420.
12. Harron, HR, Pritchard, RG, Cope, BC, Goddard, DT, "An atomic force microscope (AFM) and tapping mode AFM study of the solvent-induced crystallization of polycarbonate thin films." *J. Polym. Sci., Part B: Polym. Phys.*, 34 (1), 1996, 173-80.
13. Adelman, S, Margotte, D, Nouvertne, W, "Modified polycarbonates and a process for their preparation." US Patent 4199540, 1980.
14. Schuhmacher, P, Kricheldorf, HR, Sun, S-J, "Chiral nematic polycarbonates." US Patent 6156866, 1998.
15. Seow, WY, Yang, YY, "Functional polycarbonates and their self-assemblies as promising non-viral vectors." *J. Controlled Release*, 139 (1), 2009, 40-47.
16. Marks, MJ, Newton, J, "Branching by reactive end groups. II. Synthesis, branching, and melt rheology of (Meth)acrylate/p-t-butylphenol-coterminated bisphenol A polycarbonates." *J. Polym. Sci., Part A: Polym. Chem.*, 38 (13), 2000, 2340-2351.
17. Marks, MJ, Newton, J, Scott, DC, Bales, SE, "Branching by Reactive End Groups. Synthesis and Thermal Branching of 4-Hydroxybenzocyclobutene/p-tert-Butylphenol Coterminated Bisphenol A Polycarbonates." *Macromolecules*, 31 (25), 1998, 8781-8788.
18. Adelman, S, Margotte, D, Rosenkranz, HJ, Vernaleken, H, Nouvertne, W, Freitag, D, "Polycarbonates with double bond-containing end groups crosslinkable with UV light." US Patent 4221645, 1980.

19. Stix, W, Bottenbruch, L, Neuray, D, "Polycarbonates with end groups containing conjugated double bonds." US Patent 4518747, 1984.
20. Kim, SH, Woo, H-G, Kim, S-H, Kim, J-S, Kang, H-G, Kim, W-G, "Synthesis and Properties of Allyl-Terminated and Silicon-Containing Polycarbonates." *Macromolecules*, 32 (19), 1999, 6363-6366.
21. Scott, DW, "Thermal Rearrangement of Branched-Chain methylpolysiloxanes." *J. Am. Chem. Soc.*, 68, 1946, 356-358.
22. Fu, BX, Namani, M, Lee, A, "Influence of phenyl-trisilanol polyhedral silsesquioxane on properties of epoxy network glasses." *Polymer*, 44, 2003, 7739-7747.
23. Huang, J-c, He, C-b, Xiao, Y, Mya, KY, Dai, J, Siow, YP, "Polyimide/POSS nanocomposites: interfacial interaction, thermal properties and mechanical properties." *Polymer*, 44, 2003, 4491-4499.
24. Seino, M, Hayakawa, T, Ishida, Y, Kakimoto, M-a, "Synthesis and Characterization of Crystalline Hyperbranched Polysiloxysilane with POSS Groups at the Terminal Position." *Macromolecules*, 39, 2006, 8892-8894.
25. Fox, DM, Maupin, PH, Richard H. Harris, J, Gilman, JW, Eldred, DV, Katsoulis, D, Trulove, PC, Long, HCD, "Use of a Polyhedral Oligomeric Silsesquioxane (POSS)-Imidazolium Cation as an Organic Modifier for Montmorillonite." *Langmuir*, 23, 2007, 7707-7714.
26. Lichtenhan, JD, Vu, NQ, Carter, JA, "Silsesquioxane-Siloxane Copolymers from Polyhedral Silsesquioxanes." *Macromolecules*, 26, 1993, 2141-2142.

27. Zhao, Y, Schiraldi, DA, "Thermal and mechanical properties of polyhedral oligomeric silsesquioxane (POSS)/polycarbonate composites." *Polymer*, 46 (25), 2005, 11640-11647.
28. Hao, N, Boehning, M, Goering, H, Schoenhals, A, "Nanocomposites of Polyhedral Oligomeric Phenethylsilsesquioxanes and Poly(bisphenol A carbonate) as Investigated by Dielectric Spectroscopy." *Macromolecules*, 40 (8), 2007, 2955-2964.
29. Sanchez-Soto, M, Schiraldi, DA, Illescas, S, "Study of the morphology and properties of melt-mixed polycarbonate-POSS nanocomposites." *Eur. Polym. J.*, 45 (2), 2009, 341-352.
30. Iyer, S, Schiraldi, DA, "Role of Specific Interactions and Solubility in the Reinforcement of Bisphenol A Polymers with Polyhedral Oligomeric Silsesquioxanes." *Macromolecules*, 40 (14), 2007, 4942-4952.
31. Majumdar, P, Christianson, DA, Roesler, RR, Webster, DC, "Optimization of coating film deposition when using an automated high throughput coating application unit." *Prog. Org. Coat.*, 56 (2-3), 2006, 169-177.
32. Majumdar, P, Stafslie, S, Daniels, J, Webster, DC, "High throughput combinatorial characterization of thermosetting siloxane-urethane coatings having spontaneously formed microtopographical surfaces." *J. Coat. Technol. Res.*, 4 (2), 2007, 131-138.
33. Nakamura, M, Ishida, H, "Synthesis and properties of new crosslinkable telechelics with benzoxazine moiety at the chain end." *Polymer*, 50 (12), 2009, 2688-2695.
34. Neumann, D, Fisher, M, Tran, L, Matison, JG, "Synthesis and Characterization of an Isocyanate Functionalized Polyhedral Oligosilsesquioxane and the Subsequent Formation of an Organic-Inorganic Hybrid Polyurethane." *J. Am. Chem. Soc.*, 124, 2002, 13998-13999.

35. Majumdar, P, Lee, E, Gubbins, N, Stafslie, SJ, Daniels, J, Thorson, CJ, Chisholm, BJ, "Synthesis and antimicrobial activity of quaternary ammonium-functionalized POSS (Q-POSS) and polysiloxane coatings containing Q-POSS." *Polymer*, 50 (5), 2009, 1124-1133.
36. Lin, T-S, Wu, C-F, Hsieh, C-T, "Enhancement of water-repellent performance on functional coating by using the Taguchi method." *Surf. Coat. Technol.*, 200 (18-19), 2006, 5253-5258.
37. Boduroglu, S, Cetinkaya, M, Dressick, WJ, Singh, A, Demirel, MC, "Controlling the Wettability and Adhesion of Nanostructured Poly-(p-xylylene) Films." *Langmuir*, 23 (23), 2007, 11391-11395.
38. McNeill, IC, Rincon, A, "Thermal degradation of polycarbonates: reaction conditions and reaction mechanisms." *Polym. Degrad. Stab.*, 39 (1), 1993, 13-19.
39. Jang, BN, Wilkie, CA, "A TGA/FTIR and mass spectral study on the thermal degradation of bisphenol A polycarbonate." *Polym. Degrad. Stab.*, 86 (3), 2004, 419-430.
40. Song, L, He, Q, Hu, Y, Chen, H, Liu, L, "Study on thermal degradation and combustion behaviors of PC/POSS hybrids." *Polym. Degrad. Stab.*, 93 (3), 2008, 627-639.

CHAPTER 8. POLYCARBONATE-POLYHEDRAL OLIGOMERIC SILSESQUOXANE (PC-POSS) THERMOSET COATINGS—THE EFFECT OF POSS CONTENT AND CROSSLINK DENSITY

8.1. Abstract

ASHBY-Karstedt's catalyst in combination with TCE as a solvent were used as a replacement for Karstedt's catalyst and CH_2Cl_2 for preparation of thermoset PC-POSS coatings. With ASHBY-Karstedt's catalyst, coating solution stays stable at ambient condition without crosslinking while curing occurs immediately at elevated temperature. The variables explored in the study were POSS content and crosslinking density. The covalent bonding between PC and POSS allows up to 18 wt% POSS loading while the transparency of the thermoset coatings was maintained. Coatings were characterized using attenuated total reflectance fourier transform infrared spectroscopy (ATR-FTIR), UV-Vis spectroscopy, water contact angle, atomic force microscopy (AFM), differential scanning calorimeter (DSC), thermogravimetric analysis (TGA), dynamic mechanical analysis (DMA), pendulum harness, and abrasion resistance. The thermoset PC-POSS coatings showed higher glass transition temperature, higher char formation, and higher abrasion resistance compared to pure PC. The excess POSS molecules tend to act as nanofiller to reinforce the PC-POSS crosslinked network, giving better thermal and mechanical properties. Those coatings provide an alternative for the surface protection of thermoplastic PC substrates.

8.2. Introduction

With the development of coatings technology, the coating surfaces are sophisticatedly tuned to adapt to various applications. The nanostructured coatings have been designed or the coating surfaces have been modified to have low friction coefficient, superior hardness, wear

resistance, superhydrophobicity, and so on.¹⁻⁵ The surface properties are important in determining the coatings interaction with the environment. And the bulk properties are essential in determining the overall characteristic performance of the coatings. The design of both surface and bulk properties by appropriate selection of coating raw materials and application process to achieve desired performances still remains a challenge.⁶ In Chapter 7, we were able to tune the surface and bulk properties of the thermoset PC-POSS coatings by changing the solvent composition and curing condition. The more hydrophobic surface could be obtained in a fast-leaving solvent and low temperature curing, leaving the free POSS molecules segregating on the coatings surface. And the less hydrophobic surface was derived from a slow-leaving solvent with POSS crosslinkers stay within bulk.

Moreover, Karstedt's catalyst enabled immediate curing even at ambient condition, leading to the very limited time allowed for coating application. The time after a 2K paint components have been mixed and before the application onto substrates is defined as "pot life".⁷ Pot life is an important parameter for commercial 2K paints which allows customers to have enough time to apply the coatings before gelation occurs. In commercial coating operation, short pot life results in a significant potential waste of coating materials. Therefore, it is highly desirable and advantageous to improve pot life and reduce waste potential. Numerous efforts have been undertaken to improve the pot life of 2K coatings.⁸⁻¹⁰

In order to gain better understanding of the role of POSS molecules within the crosslinked networks and at the same time to improve the pot life of the thermoset PC-POSS coating, ASHBY-Karstedt's in combination of TCE as a solvent were used as a replacement for Karstedt's catalyst and CH_2Cl_2 for preparation of thermoset PC-POSS coatings. ASHBY-Karstedt

is a commercially available catalyst which consists of Pt-cyclovinylmethylsiloxane complex. The difference of ASHBY-Karstedt's from regular Karstedt's catalyst is that the former one only functions at elevated temperature. Therefore, the new combination of solvent and catalyst enabled the molecular dispersion of POSS molecules before gelation occurs and the well embedded state of POSS molecules within the crosslinked PC-POSS network. The surface and bulk properties were studied through various techniques.

8.3. Experimental

8.3.1. Raw Materials

Highly pure allyl-PCs with molecular weights (M_n) of 3,070 g/mol, 4,600 g/mol (determined by $^1\text{H-NMR}$) were synthesized using the process described in Chapter 5. Platinum (0)-cyclovinylmethylsiloxane complex (ASHBY-Karstedt's catalyst) was purchased from Gelest. OctaSilane-POSS® was obtained from Hybrid Plastics. 1,1,2,2-tetrachloroethane (TCE) was obtained from Aldrich. OctaSilane-POSS® was obtained from Hybrid Plastics. TCE was dried with molecular sieves activated at 300 °C. All other reagents were used as received.

8.3.2. Preparation of PC-POSS Thermoset Coatings

Pure allyl-PC oligomers with low molecular weights of 3,070 g/mol and 4,600 g/mol were used here, and simply represented as 3K PC and 5K PC. For PC5K-POSS coating, stock solutions of 20 wt % allyl-PC and 3 wt % OctaSilane-POSS® were individually prepared in TCE. For PC3K-POSS coating, stock solutions of 25 wt % allyl-PC and 3 wt % OctaSilane-POSS® were individually prepared in TCE. Table 8.1 describes the compositions of the coatings prepared. Coating solutions were prepared by combining, in an 8 ml vial, allyl-PC stock solution and ASHBY-Karstedt's catalyst (2 μL per 0.4 g 5K PC and 1 μL per 0.4 g 3K PC) and the

mixture magnetically stirred for 5 minutes before adding an OctaSilane-POSS® solution. After adding the OctaSilane-POSS® solution, the mixture was mixed well for 30 seconds using a vortex mixer and then 1.0 mL of the coating solution was deposited over a 2.54 cm X 7.62 cm glass slide using a pipette and subsequently cured at 120 °C to form a thermoset coating. The coatings were annealed at 180 °C for 1 hour to completely remove solvent before characterization.

Table 8.1. Compositions of the thermoset PC-POSS coatings produced.

PC-POSS Coatings	SiH:Vinyl	POSS Content (wt%)	PC-POSS Coatings	SiH:Vinyl	POSS Content (wt%)
PC_5K	--	0	PC_3K	--	0
PC5K-POSS_3%	0.5:1.0	3	PC3K-POSS_4%	0.5:1.0	4
PC5K-POSS_6%	1.0:1.0	6	PC3K-POSS_8%	1.0:1.0	8
PC5K-POSS_8%	1.5:1.0	8	PC3K-POSS_12%	1.5:1.0	12
PC5K-POSS_11%	2.0:1.0	11	PC3K-POSS_15%	2.0:1.0	15
PC5K-POSS_13%	2.5:1.0	13	PC3K-POSS_18%	2.5:1.0	18
PC5K-POSS_15%	3.0:1.0	15	PC3K-POSS_21%	3.0:1.0	21

8.3.3. Instrumentation

The curing was evaluated by ATR-FTIR spectroscopy using Vertex 70 Fourier Transform Infrared Spectrometer from Bruker Optics. Zinc Selenide (ZnSe) was used as a crystal for the measurement. Analyses were conducted by OPUS IR software.

UV-Vis spectroscopy was recorded using Cary 5000 UV-Vis-NIR spectrometer (Version 1.12) over a wavelength ranging from 200 to 800 nm with 1 nm resolution for films of thickness around 100 μ m.

Water contact angle measurements on the coatings were carried out using an automated surface energy measurement unit manufactured by Symyx Discovery Tools, Inc. and First Ten Angstroms. Three measurements were taken on each coating using the sessile drop method and the data reported as the average and standard deviation.

Atomic force microscopy (AFM) studies were performed in tapping mode using a Dimension 3100 $\text{\textcircled{R}}$ microscope with a Nanoscope IIIa controller from Veeco Incorporated. Topographical images were collected in air, at room temperature, using a single-lever silicon probe from NanosensorsTM. Cantilever length, width, and thickness of the silicon probe were $225 \pm 10 \mu\text{m}$, $25 \pm 7.5 \mu\text{m}$, and $3.0 \pm 1.0 \mu\text{m}$, respectively. The spring constant was 0.5-9.5 N/m with a resonant frequency 75 kHz. The set point ratio was 0.8-0.9.

Differential scanning calorimetry (DSC) experiments were carried out using a DSC Q1000 from TA instruments equipped with an auto sampler. About 5.0 mg of sample were measured. The experiments were conducted using a heat-cool-heat cycle extending from +25 $^{\circ}\text{C}$ to +200 $^{\circ}\text{C}$ at a heating/cooling rate of 10 $^{\circ}\text{C}/\text{min}$. Thermal gravimetric analysis (TGA) was carried using a TGA Q500 thermal analyzer under nitrogen atmosphere in the temperature range of +25 $^{\circ}\text{C}$ to +800 $^{\circ}\text{C}$ at a heating rate of 20 $^{\circ}\text{C}/\text{min}$, purged with N_2 at 50ml/min.

The gel contents were determined to evaluate the crosslinking density of the thermoset coatings. By measuring the weights of the dry films before (W_0) and after 3 hour Soxhlet extraction (W_{dry}) in methylene chloride, the gel content could be calculated by

$$Gel\ Content\ (wt\%) = \frac{W_{dry}}{W_0} * 100$$

Equation 8.1

Three samples were tested for each coating composition, and the average value and standard deviation were reported.

The solvent swelling tests were performed by measuring the lengths of the rectangular samples of the thermoset coatings before (L_0) and after 1 hour immersion in TCE (L_{wet}). And the swelling degree could be obtained by calculating according the following equation,

$$Swelling\ (\%) = \frac{L_{wet} - L_0}{L_0} * 100$$

Equation 8.2

The recorded value is the average swelling degree and standard deviation based on three measurements.

König pendulum hardness was measured according to ASTM D 4366 using a BYK Gardner, Pendulum Hardness Tester. The hardness values were recorded as time in seconds based on three measurements.

The abrasion resistance was determined as the change of light transmission after the films were subjected to certain cycles of abrasion test. The combi-abraser controls applied force by air pressure and controls cycles by orbital shaker, and the abrasion was performed by the rough brush heads equipped inside the chamber of the combi-abraser, as shown in Fig 8.1. Air pressure of 2 psi was applied and the samples were abraded for 100 cycles. The light transmittance of the samples were recorded in UV and visible wavelength range 200-800nm.

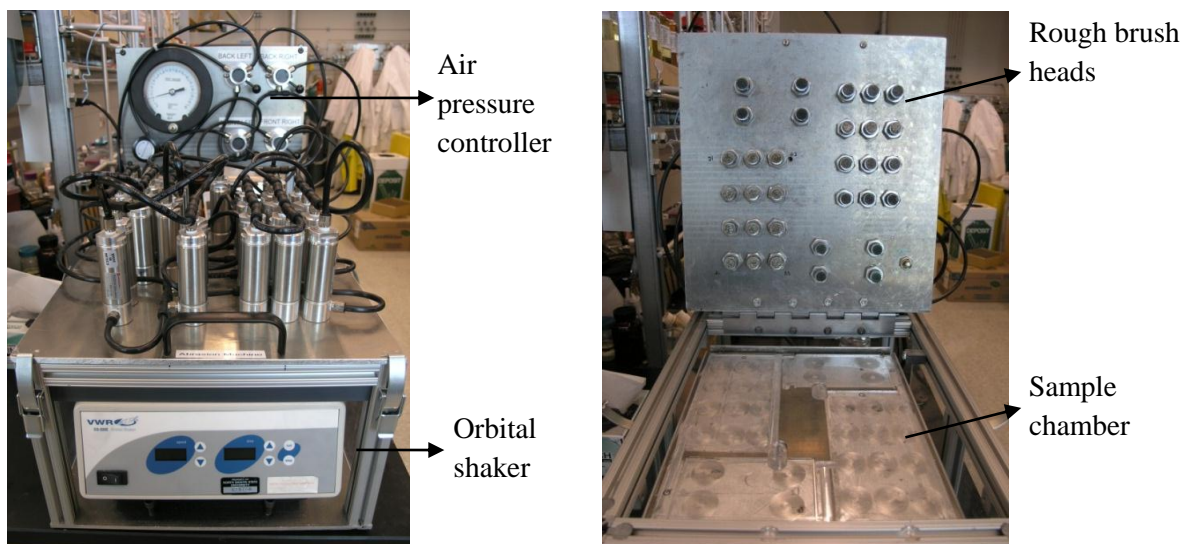
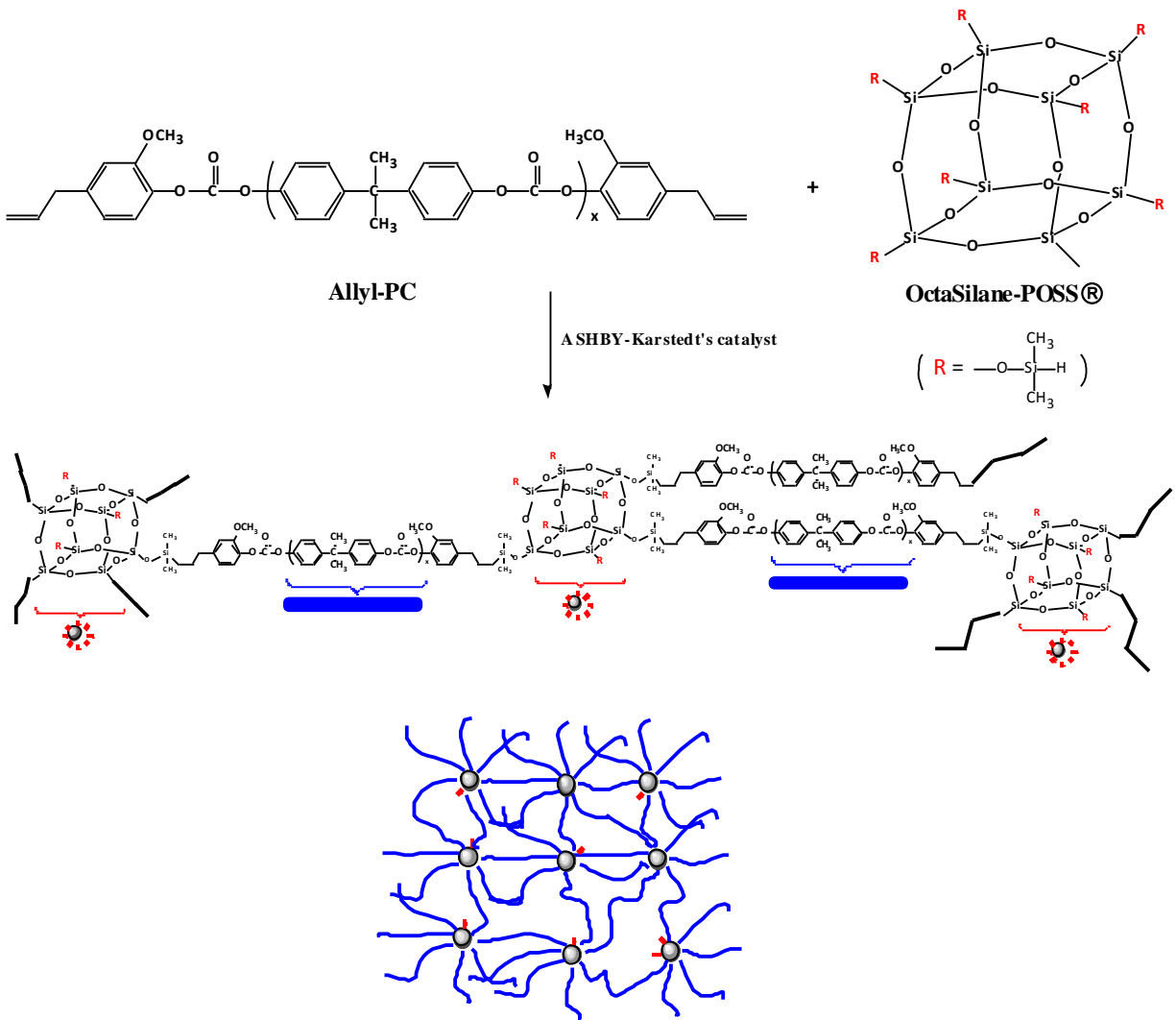


Figure 8.1. The combi-abraser used for abrasion test.

8.4. Results and Discussion

8.4.1. Preparation of PC-POSS Thermoset Coatings

In order to get most of the pot life which is an important factor in commercial 2K coating applications, the thermoset PC-POSS coatings were prepared by reacting allyl-PC with OctaSilane-POSS® in presence of ASHBY-Karstedt's catalyst. The ASHBY-Karstedt's catalyst is Pt (0) complex with cyclovinylmethylsiloxane which functions immediately at moderate elevated temperature or at ambient temperature after a long period of time. Curing of the thermoset PC-POSS coatings were accomplished at 120 °C to get the immediately cured coatings. Figure 8.1 illustrates the process that was used to produce the nanocomposite coatings. The process consisted of solution blending an allyl-PC with OctaSilane POSS® and ASHBY-Karstedt's catalyst. With this process, crosslinking and incorporation of POSS molecules into the PC matrix occurs via hydrosilylation reactions.



Scheme 8.1. A schematic illustrating the formation of crosslinked network involving allyl-PC and OctaSilane-POSS[®] to produce thermoset PC-POSS coating.

Variables investigated in this study are crosslinking density and POSS content. The crosslinking density was varied by using allyl-PCs with different molecular weight. High molecular weight of allyl-PC leads to low crosslinking density and thus poor mechanical properties. Thereby, allyl-PCs with low molecular weight of 3K (3070 g/mol) and 5K (4600 g/mol) were studied here. For PC5K-POSS coatings, POSS content was varied from 3 wt % to 15 wt % by changing Si-H:vinyl ratio from 0.5:1.0 to 3.0:1.0. For PC3K-POSS coatings, POSS

content was varied from 4 wt % to 21 wt % by changing Si-H:vinyl ratio from 0.5:1.0 to 3.0:1.0. TCE was used as a solvent here due to the relatively low vapor pressure and thus low evaporation rate. If a fast-leaving solvent is used, i.e. CH₂Cl₂, the solvent would complete evaporation before curing occurs, resulting in un-reacted mixtures. Figure 8.2 displays a schematic of the experimental design used for the investigation.

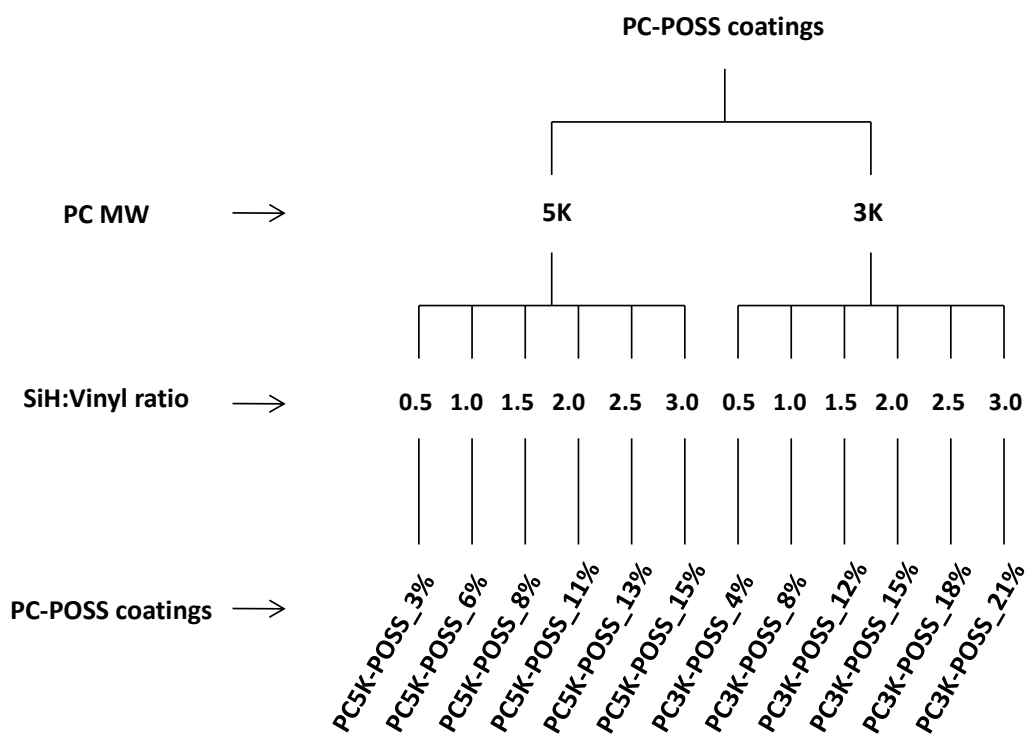


Figure 8.2. A schematic illustration of the experimental design used for coating formulations.

Figure 8.3 (a) to (d) displays the ATR spectra of allyl-PC with Mn 5K, OctaSilane-POSS®, and PC5K-POSS coatings with 8% and 15% POSS. The successful hydrosilylation coupling between Si-H and allyl functional groups are illustrated by the disappearance of the strong Si-H band at 2141 cm⁻¹ in the spectrum of PC5K-POSS_8% coating (Figure 8.3 (c)) at a 1.5:1 stoichiometry. Trace of the Si-H band could be observed when excessive OctaSilane-

POSS® were added at a 3:1 stoichiometry in the PC5K-POSS_15% coating as shown in Figure 8.3 (d). The broadening of band region of PC5K-POSS coatings at $\sim 1100\text{ cm}^{-1}$ and 860 cm^{-1} are attributed to the stretching vibration and bending of Si-O of the silsesquioxane cage.¹¹ The shoulder at 1250 cm^{-1} is assigned to stretching of newly formed Si-C linkage.¹²

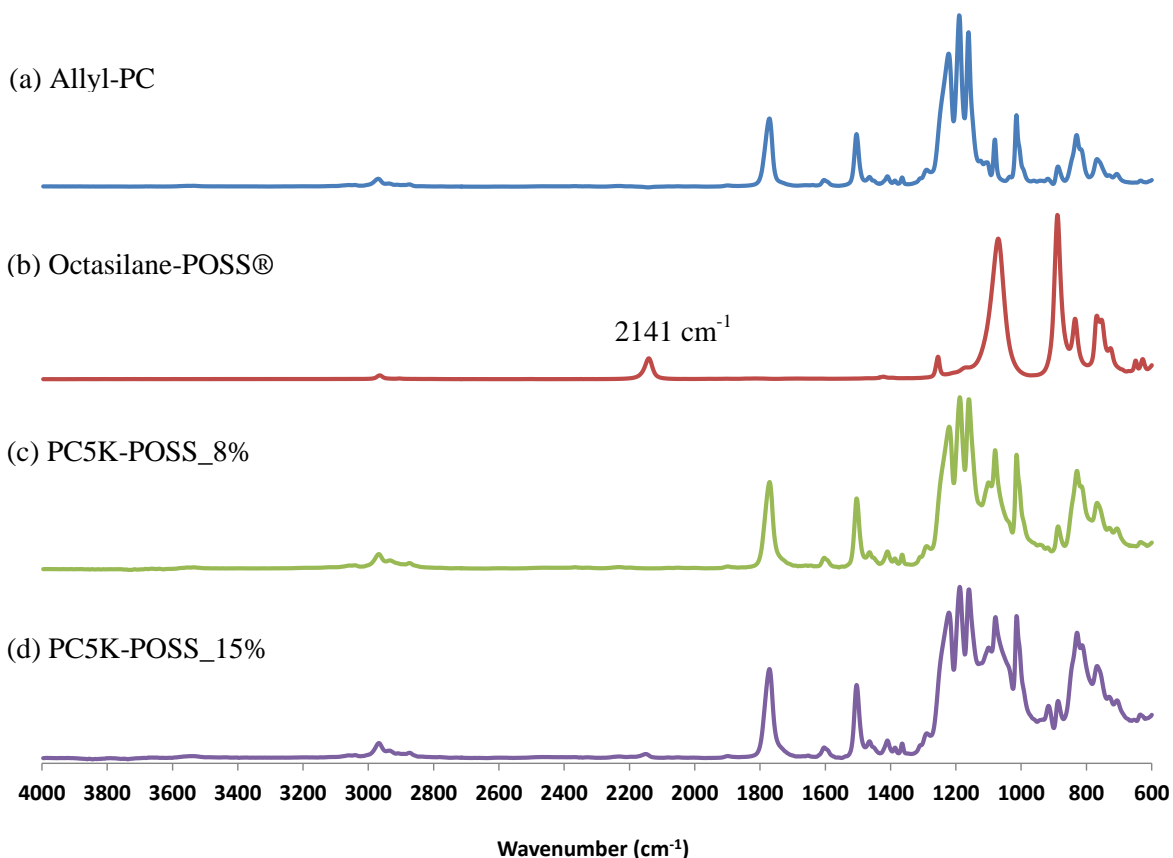


Figure 8.3. FTIR spectrum of (a) allyl-PC, (b) Octasilane-POSS® and PC-POSS coatings with (c) 8 wt% POSS and (d) 15 wt% POSS.

The gel content and swelling degree of the thermoset coatings are displayed in Figure 8.4 to evaluate the crosslinking density of the films. As expected, the gel content increased with POSS content initially and reached a plateau for both PC 5K and PC 3K coatings. At low POSS content (PC5K-POSS_3% and PC3K-POSS_4%), the stoichiometry of SiH:VN is 0.5:1, the PC chains were not fully covalently attached with POSS crosslinker. Free un-reacted PC chains were

washed away by solvent, leading to the low gel content. The gel content reached the maximum at 8 % of POSS content (1.5:1 stoichiometry) instead of 6 % (1:1 stoichiometry) for PC5K-POSS coatings at a 1:1 stoichiometry. This indicated there are un-reacted Si-H groups on periphery of POSS molecules at 1:1 stoichiometry due to the steric hindrance, and excessive POSS crosslinkers are needed to react with allyl groups. And the allyl functional groups were fully reacted at 1.5:1 stoichiometry, whereas leaving certain amount of un-reacted Si-H groups on POSS molecules. For PC3K-POSS coating, the maximum gel content reached at 1:1 stoichiometry when 8 % POSS was added. This may attributed to the shorter chains of allyl-PCs with 3K molecular weight than those of allyl-PCs with 5K molecular weight, leading to the decreased steric hindrance. It is interesting that the incorporation of large excess POSS molecules did not cause a drop of the gel content. This may result from the lack of a large amount of free un-reacted POSS molecules, which means the POSS molecules were uniformly partially reacted.

The swelling degree as a function of POSS content is shown in Figure 8.4. Sample PC5K-POSS_3% was not tested because it's too brittle to be cut for the swelling test. However from the other samples clear trend is still observed. The swelling degree dropped with POSS content, indicating that the crosslinks prevent the dissolution of polymer chains. Comparing the highly crosslinked thermoset coatings, the gel content of PC3K-POSS coatings was ca. 20 % while PC5K-POSS coatings reached a lower swelling degree of ca. 25 % due to the lower crosslinking density. The effect of crosslinking density is demonstrated.

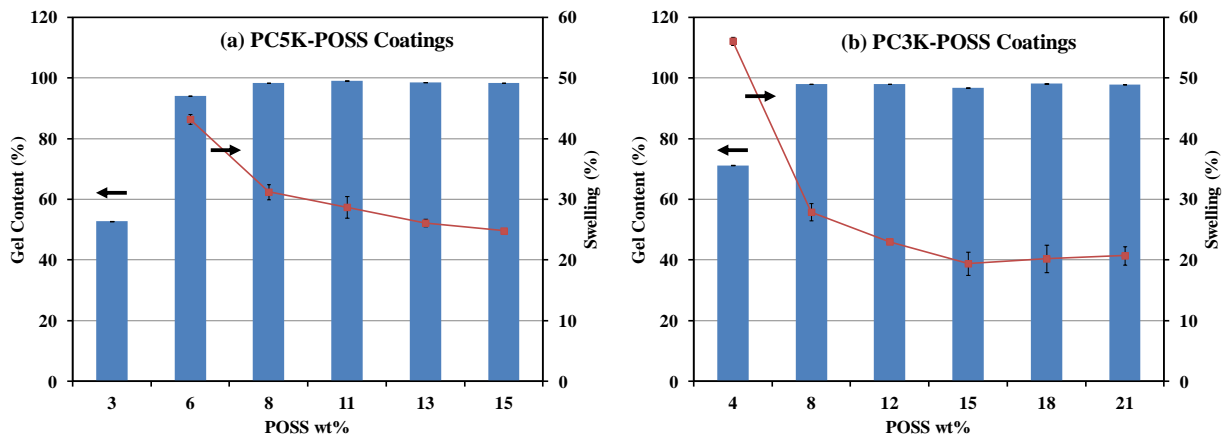


Figure 8.4. Gel content and swelling degree of PC-POSS coatings based on 5K PC and 3K PC.

8.4.2. Optical Clarity

The pictures of PC/POSS physical mixtures in absence of catalyst and thermoset PC-POSS coatings after curing on glass slides were captured shown in Figure 8.5. The samples were placed on a dark green background. The PC/POSS mixtures were powdery and grossly phase separated after solvent evaporation. In contrast, the thermoset PC-POSS coatings were smooth and transparent films, indicating the small domain size and the high degree of dispersion of the POSS molecules. The only exception is when huge amount of POSS was added, the PC3K-POSS_21% coating showed visible agglomerates of POSS molecules.

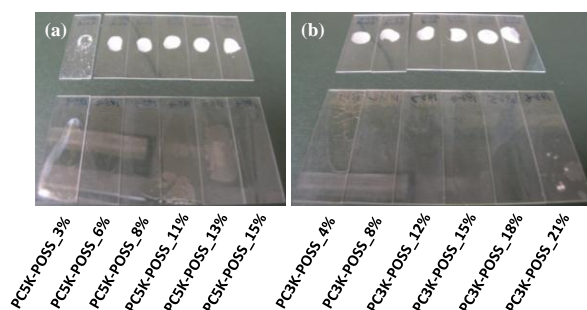


Figure 8.5. Pictures of (a) PC5K-POSS physical mixture in absence of catalyst (top) and thermoset coatings (bottom) and (b) PC3K-POSS physical mixture in absence of catalyst (top) and thermoset coatings (bottom).

To determine the transparency, the thermoset coatings were subjected to UV-Vis measurement. Figure 8.6 displays the transmittance of the films over the range of 200 to 800 nm. The film thickness of PC-POSS thermoset coatings were ca. 100 μm . It has been reported that even though when trisilanolphenyl-POSS acts as a nanofiller for PC due to its good compatibility compared with other types of POSS, the transparency of the nanocomposite could only maintain at up to 5wt% loading.¹³ However, upon crosslinking via hydrosilylation with allyl-PC, all the thermoset coatings exhibited nearly 90 % transmittance to visible wavelength ranging from 400 to 800 nm and had complete cut-off in UV range from 200 to 400 nm. The high transmittance to visible light causes the transparency of the thermoset coatings comparable to commercial PC.

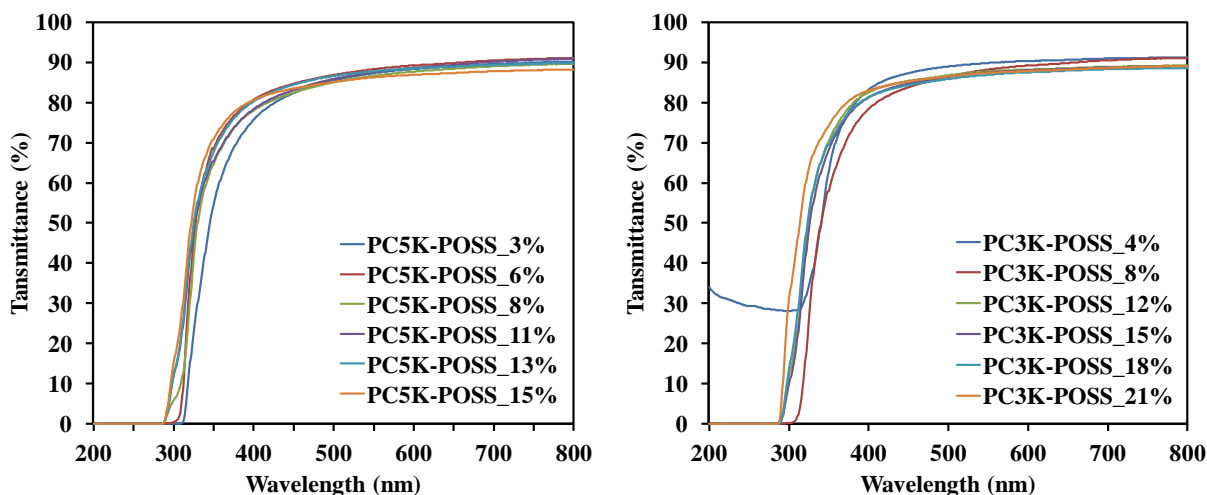


Figure 8.6. UV-Vis spectra of (a) PC5K-POSS coatings and (b) PC3K-POSS coatings.

8.4.3. Surface Properties

Figure 8.7 displays water contact angle data for the PC-POSS coatings as a function of POSS content for both sets of PC5K-POSS and PC3K-POSS coatings. Due to the low molecular weight, the PC 3K oligomer doesn't possess the capability of film formation. Thus the water

contact angle measurement could not be performed on it. The control sample of pure PC5K showed a water contact angle of 88 °. The thermoset PC-POSS coatings derived from PC 5K and PC 3K were more hydrophobic than pure allyl-PC. The increase in hydrophobicity observed for the coatings suggested surface segregation of hydrophobic POSS molecules to coating/air interface. With regard to the effect of POSS content, no significant influence of POSS content on water contact was observed for both PC5K-POSS and PC3K-POSS coatings, indicating the “locking” of excessive POSS molecules within crosslinked networks via hydrosilylation inside bulk films instead of migrating onto coating/air interface.

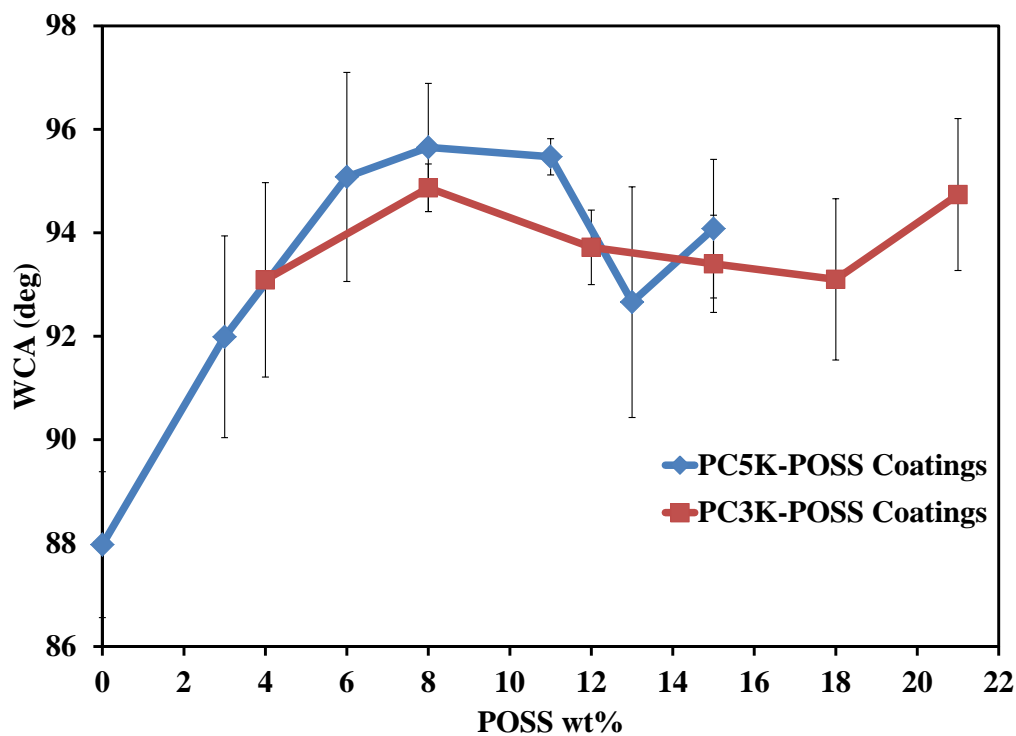


Figure 8.7. Water contact angle of PC-POSS coatings.

In order to understand the trends observed for water contact angle data, AFM was used to characterize coating surface topography. Figure 8.8 displays the AFM images of PC-POSS

coatings produced from (a) PC5K and (b) PC3K as a function of the POSS content. Again, AFM image of control sample PC 3K was not displayed here due to the poor film formation property. As expected, a homogeneously smooth surface morphology was obtained for the pure PC coating. Although the heterogeneous surface morphology was observed for PC-POSS coatings, nanoscale surface roughness was not increased with increasing POSS content which is consistent with the water contact angle data. The lack of POSS molecules at the coating/air interface again suggests the “locking” of POSS molecules within crosslinked networks via hydrosilylation in bulk films. However, the agglomeration of POSS molecules was observed when high level of POSS molecules was incorporated, especially for PC3K-POSS coatings.

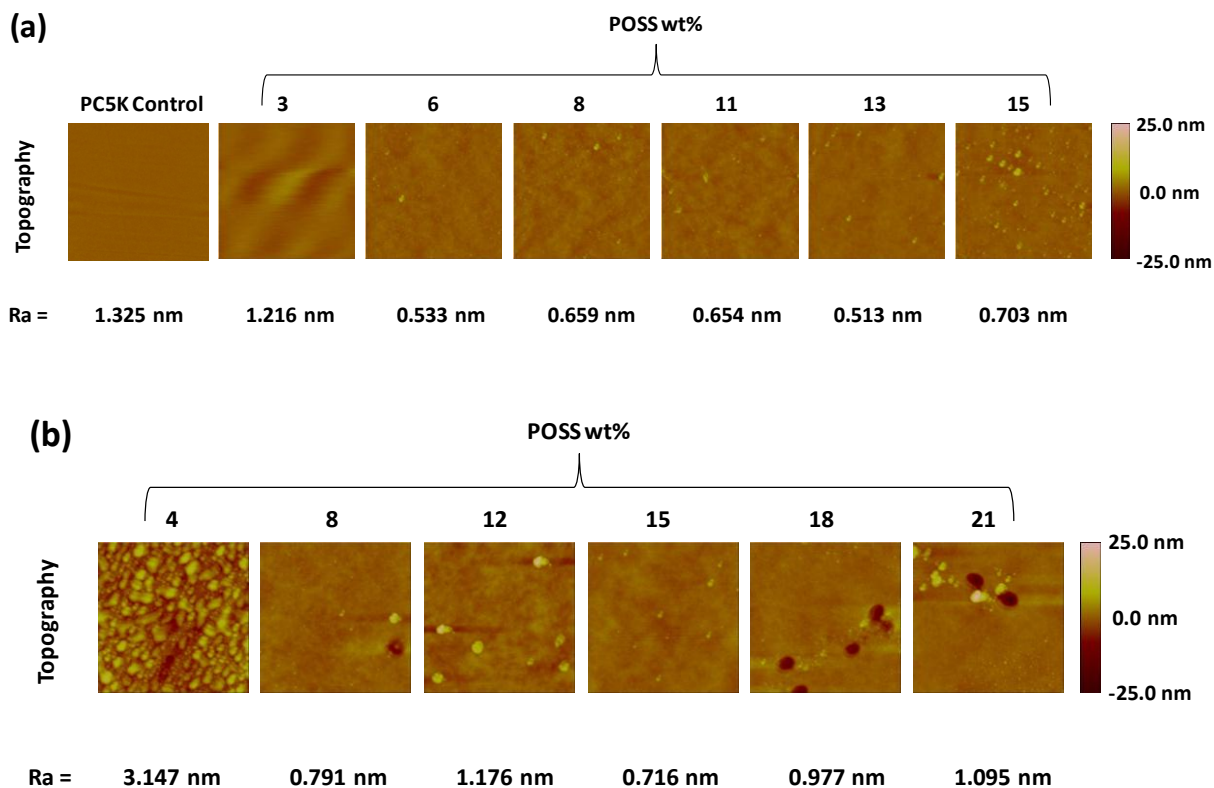


Figure 8.8. AFM images of (a) PC5K-POSS coatings and (b) PC3K-POSS coatings.

8.4.4. Thermal Properties

The thermal properties of PC-POSS coatings were characterized using DSC, TGA and DMA. Figure 8.9 displays the DSC thermographs of the coating showing the glass transition regions. Remarkable increase in T_g values were observed for PC-POSS coatings due to the covalent bonding between POSS and PC matrix. Actually the enhancement of T_g was reported not due to the covalent bonding, and in contrast, the incorporation of POSS leads to the decrease of T_g via covalent interaction.^{14,15} However, the crosslinked networks play important role in increasing the T_g of the nanocomposites.¹⁶ The change of T_g values as a function of POSS content was different for PC5K-POSS coatings and PC3K-POSS coatings as shown in Figure 8.9 (a) and (b). For PC5K-POSS coatings, the T_g increased with increasing POSS content and reached a plateau at 151 °C. While for PC3K-POSS coatings, the T_g increased initially and go through a maximum, and then decreased with increasing POSS content. The POSS molecules act as crosslinkers restricting the chain mobility of PC, thus higher temperature is required to provide adequate thermal energy for glass transition occurrence, raising the T_g . The maximum crosslinking is achieved when T_g stops increasing. When excessive un-reacted POSS molecules existed in polymer matrix, there are two conditions as could be explanation for PC5K-POSS coatings and PC3K-POSS coatings. For PC5K-POSS coatings, excessive POSS molecules tend to be “locked” by the crosslinked networks, causing the constant T_g value. For PC3K-POSS coatings, the excessive POSS molecules tend to be “free” due to the restricted volume within the crosslinked networks resulted from low molecular weight between crosslinks. The “free” POSS molecules perform as plasticizers and decrease the packing density of the polymer matrix around the POSS molecules, causing the decrease of T_g .¹⁷ Besides plasticization, the “free” POSS

molecules tend to segregate together, forming visible agglomeration as shown in the pictures in Figure 8.5.

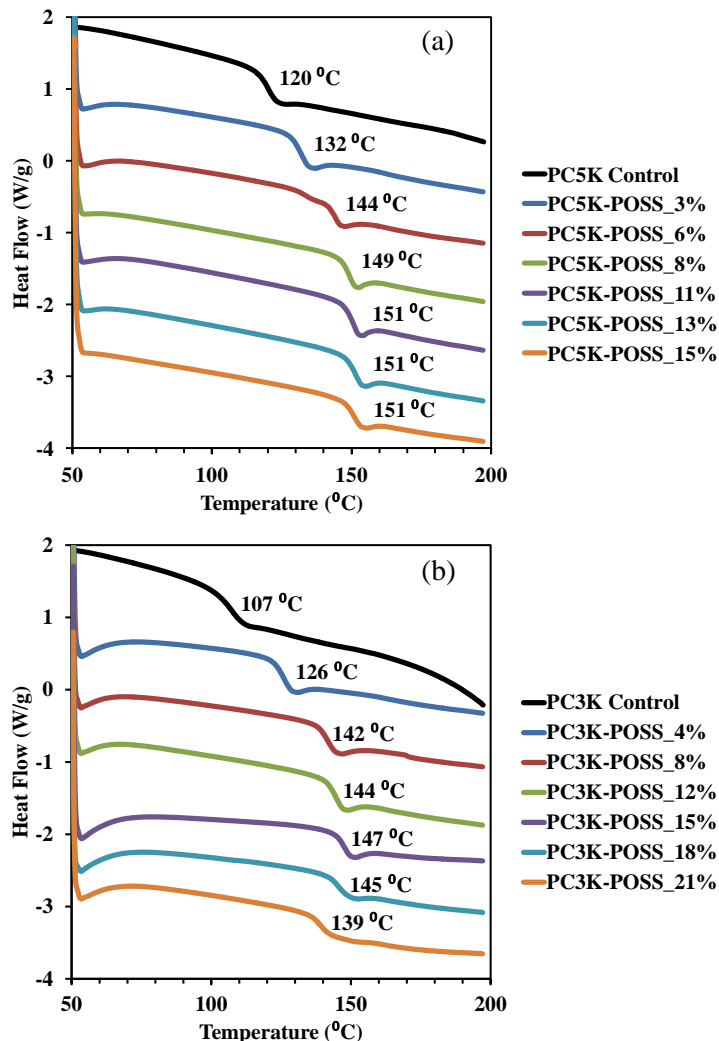


Figure 8.9. DSC curves of (a) PC5K-POSS coatings and (b) PC3K-POSS coatings.

The influence of POSS molecules on thermal degradation of coatings was evaluated using TGA. Figure 8.10 displays the TGA profiles of the thermoset PC-POSS coatings compared with pure allyl-PC and OctaSilane-POSS®. Thermoset PC-POSS coatings undergo a two-stage decomposition process under N₂, displaying same degradation mechanism as pure

allyl-PC which involves the hydrolysis/alcoholysis of carbonate linkages, chain scission of isopropylidene linkages, branching, and crosslinking at higher temperature.¹⁸⁻²⁰ The OctaSilane-POSS® exhibits poor thermal stability and starts to decompose at 220 °C. Thus the thermal stabilities of the thermoset PC-POSS coatings are significantly affected. The onset of the decomposition temperature shifted towards low temperature as a function of POSS content. However, the char yield of the PC-POSS coatings upon thermal degradation increased with increasing POSS content.

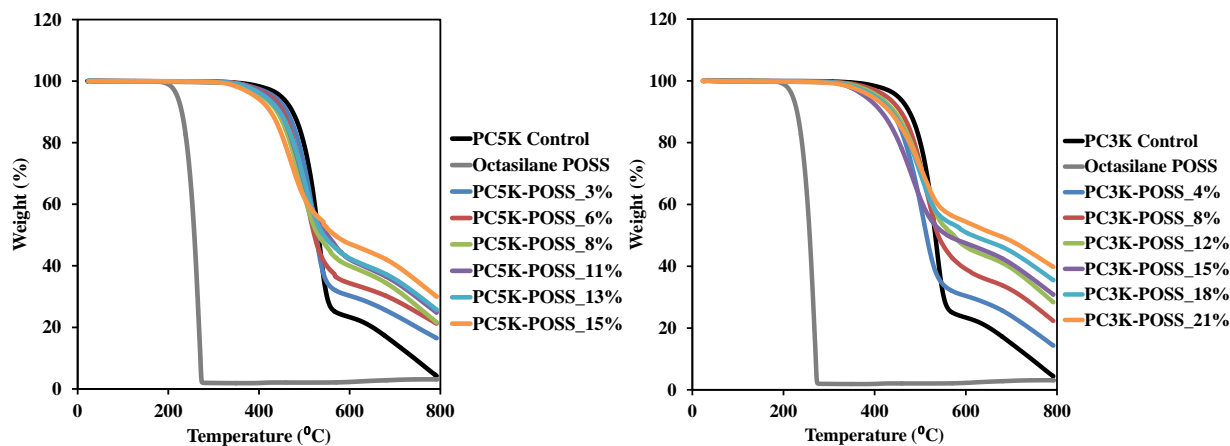


Figure 8.10. TGA curves of PC and OctaSilane-POSS® controls, and PC-POSS coatings under N₂.

Table 8.2 shows the results of onset of degradation temperature i.e. the temperature of 5 wt % and 10 wt% weight loss ($T_{-5\%}$ and $T_{-10\%}$), temperature of maximum weight loss rate (T_{max}), and the fraction of the char residue. The data clearly shows the decreased $T_{-5\%}$, $T_{-10\%}$ and T_{max} values, indicating the impaired thermal stability of the thermoset PC-POSS coatings due to the poor stability of OctaSilane-POSS®. The poor thermal stability of OctaSilane-POSS® is resulted from the siloxane units attached with POSS molecules. With increase of temperature, POSS converted to molecular silica and produced char residue. Therefore, the amount of char was

considerably higher in PC-POSS coatings compared to the pure PC, and also higher compared to the wt % of POSS in the coatings.

Table 8.2. TGA results of PC3K-POSS coatings.

Sample ID	T_{max} (°C)	T_{.5%} (°C)	T_{.10%} (°C)	Char Yield (wt%)
PC_5K	533	449	474	4.2
PC5K-POSS_3%	523	434	462	16.5
PC5K-POSS_6%	505	426	453	21.3
PC5K-POSS_8%	491	409	440	21.6
PC5K-POSS_11%	494	420	448	24.8
PC5K-POSS_13%	498	413	445	25.8
PC5K-POSS_15%	471	393	426	30.0
PC_3K	540	448	479	8.4
PC3K-POSS_4%	507	408	439	14.3
PC3K-POSS_8%	510	425	457	22.3
PC3K-POSS_12%	517	408	444	28.4
PC3K-POSS_15%	485	379	415	30.8
PC3K-POSS_18%	501	400	438	35.5
PC3K-POSS_21%	505	393	434	39.8

Figure 8.11 displays the char yield upon thermal degradation as a function of POSS content. Both char yield of PC5K-POSS coatings and PC3K-POSS coatings increase linearly with the POSS content. The incorporation of POSS into PC resulted in a significantly higher char yield as compared with the POSS content in PC-POSS coatings.

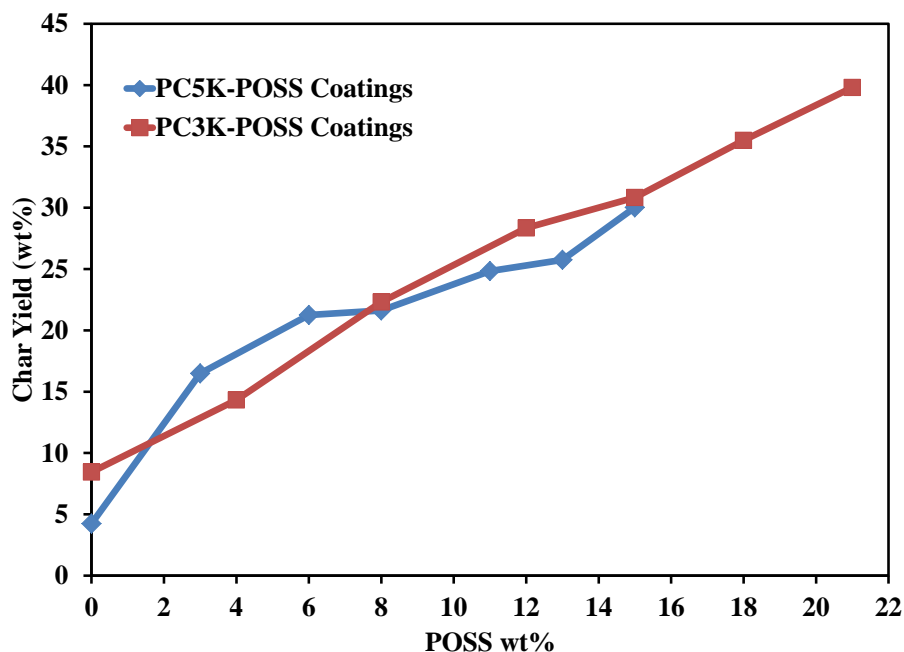


Figure 8.11. Char yield of PC-POSS coatings determined by TGA.

Table 8.3 displays the storage modulus E' data of the coating at 25 °C and at high temperature well above the glass transition (rubbery state). Control sample PC5K and PC3K, and coating sample PC5K-POSS_3% and PC3K-POSS_4% at stoichiometry of 0.5:1.0 were not tested due to the inherent brittleness. The modulus at glassy state didn't shown clear trend, while the modulus at rubbery state increased with POSS content for PC5K-POSS coatings. The increased storage modulus at rubbery state indicated the reinforcement of the POSS molecules as crosslinkers and nanofillers. The crosslinked and immobilized POSS molecules restricted the mobility of polymer matrix through strong covalent bonding, leading to the improved mechanical property of the nanocomposite. For PC3K-POSS coatings, the storage modulus at rubbery state increased with POSS content as well, except the sample PC3K-POSS_21%. This is consistent with DSC result and the same trend has been observed elsewhere.⁶

Table 8.3. DMA results of PC5K-POSS coatings.

Sample ID	E' _{25°C} (MPa)	E' _{195°C} (MPa)	Sample ID	E' _{25°C} (MPa)	E' _{195°C} (MPa)
PC_5K	--	--	PC_3K	--	--
PC5K-POSS_3%	--	--	PC3K-POSS_4%	--	--
PC5K-POSS_6%	1247	6.6	PC3K-POSS_8%	1401	6.9
PC5K-POSS_8%	1547	7.3	PC3K-POSS_12%	1447	17.0
PC5K-POSS_11%	1482	7.8	PC3K-POSS_15%	843	14.1
PC5K-POSS_13%	2003	13.6	PC3K-POSS_18%	1162	24.4
PC5K-POSS_15%	741	21.2	PC3K-POSS_21%	1359	20.9

8.4.5. Coatings Hardness

Pendulum hardness of the thermoset PC-POSS coatings was measured as a function of POSS content, as displayed in Figure 8.12. Film produced by PC with 5 K molecular weight was tested as a control. PC oligomer with 3K molecular weight was not able to be processed into films for testing due to the low molecular weight and the lack of chain entanglement. From Figure 8.12 (a), a substantially increased hardness of thermoset PC-POSS coatings was observed as compared with pure PC. The improvement is attributed to the rigidity of the crosslinked networks and the robust inorganic structure of POSS molecules. As shown in both Figure 8.12 (a) and (b), with the increase of POSS content, hardness dropped which might be due to the lack of interactions of free POSS molecules and the increased free volume.²¹

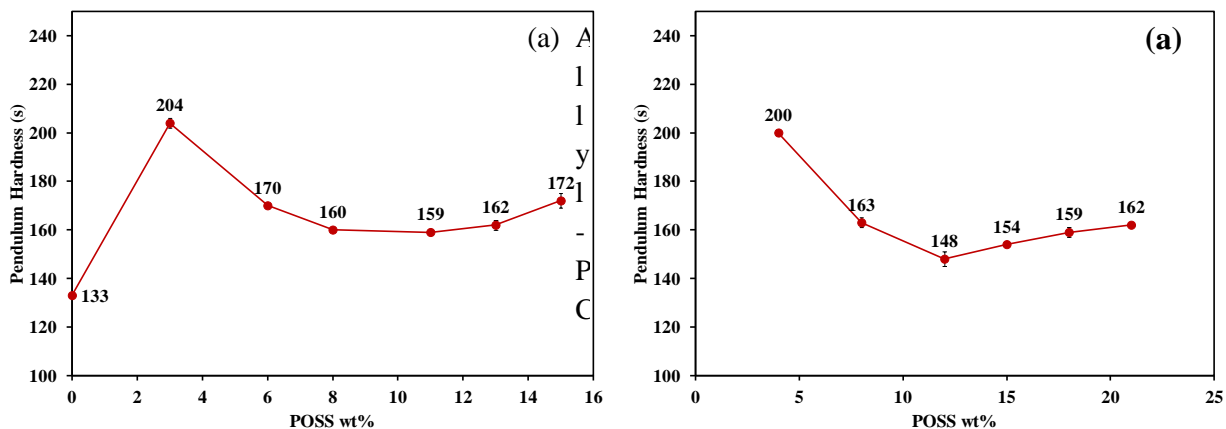


Figure 8.12. Pendulum hardness of (a) PC5K-POSS coatings and (b) PC3K-POSS coatings.

8.4.6. Abrasion Resistance

The thermoset PC-POSS coatings were applied onto commercial PC substrate by spin coating and the abrasion resistances of the spin-coated films were compared with bare PC substrate as shown in Figure 8.13. The abrasion resistance is expressed as the decrease of light transmission after the abrasion test. Before abrasion, the PC-POSS coatings possess as high transparency as pure commercial PC substrate. After 100 abrasion cycles, all samples lost certain amount of transparency due to the light scattering from roughened surfaces. The less reduction of transparency of PC-POSS coatings suggested the better abrasion resistance. The better performances of the thermoset PC-POSS coatings are derived from the crosslinked networks and the incorporation of POSS molecules.^{22,23} The PC3K-POSS coatings showed even better abrasion resistance than PC5K-POSS coatings, due to the higher crosslinking density.

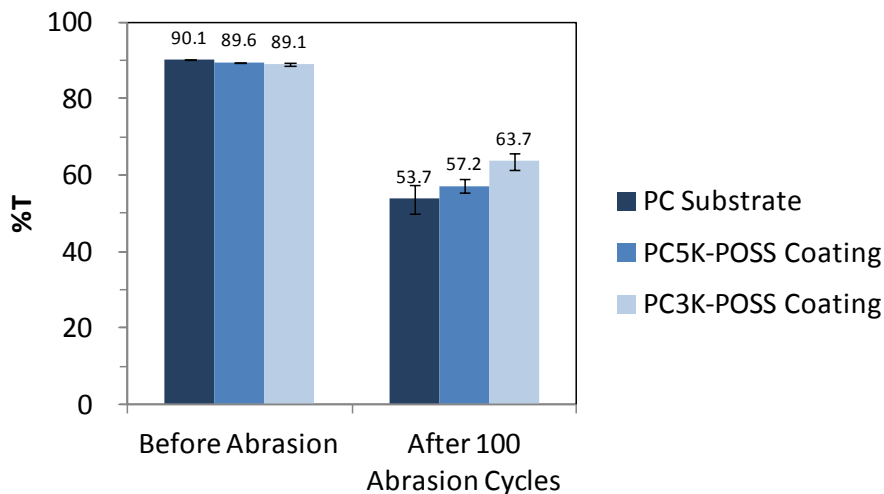


Figure 8.13. Abrasion resistance of PC-POSS coatings.

8.5. Conclusion

The thermoset PC-POSS coatings with less hydrophobicity were prepared by using ASHBY-Karstedt as a catalyst and TCE as a solvent. With ASHBY-Karstedt's catalyst, coating solution stays stable at ambient condition without crosslinking while curing occurs immediately at elevated temperature, significantly improving the pot life. The slow-leaving solvent TCE allows the complete cure before solvent evaporation, inhibiting the segregation of POSS molecules onto the coating/air interface. Thus the coating surfaces are less hydrophobic. The covalent bonding between PC and POSS allows up to 18 wt% POSS loading while the transparency of the thermoset coatings was maintained. The thermoset PC-POSS coatings showed higher glass transition temperature, higher char formation, and higher abrasion resistance compared to pure PC. The excess POSS molecules tend to act as nanofiller to reinforce the PC-POSS crosslinked network, giving better thermal and mechanical properties. The coatings with higher crosslinking density have better swelling resistance and abrasion resistance. Those coatings provide an alternative for the surface protection of thermoplastic PC substrates.

8.6. References

1. J.-P. Hirvonen, J. Koskinen, J.R. Jervis, M. Nastasi, Present progress in the development of low friction coatings, *Surface and Coatings Technology* 80, 1996, 139-150
2. Sam Zhang, Deen Sun, Yongqing Fu, Hejun Du, Recent advances of superhard nanocomposite coatings: a review, *Surface and Coatings Technology* 167, 2003, 113–119
3. A.A. Voevodin, M.S. Donley, J.S. Zabinski, Pulsed laser deposition of diamond-like carbon wear protective coatings: a review, *Surface and Coatings Technology*, 92 (1–2), 1997, 42-49
4. D.I. Proskurovsky, V.P. Rotshtein, G.E. Ozur, Yu.F. Ivanov, A.B. Markov, Physical foundations for surface treatment of materials with low energy, high current electron beams, *Surface and Coatings Technology*, 125 (1–3), 2000, 49-56
5. Xue-Mei Li , David Reinhoudt and Mercedes Crego-Calama, What do we need for a superhydrophobic surface? A review on the recent progress in the preparation of superhydrophobic surfaces, *Chem. Soc. Rev.*, 36, 2007, 1350-1368
6. L.R. Zhao, K. Chen, Q. Yang, J.R. Rodgers, S.H. Chiou, Materials informatics for the design of novel coatings, *Surface and Coatings Technology*, 200 (5–6), 2005, 1595-1599
7. Zeno W. Wicks, JR. Frank N. Jones, S. Peter Pappas, Douglas A. Wicks, *Organic Coatings: Science and Technology* (3rd edition), John Wiley & Sons, Inc., 2006
8. Wen-Hsuan Chang, Marvis E. Hartman, Roger L. Scriven, US Patent 4,043,953, 1977
9. Jyotindra K. Doshi, Scott A. Wallenberg, US Patent 4,341,689, 1982
10. Douglas A. Wicks, Philip E. Yeske, US Patent 5,243,012, 1993

11. A. Fina, D. Tabuani, F. Carniato, A. Frache, E. Boccaleri G. Camino, Polyhedral oligomeric silsesquioxanes (POSS) thermal degradation, *Thermochimica Acta* 440, 2006, 36-42
12. IRADA S. ISAYEVA, JOSEPH P. KENNEDY, Amphiphilic Membranes Crosslinked and Reinforced by POSS, *Journal of Polymer Science: Part A: Polymer Chemistry*, 42, 2004, 4337–4352.
13. Yiqiang Zhao, David A. Schiraldi, Thermal and mechanical properties of polyhedral oligomeric silsesquioxane (POSS)/polycarbonate composites, *Polymer* 46, 2005, 11640–11647
14. Yuan-Jyh Lee, Jieh-Ming Huang, Shiao-Wei Kuo, Jian-Shing Lu, Feng-Chih Chang, Polyimide and polyhedral oligomeric silsesquioxane nanocomposites for low-dielectric applications, *Polymer* 46, 2005, 173-181
15. Hongyao Xu, Shiao-Wei Kuo, Juh-Shyong Lee, and Feng-Chih Chang, Preparations, Thermal Properties, and Tg Increase Mechanism of Inorganic/Organic Hybrid Polymers Based on Polyhedral Oligomeric Silsesquioxanes, *Macromolecules* 2002, 35, 8788-8793
16. Hongzhi Liu, Sixun Zheng, Polyurethane Networks Nanoreinforced by Polyhedral Oligomeric Silsesquioxane, *Macromol. Rapid Commun.* 2005, 26, 196–200
17. Zhao, Y, Schiraldi, DA, "Thermal and mechanical properties of polyhedral oligomeric silsesquioxane (POSS)/polycarbonate composites." *Polymer*, 46 (25), 2005, 11640-11647.
18. McNeill, IC, Rincon, A, "Thermal degradation of polycarbonates: reaction conditions and reaction mechanisms." *Polym. Degrad. Stab.*, 39 (1), 1993, 13-19.

19. Jang, BN, Wilkie, CA, "A TGA/FTIR and mass spectral study on the thermal degradation of bisphenol A polycarbonate." *Polym. Degrad. Stab.*, 86 (3), 2004, 419-430.
20. Song, L, He, Q, Hu, Y, Chen, H, Liu, L, "Study on thermal degradation and combustion behaviors of PC/POSS hybrids." *Polym. Degrad. Stab.*, 93 (3), 2008, 627-639.
21. Chyi-Ming Leu, Yao-Te Chang, and Kung-Hwa Wei, Polyimide-Side-Chain Tethered Polyhedral Oligomeric Silsesquioxane Nanocomposites for Low-Dielectric Film Applications, *Chem. Mater.* 15, 2003, 3721-3727
22. G. Schottner, K. Rose, U. Posset, Scratch and Abrasion Resistant Coatings on Plastic Lenses—State of the Art, Current Developments and Perspectives, *Journal of Sol-Gel Science and Technology* 27, 2003, 71–79.
23. Y.S. Lai, C.W. Tsai, H.W. Yang, G.P.Wang, K.H.Wu, Structural and electrochemical properties of polyurethanes/polyhedral oligomeric silsesquioxanes (PU/POSS) hybrid coatings on aluminum alloys, *Materials Chemistry and Physics* 117, 2009, 91–98.

CHAPTER 9. OVERALL CONCLUSION

Overall, the silicon-based HOI polymers and coatings were successfully produced by incorporating the organo-silicon compounds. All four types of the organo-silicon compounds ($R_3SiO_{0.5}$, R_2SiO , $RSiO_{1.5}$ and SiO_2) were explored. The colloidal silica (SiO_2) and phenethyl trimethoxysilane ($R_3SiO_{0.5}$) were used to make HOI binders via sol-gel chemistry for Mg-rich primers for corrosion protection. The polydimethylsiloxane (R_2SiO) was coupled with polycarbonate via hydrosilylation to produce PC-PDMS block copolymers as an impact resistant material. And polyhedral oligomeric silsesquioxane ($RSiO_{1.5}$) was used to crosslink PC via hydrosilylation generating the thermoset PC-POSS coatings which provide an alternative for surface protection of thermoplastic PC substrates. The synthetic method, preparation aspects, property characterization were explored in an effort to gain a fundamental understanding of the structure-property relationships.

For the HOI binders and the derived Mg-rich primers, the addition of the condensation catalyst TBAF enabled higher crosslink densities by promoting the condensation reactions between silane and silanol, however caused blistering in Mg-rich primers due to hydrogen gas been released resulted from the rapid oxidation of Mg particles by fluoride ions during salt spray exposure. Thereby a non-ionic condensation catalyst DBTDL is highly desired and the preliminary results showed that DBTDL catalyzed the condensation reactions but it has lower catalysis strength than TBAF.

For the perfectly alternating PC-PDMS multiblock copolymers, Figure 9.1 summarized the optical and mechanical properties. It was amazingly found that the excellent optical clarity could be maintained at up to 62 wt% PDMS content which is attributed to the partial miscibility

and the microphase separated morphology of PC hard domain and PDMS soft domain. In contrast, at high PDMS content and with long block lengths, the block copolymers appear cloudy and opaque due to the macroscopically phase separation. The microphase separated morphology was observed by TEM and SAXS and the near-lamellar morphology was confirmed as evident by SAXS. According to AFM and water contact angle measurement, the surface segregation of PDMS segments occurred and leads to the hydrophobic surfaces. Furthermore, the incorporation of PDMS blocks decreased the thermal decomposition rate and increased the char yield. Most importantly, the Izod impact strength of the synthesized block copolymers was shown much better than the pure PC, even though is not comparable with commercial products.

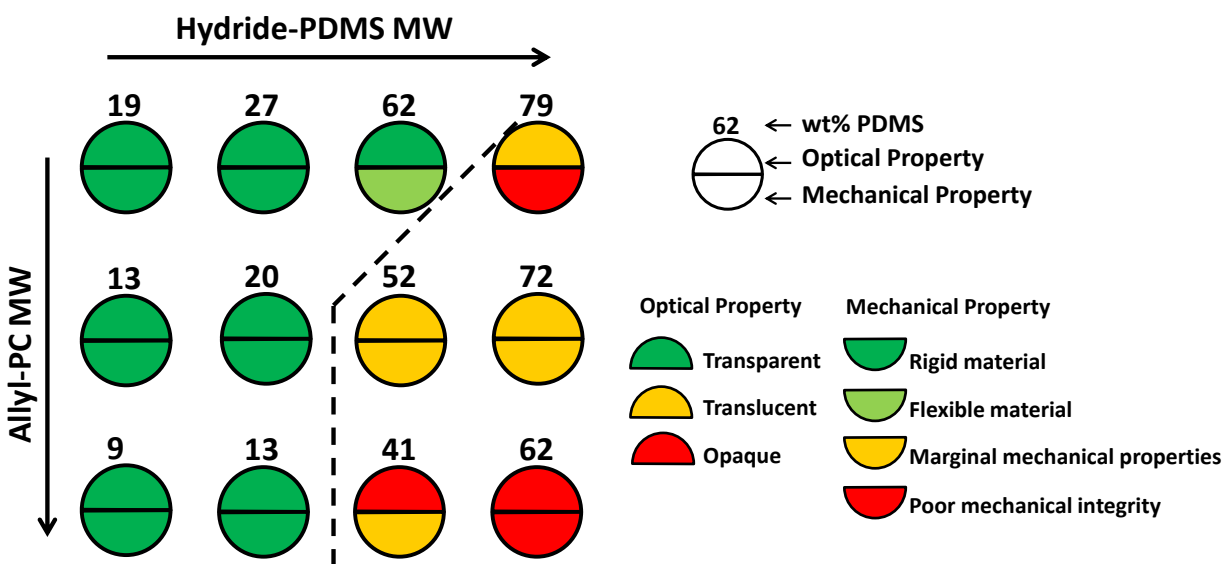


Figure 9.1. The optical and mechanical properties of PC-PDMS block copolymers.

For the thermoset PC-POSS coatings, it was found the surface could be tuned by selecting appropriate solvent composition and curing condition as summarized in Figure 9.2. With fast-leaving solvent and low temperature curing, the surface tends to be rougher and more hydrophobic due to the segregation of POSS molecules onto the surface, while with slow-leaving

solvent and high temperature curing, the surface tends to be smoother and less hydrophobic due to the lack of POSS molecules on surface. The excess POSS molecules beyond the 1:1 stoichiometric ratio behave differently in two systems. Aggregating on surface, the excess POSS molecules plasticize the coatings, while reinforcing the coating when stay within crosslinked networks. In either condition, transparency of the thermoset coatings was maintained at up to 18 wt% POSS content. The thermal decomposition temperatures were much lower due to the poor thermal stability of POSS, while the incorporation of POSS increased the char yield significantly. In addition, it has been found that the hardness and abrasion resistance were improved for the thermoset PC-POSS coatings.

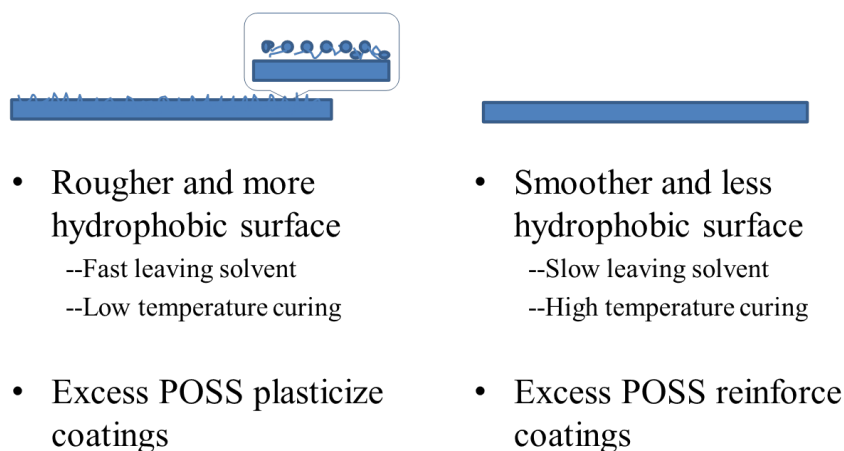


Figure 9.2. Tunable surface and bulk properties of thermoset PC-POSS coatings by varying the preparation condition.

In conclusion, these novel silicon-based HOI materials derived from organo-silicon compounds are highly desirable for various applications in areas such as corrosion protection, impact resistance, and surface protection over thermoplastic parts.

CHAPTER 10. FUTURE WORK

10.1. Novel HOI Binders for Mg-Rich Primers

The promising corrosion protection of Mg-rich primers enabled them to be good candidates for aerospace coating system. To optimize the Mg-rich primers based on HOI materials, more characterization needs to be done. From the preliminary results of using DBTDL as a condensation catalyst, the intermediate catalytic strength of DBTDL for condensation reactions was identified. As future work, HOI colloidal solutions using DBTDL should be applied onto aluminum substrates and EIS tests performed to determine barrier properties. In addition, the HOI binders should then be mixed with Mg particles and other additives to make Mg-rich primers. After applying the Mg-rich primers with polyurethane topcoats on AA2024-T3 substrates, the corrosion protection performance should be evaluated using EIS and B117 salt spray exposure. During the accelerated salt spray exposure, blistering of Mg-rich primers with DBTDL as catalyst will be monitored as compared with those with TBAF as catalyst. The use of DBTDL is expected to eliminate the blisters under long-term salt spray exposure, while maintaining good barrier properties.

Crosslink density of coatings is of importance to provide adequate barrier properties. To get higher crosslink density, organosilanes with polymerizable groups, i.e. vinyl or acrylate, should be investigated to make Mg-rich primers through a dual-cure mechanism. Or, through the polymerizable groups, polymers, i.e. acrylics, can be synthesized and incorporated into HOI coatings to increase the organic portion and to improve the cohesion within Mg-rich primer layer. With higher barrier properties, the corrosion performance will be better.

The organosilane, PhEtMTS, was promising in making Mg-rich primers based on heterogeneous HOI binders with excellent corrosion protection properties. The capability of using PhEtTMS in making a homogeneous HOI binder has not been investigated. Therefore, PhEtTMS, can be also used for making homogeneous HOI coating, in which tetraethyl orthosilicate (TEOS) can be used to form the inorganic component. It would be of interest to compare the corrosion protection performance of the homogeneous HOI coatings with heterogeneous HOI coatings. The effect of organosilane and inorganic TEOS on coatings performance should be evaluated. Homogeneous HOI coatings are expected to also have good adhesion to aluminum substrate as well as to the topcoat.

10.2. Perfectly Alternating PC-PDMS Multiblock Copolymers

To further the structure-property relationship of the PC-PDMS block copolymers, all twelve block copolymers should be synthesized at larger scale and processed for Izod impact strength testing. The effects of block length, PDMS content, and phase structure on mechanical properties should be studied.

The compatibility between PC and PDMS depends on their chemical structure. As a result, it would be of interest to further develop the structure-property relationships by investigating other siloxane blocks beyond PDMS. For example, hydride-terminated polymethylphenyl siloxane and polydiethyl siloxane should be synthesized and used to produce multiblock copolymers.

10.3. Thermoset PC-POSS Coatings

Higher crosslink density usually gives better chemical and abrasion resistance to coatings. Thus, crosslink density should be further increased by lower the molecular weight of PC

oligomers. Molecular weight of under 1,000 g/mol should be expected to give promising coating performance. Other than chemical and abrasion resistance, highly crosslinked PC-POSS thermosets should be measured for coefficient of thermal expansion and evaluated for electronics application.

10.4. Highly Pure Allyl-PCs

To take advantage of the highly pure allyl-PCs with well-controlled molecular weight, amphiphilic block copolymers with well-defined architectures should be prepared. PC serves as a hydrophobic segment, so hydrophilic polymers such as polyethylene glycol, sodium polyacrylate, polystyrene sulfonate, amine-functional polymers, and carboxylic acid-functional polymers can be copolymerized to form amphiphilic structures. Those amphiphilic copolymers could be used as interfacial modifier and stimuli-responsive polymer systems.

The allyl group is a versatile functional group which allows various chemical modifications. Besides hydrosilylation chemistry used in this research, allyl end groups allow other chemistries such as thiol-ene chemistry. Other possible chemical strategies include transforming allyl groups into epoxy or hydroxyl functional groups and subsequently being cured using crosslinkers.